

University of Sheffield

Peak Voltage Stress in Inverter-Fed Machines and its Mitigation Measures



by
Shubham Sundeep

Supervisor: Prof. Jiabin Wang & Dr. Antonio Griffo

A report submitted in partial fulfilment of the requirements for the degree of Doctor of
Philosophy in Electrical Engineering.

in the
Department of Electronics and Electrical Engineering

June, 2022

CERTIFICATE

I, the author, confirm that the Thesis is my own work. I am aware of the University's Guidance on the Use of Unfair Means (www.sheffield.ac.uk/ssid/unfair-means). This work has not previously been presented for an award at this, or any other, university.

Name: Shubham Sundeep

Signature: 

Date: June 8, 2022

To, Maa & Papa

This thesis is dedicated to you.

If there was a word in the English dictionary whose meaning conveyed more gratitude and respect than the words Thank You, I would be saying that word to both of you a million times over.

ABSTRACT

Greenhouse gas (GHG) levels are at their highest in 2 million years, and emissions are continuing to grow. The major source of GHG emissions is the combustion of gasoline for transportation. Today, the transport industry is the biggest GHG emission sector in the UK, accounting for 28% of total emissions. Out of which, road transport accounts for 87%. Therefore, governments are making strides in increasing the use of electric vehicles (EVs).

In this context, EVs are the future strides. The translation to a sustainable electrified powertrain requires an electric traction system to offer better economy, extended range, fast charging, and autonomous driving. These capabilities are enabled using wide bandgap (WBG) devices in the electrified traction system, which are capable of operating at a higher switching frequency and fast switching speed.

However, a high voltage system with a higher switching frequency and fast switching speed cause enormous problems such as excessing voltage stress within winding causing premature failure, high-frequency (HF) common-mode and bearing current causing electromagnetic interference (EMI). The voltage stress across the insulation of the winding may cause premature failure resulting in unexpected downtime. As a result, the WBG based traction systems would suffer substantial economic and safety consequences. Therefore, a study is required to enhance the scientific understanding of the HF voltage excitation on the machine insulation and to suggest mitigation measures.

An HF model of the stator winding of the traction motor is proposed for the prediction of the voltage stress. The distinctive feature of the model lies in its explicit representation of the mutual coupling between the turns of the single or double layer winding in time-domain. The comprehensive modelling approach proclaims that the voltage distribution is a result of the anti-resonance phenomenon which can be characterised by the well-known voltage oscillations at the motor terminals, besides the proclaimed voltage oscillations at the neutral point. It is the latter, which engenders peak voltage stress and prevails under simultaneous excitation of the phase. The existing voltage mitigation measures are ineffectual in mitigating the newly found voltage stress. Therefore, this analysis proposes a mitigation measure, which is experimentally validated on the automotive grade 60kW motor employed in Toyota Prius hybrid vehicle.

ACKNOWLEDGEMENT

A doctorate degree is a challenging yet rewarding experience. I am deeply indebted to my supervisors, Prof. Jiabin Wang and Dr. Antonio Griffo without whom this experience would be unthinkable. Besides their engineering knowledge, their motivation drives me to a larger viewpoint, even beyond the field of electrical machines and drives. I am extremely grateful for the extent of freedom I received during this experience, which helped me in exploring the discipline unboundedly. Throughout the course, their insightful feedback and recommendations helped in shaping this research.

I would also like to extend my deepest gratitude to the Engineering and Physical Sciences Research Council (EPSRC) for supporting this research financially. I must also thank the Electronics and Electrical Engineering department for furnishing the laboratory with the state-of-art equipment required for the experimental validations.

Special thanks to the laboratory technical staff: Mr. Andrew M Race, Mr. Thomas Templeman, and Mr. Sam Marples, who assisted in developing the laboratory prototype. I gratefully acknowledge the assistance of Mr. Fahmi Mohammad, for lending the IT support, which was required for the development of the simulation environment, as well as assistance in utilising the high-performance computing facility of the university. I very much appreciate the Department Technical Manager, Dr. Stephen Mason and the Department Safety Officer, Mr. Stephen Gricmanis, for conducting this research on safe premises.

I also had the great pleasure of working with Dr. Fernando Alvarez Gonzalez, Dr. David Hewitt and Mr. Yinka Leo Ogundiran and wholeheartedly acknowledge the help and companionship I received over the years. The completion of this research could not have been accomplished without the support of my friends. Thank you for allowing me time away from you to research and write.

Finally, I express my heartfelt thanks for the unwavering support and encouragement of my Maa and Papa, which have always fuelled me to contribute back to society. Shivam, my brother, I have lived my life and shared everything with you since we were born. It's now the time to share this research with you. I cannot leave without mentioning my partner, Ipsita, whose relentless support and profound belief in my abilities have always kept me motivated.

TABLE OF CONTENTS

Abstract.....	i
Acknowledgement.....	iii
List of Acronyms.....	xi
List of Figures.....	xiii
List of Tables.....	xxi
Chapter 1: Introduction.....	1
1.1 Motivation	1
1.2 Scope and Aim	3
1.2.1 Scope of the Thesis.....	6
1.2.2 Aim of the Thesis	7
1.3 Disposition of Thesis.....	8
1.4 Contribution.....	11
1.5 Publications	12
1.5.1 Journal Papers (2).....	12
1.5.2 Journal Papers (Under Review) (2).....	12
1.5.3 Conference Papers (5)	12
Chapter 2: Literature Review	15
2.1 General	15
2.2 Insulation System	16
2.3 Stress on Insulation System.....	18
2.3.1 Thermal Stress	18
2.3.2 Electrical Stress	19
2.3.3 Ambient Stress.....	20

2.3.4 Mechanical Stress	21
2.4 Effect of High Frequency Voltage Excitation on Machine Winding	22
2.4.1 Voltage Stress within Machine Winding	23
2.4.2 High Frequency Ground Return Current	24
2.4.3 Bearing Currents	25
2.5 High Frequency Model of Cable and Stator Winding	27
2.6 Voltage Stress Mitigation Technique	39
2.6.1 Passive Filtering Technique	39
2.6.1.1 Passive Termination Filter	40
2.6.1.2 Inverter Output Filter	42
2.6.2 Active Filtering Technique	53
2.7 Summary	56
Chapter 3: Modelling High Frequency Behaviour of Shielded Cable	59
3.1 General	59
3.2 Multi-Conductor Transmission Line Model	60
3.2.1 Transmission Line Parameters	63
3.2.2 Transmission Line Equation	65
3.2.3 Time-Domain vs Frequency-Domain Solution	67
3.2.4 Equivalent Circuit Representation	69
3.3 Computation of Model Parameters	73
3.3.1 Capacitance Calculation	76
3.3.2 Inductance and Resistance Calculation	79
3.4 Representation of Frequency Dependent Parameters	82
3.5 Representation of Mutual Resistive and Inductive Coupling	88
3.6 Experimental Validation	90
3.6.1 Common-Mode and Differential-Mode Impedance Validation	90

3.6.2 Time-domain Validation	93
3.7 Summary.....	95
Chapter 4: Modelling High Frequency Behaviour of Machine Winding.....	97
4.1 General	97
4.2 Comparison between Power Cable Model and Machine Winding Model	98
4.3 Multi-Conductor Transmission Line model	102
4.3.1 Computation of Model Parameters.....	104
4.3.1.1 Capacitance Calculation.....	107
4.3.1.2 Inductance and Resistance Calculation.....	109
4.3.1.3 Core loss resistance calculation	111
4.3.1.4 Overhang inductance calculation	112
4.3.2 Representation of Frequency Dependent Parameters.....	113
4.3.3 Representation of Mutual Resistive and Inductive Couplings	113
4.4 Experimental Validation.....	120
4.4.1 Common-Mode and Differential-Mode Impedance Comparison	121
4.4.2 Time-domain Validation	127
4.5 Summary.....	130
Chapter 5: Voltage Distribution under PWM Voltage Excitation.....	133
5.1 General	133
5.2 Anti-Resonance Phenomenon	133
5.3 Voltage Stress at the Stator Terminal	135
5.3.1 Condition for Minimum Terminal Voltage Stress.....	136
5.3.2 Surge Impedance Calculation.....	139
5.3.3 Voltage Stress within Stator Winding under Single Voltage Pulse Excitation .	143
5.4 Voltage Stress Distribution within Winding	145
5.5 Voltage Stress at the Neutral Point.....	152
5.5.1 Travelling Wave Theory.....	152

5.5.2 Analytical Model of the Neutral Point Voltage Stress	154
5.6 Experimental Validation.....	156
5.6.1 Overshoot Factor Calculation.....	158
5.6.2 Analytical Model of the Neutral Point Voltage.....	160
5.6.3 Effect of Dwell Time between Switching Events	163
5.6.4 Effect of Switching Frequency	166
5.7 Interaction Between the Anti-Resonance Frequency of the Cable and Stator Winding	167
5.8 Summary.....	171
Chapter 6: Voltage Stress Mitigation Technique	175
6.1 General	175
6.2 Voltage Stress Mitigation at the Machine Terminals	175
6.2.1 Changing the system configuration	177
6.2.1.1 Influence of Cable Length	177
6.2.1.2 Influence of Cable Material Properties	177
6.2.2 Changing the Inverter Characteristics	178
6.2.2.1 Increasing Rise time:.....	178
6.2.2.2 Preventing Double Pulsing and Cross-Switching.....	178
6.2.2.3 Reducing Voltage Step during Switching.....	179
6.2.3 Installing Active/Passive Filters	180
6.3 Voltage Stress Mitigation using Sinewave Filter	181
6.4 Voltage Stress Mitigation using dV/dt Filter.....	183
6.5 Voltage Oscillations at the Neutral Point	186
6.6 Design of a Low Cost, Retrofit, Passive RC Filter.....	189
6.7 Experimental Validation.....	192
6.7.1 Voltage Stress Mitigation using Passive RC Filter	193
6.7.2 Optimum RC Filter Selection	195

6.7.3 Design Modification of dV/dt Filter	200
6.7.4 Effect of Combined dV/dt Filter and Proposed RC Filter	202
6.8 Summary.....	204
Chapter 7: Conclusion and Future Work.....	205
7.1 General	205
7.2 Conclusion.....	206
7.2.1 High-Frequency Modelling of Cable.....	206
7.2.2 High-Frequency Modelling of Stator Winding	207
7.2.3 Voltage Distribution under PWM Voltage Excitation	209
7.2.4 Voltage Stress Mitigation Technique	211
7.2.5 Guidelines for Safe Use of Electrical Machines under PWM Voltage Excitation:	212
7.2.6 Recommendations for the Revision of IEC 60034:25:2014 [15], IEC 60034:18:41 [56], and NEMA MG 1-2016 [172] Standards:.....	213
7.3 Future Work.....	214
7.3.1 High Frequency Model of Stator Winding.....	214
7.3.1.1 Representation of non-linear magnetic properties of core:.....	214
7.3.1.2 Representation of laminated core:	215
7.3.1.3 Core Loss model:	215
7.3.1.4 Modelling overhang region:.....	215
7.3.1.5 Modelling of the rotor core:.....	216
7.3.2 High-Frequency Model of the Voltage Source Inverter.....	216
7.3.3 Insulation Integrity and Lifetime Assessment under Voltage Stress.....	216
Appendix A: Cable Parameters	219
Appendix B: Stator Winding Parameters	221
Appendix C: MATLAB [®] Based High Frequency Model of the Stator Winding.....	223
References.....	225

LIST OF ACRONYMS

ACC	Active Common-noise Canceller
ASD	Adjustable Speed Drive
CM	Common Mode
DM	Differential Mode
EDM	Electrostatic Discharge Machining
EMI	Electromagnetic Interference
ESL	Equivalent Series Inductance
ESR	Equivalent Series Resistance
EV	Electric Vehicle
FAME	Faster Adoption and Manufacturing of Hybrid and Electric Vehicles in India
FE	Finite Element
FEM	Finite Element Method
GHG	Greenhouse Gas
HF	High Frequency
IATA	International Air Transport Authority
IPCC	Intergovernmental Panel on Climate Change
IR	Impedance Regulator
LF	Low Frequency
MCTL	Multi-Conductor Transmission Line
MV	Medium Voltage
OF	Overshoot Factor
PAI	Polyamide-Imide

PD	Partial Discharge
PDF	Probability Distribution Function
PDIV	Partial Discharge Inception Voltage
PE	Protective Earth
PILC	Paper Insulated Lead Covered
PMSM	Permanent Magnet Synchronous Machine
PWM	Pulse Width Modulation
SPWM	Sinusoidal Pulse Width Modulation
SVPWM	Space Vector Pulse Width Modulation
TEM	Transverse Electromagnetic
UK	United Kingdom
VF	Vector Fitting
VFD	Variable Frequency Drive
VPI	Vacuum and Pressure Impregnation
VSI	Voltage Source Inverter
WBG	Wide-Bandgap
XLPE	Cross-Linked Polyethylene
ZEV	Zero Emission Vehicle

LIST OF SYMBOLS

μ_0	Absolute permeability of the medium
ϵ_0	Absolute permittivity of the medium
W_{AV}	Average energy stored in the field
l_c	Cable length
Z_{0c}	Cable surge impedance
V_c	Cable voltage
C	Capacitance
C_{ov}	Capacitance between conductor and core in overhang region
C_{slot}	Capacitance between conductor and core in slot region
c	Capacitance per-unit length
ρ	Charge distribution
N_C	Coils per phase
Z_{CM_0}	Common-mode impedance at anti-resonance frequency
G	Conductance
g	Conductance per-unit length
R_e	Core loss resistance
$l_{cable_{cr}}$	Critical cable length
I_0	Current amplitude
\vec{j}	Current density
ω_c	Cut-off frequency
ζ	Damping factor
V_{DC}	DC-Link voltage

Z_{DM_0}	Differential-mode impedance at anti-resonance frequency
I_d	Displacement current
D	Duty ratio
T_a, T_b	Dwell time of active vectors
I_e	Eddy current
\vec{E}	Electric field intensity
\vec{E}_t	Electric field intensity in transverse direction
\vec{D}	Electric flux
C_f	Filter capacitance
Z_{filter}	Filter impedance
L_f	Filter inductance
R_f	Filter resistor
ω_f	Filter resonant frequency
$f_{ar_{c(1)}}$	First anti-resonance frequency of cable
$f_{ar_{(c+m)(1)}}$	First anti-resonance frequency of combined cable and machine winding
$f_{ar_{m(1)}}$	First anti-resonance frequency of machine winding
$f_{r_{c(1)}}$	First resonance frequency of cable
$f_{r_{m(1)}}$	First resonance frequency of machine winding
Ψ_{ij}	Flux linkage between conductor i and j
ω_s	Fundamental frequency in $rads^{-1}$
I_g	Ground return current
L	Inductance
L_{ovT}	Inductance of a turn in overhang region

l	Inductance per-unit length
v_L	Inductor voltage drop
V_{in}	Inverter terminal voltage
l_{cable}	Length of cable
l_{ov}	Length of conductor in overhang region
l_m	Length of machine winding
l_{medium}	Length of medium in the direction of propagation
Z_{0m}	Machine surge impedance
V_t	Machine terminal voltage
\vec{B}_t	Magnetic field density in transverse direction
\vec{H}	Magnetic field intensity
\vec{H}_t	Magnetic field intensity in transverse direction
\vec{A}	Magnetic vector potential
ϕ_{max}	Maximum flux linkage
f_{max}	Maximum frequency of oscillation of TEM
L_{ij}	Mutual inductance between conductor i and j
v_N	Neutral point voltage
N_p	Parallel conductors per turn
μ_c	Permeability of the cable
μ_m	Permeability of the machine winding
μ	Permeability of the medium
ε	Permeability of the medium
ε_c	Permittivity of the cable
ε_m	Permittivity of the machine winding

C_c	Per-unit length cable capacitance
L_c	Per-unit length cable inductance
t_p	Propagation delay
Γ	Reflection coefficient
μ_r	Relative permeability of the medium
ε_r	Relative permittivity of the medium
R	Resistance
r	Resistance per-unit length
P	Resistive power loss
I_{rms}	RMS current
$f_{ar_{c(2)}}$	Second anti-resonance frequency of cable
$f_{ar_{(c+m)(2)}}$	Second anti-resonance frequency of combined cable and machine winding
$f_{ar_{(f+c+m)(2)}}$	Second anti-resonance frequency of combined filter, cable and machine winding
$f_{ar_{c(2)}}$	Second anti-resonance frequency of machine winding
λ_{min}	Shortest wavelength of the TEM
δ	Skin depth
t_r	Slew rate
I_S	Source current
l_{stack}	Stack length of the stator core
W_e	Stored energy in electrostatic field
Z_0	Surge impedance
f_{sw}	Switching frequency
\mathcal{G}	TEM wave velocity in a medium

\mathcal{G}_c	TEM wave velocity in cable
\mathcal{G}_m	TEM wave velocity in machine winding
N_T	Turns per coil
τ_A	Voltage pulse impinging instant at phase A terminal
τ_B	Voltage pulse impinging instant at phase B terminal
τ_C	Voltage pulse impinging instant at phase C terminal

LIST OF FIGURES

Figure 1.1: Drivetrain of an electric vehicle [11].	5
Figure 1.2: Schematic representation of the traction motor fed by a traction inverter through a power cable.	5
Figure 2.1: Cross-section of a random wound machine stator slot representing the insulation system [45]......	16
Figure 2.2: Schematic of VSI fed drive representing the path of bearing currents, ground return current and the cable discharge current	23
Figure 2.3: Classical inductive bearing current, (a) unsymmetrical flux in the four pole machine due to reluctance fault [82], (b) bearing current due to flux encircling the shaft.....	25
Figure 2.4: Schematic of VSI fed drive representing the path of bearing currents, ground return current and the cable discharge current.	26
Figure 2.5: Schematic of VSI-fed drive with Parallel resistors connected at the machine terminals.....	41
Figure 2.6: Schematic of VSI-fed drive with filters connected at the machine terminal, (a) First order termination filter, (b) Second order termination filter.	42
Figure 2.7: Schematic of VSI-fed drive with reactor filter connected at the inverter terminals.	43
Figure 2.8: Schematic of VSI-fed drive with sinewave filter connected at the inverter terminals.....	45
Figure 2.9: Schematic of VSI-fed drive with a combination of sinewave and LC trap filter connected at the inverter terminals.	45
Figure 2.10: Schematic of VSI-fed drive with dV/dt filter connected at the inverter terminals.	46
Figure 2.11: Schematic of VSI-fed drive with CM filter connected at the inverter terminals.	48
Figure 2.12: Schematic of VSI-fed drive with CM filter connected at the inverter terminals; (a) CM filter connected with RC network, (b) CM filter connected with 3-phase transformer.	49
Figure 2.13: Schematic of VSI-fed drive with combination of sinewave and CM filter connected at the inverter terminals.	50

Figure 2.14: Schematic of VSI-fed drive with active common-noise canceller circuit connected at the inverter terminals.54

Figure 2.15: Schematic of VSI-fed drive with sinewave filter connected at the inverter terminals and an active motor impedance regulator is connected at the motor terminals.54

Figure 2.16: Schematic of VSI-fed drive with active common-noise canceller (ACC) realised using isolated power supplies and connected at the inverter terminals.55

Figure 3.1: Multi-conductor transmission line embedded in homogeneous medium.....61

Figure 3.2: Transverse electromagnetic field structure in a multi-conductor transmission line representing (a) electric field intensity, (b) magnetic field intensity.61

Figure 3.3: (a) lumped parameter circuit representing a section of a cable, (b) Continuum of lumped parameter circuit used for cable model66

Figure 3.4: (a) A periodic pulse train representing the output of the PWM inverter, (b) Spectral spread of the pulse train.70

Figure 3.5: Lumped parameter circuit representing a section of cable called cell; (a) lumped-Pi circuit, (b) lumped-T circuit72

Figure 3.6: Schematic of the method to obtain the time-domain response of a lumped parameter transmission line circuit.73

Figure 3.7: Schematic diagram of the cross-section of 4-wire shielded cable.....74

Figure 3.8: Conductor cross-section representing (a) the magnetic field distribution, (b) Meshing used to calculate the frequency dependent parameters.75

Figure 3.9: Frequency dependent self-impedance of phase A conductor computed using FEM.82

Figure 3.10: (a) Cross-section of a phase conductor divided into the annular region; (b) Ladder circuit representing the impedance of each annular region.83

Figure 3.11: Proposed procedure for the development of the Ladder circuit using vector fitting.....85

Figure 3.12: Time-domain circuit representing frequency dependent series impedance of phase A conductor, (a) RL-Ladder circuit, (b) Frequency response of the RL-Ladder circuit.86

Figure 3.13: Time-domain circuit representing frequency dependent shunt impedance, (a) CG-Ladder circuit, (b) Frequency response of the CG-Ladder circuit.....87

Figure 3.14: HF model of the cable using lumped parameter circuit connected in continuum.89

Figure 3.15: Experimental rig used for measuring the CM and CM impedance of the cable. 91

Figure 3.16: Schematic of experimental measurement of common-mode and differential-mode impedance.91

Figure 3.17: Impedance comparison between experimental measurement and prediction; (a) Common-mode impedance, (b) Differential-mode impedance.92

Figure 3.18: Schematic diagram of the experimental rig used for the validation of cable model.....94

Figure 3.19: Experimental rig used for the time-domain validation of the cable model under PWM voltage pulse excitation.94

Figure 3.20: Experimental validation of cable model under PWM voltage excitation with 200V DC link voltage, 40kHz switching frequency, and 60ns rise time; (a) Load end voltage comparison, (b) Load end voltage over one switching instant.95

Figure 4.1: B-H curve of the electrical steel representing non-linear magnetic properties. .. 100

Figure 4.2: Continuum of lumped- Γ circuit representing MCTL model of the stator winding. 104

Figure 4.3: Schematic diagram of the cross-section of a stator slot of the stator winding. ... 105

Figure 4.4: Stator winding [29] of the 60kW PMSM employed in Toyota Prius electric vehicle. 107

Figure 4.5: Overhang region of the winding representing the separation between the core and the winding..... 108

Figure 4.6: Frequency dependent impedance of turn 1 with and without core loss resistance. 112

Figure 4.7: Proposed procedure for the development of the Ladder circuit using vector fitting [144]. 114

Figure 4.8: Frequency response of 6th order Ladder circuit representing the self-impedance of turn 1 of line end coil. 114

Figure 4.9: Lumped parameter model of a phase winding representing the frequency dependent self-impedance with explicit representation of the mutual coupling between the turns..... 116

Figure 4.10: Mutual resistive coupling between turn 1 and the remaining 10 turns embedded in the same slot..... 117

Figure 4.11: Lumped parameter model of a phase winding representing the frequency dependent self-impedance with a simplified representation of the mutual coupling between the turns..... 118

Figure 4.12: Flowchart representing the HF modelling of the machine winding..... 120

Figure 4.13: Experimental rig used for measuring the CM and CM impedance of the stator winding 121

Figure 4.14: Experimental impedance measurement of the stator winding under study, (a) schematic of the CM impedance measurement, (b) schematic of the DM impedance measurement. 122

Figure 4.15: Comparison between the predicted and measured impedance (a) CM impedance, (b) DM impedance. 122

Figure 4.16: Effect of mutual coupling on the impedance (a) CM impedance, (b) DM impedance. 124

Figure 4.17: Comparison between the methods to include mutual coupling in the model, when only the first 5 turns are modelled with rest turns are represented by lumped circuit [37], and mutual-impedance is added to the self-impedance [38]. (a) CM impedance, (b) DM impedance. 125

Figure 4.18: Comparison of the impedance of the model between explicit and simplified representation of the mutual coupling, (a) CM impedance, (b) DM impedance. 126

Figure 4.19: Schematic representation of the stator winding fed by a SiC MOSFET based inverter through a 2.5m long shielded cable..... 128

Figure 4.20: Experimental rig illustrating Toyota manufactured stator sample fed by 3-phase MOSFET based inverter through 2.5 m shielded cable..... 128

Figure 4.21: Coil-to-core voltage under PWM voltage excitation, 500V DC link voltage, 20ns rise time and 40kHz switching frequency (a) Measured, (b) Predicted..... 129

Figure 5.1: An open ended uncharged 2.5m long cable excited through a three phase VSI. . 134

Figure 5.2: Voltage stress at the open end of the cable under single pulse excitation..... 135

Figure 5.3: CM Impedance of a 2.5m long shielded cable. 135

Figure 5.4: Variation of OF w.r.t. cable length for an uncharged cable under single pulse voltage excitation..... 137

Figure 5.5: Variation of OF w.r.t. ratio of cable length and critical cable length for an uncharged cable under single pulse voltage excitation..... 138

Figure 5.6: CM impedance of a 2.5m long shielded cable under study, (a) schematic of the CM impedance measurement, (b) the measured CM impedance. 141

Figure 5.7: CM impedance of the stator winding under study, (a) schematic of the CM impedance measurement, (b) the measured CM impedance. 142

Figure 5.8: Voltage stress at the machine terminal under single voltage pulse excitation. ... 142

Figure 5.9: Electrical machine under excitation using a three phase VSI through a 2.5 long cable. 143

Figure 5.10: Coil-to-core voltage representing voltage distribution within winding under single voltage pulse excitation. 144

Figure 5.11: Measure CM impedance of the cable, stator winding and the cable connected stator winding..... 144

Figure 5.12: Coil-to-core voltage representing voltage distribution within winding at 550V DC link voltage under PWM voltage pulse excitation. 146

Figure 5.13: Enlarged view of the Coil-to-core voltage for the first and the last coil from the terminal end at 550V DC link voltage under PWM voltage pulse excitation 146

Figure 5.14: Voltage across the coils at 550V DC link voltage under PWM voltage pulse excitation; (a) voltage across 8 coils, (b) enlarged view during a switching event. 147

Figure 5.15: Phase-to-core and phase-to-phase voltage measured at 0.5 modulation index, 40kHz switching frequency, 20ns rise time and 550V DC link voltage, under PWM voltage pulse excitation. 148

Figure 5.16: Enlarged view of voltage stress during a switching event under PWM voltage pulse excitation; (a) phase-to-core, (b) phase-to-phase voltage..... 149

Figure 5.17: Voltage across the turns of the first coil of phase A under PWM voltage pulse excitation; (a) voltage across first five turns and the last urn of the coil, (b) enlarged view during a switching event. 151

Figure 5.18: Peak voltage across the first turns of first coil of phase A with respect to the rise time under PWM voltage pulse excitation..... 152

Figure 5.19: Experimental rig illustrating Toyota manufactured stator sample fed by 3-phase MOSFET based inverter through 2.5 m shielded cable. 157

Figure 5.20: Schematic diagram of the 3-phase MOSFET based inverter fed electrical machine through 2.5 m shielded cable..... 158

Figure 5.21: Experimentally measured coil-to-core voltage under PWM voltage excitation. 158

Figure 5.22: Experimentally measured CM impedance of (a) 2.5m long shielded cable, (b) Stator winding used in Toyota Prius hybrid vehicle..... 159

Figure 5.23: Experimental measurement of damping factor (ζ) and damped frequency of oscillation (ω). 160

Figure 5.24: Implementation of the analytical model for calculating the voltage stress at the neutral point. 161

Figure 5.25: Flowchart representation of the analytical model for predicting neutral-to-core voltage..... 162

Figure 5.26: Experimental validation of the proposed analytical model at 40 kHz switching frequency and 100V DC link voltage; (a) $m = 0.01$, (b) $m = 0.3$, (c) $m = 0.5$ 164

Figure 5.27: Peak-to-peak neutral-to-core voltage expressed in per-unit with respect to the 100V DC link voltage under PWM inverter operation at 40 kHz switching frequency..... 166

Figure 5.28: Peak-to-peak neutral-to-core voltage expressed in per-unit with respect to the 100V DC link voltage under PWM inverter operation at 20 kHz switching frequency..... 166

Figure 5.29: Comparison of CM impedance measured experimentally with different lengths of cable; (a) CM impedance of the cable, (b) CM impedance of cable connected to the stator winding. 168

Figure 5.30: Experimentally measured voltage stress at the terminal and at the neutral point of the machine with respect to the core (DC Link voltage = 300 V); (a) when the cable length is 2.5 m, (b) when the cable length is 163 m, (c) when the cable length is 180 m. 169

Figure 5.31: Experimental validation of the proposed analytical model at 40 kHz switching frequency with 163m long cable..... 170

Figure 5.32: Peak-to-peak neutral-to-core voltage expressed in per-unit with respect to the 100V DC link voltage under PWM inverter operation at 40 kHz switching frequency and 163m long cable..... 170

Figure 6.1: Schematic of a Toyota Prius hybrid vehicle employed stator winding fed by a SiC based VSI through a 2.5 long shielded cable..... 176

Figure 6.2: Schematic of VSI-fed drive with sinewave filter [118]. 181

Figure 6.3: CM impedance measurement with sinewave filter. 183

Figure 6.4: Voltage stress within the winding with Sinewave filter.....	183
Figure 6.5: Schematic of VSI-fed drive with dV/dt filter [121].	184
Figure 6.6: CM impedance measurement with dV/dt filter.	185
Figure 6.7: Voltage stress within the winding with dV/dt filter.	185
Figure 6.8: Conventional VSI-fed drives, wherein, the electrical machine is connected to the VSI through a 2.5m long shielded cable.	187
Figure 6.9: Experimentally measured neutral point voltage at three modulation indexes (m); (a) m = 0.01, (b) m = 0.3, (c) m = 0.5.	187
Figure 6.10: Experimentally measured CM impedance of the machine winding.....	188
Figure 6.11: Experimentally measured neutral point voltage at different cable length (l); (a) l = 2.5m, (b) l = 0.5m.	189
Figure 6.12: Experimental measured CM impedance of the cable connected stator winding with and without a resistor connected across the neutral point and the core of the machine.	190
Figure 6.13: Proposed passive filter connected between the neutral point and the core of the machine.	190
Figure 6.14: Experimental impedance measurements used for filter design (a) CM impedance, (b) DM impedance.	191
Figure 6.15: Experimentally measured CM and DM impedance of the cable connected machine winding.	192
Figure 6.16: Frequency-dependent equivalent circuit of the machine based on CM DM impedance measurement, (a) II circuit, (b) T Circuit, (c) Equivalent circuit with a proposed RC filter.	192
Figure 6.17: Experimental rig understudy illustrating Toyota Prius vehicle connected to a three-phase VSI through 2.5m long shielded cable.	193
Figure 6.18: Experimentally measured voltage stress within winding when no filter connected to the machine.	194
Figure 6.19: Experimental prototype of the proposed RC filter connected to the Toyota Prius hybrid vehicle employed stator winding.	194
Figure 6.20: Experimentally measured CM impedance with a proposed RC filter.	195
Figure 6.21: Experimentally measured voltage stress within winding with RC Filter, R = 165Ω, C = 4.7nF.	195
Figure 6.22: Performance of the proposed RC filter with different capacitance.	196

Figure 6.23: Performance of the proposed RC filter with different resistance. 197

Figure 6.24: Experimentally measured voltage stress within winding with RC Filter ($R = 75\Omega$, $C = 2.2nF$). 197

Figure 6.25: Comparison between different RC filter w.r.t experimentally measured parameters, (a) Filter loss comparison, (b) Filter RMS current comparison, (c) Neutral point voltage stress comparison 198

Figure 6.26: Schematic of dV/dt filter, (a) 3-Phase circuit, (b) Single phase equivalent circuit. 200

Figure 6.27: Schaffner Manufactured dV/dt Filter [171], (a) Actual filter, (b) Schematic of the filter..... 201

Figure 6.28: Experimentally measured CM impedance with Schaffner manufactured dV/dt filter..... 202

Figure 6.29: Experimentally measured voltage stress within winding with different filters. 203

Figure 6.30: Effect of the resonance frequency of dV/dt filter on its CM impedance and filter parameters. 203

LIST OF TABLES

Table 2.1: A comparative analysis of the modelling methods.....	35
Table 2.2: A comparative analysis between different types of inverter output filters.....	51
Table 3.1: Parameters of shielded cable	74
Table 3.2: Parameters of RL-Ladder circuit representing the impedance of phase A conductor	86
Table 4.1: Stator dimensions [29] and properties of insulation.....	105

Chapter 1: Introduction

1.1 Motivation

Climate change is already having a visible impact on the planet. We are already facing devastating consequences around the world like changing rainfall patterns, rising sea levels and rising average global temperature. These changes are causing fire-ravaged Amazon, historic drought and wildfire in the west USA, unprecedented flooding, and storms in the southwest USA, and shrinking coastline of many pacific islands, such as Maldives, Tuvalu, and the Marshall Islands to the name just a few are in danger of disappearing over the coming decades, sweltering urban centres of India's national capital, Delhi, and record heatwaves across the world. In a recent report, the Intergovernmental Panel on climate change (IPCC) reveals that the average global temperature is increasing by 1.5 to 2⁰ C due to global warming [1]. However, unless we take steps to curb global warming the increase in temperature is likely to exceed 2⁰ C [1]. By the end of this century, the temperature rise could reach 4⁰C, possibly more [1]. According to IPCC, the average global temperature has increased more than 1⁰ C since the 1850s [2]. 2015-2020 were the hottest year recorded ever [1]. Due to increasing temperature, the ice sheets in the Arctic region are melting fast. The thick ice sheets are now 65% thinner than in 1975 [1]. When the ice sheets and glacier melts, freshwater flows into the sea, which increases its level. Since 1880, the mean sea level has increased by 21-24 cm [3]. Nearly 39% of the population living within 100km of the seacoast are at the risk of flooding due to increasing sea levels [4].

Climate change is also warming the United Kingdom (UK). As of the summer of 2018, heat waves are 30 times more likely to happen every other year due to climate change [1]. In 50 years, by 2070, the winter will be 1 - 4.5⁰ C warmer and up to 30% wetter, and the summer will be 1 – 6⁰ C warmer and up to 60% dryer [1]. Since 1998, the UK has seen six out of ten wettest years on record [4]. Winter storms like 2015, are at least 40% more likely to happen because of climate change [4].

The science is very clear: we are heading towards climate disaster unless we achieve net-zero emission until mid-century. The time is now for decisive action. The world is now united

under an international treaty on climate change such as Paris Agreement-21 [5], and the UN Framework Convention on Climate Change to lay action plans for curbing climate change.

The main cause of climate change is greenhouse gases (GHGs) which are emitted by burning fossil fuels such as oil, gas, and coal. Today, in the UK, the transport sector is emitting 28% of GHG emissions [6], the largest GHG emitter. Out of which, road transport accounts for 87% [6]. Already the world is making strides in increasing the market share of Zero Emission Vehicle (ZEV) and many billions of pounds of private investments are pledged across the globe in the research and development of electric vehicles (EVs), batteries, and infrastructure for charging stations. A ZEV is an EV that runs completely CO₂-free in Tank-to-Wheel mode, which requires a renewable energy powered charging network.

UK government is committed to phasing out the sales of all gasoline-based cars and vans by 2030 and all the new cars and vans will be fully zero-emission at the tailpipe from 2035 [7]. By 2027, all the government car and van fleets to be 100% emission-free [7]. In 2021, the USA re-joined Paris Agreement and set an ambitious target to reduce net GHG emissions by 50-52% in 2030 and commits to achieving net-zero emission no later than 2050 [8]. To support this ambitious target, the USA has set a goal for half of all new light-duty cars sold in 2030 to be ZEVs [8]. India is also committed to reducing the emission to net zero by 2070 with a 45% reduction in emissions by 2030 [9]. The Indian government has set aside \$96.8 million for a programme called FAME (Faster Adoption and Manufacturing of Hybrid and Electric Vehicles in India) [9], as well as other supply and demand-side incentives to encourage people to convert to EVs. 18 of the 28 states in India have either drafted or already announced their own ambitious EV goals.

The aviation sector is also a major emitter of GHGs. The International Air Transport Authority (IATA) has launched an aircraft technology roadmap to 2050 in which all stakeholders of the aviation industry are committed to reducing net carbon aviation emissions by 50% by the year 2050 relative to 2005 [10]. The USA is committed to producing 3 billion gallons of sustainable aviation fuel by 2030 [8]. Electric propulsion does not emit GHGs, this makes them crucial technology in achieving the environmental goal by 2050. Under the 2050 goal, electric air taxi service will be introduced for urban mobility by 2025, small hybrid-electric aircraft for commercial and business purposes will be introduced by 2030, and battery-powered aircraft on short-haul flights will be introduced by 2050 [10].

In this context, EVs and; All-electric and hybrid-electric aircraft are the future strides. The translation to a clean, efficient and sustainable electrified powertrain requires high power electric traction system to offer enhanced performance, controllability and capabilities such as better economy, extended range, fast charging, and autonomous driving. These features are possible by the adoption of wide-bandgap (WBG) based devices which are capable of operating at a higher switching frequency and fast switching speed. Currently, Tesla has unveiled a powertrain using 650V, 100A SiC MOSFET employed in its Model S vehicle [11]. Also, Siemens has developed a 104 kVA SiC based inverter for electric and hybrid-electric aircraft which fits in a box of 1.58 × 3.7 × 5.55 in and weighs only 1.98 pounds [12]. In addition, the SiC based power converters developed by Siemens for rail vehicles and electric busses incur 50% fewer losses with twice the power-weight ratio [13]. A high switching frequency can reduce the filter component which increases the power density of the traction system and a faster switching speed reduces the switching losses which makes the traction system efficient. With the adoption of WBG based devices, higher DC link voltage is being considered for the traction system which results in lower current. A low current system has the advantage of copper saving, high power density, fewer copper losses, and efficient cooling.

However, a high voltage system with a higher switching frequency and fast switching speed cause enormous problems such as voltage overshoot at the traction motor terminals [14-19], excessive voltage stress within winding causing premature failure [20-21], high frequency (HF) common mode (CM) ground current [22] and bearing current [23-25] causing electromagnetic interference (EMI) [26]. The voltage stress across the insulation of the winding may cause premature failure resulting in unexpected downtime. As a result, WBG based traction systems in all applications, including safety-critical transportation systems, would suffer substantial economic and safety consequences. Therefore, a study is required to enhance the scientific understanding of the impact of WBG based devices on the machine insulation and to suggest mitigation measures.

1.2 Scope and Aim

Almost all electric traction system requires the same power electronics components on board. A typical electric traction system installed in an EV is illustrated in Figure 1.1, which comprises a traction battery pack feeding the traction motor which drives the vehicle's wheel, a traction inverter which converts battery DC power to feed AC motor, DC fast charging system and

auxiliary power converter which supplies power to ancillary loads. The main power electronic components responsible for the vehicle propulsion is illustrated in Figure 1.2 and includes a traction battery pack connected to voltage source inverter (VSI) which feeds the traction motor through the power cable. The system as a whole is often called an electric drive. Each component of the drive has a key role in propulsion, as described below:

- *Traction battery pack*: Onboard, is the prime source of energy which drives the traction motor. Commonly, its nominal voltage ranges from 350 to 400V [27] with battery capacity varying between 10kWh and 100kWh, depending upon the vehicle's power and mileage. Recently, significant efforts are made to increase the voltage level to 800V [27] to leverage its benefits of lower losses, higher efficiency, copper saving and lighter vehicle.
- *Voltage Source Inverter (VSI)*: It acts as a power conversion device also known as a traction inverter which converts the DC power stored in the traction battery to AC power, which is required for the AC traction motor. The output of the VSI is three phase pulse width modulated (PWM) rectangular voltage pulse. The VSI manages the flow of power required for controlling the torque and speed of the motor by adjusting the fundamental frequency and the frequency of the voltage pulse. During braking, the kinetic energy of the wheel is transferred back to the battery pack by reversing the power flow using VSI. This form of braking is called regenerative braking [28]. It is more effective than conventional braking as the energy dissipated in the form of heat resulting from the friction between the brake pads and the wheel is captured back in the form of electrical energy. This extends the range of the EV. However, the efficiency of capturing the energy varies between 16 to 70% [28].
- *Power Cable*: The power cable is used to transfer power from the VSI to the traction motor. Generally, shielded three phase cable is used to reduce the EM emission and interference.
- *Traction motor*: It is directly connected to the wheels through differentials to provide the required torque and speed. Its power rating ranges from 10kW to 100kW depending upon the vehicle power and mileage. The third generation of the Toyota Prius vehicle uses a 60kW permanent magnet synchronous machine (PMSM) [29].

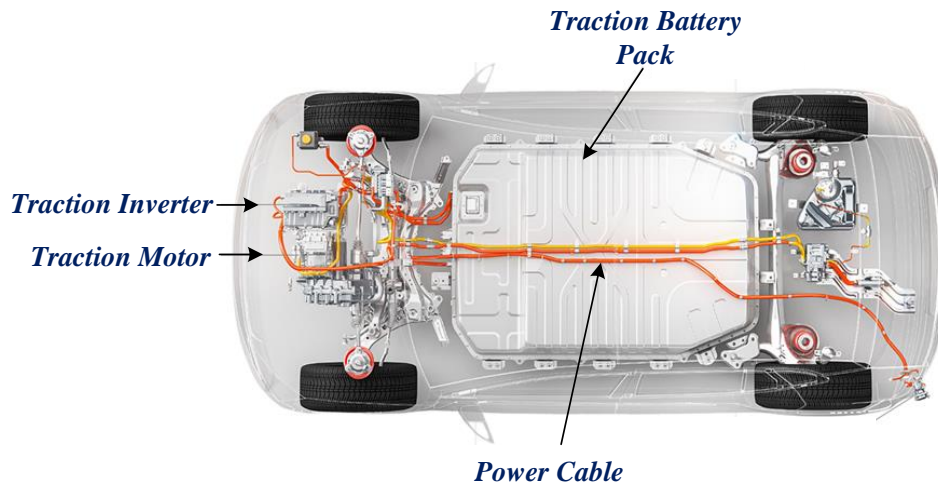


Figure 1.1: Drivetrain of an electric vehicle [11].

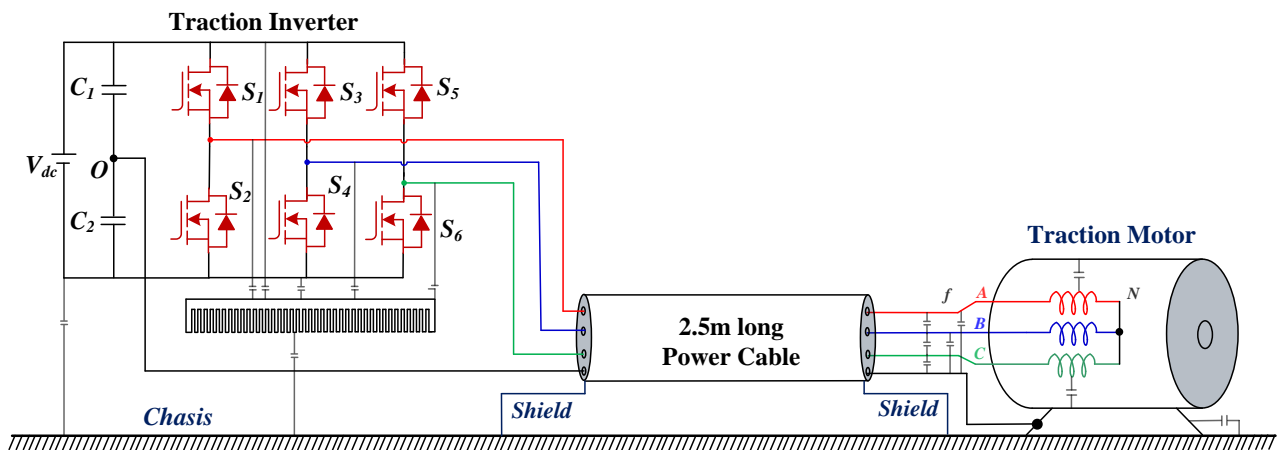


Figure 1.2: Schematic representation of the traction motor fed by a traction inverter through a power cable.

On the demand of government regulations and consumer preferences, there has been a continuous pursuit for the EV with high-performance parameters including, low emission, long driving range, high speed, lightweight, fast charging, and high efficiency. Electrification inevitably requires the processing of power in MW in aviation applications and several hundreds of kW in EV applications. Consequently, extremely high efficiency as high as 99% with a power density higher than 20kW/kg is required for the onboard power electronics converters [30]. Such an ambitious target is difficult to achieve with Si based semiconductor devices. This is possible with the synergy between the WBG based devices and EVs. The WBG based semiconductor devices have lower on-state resistance and fast switching speed as compared to their Si counterpart [31-33]. Thereby, the conduction loss and the switching loss are less in the WBG based devices. The WBG based devices can operate at higher switching frequencies and under higher ambient temperatures [34-35]. Thus, they are best suited for long-

range EVs with low inductance motors. Higher switching frequency translates to reduced filter size, resulting in increased power density of the VSI. Further, lower losses lead to efficient power conversion, which translates to reduced power consumption, extended driving range and increased passenger compartment in the vehicle. Illustratively, when the Si based IGBT and diodes in the 2010 Toyota Prius vehicle is replaced by SiC based MOSFETs and JBS diodes, the fuel economy is increased by 5%, with 80% reduction in power conversion unit [36].

However, adopting these features of the WBG based devices brings new challenges. Fast switching under a high switching frequency results in high dV/dt which excites the parasitic capacitance of the DC bus, cable and the motor and generates additional EMI [26]. In addition, the high dV/dt of the voltage excitation causes unenviable voltage stress across the winding insulation [14-19]. Under HF voltage excitation, the current leaks through these parasitic capacitances and flows through the local ground which is termed CM current [22]. The HF CM current therein interferes with the nearby electronic or electrical appliances and causes malfunction. Indeed, these issues can be addressed by reducing the switching speed of the devices. However, switching at a lower speed will result in underutilization of the benefits of the WBG devices which are crucial to offsetting its high cost. Moreover, switching at a lower speed will increase the switching losses, thus requiring an enhanced cooling mechanism which will downsize the power density of the converter. These measures will adversely affect the performance parameters of the drivetrain such as an increase in power consumption, reduced driving range, increased weight, and the reduction in the passenger compartment. Inevitably, following the government regulations and the customer demands, the benefits of the WBG devices cannot be ignored. Thereby, a comprehensive study is required to overcome the challenges involved in the proliferation of the WBG devices in the drivetrain.

1.2.1 Scope of the Thesis

The proliferation of the WBG devices poses several challenges mainly the excessive voltage stress across the winding insulation. The output of the traction inverter is a train of the steep fronted voltage pulse. Several studies in the literature [14-19] show that the steep fronted voltage transients emerging from traction inverter result in excessive voltage stress at the terminals of the traction motor with non-uniform voltage distribution within its winding. Further, the peak voltage stress occurs across the first few turns of the winding from the line end. Consequently, the voltage stress may lead to premature insulation failure. Also, the peak

voltage stress increases as the voltage slew rate increases, which further aggravates insulation deterioration.

The scope of the thesis spreads to the investigation of voltage stress within the winding under fast slew rate PWM voltage excitation and the development of the mitigation techniques for suppressing the excessive voltage stress leading to a prolonged lifetime of the motor. Based on the analysis, the thesis will draw the recommendations and suggestions for safe and prolonged use of the WBG based inverters in electric drives.

1.2.2 Aim of the Thesis

Recent WBG based semiconductor devices are pivotal in the electrification of the transportation sector. Although their supremacy has the potential to achieve ambitious targets, several challenges impede their proliferation. Accordingly, the aim of the thesis spreads to the identification and analysis of these barriers, developing the necessary tools and methodology to resolve the challenges and exploring and demonstrating the solutions. In particular, the scope of the thesis spreads to the following:

- *High Frequency Modelling*: The behaviour of the electric drive must be thoroughly understood to comprehend the influence of the HF voltage excitation. Previously, many studies [30-33] have used the HF model to represent the behaviour. The HF model includes the representation of the parasitic impedance of the electric drive such that it behaves similar to the drive over a wide range of frequencies. However, it involves several challenges, in particular, the representation of the frequency dependent mutual coupling in time domain analysis. Henceforth, the following work aims to develop an HF model of the cable connected traction motor which represents its behaviour over a wide range of frequencies with explicit representation of the frequency dependent mutual couplings.
- *Characterising Voltage Distribution*: It is necessary to identify the location of excessive voltage stress under PWM voltage excitation. This can be accomplished by characterising the voltage distribution within the cable connected motor. One of the ways is to excite the cable connected motor with a PWM voltage pulse and record the voltage stress at a different location within the motor. However, in general, only the terminal ends of the motor are accessible. Therefore, this work aims to characterise the voltage distribution using the developed HF model. Further, characterising the

voltage distribution will aid in identifying the location of excessive voltage stress within the winding.

- *Voltage Stress Mitigation Technique*: For prolonged use of the motor under PWM voltage excitation, the insulation under excessive voltage stress must be relaxed. Therefore, this research work aims to devise a method to suppress the voltage stress.
- *Recommendations for the Safe Use of Motor with WBG based Inverter*: Based on the observations and the results, this research work aims to outline the guidelines and recommendations for the safe use of the motor with the WBG based inverter.

1.3 Disposition of Thesis

The thesis is organised into seven chapters, whose content is summarised as follows:

- *Chapter 1: Introduction*

In this chapter, the problem statement addressed in this thesis is introduced. The chapter includes the pursuit of achieving zero-emission in the transportation sector which is impractical without the proliferation of WBG based devices. However, using WBG devices in onboard power electronics devices involves several challenges including voltage stress across the motor insulation. Excessive voltage stress may cause premature failure of the insulation resulting in unexpected downtime and revenue loss. Therefore, the thesis aims to address the voltage stress across the insulation. Later, the scope of the thesis is defined which expands to the exploration of the methods to characterise, assess, and mitigate the voltage stress. Further, the aim of the thesis is defined which spreads to the modelling HF behaviour of the cable and the motor winding, characterisation and prediction of the voltage stress within the winding, understanding of the mechanism governing the voltage stress, mitigation methods of the voltage stress, and the recommendations and suggestions for safe use of the WBG based inverter with the electric motors. Next, the disposition of the thesis and the contribution made during the study are mentioned. In the end, the key findings of this research disseminated in the form of publications are listed.

- *Chapter 2: Literature Review*

This chapter includes a comprehensive review of the literature which studies the methods of modelling HF behaviour of the cable connected stator winding of the motor. The chapter assesses the merits and demerits of the methods and propounds the best method in terms of

representation, parametrization, and implementation, which is used in this research. Later, the chapter reviews the previous studies which establish the voltage distribution within the winding, identifies the location of peak voltage stress and describes the mechanism of voltage distribution within the winding. Next, the chapter reviews the mitigation methods for suppressing the voltage stress, especially the voltage stress at the machine terminals. The chapter reviews both, the active and passive mitigation techniques and list their merits and demerits. In the end, the chapter summarises the recommendations made in the IEC standards for the safe use of WBG based VSI in the electric drive.

- *Chapter 3: Modelling High Frequency Behaviour of Shielded Cable*

In this chapter, HF modelling of the shielded cable is comprehensively discussed. In particular, the chapter describes the multi-conductor transmission line (MCTL) model for realising the wave propagation and reflection phenomenon within the cable. Due to the complex solution of the transmission line equation, while incorporating frequency dependent mutual coupling, the chapter describes the model as a continuum of lumped parameter circuits. The chapter describes a method for parameterization, which is based on the finite element (FE) modelling of the cable cross-section. Further, the chapter proposes a method to represent the frequency dependent mutual coupling in the time domain solution. In the previous models, either the mutual impedance was ignored or added together with the self impedance while modelling the HF behaviour. However, the proposed model explicitly represents the mutual impedance between the conductors. Next, the chapter elucidates the validation of the developed model using CM and differential mode (DM) impedance. The chapter also compares the experimentally measured voltage at the terminals against the prediction using the developed model. The conformity between the two elucidates the validity of the model.

- *Chapter 4: Modelling High Frequency Behaviour of Stator Winding*

This chapter illustrates the HF modelling of the stator winding of the electrical machinery, in particular the traction motor. First, the chapter describes the similarities and the differences between the cable and the stator winding model. Later, the chapter explains the modelling of the stator winding using the model developed for the cable. Further, the validation of the model using CM and DM impedance is explained. Using the HF model, the chapter explains the significance of representing the mutual coupling between the turns. Later, the chapter proposed a method to simplify the representation of the frequency dependent mutual impedance between

the turns without loss of accuracy. In the end, the chapter validates the model by comparing the experimentally measured voltage stress with the prediction.

- *Chapter 5: Voltage Distribution within Stator Winding*

This chapter characterises the voltage stress distribution under PWM voltage excitation. For instance, the chapter demonstrates the voltage stress at the winding terminals along with the stress within the winding under PWM voltage excitation. Firstly, the chapter demonstrates the voltage stress at the terminals and the influence of the cable length and its material properties. Further, the chapter proposes a method to predict the peak voltage stress without excitation. The proposed method uses the CM impedance of the cable and the machine winding for prediction. Later, the chapter illustrates the voltage distribution within the winding which can be characterised by two oscillatory responses. Out of the two, one oscillates at HF and causes voltage stress at the winding terminals, whereas the other oscillates at low frequency (LF) causing voltage stress at the neutral point. While the HF voltage oscillations have been covered extensively, the LF voltage stress has not been discussed in the past. The LF voltage oscillation is a key contribution to this work. These voltage oscillations can be characterised using the anti-resonance phenomenon. In the following study, it has been found that voltage stress can be understood as the superposition of transverse electromagnetic (TEM) voltage waves travelling in different phases. Later, the chapter demonstrates that the peak voltage stress depends on the constructive or destructive interference between the travelling waves which depends on the dwell time between the excitation at different phases. Finally, the chapter illustrates the voltage stress under the different operating conditions of the VSI, especially the modulation index and the switching frequency.

- *Chapter 6: Voltage Stress Mitigation Technique*

In this chapter, methods for suppressing the voltage stress are illustrated. The chapter explains the efficacy of the conventional passive filters, in particular, the sinewave and the dV/dt filter, in suppressing the voltage stress. The results illustrate that, although both the filter suppress voltage stress at the terminal end, the sinewave filter aggravates the neutral point voltage stress whereas, the dV/dt filter is partially effective. Thereupon, a low pass passive retrofit RC filter is proposed to suppress the neutral point voltage stress. Later, the chapter illustrates the impact of the filter parameters on voltage stress suppression.

- *Chapter 7: Conclusion and Future Work*

The major contributions of this thesis, i.e., characterising voltage stress within the stator winding, voltage stress at the neutral point, and the passive RC filter which enables the unprecedented proliferation of the WBG devices in the electrification of the transportation sector are summarised in this chapter besides the new research areas identified for the future research work.

1.4 Contribution

The major contribution of this research work is outlined as follows:

- An explicit representation of the frequency dependent mutual coupling in the time domain HF model is proposed. The proposed method represents the mutual coupling lucidly without convolution, Fourier transform or modal transformation.
- A method based on impedance measurement is devised to predict the voltage stress at the winding terminals. The primacy of the method is that the voltage stress can be predicted at the design stage without voltage excitation. Later, the peak voltage stress is characterised under the different operating conditions of the VSI.
- A new mode of voltage oscillation causing peak voltage stress at the neutral point is identified. The analysis exhibits that the voltage distribution within the winding is a consequence of the superposition of TEM voltage wave in three phases. The combined effect can also be interpreted as the discontinuity encountered by the CM voltage at the neutral point.
- An experimentally validated analytical approach has been proclaimed to characterise the voltage distribution and the location of peak voltage stress is identified within the winding, which accounts for the transient elicited due to previous switching events.
- A passive RC filter is proposed which is connected between the neutral point of the winding and the core of the machine to mitigate the peak voltage stress at the neutral point. As no magnetic component is involved, the proposed filter is a low-cost compact solution for mitigating the voltage stress which oscillates at much lower frequency than those at the machine terminals.

1.5 Publications

The major findings of the research work are disseminated in the following Journal and Conference papers:

1.5.1 Journal Papers (2)

- **S. Sundeep**, J. Wang and A. Griffo, “Holistic modeling of high-frequency behavior of inverter-fed machine winding, considering mutual couplings in time domain,” *IEEE Trans. Ind. Appl.*, vol. 57, no. 6, pp. 6044-6057, Nov.-Dec. 2021. (doi: [10.1109/TIA.2021.3105954](https://doi.org/10.1109/TIA.2021.3105954))
- **S. Sundeep**, J. Wang, A. Griffo and F. Alvarez-Gonzalez, “Antiresonance phenomenon and peak voltage stress within PWM inverter fed stator winding,” *IEEE Trans. Ind. Electron.*, vol. 68, no. 12, pp. 11826-11836, Dec. 2021. (doi: [10.1109/TIE.2020.3048286](https://doi.org/10.1109/TIE.2020.3048286))

1.5.2 Journal Papers (Under Review) (2)

- **S. Sundeep**, J. Wang and A. Griffo, “A low-cost passive retrofit filter for mitigating neutral-point voltage stress in inverter-fed drives,” communicated in *IEEE Trans. Power Electron.* (manuscript number: TPEL-Reg-2022-02-0443)
- D. A. Hewitt, **S. Sundeep**, J. Wang and A. Griffo, “High frequency modelling of electric machines using finite element analysis derived data,” communicated in *IEEE Trans. Ind. Appl.* (manuscript number: 22-TIE-4269)

1.5.3 Conference Papers (5)

- **S. Sundeep**, J. Wang, A. Griffo and F. Alvarez-Gonzalez, “Peak voltage stress on stator winding in PWM inverter fed drives,” in *Proc. International Conference on Electrical Machines (ICEM)*, Gothenburg, Sweden, pp. 1579-1585, 2020. (doi: [10.1109/ICEM49940.2020.9270790](https://doi.org/10.1109/ICEM49940.2020.9270790))
- **S. Sundeep**, J. Wang and A. Griffo, “Prediction of transient voltage distribution in inverter-fed stator winding, considering mutual couplings in time domain,” in *Proc. IEEE Energy Conversion Congress and Exposition (ECCE)*, Detroit, MI, USA, pp. 517-524, 2020. (doi: [10.1109/ECCE44975.2020.9235981](https://doi.org/10.1109/ECCE44975.2020.9235981))

- **S. Sundeep**, I. Tsyokhla, J. Wang, and A. Griffo, “Online monitoring of ground-wall insulation impedance under cyclic load operation,” in *Proc. IET 10th International Conference on Power Electronics, Machines and Drives (PEMD)*, UK, pp 110-115, 2021, (doi: [10.1049/icp.2021.1069](https://doi.org/10.1049/icp.2021.1069))
- **S. Sundeep**, D. A. Hewitt, A. Griffo, J. Wang, F. Alvarez-Gonzalez, M. S. Diab, X. Yuan, “Detection of partial discharge activity in thermally aged SiC inverter fed stator winding samples and impact of partial discharges on their lifetime,” in *Proc. IET 11th International Conference on Power Electronics, Machines and Drives (PEMD)*, UK, pp. 271-277, 2022. (doi: [10.1049/icp.2022.1062](https://doi.org/10.1049/icp.2022.1062))
- D. A. Hewitt, **S. Sundeep**, J. Wang, A. Griffo, M. Diab, and X. Yuan “An experimental assessment of the impact of high dv/dt SiC converters on insulation lifetime of electrical machines,” in *Proc. IEEE Energy Conversion Congress and Exposition (ECCE)*, Detroit, USA, 2022.

Chapter 2: Literature Review

2.1 General

As mentioned in the previous chapter, there has been a continuous pursuit for the development of a sustainable transportation system, with the electrification of transportation vehicles taking centre stage. Meanwhile, a great effort is led by the government regulations for the proliferation of the wide band gap (WBG) based semiconductor devices in the onboard power conversion system for increasing its efficiency, and power density at a reduced cost. There are several opportunities for using WBG based power conversion system in electrified vehicles. For example, the Si-based diode can be replaced in the Si IGBT based inverter by SiC based Schottky diode, the losses reduce by 10.7% [41]. These inverters are prominent in the power conversion system and are referred to as hybrid inverters. In [42], the SiC based inverter has 13.1% higher efficiency as compared to its Si counterpart. As the operating junction temperature of the WBG based devices is higher, a SiC based inverter is developed in [43], which can operate at 120⁰C with forced air cooling which simplifies the cooling system. In [44], the use of the WBG device has increased the fuel economy of the vehicle from 3.94 to 3.36L/100km with a 14.7% reduction in fuel consumption.

However, there are challenges in using the WBG based devices in the power conversion system. In the electric traction system, the WBG based devices are used in the pulse width modulated (PWM) inverter, which enables the inverter to operate at a higher switching frequency and higher switching speed. However, the voltage pulse with short rise or fall time propagating through the cable, partially reflects back at the cable and machine interface, causing voltage oscillations which reduces the service life of the machine insulation [16-18]. Moreover, the high slew rate (dV/dt) of the voltage pulse excites the capacitive coupling of the cable, which results in the flow of cable discharge current. In addition, the high slew rate (dV/dt) common mode (CM) voltage pulse at the machine terminals excites the capacitive coupling between the winding and the core of the machine separated by the insulation, resulting in the flow of ground return current [22]. This ground return current is responsible for the conducted and radiated electromagnetic (EM) emission [26]. The CM voltage is also

responsible for the induction of voltage across the electrostatic coupling between the stator and the rotor, also referred to as shaft voltage, which leads to bearing current responsible for increased bearing failure.

The cause of these issues and the current state-of-the art in addressing them are discussed in length in the following sections. Firstly, the insulation system used in the machine winding is discussed. Later, the stress encountered by the insulation during service is reviewed. Furthermore, the detrimental effect of the PWM voltage excitation on the insulation system is discussed, especially the voltage stress across the insulation within the winding. Later, the high frequency (HF) modelling of the machine is studied which will help in characterising the voltage stress within the winding, so that voltage stress across the insulation system can be predicted before commissioning it in service. In the end, the voltage stress mitigation methods are studied to prolong the lifetime of the insulation system.

2.2 Insulation System

The basic insulation system comprises 3 components: strand and turns insulation, ground-wall insulation, and phase insulation. Different components of the insulation system are illustrated in Figure 2.1.

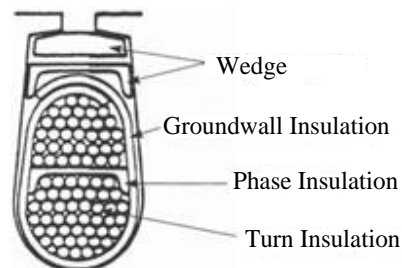


Figure 2.1: Cross-section of a random wound machine stator slot representing the insulation system [45].

Generally, in low voltage (<800V) motors, the windings are random wound with round conductors insulated with polyamide-imide (PAI) insulation or a combination of polyester with PAI insulation, having a thermal class of 180⁰C ~ 220⁰C. The turn conductor is divided into multiple strands to limit the skin effect. As a result, the small strands must be insulated from one another, or they will act as a single conductor. When turn-to-turn voltage stress is deemed high, the strand insulations may comprise two layers of Dracon[®]-glass filament wrapped in the opposite direction to ensure that the copper conductors are separated from each other. In some applications, where a high fill factor is required, Dracon[®]-glass filament is replaced by enamel or Kapton[®]. The magnet wire or enamelled wire coating in form of enamel or polymer film

may also contain materials resistive to discharge, in particular alumina, to reduce the chances of partial discharge (PD) [45]. Such corona resistant material has been in practice as turn insulation since the inception of adjustable speed drives (ASDs). The corona resistive insulation enhances the voltage endurance, allowing higher turn-to-turn voltage stress with reduced ground-wall insulation [46]. With the fast switching time (20ns) of the voltage source inverter (VSI) employed in various applications, UltraShield® plus enamelled wire [47], specifically designed for the high voltage spikes present in the VSI-fed drives, or equivalent may be used. The combination of polyester basecoat and PAI topcoat enhances the resistance to PD, improves abrasion resistance to repeated scrape and increases its mechanical strength [47].

The purpose of the ground-wall insulation is to separate the copper conductors from the core. Generally, the insulation comprises half-lapped layers of polyester sheets. These sheets are bonded together with polyester or epoxy resins. For protecting the polyester sheets against oxidation, hydrolysis, and mechanical damage even at high temperatures, an aramid paper overlay on both sides [48]. The aramid paper is used due to its exceptional resistance to chemicals and solvents and no change in the specific dielectric resistance and the dielectric strength for up to 200°C.

Apart from the above-mentioned insulation, impregnating varnish or resins are often used to increase the electrical insulating strength, mechanical strength and resistance to the ambient conditions such as moisture ingress, dust, and atmospheric pressure changes, while improving thermal dissipation. Moreover, in the electric traction, the machines are completely impregnated with the epoxy or the silicon materials with an improved thermal conductivity as compared to the conventional resins. For achieving PD resistant insulation system, the small air gaps in the impregnations must be avoided, as the breakdown voltage of the air is much lower than the solid insulation. Therefore, vacuum and pressure impregnation (VPI) [49] is generally applied resulting in improved penetration of resins in the small gaps along with the complete encapsulation of the insulation system. However, the VPI method is time-consuming and complicated as compared to other impregnation methods, such as the dipping and trickling process [50].

Mainly, the insulation system comprises polymer chains of organic compounds, which contain long chains of hydrocarbons. By way of example, the polyester used in the turn and

ground-wall insulation comprises a chain of hydrocarbon connected to form inter-twining chains and the length of the chain is referred to as the degree of polymerization.

The phase insulation is often used between the turns of two coils of different phases. Generally, the phase insulation separates the two coils of different phases in the overhang region. However, in the double layer winding, it is also placed between the turns of different phases embedded in the same slot. Illustratively, Figure 2.1 shows the cross-section of a stator slot of double layer winding, wherein; turns of two phases are embedded in the same slot and is separated by the phase insulation. If the two coils are the end coils of their respective phases, the phase insulation must withstand the phase-to-phase voltage. The most common phase insulation is ‘papers’ made up of aramide. These insulations provide insulations resistant of chemical attacks and has excellent mechanical strength with 220⁰C thermal class. Based on the voltage class, the paper is available in different range of thickness from 0.1mm to 0.5mm thick. Another material, which is commonly used as the phase insulation, is Dacron[®] or DMD[®], which has better mechanical strength as compared to paper [45]. In the harsh nuclear environment, or in chemically harsh application sealed random wound machine is used wherein, the end windings are insulated with the Dacron[®] tape to retain the varnish and then the stator is global vacuum pressure impregnated.

2.3 Stress on Insulation System

The basic stresses occurring on the insulation system are primarily classified as Thermal, Electrical, Ambient and Mechanical, often acronym as TEAM.

2.3.1 Thermal Stress

Both, the ambient temperature and the losses in the machine, cause thermal stress on the machine insulation. Upon prolonged exposure to the high temperature, the chemical properties, and hence, the electrical properties changes. In [51-52], it is illustrated that a longer polymer chain of insulation exhibits stronger mechanical properties. Similarly, cross-linking of polymers reduces the DC conductivity of the insulation at the expense of material ductility [53]. Therefore, higher cross-linking polymers are used in the high-voltage application. Over the service life, the polymer chains break, leading to weaker insulation [51-54]. Indeed, operation under high temperature accelerates the breakdown of polymer chains resulting in a

steady decline in their mechanical and electrical properties. The general mechanism of thermal degradation can be explained in three steps [55]:

- *Initiation:* When the polymer is exposed to excessive heat, it undergoes oxidative degradation, initiated when the polymer chain forms radicals ($R\bullet$) either by hydrogen abstraction or by homolytic scission of the carbon-carbon bond.
- *Propagation:* The propagation of thermal degradation is a result of a number of reactions. Firstly, the free radical ($R\bullet$) reacts with oxygen to form a peroxy radical ($ROO\bullet^*$), which abstracts a hydrogen atom from another polymer chain and forms hydroperoxide ($ROOH$). Further, the hydroperoxide splits into two new free radicals ($RO\bullet$) + ($\bullet OH$), which abstract liable hydrogen from another polymer. As each initiating radical produces two free radicals, the process accelerates depending on how fast the free radical undergoes termination or extracts hydrogen from other polymer chains.
- *Termination:* The termination of polymeric reaction undergoes two different processes, either by recombination of polymer chains or by disproportionation reaction. The degradation of the polymer depends on the termination. Recombination reaction results in an increase in molecular weight and crosslinking density, whereas, disproportionation reaction, on the other hand, results in a decrease in molecular weight leading to softening of the polymer and reduction of mechanical properties.

Weakened mechanical properties of the insulation results in delamination and hence crack will develop on the surface which compromises its safe use.

2.3.2 Electrical Stress

The motor insulation is subjected to high electrical stress when fed through a PWM inverter rather than excited using a sinusoidal voltage source [16-18]. The output of a PWM inverter is a rectangular voltage pulse with varying width and frequency and, a fast rising and falling edge, which distributes non- uniformly across the machine winding when impinges at its terminals [16-18] [19][40]. The studies [19][40] depict that 80% of the voltage stress occurs across the turns of the first coil from the terminal end with peak voltage stress across the turn insulation of the last turn of the first coil. Furthermore, the voltage stress across the ground-wall insulation close to the terminals may reach 2 times the DC link voltage or may exceed under double transitions [56]. Additionally, the voltage stress across the ground-wall insulation close to the

neutral point may reach 4 times the DC link voltage [26]. The stress aggravates with the short rise time and high switching frequency. The voltage stress at the terminals occurs as a result of reflected wave at the interface of the cable and the machine due to the impedance mismatch and depends on the inverter output, cable impedance, cable length, and rise time [57-59]. Similarly, the voltage stress at the neutral point occurs due to the superposition of voltage wave travelling through the phase windings and depends on the anti-resonance frequency of the cable connected winding, inverter output, and dwell time between the excitation of the phases [20][21].

High voltage stress may reduce the lifetime of the insulation system if they exceed its repetitive voltage strength. If the voltage stress exceeds a critical limit, localised intermittent discharge of the charges occurs within the insulation, which degrades its electrical properties. The localised discharge is called PD and the critical limit is called partial discharge inception voltage (PDIV). The frequency spectrum of the PWM voltage with short rise time spreads over a wide range, thereby, exciting the parasitic capacitive coupling between the winding and the core which engenders bearing current and HF ground return current [22]. Pitting, fluting and frosting are some of the damages caused by bearing current which leads to premature failure of the bearing, thereupon, the machine fails [23-25]. This HF bearing current causes interference with the nearby electronic equipment [23-25].

2.3.3 Ambient Stress

Inevitably, under service life, the machine may operate in a hostile environment leading to ingress of surrounding contamination, which may accelerate insulation degradation. For example, in [61-62] moisture ingress is the prime cause of insulation degradation. As the dielectric constant of the water is 40 times higher than insulation [63], the moisture ingress may increase the dissipation factor and the capacitance of the insulation system. In [63], moisture ingress results in a 5% increase in capacitance.

End windings of the open loop air cooled machines are exposed to the ambient condition. Thus, conductive particles in the air, salt, dust or highly reactive chemicals may cause contamination. In several instances, the contamination gives rise to electrical treeing leading to current flow between the phases and phase-to-ground of the end winding region [63]. Electrical treeing is a common electrical pre-breakdown phenomena that occurs in solid insulation as a result of partial discharge and advances through stressed dielectric insulation in

the shape of tree branches. The contamination carbonises the tracks leading to a reduction in path resistance. Subsequently, the growth of the electrical treeing leads to PD [64] and finally a short circuit. It is easy to detect using an offline DC resistance test [65] as it lowers the insulation resistance between the phases, and phase and ground.

2.3.4 Mechanical Stress

Mechanical stress on the insulation system may occur due to electrodynamic reaction force, abrasion due to different thermal expansion coefficients of the elements of the insulation, and vibration due to external movement. Poor impregnation is one of the causes leading to delamination and the creation of air pockets. Indeed, air pockets in the insulation may lead to PD activity which aggravates the degradation.

In the early stage of the PWM inverter fed machine, more focus was on the thermal stress arising due to the copper loss, especially in the low-speed motor, where external cooling ducts and vents were required. Moreover, research on the shape of the rotor bars in induction machines was also pivotal in lieu of the winding insulation since the bar shape influences the torque-speed characteristics of the machine. Mechanical stress on the winding due to torque pulsation was also comprehensively studied.

However, with the proliferation of the PWM based inverter in the electrical drive, especially the WBG based inverter, there has been a continuous pursuit for exploring the impact of the electrical stress on the machine insulation rather than the mechanical stress, as it greatly affects the lifetime of the machine. There are many incidences of premature failure of the electrical machine under PWM voltage excitation. The cause of the premature failure is still understudy by many scholars. Inevitably, during failure, the machine will be out of service leading to unexpected downtime, which results in economic losses. In [66], the economic losses in different studies due to the downtime are studied, which illustrates that the automotive sector is affected most. Therefore, a comprehensive study is required to study the cause of premature failure and develop a predictive method, which immediately identifies the incipient failure and proposes necessary actions that can be scheduled to avoid downtime. As a result, it is apparent that a great emphasis is needed primarily on two aspects; (a) examining electrical stress that the insulation must withstand during its service life and (b) an investigation of the degradation mechanism of the insulation due to the electrical stress. Such investigations have sparked an

intense research effort over the years with the goal of a rational motor insulation design by evaluating the voltage distribution within the machine's stator winding using its HF model.

Considering the degradation mechanism of the insulation, an experiment on the epoxy insulation illustrates that a higher switching frequency and short rise time of the PWM voltage pulse reduces the lifetime of the insulation [67]. A similar study [68-69] on the lifetime of the insulation illustrates that the insulation lifetime is greatly influenced by the rise time as compared to its magnitude. Repetitive PWM voltage pulse significantly influences the partial discharge mechanism, space charge and surface charge accumulation, thereby, ageing the insulation [70-71]. In [72-74], the correlation between the partial discharge and the rise time and switching frequency of the PWM voltage pulse is established which characterises the lifetime with the short rise time and the high switching frequency of the PWM voltage. As a result, developing an HF model of the machine winding for characterising the voltage distribution within the winding is critical, as it aids in identifying the location of excessive voltage stress that causes partial discharge, bearing current [23-28], and EMI [26].

In the following section, a comprehensive overview of the HF modelling of the machine winding adopted in past research is presented. Generally, the HF modelling of the cable is derived from the machine modelling; hence it is ignored in the following section and discussed comprehensively in chapter 3. Later, a review of the location of the peak voltage stress and its mitigation measures under PWM voltage pulse excitation is presented.

2.4 Effect of High Frequency Voltage Excitation on Machine Winding

For analysing the voltage distribution with the machine winding, a schematic of VSI fed drive is depicted in Figure 2.2. Unless otherwise specified, voltages measured at inverter terminals (V_{in}) are measured with respect to the DC link's midpoint, whereas voltages measured at motor ends are measured with respect to the machine's core. At the machine end, the voltage is measured at both the machine terminal and the star-connected neutral point. The voltage measured at the machine terminal is often referred as machine terminal voltage (V_t), whereas, the voltage measured at the star-connected neutral point is referred as neutral point voltage (V_N). Similarly, the voltage measured at the floating ended cable is referred as cable voltage (V_c). The three phase current leaking through the capacitive coupling between the winding and the core, returns through the protective earth wire which is referred as ground return current (I_g).

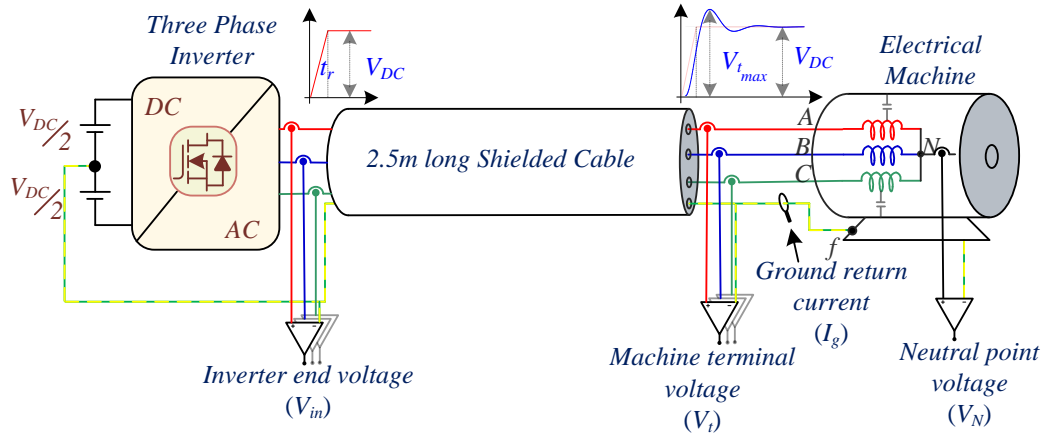


Figure 2.2: Schematic of VSI fed drive representing the path of bearing currents, ground return current and the cable discharge current

In a balanced and symmetrical three-phase sinusoidally excited electric drive, the neutral voltage is zero. However, this is not the case under PWM voltage excitation wherein the DC voltage is converted into three phase voltages. Albeit the balanced and symmetrical fundamental frequency component of the output voltage, the instantaneous sum of the output voltages is non-zero. This non-zero voltage appears across the neutral and the core of the machine, which is well known as common mode (CM) voltage or neutral point voltage (V_N). The magnitude of the voltage is proportional to the DC bus voltage and its frequencies are a function of the switching frequency and modulation index of the inverter. The CM voltage has several deleterious effects namely, voltage stress at the neutral point of the winding, HF ground return current [22] causing EMI [26], and HF bearing current [23-25] responsible for the bearing damage. These effects are discussed comprehensively in the following section.

2.4.1 Voltage Stress within Machine Winding

While propagating through the cable, the PWM output voltage at the inverter terminals with a short rise time behaves as a transverse electromagnetic (TEM) wave. The wave partially reflects as it reaches the cable and machine interface. As a result, the voltage at the interface is a damped voltage oscillation whose amplitude is determined by the surge impedance of the cable and machine. If the rise time of the voltage wave is less than twice the propagation time through the cable, the voltage reflection will lead to a voltage doubling effect, wherein, the peak voltage stress may reach twice the DC link voltage [16-18][60]. The overvoltage may surpass twice the DC link voltage if the dwell time between the two switching events either in the same phase or in the different phases is less than the time constant of the cable [57-59]. The

peak phase-to-ground voltage at the machine terminals determines the maximum voltage stress across the ground-wall insulation.

Amongst several studies investigating the effect of voltage stress on insulation degradation, Kaufhold [75] investigated deeply the relationship between the voltage magnitude, PD inception probability and the breakdown time. In fact, he observed that the inception of PD depends on the peak voltage stress above the inception voltage. However, views on the PD inception in relation to the voltage polarity are mixed. Kaufhold illustrates that the bipolar rectangular voltage pulse could be more stressing than the unipolar rectangular pulse of the same amplitude, whereas, Lebey [76-78] suggest a contrary trend and Yin [79-80] illustrates that the voltage polarity has a marginal effect on PD inception.

2.4.2 High Frequency Ground Return Current

When the CM voltage generated by the inverter impinges machine terminals, its high dV/dt excites the parasitic capacitive coupling of the winding with the core. Due to high dV/dt , the CM current leaks through the capacitive coupling and returns to the inverter source ground through the cable shielding or the potential earth conductor connecting the core and the enclosure of the inverter. The flow of CM current through the potential earth conductor will cause a potential drop across it due to its non-zero HF impedance. Consequently, the potential of the core rises with respect to the source ground. If the impedance of the intended return path is high, some of the CM currents may flow through the unintended path present in the field causing EMI with the nearby electronic equipment. If these PWM inverter fed machines are installed in the drivetrain of the traction applications such as electric vehicles, electric ships, and more-electric aircraft, the vicinity of the sensitive equipment in the mobile environment necessitates tight control of EMI [26]. EMI is an unwanted electrical signal that interferes with surrounding equipment, degrades its performance, and can cause malfunction or non-operation in some cases.

If the impedance of the return path is high enough, the core voltage may exceed 100V [26]. Moreover, if the driven equipment is grounded, a part of the CM current will flow through the shaft to the driven equipment and then back to the source ground. If the driven load is not grounded, the CM current may flow via the load machine bearing which may damage before the machine bearing.

2.4.3 Bearing Currents

Before the introduction of the PWM inverter fed machines, bearing current is the major challenge in the large electrical machine. This phenomenon has been known since the 1920s [81] which is more pronounced in the large machines with magnetic asymmetries. The magnetic asymmetry, as shown in Figure 2.3 (a), engenders a yoke variable magnetic flux which induces a voltage across the shafts, called shaft voltage. The shaft voltage is large enough to break down the oil film in the bearing [82] and induces a circulating shaft current which is inductive in nature, as illustrated in Figure 2.3 (b). Due to the automated process of machine manufacturing methods and the anisotropic properties of the materials, perfect symmetrical flux is difficult to achieve. The shaft voltage may also be induced by the electrostatic charging of the shaft [83]. The induced shaft voltage due to electrostatic charges induces a bearing current of capacitive nature.

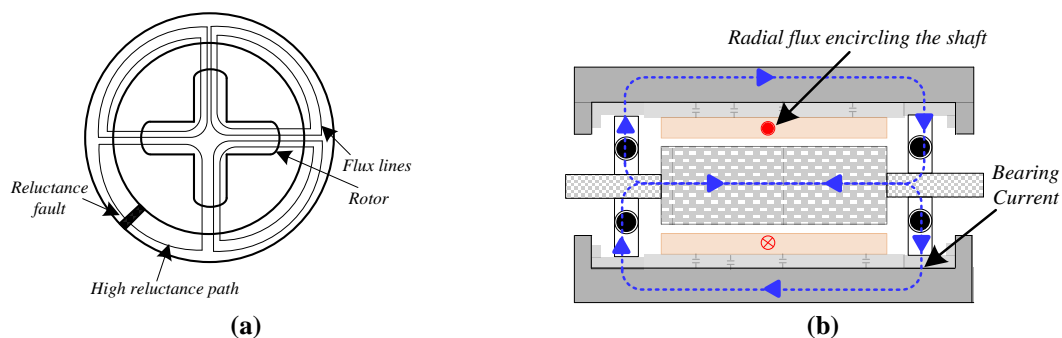


Figure 2.3: Classical inductive bearing current, (a) unsymmetrical flux in the four pole machine due to reluctance fault [82], (b) bearing current due to flux encircling the shaft.

Interestingly, with the emergence of PWM inverter fed machines, failure due to the bearing current has rapidly increased. By way of example, the lifetime of the motor fed through the PWM inverter falls by 7 times as compared to the sinusoidal excitation [84]. The HF CM voltage induces CM current, part of which flows through the bearing of the motor or the driven equipment. The CM current flowing through the bearing also generates a CM voltage across the bearing by transformer action. The bearing currents can be further classified into the following types:

- *Circulating current:* In large machines, the capacitive current escaping the winding through the capacitive coupling between the winding and yoke induces an HF circulating flux around the stator yoke as shown in Figure 2.4. This HF circulating flux induces the shaft voltage. If it exceeds the breakdown voltage of the thin oil film

in the bearing, a compensating current flow through the shaft, bearing and the stator frame to balance the flux. These HF circulating bearing currents may superimpose on the low frequency bearing current induced due to magnetic asymmetry.

- *Shaft earthing current*: Any current leaking from the winding through the capacitive coupling must return to its source, which is a PWM inverter. Due to the impedance of the return path, the voltage of the core of the machine rises with respect to the source ground. If the machine shaft is earthed via the driven equipment, the core voltage appears across the bearing. If the voltage exceeds the breakdown voltage of the thin oil film in the bearing, a current flows through the bearing, the shaft, the driven equipment and back to the inverter, as illustrated in Figure 2.4.
- *Capacitive discharge current*: If the shaft of the machine is not grounded via the driven equipment and the core of the machine is grounded for protection a current is induced by the bearing voltage, which is called electrostatic discharge machining (EDM) current.

To discern the cause of the detrimental effect of the HF voltage excitation on the machine winding, especially the excessive voltage stress across the insulation and the non-uniform voltage distribution, ground return current causing EMI and bearing current, it is, therefore, important to predict the behaviour of the stator winding under VSI excitation for an optimised solution without costly design iterations. For this purpose, a modelling approach representing the high-frequency (HF) behaviour of the machine winding is prevalent in the literature.

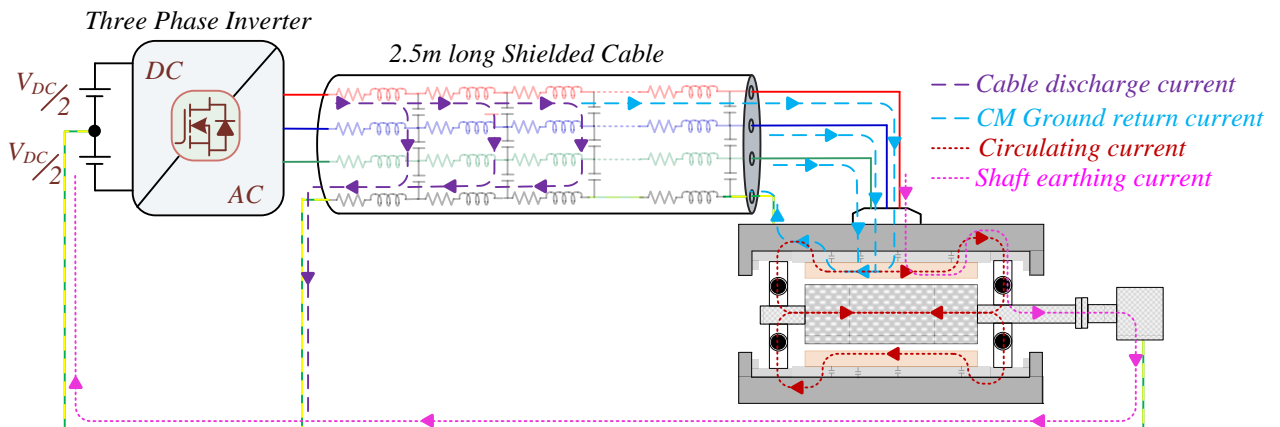


Figure 2.4: Schematic of VSI fed drive representing the path of bearing currents, ground return current and the cable discharge current.

2.5 High Frequency Model of Cable and Stator Winding

The simplest approach to predicting the voltage distribution within the winding due to an incoming PWM voltage surge is to consider the winding as a simple transmission line, the well-known transmission line equation is then valid to calculate the voltage and current at any location within the winding. However, the distributed nature of the impedance of the winding is frequency dependent. By way of example, due to the skin and proximity effect, the resistance and the inductance of the conductor embedded in the slot are frequency dependent. Similarly, the dielectric loss of the insulation varies with frequency. Additionally, the conductors embedded in the slot are mutually coupled. Representing the mutual coupling and the frequency dependent parameters of the machine using a transmission line equation requires complex mathematical operations such as Fourier transform, inverse Fourier transform, modal transformation and convolution which is cumbersome.

Modelling of HF behaviour of the machine winding, in particular, characterising the voltage distribution within the winding, and predicting the HF ground return current, involves accurate representation of wave propagation and reflection phenomenon within the winding. This can be realised by representing the winding conductors using a transmission line model. HF behaviour of the winding can also be represented as a per-phase lumped parameter model [87-89] also called as a behaviour-based model, wherein, the parameters of the model are derived from the terminal impedance measurement. However, in such models, voltage stress across individual turns and coils is inaccessible. Moreover, the physical measurement of the terminal impedance is required, which mandates the physical availability of the machine winding and hence excluding such analysis in the design stages.

In the transmission line model, appropriate length of a winding, e.g., each turn or a coil is represented as a unit cell, thereby, the turn or the coil voltages are accessible, and the model is solved either in the time domain or in the frequency domain to predict voltage distribution within the winding. Also, the transmission line model can be used in the design stage, without the physical availability of the machine. Therefore, the majority of the work reviewed in the following sections focuses on representing the winding as a continuum of lumped parameter circuits, allowing the voltage distribution to be predicted without solving complex transmission line equations. A comprehensive discussion of the solution to the transmission line equation is mentioned in chapter 3.

Since the early 19th century, the theoretical investigation on the surge phenomenon engendered from the fast transients such as lightning or switching surges was concentrated on the overhead lines and the transformer winding, owing to their severe vulnerability. A comparison of the work on voltage distribution within the machine coils with that done on the transformer coils has met only partial success because the work on the transformer coils is able to predict the coil voltage and not the turn voltage. In the HF model developed by Rudenburg [90] on the transformer coils when applied to machine coils, the coil voltage is predictive without the turn voltage. However, the accuracy of the results is doubtful, as it is implicitly assumed that there are a large number of turns within the coils to enable the problem to assume distributed nature of the parameter, instead the form wound machines have few turns per coil (N_c).

In a similar approach [91], a ladder circuit is used to represent the coil as a unit cell. As a result, voltage distribution within the coil cannot be predicted. If the analysis is adapted to represent the voltage stress within the turn by representing the turn as a unit cell, the turn voltage can be predicted. This would not, however, leads to accurate results, as the ladder circuit does not account for the mutual coupling between the turns. The ladder network designed in [91], was superseded by [92] with mutual inductance between the adjacent conductors embedded in the same slots. However, no account of mutual coupling between the non-adjacent conductors is made, and so this method is not valid for the multi-turn coil.

A concise study of a single conductor embedded in an iron slot performed by Heller and Vevarka [93], suggests that at HF, the iron core act as a flux barrier. Later, the analysis shows that set of differential equations can be used to represent the voltage distribution in a loss-less winding. The analysis assumes the coil as a unit cell and high inter-turn capacitance results in the uniform distribution of voltage within the coil. The results illustrate that the first coil from the line end is most stressed with less severe stress across the remaining coils. Therefore, it was advised to the manufacturer to increase the turn and ground wall insulation in the line end coil. The experimentally measured voltage illustrated in the analysis conforms with the prediction, however, no mention was made of the variation of the voltage stress with the rise time of the voltage wave.

Parrot [94] was the first to illustrate that the voltage wave with a short rise time ($<600\text{ns}$) results in non-uniform distribution of voltage within the first coil with the peak inter-turn

voltage stress across the last turn of the first coil. The experimental validation of his theory led him to conclude that the voltage stress within the winding is a result of the superposition of travelling waves. This conclusion has never been included in any comprehensive analysis. Another work [95] supports the finding of Parrot that the short rise time leads to non-uniform voltage distribution and confirmed by the investigation performed in [68].

The voltage distribution within the winding occurs because of wave propagation and reflection at the ends of the coil which is evident in [97]. It is also demonstrated that the number of turns within the coil has little effect on the inter-turn voltage. Different from [94], the results show that the voltage stress across the first coil of a phase winding is independent of the excitation of the other two phases. The experimental evidence herein discussed in chapter 5, however, does not align with this conclusion and demonstrates that the excitation on the other two phases affects the voltage stress across the first coil.

Cornick and Adjaye [98] are the first to use a cascaded two-port network to predict the voltage distribution. Each coil is represented as a two-port network with an assumption that the voltage distributes uniformly within the coil. Any attempt at a detailed comparison of the prediction with the experimental measurement fails since the mutual coupling is not accounted for. Additionally, only the first 4 coils are represented as a two-port network with the remaining 20 coils as lumped parameters. Herein, however, it is demonstrated that representation of full winding in the HF model is necessary for accurate prediction (see chapter 4).

The simplest approach to predict the voltage stress is by assuming the coil as an elemental section of the model with a series inductance and shunt capacitances. This approach is followed in the aforementioned analysis, but the work has the inherent disadvantage of being unable to predict voltage distribution within the coil. They assumed that the voltage stress within the coil is uniformly distributed. The work done in 1964 by Clowes [99] infers that a simpler model with assumptions displays general features of the phenomenon whilst lacking detailed comparison with the experimental results.

Consequently, in [100-102], each turn is modelled as a unit cell and a continuum of cells is used to represent the winding. The influence of the rotor is ignored since the rotor iron core acts as a flux barrier, and the airgap reluctance is larger. Following the inferences of Parrot [94], the analysis assumes that the flux is confined within the slot, like the iron core act as a flux barrier. Additionally, the mutual coupling between the turns of the coil embedded in the

same slot is considered. On the account of these assumptions, they proclaim that the peak turn-to-core voltage stress occurs at the first turn and the last turn-to-turn insulation between the last two turns of the line end coil is most stressed. In [101], the inter-turn voltage distribution in the line end coil is non-uniform with up to 40% of the incoming surge appearing across the insulation between the last two turns of the coil. In addition, [100] illustrates that the number of coils required for the accurate prediction of voltage increases with decreasing number of turns per coil (N_c). However, the accuracy of the results is doubtful because it is implicitly assumed that the accurate prediction can be made without representing the full winding in the HF model. Illustratively, [101-102] only represents the line end coil as a cell and the remaining coil is represented as a lumped parameter. In [100], the capacitance is calculated by ignoring the fringing effect, and the inductance is calculated using the duality principle with an assumption that the velocity of propagation of wave within the winding is constant. However, the inclusion of losses in the model invalidates this assumption.

Like [100], [103] has computed the parameters and proclaimed a similar voltage distribution. Different from [100], however, [103] analyses the model in the frequency domain using modal analysis, whereas, [100] analyses in the time domain using convolution. The HF model can be analysed either in frequency or in the time domain, based on its advantages and disadvantages. In the frequency domain analysis, the incoming surge is divided into its spectral component using Fourier transform and fed to the corresponding model representing the winding over that frequency. Later, the response of each circuit is added together using the superposition principle and the inverse Fourier transform is used to get the voltage distribution in the time domain. However, this approach requires a large number of HF models, each representing the winding at a unique frequency, as the spectral component of the voltage surge with short rise time spreads over the wide frequency range. Alternatively, in the time domain analysis as illustrated in [100], convolution is used which is a complex mathematical tool for incorporating the frequency dependency of the parameters. The time domain analysis has an advantage over its counterpart, as the physical signals are measured in the time domain, which implies that a complex sequence of Fourier transforms, and inverse Fourier transform is not required. In the proposed work, herein, the frequency dependent parameters are incorporated into the model, without complex mathematical operations, in particular, the Fourier transform, Inverse Fourier transform, Modal analysis and Convolution, using a ladder circuit and current controlled voltage source.

A theory of induced eddy current in the iron core under HF excitation is expounded in [104], wherein, it is assumed that the flux penetrates the iron core up to penetration depth (δ). Also, following the conclusions of the past research [90-103] illustrating the concentration of incoming surge across the first coil, the winding is assumed as a continuum of an infinite number of cells, wherein each cell represents a turn. The accuracy of the model, however, is uncertain as the iron core is approximated as an infinite one-dimensional slab which is true for the conductor but inapplicable for the laminations. A similar assumption can be encountered in [104], wherein, the core is assumed as a solid iron block with exponentially decaying flux along with the penetration depth which can be expressed using a one-dimensional differential equation. As a result, even under LF excitation, the flux will penetrate the iron core, which is inaccurate.

The HF model of the random wound machine is firstly explored in [106], which presents a simplified model with the first five turns as a transmission line cell representing the turn resistance, inductance and capacitive coupling, and the remaining turns are represented using lumped impedance. The model assumes that the incoming voltage surge distributes non-linearly with peak voltage stress occurring across the first few turns. Similar work is also reported in [37]. The work illustrates that, if only the turn-to-turn capacitive coupling is represented, the incoming voltage will distribute uniformly. The turn-to-core capacitance is responsible for the non-uniform distribution of voltage. Differently, however, in [40], it is illustrated that the turn-to-turn capacitance is more influential in the non-uniform voltage distribution. A 49-turn coil is depicted in [107], with only the first two turns and the last three turns are represented as transmission line cells with the remaining turns lumped together as an impedance. Different from [106] [40], the work [37] illustrates that the non-uniform voltage distribution is influenced by the ratio between the turn-to-turn and turn-to-core capacitance. The different inferences may be the result of different methods of parameter calculation. In [106], the parameters of the coil are calculated at low frequency and is assumed distributed uniformly among the turns. In [40], the parameters are calculated using the solution of the electrostatic and magnetic field by the finite element method (FEM). In [107], the parameters are measured experimentally at low frequency for a 5 turn coil wound on E type core and assumed the same for the 49 turns coil. None of them calculates the parameter of each turn accurately. For an accurate representation of a winding, each turn must be represented

explicitly, wherein each turn must be represented using the capacitive coupling between the turn and core, and turn and turn, the frequency dependent resistance and inductance, mutual resistive and magnetic coupling between the turns and the accurate representation of the core is required. The capacitive elements may be calculated using the energy stored in the electrostatic field whereas, the resistive and inductive elements may be calculated using losses and energy stored in a magnetic field.

In [106], a discrete Fourier transform is used to dissociate the incoming voltage surge into its spectral content and a transference matrix is used to calculate the voltage distribution under each frequency of excitation. Later inverse Fourier transform is used to predict the voltage distribution. One of the key advantages of the transference matrix is, that it can account for the frequency dependent mutual coupling between the turns. However, the parameters are calculated using the method followed in [104], wherein the proximity effect is ignored.

Yifan [40] has performed a detailed analysis of the finite difference method in the frequency domain to predict the voltage distribution using the HF model. The model is developed for the form wound machine which illustrates that the adjacent conductor shields most of the flux, thereby, mutual magnetic coupling exists only in adjacent coils. Akin to the previous work, the iron core is assumed a flux barrier. However, the voltage distribution is studied for single voltage pulse excitation in isolation which leads to the inference that the peak turn-to-core voltage stress occurs at the terminal end and the turn insulation between the last two turns of the first coil is most stressed.

A 3-D model of half thick laminated sheet of the iron core with the insulation is expounded in [108], for calculating the induced eddy current in the core. Additionally, a 3-D model of the end winding region is developed to calculate the end winding parameters. The effect on the turn parameters by the induced eddy current in the core is elucidated by comparing the parameters calculated using the 3D model and 2D model. In the 2D model, the core is assumed conductive without any lamination. Predictably, the inductance calculated at HF using the 2D model will decline rapidly, as the induced eddy current confines the flux within the slot region. Furthermore, the confined flux within the slot regions links with the conductors, resulting in an induced eddy current that increases the resistance. Thereupon the 2D model overestimates the resistance and underestimates the inductance of the turn. While the reasonable comparison between the measured and predicted common mode (CM) and differential mode (DM)

impedance is illustrated, no attempt was made to analyse the voltage stress within the winding. Although the analysis estimates the induced eddy current using 3D model of the core, no account was taken of the hysteresis loss and the frequency dependency of conductivity and the permeability of the core, so this method does not represent the winding accurately. Additionally, the inevitable mutual inductance between the turns embedded within the same slot is ignored which is necessary for representing the HF behaviour of the winding.

The recent publication [109] calculated the resistive and inductive parameters of the turns using a 2D slot model, wherein, the iron core is assumed as a flux barrier. The losses in the core occurring due to induced eddy current under HF of excitation are represented using a resistance. However, the results would be of limited value since the frequency independent parameters calculated at 20MHz are used and the parametrisation of the resistor representing the eddy current is not discussed. The HF model discussed in [37] is superseded in [110], wherein the parameters of the model are calculated using the electrostatic and magnetic field solution. However, in both the analysis, the core loss and the frequency dependent mutual magnetic and resistive coupling are ignored.

In [111], the frequency dependent dielectric loss is accounted for. It introduces a method wherein; the frequency dependent dielectric loss is represented using s-parameters and is incorporated in the time domain circuit simulation using a controlled voltage source. This method has met with only partial success as the resistive and the inductive parameters used in the model are frequency independent and lamination of the iron core is ignored.

Recently, in [39] FEM is used to calculate the parameter. Different from others, capacitive coupling is calculated by solving the electrostatic field and is included in the magnetic field solver to calculate the resistive and the inductive parameters. However, the accuracy is questionable due to a lack of clarity in the iron core modelling. The experimental validations are performed on the manually wound coil which depicts the differences between the measurement and prediction in the peak voltage stress and voltage oscillations.

The frequency dependent parameters in the time domain circuit are best represented in [112], wherein, the Foster and Cauer network is used for the representation. A similar approach is followed in [38], which uses a ladder circuit to represent the frequency dependency. The Foster and Cauer network and the ladder circuits approximate the frequency response of the impedance using frequency independent parameters. However, the mutual coupling between

the turns is considered inappropriately. In [112], the mutual coupling is ignored whereas, in [38], the mutual coupling is added together with the self parameter by implicitly assuming that the capacitive current during the transients is negligible. On the other hand, the model in [39] represented the frequency dependence of the inductive and resistive coupling by embedding the capacitive coupling in the time-harmonic finite element (FE) simulations. Such an approach requires excessively large computation time and resources. A brief summary of the modelling work reviewed above is summarised in Table 2.1.

In the previous work, no account was made to represent the frequency dependent mutual resistive and inductive coupling between the turns in the time domain analysis. It is clear that none of the investigations reviewed above has developed a model for the machine winding which can predict the voltage distribution under PWM voltage excitation which may help in identifying the location of excessive voltage stress within the winding. Additionally, the previous analyses are erroneous since the induced eddy current in the iron core is either ignored or approximated to make the models tractable. Therefore, no modification of these analyses will result in an accurate coil model.

The HF model proposed in [38] concerning the role of the iron core as a flux barrier by assuming zero conductivity of the iron core, and core loss representation using a resistor is of great importance in the following analysis. The HF modelling of the machine winding is thoroughly discussed in chapter 4, wherein, the frequency dependent mutual coupling is accounted for explicitly and the core is represented as mentioned in [38].

Table 2.1: A comparative analysis of the modelling methods.

	Model	Method	Elemental Section	Core Modelling	Parameter Representation	Mutual Coupling Representation	Location of voltage stress		Remark
							Turn-to-core	Interturn	
Frequency Domain Analysis	[98]	2-Port Network	Coil	Flux barrier	Frequency dependent	Ignored	First turn	Last turn of the first coil	Voltage within the coil is uniformly distributed. Only 1 st coil is modelled.
	[101]	Transmission line equation is solved using discrete Fourier transform	Turn	Flux barrier	Frequency dependent	Considered	First turn	Last turn of the first coil	First 2 coil is modelled. Inductance is calculated using the principle of duality.
	[103]	Modal analysis and discrete Fourier Transform	Turn	Flux barrier	Frequency dependent	Considered	First turn	Last turn of the first coil	Only one phase is excited.
	[104]	Transference matrix and discrete Fourier transform	Turn	Flux penetrates the solid iron core. Core Laminations are ignored	Frequency dependent	Considered	First turn	First turn of the first coil	Only 1 st coil is modelled.
	[40]	Finite difference method	Turn	Flux barrier	Frequency dependent	Considered	First turn	First turn of the first coil	Only the mutual coupling between the

								adjacent turn is considered. Proximity effect is ignored.
	[107]	Circuit simulation	Coil	Flux barrier	Frequency dependent	Considered	--	Parameters are measured experimentally on a motorette sample with 5 turns wound on E type core.
Time Domain Analysis	[100]	Scatter matrix solved using convolution	Turn	Flux barrier	Frequency independent	Ignored	First turn Last turn of the first coil	Only the first 2 coils are modelled. Inductance is calculated using principle of duality
	[102]	Modal analysis and convolution	Turn	Flux barrier	Frequency dependent	Considered	First turn Last turn of the first coil	Only 1 st coil is modelled.
	[106]	Circuit simulation	Turn	Flux barrier	Frequency independent	Ignored	First turn First turn of the first coil	Only the first five turns are modelled.
	[112]	Circuit simulation	Turn	Flux penetrates the solid iron core. Core	Frequency dependent	Considered	First turn First turn of the first coil	Only modelled the phase winding.

			Laminations are ignored.					
[108]	Circuit Simulation	Turn	Flux penetration is calculated using 3-D model of the core	Frequency independent parameters calculated at 25MHz are used.	Ignored	--		Hysteresis loss in the core is ignored. Only the frequency dependence of the dielectric loss is considered.
[109]	Circuit Simulation	Turn	Flux barrier	Frequency independent	Ignored	--		Proximity effect is ignored. Turn resistance and inductance are calculated using analytical assumptions.
[110]	Circuit Simulation	Turn	Flux barrier	Frequency independent	Ignored	First turn	First turn of the first coil	Core loss is ignored. Voltage stress is measured under single voltage pulse excitation.
[111]	Circuit Simulation	Turn	Flux barrier	Frequency independent	Considered	--		Solid iron core is used for modelling. Parameters are calculated at 33.8MHz.

								Parameters are calculated analytically.
[37]	Circuit Simulation	Turn	Flux barrier	Frequency independent	Ignored	First turn	First turn of the first coil	Voltage stress is measured under single voltage pulse excitation.
[38]	Circuit Simulation	Turn	Flux barrier	Frequency dependent	Considered with self parameters.	First turn	First turn of the first coil	Voltage stress is measured under single voltage pulse excitation.

2.6 Voltage Stress Mitigation Technique

In section 2.4, the detrimental influence of the HF inverter output voltage with a short rise or fall time is discussed in detail. The HF voltage wave with a short rise time leads to overvoltage at the terminals and non-zero CM voltage, which induces CM ground return current. In addition, the short rise or fall time contributes to the bearing current [23-25] and EMI [26]. If a long cable is used between the inverter and the motor, or a large machine is used with a significant capacitive coupling between the winding and its core, or the rise or fall time is shortened, or the DC link voltage is raised, the situation will deteriorate. Large voltage overshoot ensues at the motor terminals, and the HF cable charging current leading to EMI, increases if the cable length exceeds the critical cable length. Furthermore, the fast rise and fall times, as well as the increased DC link voltage, will result in an excessive CM voltage amplitude and HF ground returns current. This phenomenon leads to insulation deterioration and subsequently the premature failure of the machine [16-18]. The voltage stress at the terminals occurs due to a mismatch between the surge impedance of the cable and the machine. Generally, the voltage stress in the large machine is less severe as the surge impedance of the large machine is low and comparable to cable surge impedance. However, in a field scenario, where the parallel cable is used to feed power, the voltage stress is severe, as paralleling the cable lowers its surge impedance.

The HF voltage pulse impinging machine terminals and PWM ripple current lead to the generation of acoustic noise in the machine. The acoustic noise is generated mainly due to resultant PWM force/torque ripple and the magnetic core through magnetostriction, motor bearing or motor ventilation. In addition, the HF voltage oscillation at the terminals is a potential EM noise source. Besides this, CM voltage between phase and ground and the switching of semiconductor devices is a potential source of EM noise.

The state-of-art solution to the problems, mainly the excessive voltage stress and the EMI can be resolved by limiting the rate of change of voltage at the rising and the falling edge and by alleviating the CM voltage, which is explored in the following categories:

2.6.1 Passive Filtering Technique

A passive filter is installed in between the inverter and motor terminals to reduce the voltage stress, especially at the machine terminals and the neutral point. Depending on their design, the

passive filters can be installed at the inverter end or the machine terminals. The filters installed at the machine terminal are designed to terminate the cable ends at their surge impedance, thereupon named termination filters, whereas the filters installed at the inverter output terminals are termed inverter output filters.

2.6.1.1 Passive Termination Filter

As stated in the previous discussion, the overvoltage at the terminals of the motor is due to voltage wave propagation and reflection phenomenon. The voltage reflection occurs due to a mismatch of impedance at the cable and machine interface. Generally, for small motors (< 25 hp), the characteristic impedance is 10 to 100 times larger than the cable. However, the surge impedance of the large machine (> 50 hp), is comparable to the cable impedance. Illustratively, the magnitude of voltage stress at the machine terminals (V_t) with its surge impedance (Z_{0_m}), DC link voltage (V_{DC}), and cable surge impedance (Z_{0_c}) is expressed as [87],

$$V_t = \left(1 + \frac{Z_{0_m} - Z_{0_c}}{Z_{0_m} + Z_{0_c}} \right) V_{DC} \quad (2.1)$$

The surge impedance often referred as characteristics impedance is the ratio of the amplitude of the TEM voltage and current waves propagating within a medium, herein the cable and the machine, in the absence of reflection. The influence of the surge impedance in the voltage stress at the machine terminals can be expressed using (2.1) and is discussed comprehensively in section 5.3. As a result, the voltage reflection, and hence, the voltage overshoot is more pronounced in a small machine. Howbeit, if the surge impedance of the motor and cable are equal, the voltage stress at the terminals is restricted to the DC link voltage. With the termination filter, the cables are terminated with the passive element whose impedance is equal to the surge impedance of the cable. Based on their order, the filters are classified into the following section:

- *Parallel Resistor Termination:*

As the name suggests, in the parallel resistor termination filter, three phase star connected parallel resistor is connected at the cable machine interface as shown in Figure 2.5. The shunt resistor (R_f) is selected as the surge impedance of the cable as illustrated in (2.2) [113]:

$$R_f = \sqrt{\frac{L_c}{C_c}} = Z_{0c} \quad (2.2)$$

where, L_c and C_c are the per-unit length inductance and capacitance of the cable. However, the power loss in the resistor is significant, therefore, this method is rarely used. By way of example, for a 440V system with a 100 ft long cable, a 190Ω shut resistor is used which incur 1.1kW loss [113].

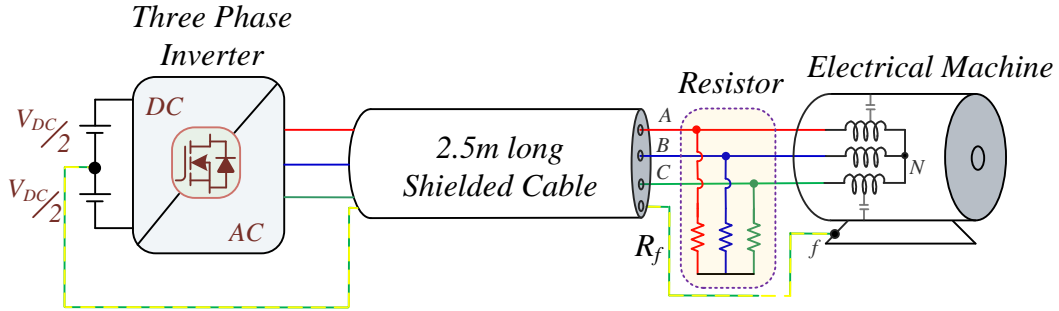


Figure 2.5: Schematic of VSI-fed drive with Parallel resistors connected at the machine terminals

- *First Order Capacitor Resistor Termination:*

In this method, the cable is terminated using a first order filter consisting of star connected three phase capacitors(C_f) with resistors (R_f) connected in series. The filter is connected in parallel at the cable and machine interface as illustrated in Figure 2.6 (a). The filter is designed to match the surge impedance of the cable. Hence, the equivalent impedance of the filter is expressed as [113],

$$Z_{eq} = \sqrt{R_f^2 + \left(\frac{1}{\omega_f C_f}\right)^2} = \sqrt{\frac{L_c}{C_c}} = Z_{0c} \quad (2.3)$$

The resistor is designed for an overdamped system as [87],

$$R_f > \sqrt{\frac{4L_c}{C_c}} \quad (2.4)$$

Equation (2.3-2.4) can be solved to achieve the filter parameters for optimum voltage stress at the machine terminals. In [113] a second order termination filter is proposed with an additional inductance connected in parallel with the resistor as illustrated in Figure 2.6 (b). The losses in the resistor are decreased with the inclusion of the inductor, but the voltage stress is

marginally reduced. The parameters of the second order filter can be deduced using (2.5) as [113],

$$Z_{eq} = \sqrt{\left(\frac{R_f \omega_f^2 L_f^2}{R_f^2 + \omega_f^2 L_f^2}\right)^2 + \left(\frac{R_f^2 \omega_f^2 L_f^2}{R_f^2 + \omega_f^2 L_f^2} - \frac{1}{\omega_f C_f}\right)^2} = \sqrt{\frac{L_c}{C_c}} = Z_{0c} \quad (2.5a)$$

$$R_f > \frac{\sqrt{L_f C_f}}{2C_f} \quad (2.5b)$$

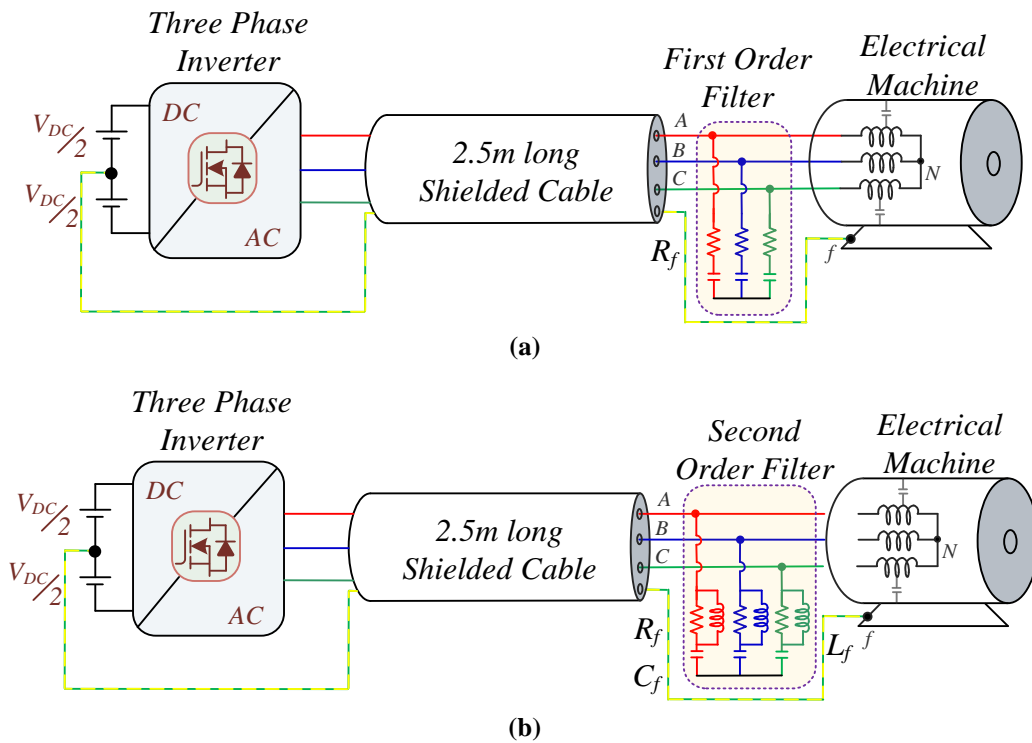


Figure 2.6: Schematic of VSI-fed drive with filters connected at the machine terminal, (a) First order termination filter, (b) Second order termination filter.

2.6.1.2 Inverter Output Filter

The primary role of the inverter output filter is to limit the dV/dt of the inverter output voltage below a detrimental critical value, preventing overvoltage at the machine terminals, ground return current and bearing current. Although, the passive termination filter is effective in suppressing the voltage stress, in several applications such as submersible pumps, however, the machine terminals are inaccessible. Moreover, since the inverter output filter is connected to the inverter terminals, it can be integrated into the same enclosure as an inverter, which leads

to a compact, less bulky and cost-effective solution. Therefore, the inverter output filter is a more promising solution which is classified into the following types:

- *Reactor Filter:*

The output reactor is the simplest and low-cost method of conditioning the voltage stress [114]. It comprises a three phase inductor connected in series between the inverter and cable as illustrated in Figure 2.7. It reduces the dV/dt at the inverter terminals which in turn reduces the dV/dt at the motor terminals. However, it should be installed with care as, if the reactor is wrongly selected, it can extend the duration of the peak voltage. In general, the output reactor is designed with 3-5% impedance at the operating frequency and the overvoltage suppression depends on its impedance. The inductance of the filter can be deduced using (2.6) as [114],

$$L_f = 0.03 \frac{V_{DC}}{2\sqrt{2}\omega_s I_{ph}} \quad (2.6)$$

where, ω_s is the fundamental frequency, I_{ph} is the rated phase current and V_{DC} is the DC link voltage. Although the impedance of the reactor can be increased to achieve effective voltage suppression, a higher impedance causes a rapid increase in cost, weight, and size. Additionally, the higher impedance at the fundamental frequency results in increased voltage drop across the reactor, thereby, the fundamental component of voltage will reduce at the motor terminals. A large voltage drop, especially during overload, may result in torque inadequacy due to insufficient voltage at the motor terminals. These reactors can be used to compensate for the cable charging current and can be used in the large drives, or the drive with cable lengths up to several hundred meters.

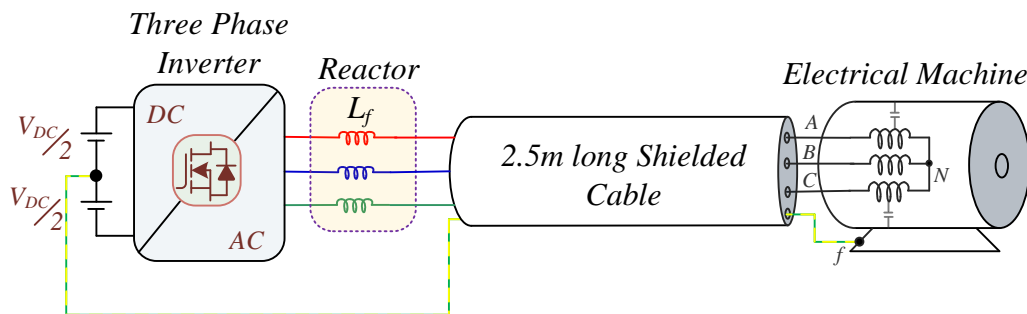


Figure 2.7: Schematic of VSI-fed drive with reactor filter connected at the inverter terminals.

The major drawback of the reactor is core saturation. Core saturation leads to a reduction in inductance, which increases voltage overshoot [114]. As a result, consideration should be given

to ensure that the reactor's magnetic core is not saturated. The reactor should be designed to withstand the peak transient current, resulting in increased size, weight, and expense.

- *Sinewave Filter (LC Filter):*

The sinewave filters [116-119] are installed at the inverter output terminals to suppress the switching harmonics in the voltage which converts the HF voltage pulse into sinusoidal excitation. In this filter, three phase inductor (L_f) is connected in series with the inverter and the star connected capacitor (C_f) is connected in shut between the inductor and the cable, as illustrated in Figure 2.8. The resistor (R_f) is used to dampen the oscillations at the resonance frequency of the filter and is typically recommended for applications with requirements on torque ripple, speed, and audible noise. In addition, since the capacitor acts as a low impedance element at high frequency, the resistance of the resistor is kept equal to the characteristics impedance of the cable to absorb the reflected energy. On the other hand, the resistor is a passive element, which incurs power loss. The transfer function (H) of the filter is expressed as [119],

$$H = \frac{1 + j\omega R_f C_f}{1 - \omega^2 L_f C_f + j\omega R_f C_f} \quad (2.7)$$

where, the attenuation (A) offered by the filter at HF is [89],

$$A = 20 \log \left| \frac{1}{H} \right| \quad (2.8)$$

Generally, for effecting suppression of the HF voltage without affecting the fundamental voltage, the cut-off frequency (ω_c) of the filter should be an order less than the switching frequency (f_{sw}) and higher than the fundamental frequency (f_s). The resistance (R_f) of the filter can be deduced for an overdamped system using (2.9) as [119],

$$R_f \geq \sqrt{\frac{4L_f}{C_f}} \quad (2.9)$$

A 3-dB attenuation at the filter cut-off frequency, (2.7-2.9) can be solved for the parameters of the filter. In [117], the star point of the filter is connected to the mid-point of the DC bus. Referencing the star point of the filter to the mid point offers an additional reduction in the

dV/dt of the voltage pulse. The filter losses, however, surge by 127% [117]. Few other developments are reported in [118-119] illustrating an additional reduction in the dV/dt of the voltage at the machine terminals. In [119], an LC trap filter is connected in a cascade between the inverter and the filter which is tuned to the inverter switching frequency as illustrated in Figure 2.9. It acts as an open circuit for the switching frequency component of the voltage, which eliminates the requirement of a lower cut-off frequency of the sinusoidal filter. However, with the additional LC trap filter, a relatively large inductor is required for the sinusoidal filter. Illustratively, the inductance of the sinewave filter designed for a 25 hp drive was 0.135mH which increases to 0.27mH when used with the LC trap filter [119]. In [118], the magnetizing inductance and the winding leakage inductance are used for developing the filter. Different from the conventional filter, the damping resistor is connected in series with the inductor. This type of filter design yields improved performance with lower filter parameters. In Chapter 6, the design process and its results are thoroughly examined.

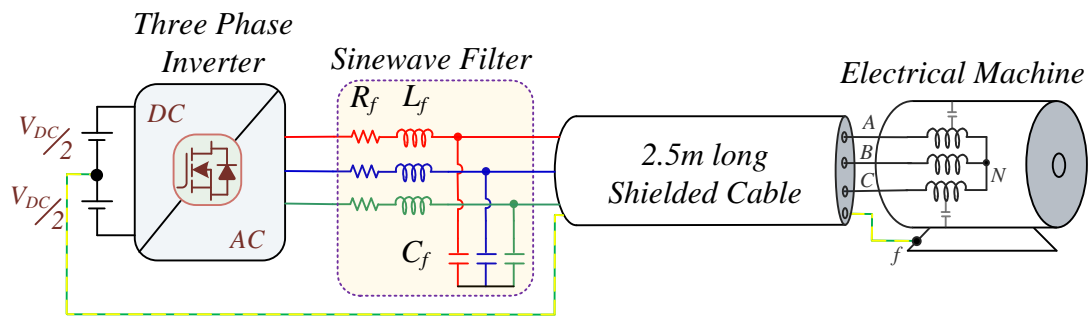


Figure 2.8: Schematic of VSI-fed drive with sinewave filter connected at the inverter terminals.

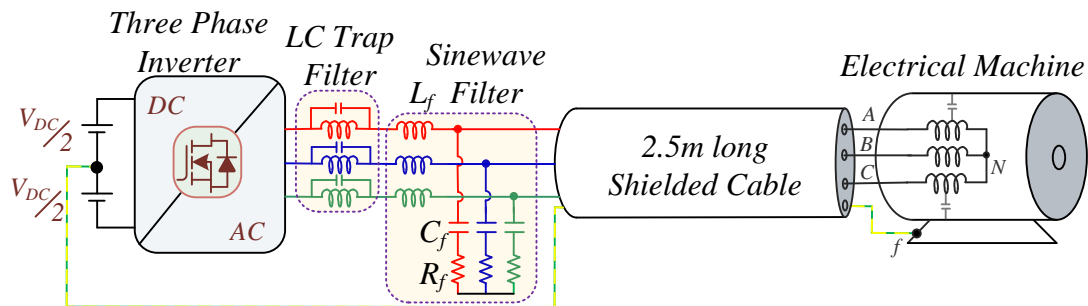


Figure 2.9: Schematic of VSI-fed drive with a combination of sinewave and LC trap filter connected at the inverter terminals.

- *Voltage Limiting Filter (dV/dt Filter):*

The dV/dt filter [120-122] comprises a three phase series connected inductor followed by a three phase star connected capacitor connected in shunt as shown in Figure 2.10, whose cut-off frequency is higher than the switching frequency. The dV/dt filter reduces the peak voltage

and increases the peak rise time by limiting the dV/dt of the voltage pulse at the machine's terminals. However, different from the sinewave filter, the machine terminal voltage remains the rectangular pulse with increased rise time. Reduced dV/dt at the machine terminals leads to reduced voltage stress with uniform voltage distribution within the winding [94-96] [106-38]. Compared to the sinewave filter, the inductor and the capacitor used in the dV/dt filter is lower, thus they are compact, cheaper, and less bulky. Due to its small size parameters, the filter does not impede the dynamic performance of the filter.

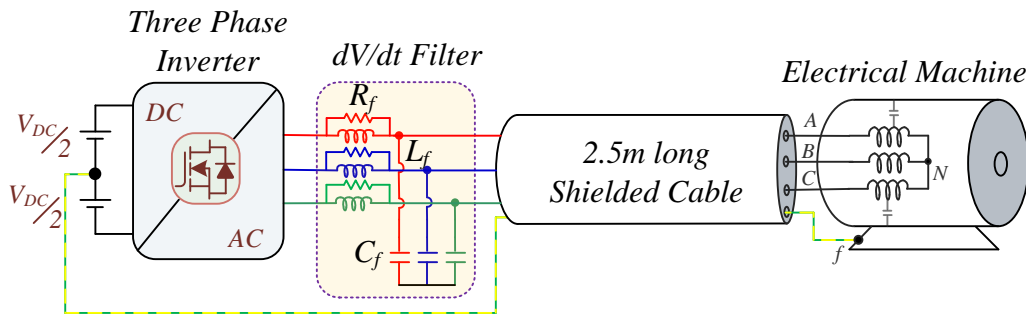


Figure 2.10: Schematic of VSI-fed drive with dV/dt filter connected at the inverter terminals.

The combination of the inductor (L_f) and the capacitor (C_f) forms a second order low pass filter, and the resistor (R_f) is used to dampen the voltage oscillations. The series parameters of the filter are designed by limiting the voltage drop (v_L) across it to 1.5% of the DC link voltage (V_{DC}) as [120],

$$v_L = \frac{i}{\left(\sqrt{\frac{1}{R_f^2} + \frac{1}{(2\pi f_s L_f)^2}} \right)} \leq 0.015V_{DC} \quad (2.10)$$

where i is the phase current and f_s is the fundamental frequency. According to the NEMA standard MG1-part 31 [123], the recommended dV/dt limit for safe use at the motor terminals is $4\text{ kV}/\mu\text{s}$. Thus, the inductance and the capacitance of the filter should be selected such that the time period of one resonant cycle is equal to at least 4 times the rise time at the motor terminals which is expressed as [123],

$$L_f C_f \geq 4 \frac{V_{DC}}{4} \times 10^9 \quad (2.11)$$

The damping resistor decides the damping factor (ξ) of the voltage oscillations. The higher the damping factor, the lesser will be the resistance, and the better will be the damping. Thence, the R_f can be reckoned using (2.12) as [120],

$$R_f = \frac{1}{2\xi} \sqrt{\frac{L_f}{C_f}} \quad (2.12)$$

Using (2.10-2.12), the parameters of the filter can be determined. The dV/dt filter reduces the voltage stress at the motor terminals, however, the CM voltage remains unaddressed. As a result, the shaft voltage that induces bearing current and generates EMI is not reduced.

- *Common Mode Filter:*

The sinewave filter reduces the voltage overshoot at the terminals by converting the inverter's pulse voltage output to sinusoidal excitation, whereas the dV/dt filter does so by extending the voltage pulse's rising time. However, both the filters are ineffectual in reducing the CM voltage. Consequently, the high magnitude of the bearing current and the ground return current induced by the CM voltage interfere with the ground fault protection system installed in the field and contribute to EMI, damage to the bearing such as pitting, and fluting and leads to subsequent failure. Therefore, the CM voltage must be suppressed to avoid premature failure.

The CM voltage can be suppressed by using a CM transformer [124-126]. The CM transformer is a four winding transformer wound on the same core to ensure tight coupling between them and is illustrated in Figure 2.11 [124]. The three primary windings are connected in series between the inverter and the cable, and the fourth secondary winding is connected to a damping resistor. The three primary windings are wound in the same direction, whereas the secondary winding is wound in the opposite direction. As the coupling polarity of the three phase windings is the same, no flux is induced in the core due to the DM current. Therefore, different from the reactors, no core saturation occurs due to DM current. However, the CM current flowing through the phase windings induces flux in the core. Hence, the CM transformer acts as a damping resistor only for the CM current. On the other hand, since the secondary winding is wound in opposite direction, the secondary current prevents the change in flux in the core and suppresses the CM current. The short circuit of the secondary winding with a damping resistor dissipates the power due to the flow of the CM current.

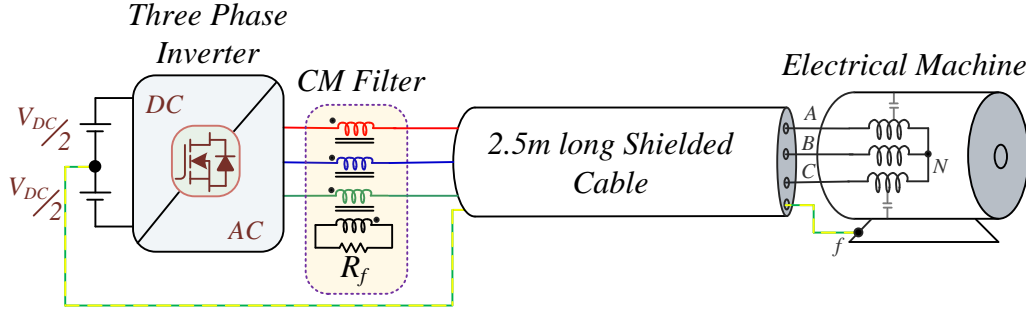


Figure 2.11: Schematic of VSI-fed drive with CM filter connected at the inverter terminals.

The damping resistor of the CM filter is deduced using (2.13) as [124],

$$R_f = \frac{3CV_{DC}^2 f_{sw}}{I_{rms}^2} \quad (2.13)$$

where, C is the CM capacitance of the machine winding, which can be measured using its CM impedance, f_{sw} is switching frequency, I_{rms} is the maximum permissible RMS current through the ground return path, and V_{DC} is the DC link voltage. The inductance (L_f) of each primary winding and the maximum flux linkage (Φ_{max}) of the secondary winding is expressed as [124],

$$L_f = 4R_f^2 C \quad (2.14a)$$

$$\Phi_{max} = 3CR_f V_{DC} \quad (2.14b)$$

In another approach [125], the secondary winding is excited by the pseudo-neutral potential which is created using three phase RC network as illustrated in Figure 2.12 (a). The voltage on the secondary winding is impressed with respect to the source ground. Since the RC network is linked to the phase terminals, it has a high resistance and a low capacitance to limit the DM current through it. However, small capacitance results in small pseudo-neutral potential which reduces the effectiveness of suppression of the CM current through the secondary winding. The solution to this problem is proposed in [126], wherein, a three phase ‘wye’ connected winding housed in a three phase iron core is used, as depicted in Figure 2.12 (b). In addition, the secondary winding is wound in the same direction as the primary winding and the voltage at the secondary winding is impressed with respect to the mid-point of the DC bus. As a consequence, the secondary winding is no longer reliant on the grounding system. A decoupling capacitor is however connected in series with the three phase inductor to prevent core saturation in the event of a low frequency saturation current flow. However, these modifications result in an additional suppression of the CM voltage and ground return current

at the expense of the high leakage inductance of the filter. Illustratively, in [125], for a 0.75 kW induction motor drive, a CM transformer with 4mH leakage inductance is used, whereas, in [126], a CM transformer with 2mH leakage inductance is employed in a 5hp drive. Large filter inductance leads to large, costly, and bulky filters, sometimes the cost and size of the filter are comparable to the overall drive, especially in large power drives. Furthermore, the filters are prone to core saturation due to transient peak current which induces flux in the core beyond its rated limit. Nevertheless, these methods provide a low impedance path to the low frequency CM voltage, particularly, the third harmonic voltage component which, is added to extend the linear limit of the PWM and thus the DC bus utilization, resulting in the inclusion of low frequency leakage current with significant amplitude in the power line.

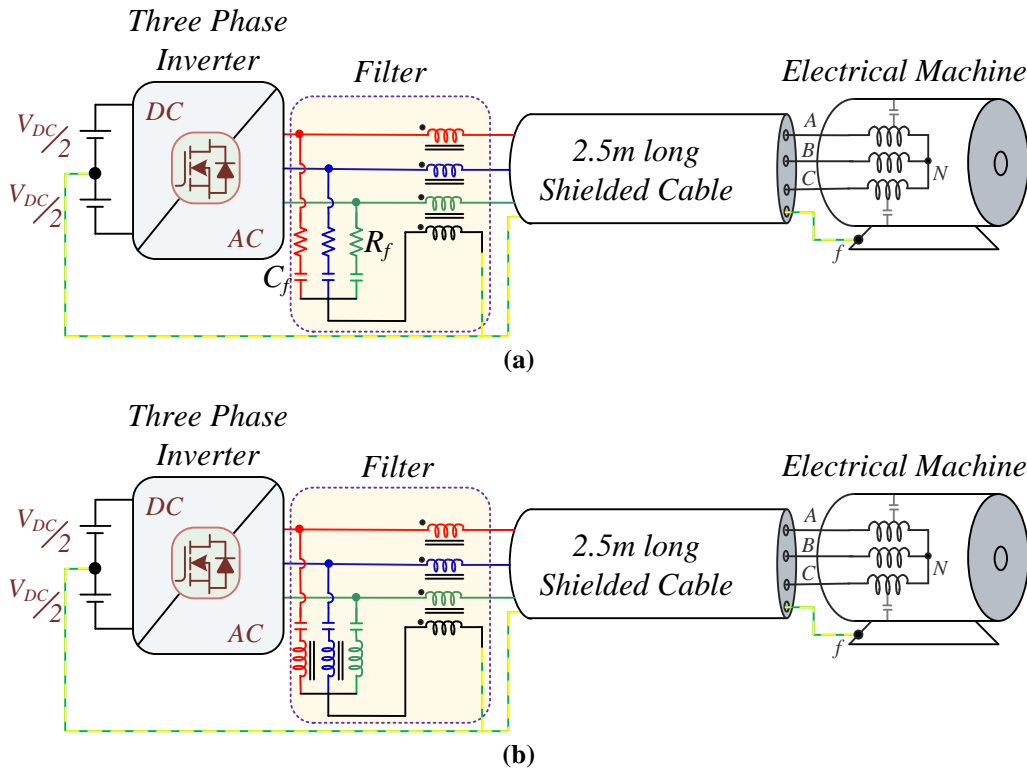


Figure 2.12: Schematic of VSI-fed drive with CM filter connected at the inverter terminals; (a) CM filter connected with RC network, (b) CM filter connected with 3-phase transformer.

The implications of the different methods of inverter output filters in the voltage stress and EMI suppression are summarised in Table 2.2.

Notably, the CM transformer does not suppress the voltage stress at the machine terminals since it does not affect the dV/dt of the voltage pulse. Therefore, several combinations of CM filters with the dV/dt filters and sinewave filters are proposed in the literature [128-130]. In [128], a CM filter in combination with the sinewave filter is used to suppress the voltage stress

at the machine terminals along with the CM voltage as illustrated in Figure 2.13. The results illustrate that the sinusoidal filter converts the pulse voltage excitation into sinusoidal voltage excitation with a 50% reduction in ground return current, however, it does not contribute to reducing its RMS current. When the CM filter is added to the drive along with the sinewave filter, the peak ground return current reduces by a factor of 20 with a 50% reduction in shaft voltage. Moreover, with the addition of a feedback path between the neutral of the sinewave filter and the mid-point of the DC bus, through an RC circuit, the ground return current and the shaft voltage is extensively suppressed. The feedback path provides a low impedance path to the CM voltage and current, so no CM voltage appears at the motor terminals. In yet another study [129], with the combination of the sinewave filter and the CM filter, the peak CM voltage is reduced by 78% and the RMS voltage is reduced by 82% with respect to the voltage with only the sinewave filter. Furthermore, the peak voltage at the machine terminal is reduced by half in both cases. Another study [130] found that, with a 15hp drive, incorporating 740ft cable length, 5Hz output frequency, and 4kHz switching frequency, the combination of CM filter with the dV/dt filter reduces the peak ground return current by 23.5%, and a reduction of 25% is recorded in the RMS current. Nevertheless, these benefits come at the expense of increased passive components including large magnetic components.

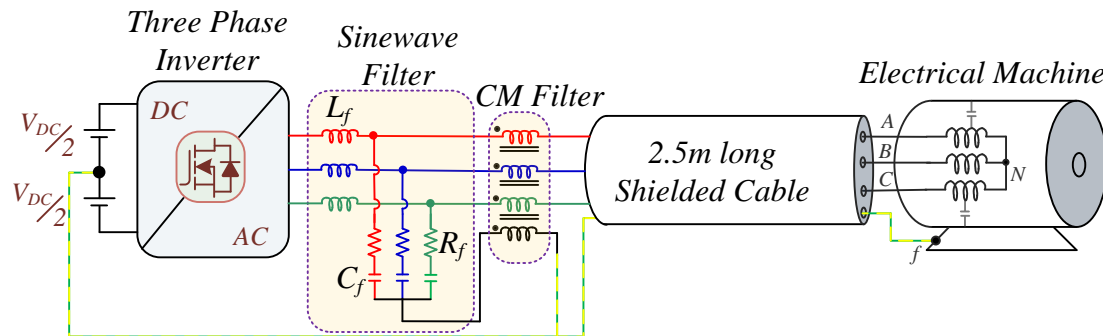


Figure 2.13: Schematic of VSI-fed drive with combination of sinewave and CM filter connected at the inverter terminals.

Table 2.2: A comparative analysis between different types of inverter output filters.

Performance Criteria	Sinewave Filter	dV/dt Filter	CM Filter
Insulation stress	Converts the HF rectangular voltage pulse into sinusoidal excitation. Completely alleviate the voltage stress. Complies with the IEC 60034-17 and NEMA-MG1 requirements for drives with cable length up to 500m.	Reduces the dV/dt at the machine terminal, thus, reduces the voltage stress at the machine terminal. Complies with IEC 60034-17 for cable length up to 150m.	Ineffectual in suppressing voltage stress at the motor terminals.
Bearing current	Reduces bearing current caused by the circulating current. Does not suppress the bearing current induced due to CM voltage.	Reduces bearing current caused by the circulating current. Partial suppression of the bearing current induced due to CM voltage, especially in large motors.	Effectual in the reduction of bearing current due to CM voltage. Not effective in low speed range.
EMC performance	Eliminates voltage oscillations at the machine terminal. Does not change the emission class.	Eliminates voltage oscillations at the machine terminal. Does not change the emission class.	Reduces HF emission up to 1MHz. Does not change the emission class.
Acoustic Noise	Eliminates acoustic noise caused by magnetostriction, as the voltage at the motor terminal is sinusoid.	Does not eliminate switching noise as switching frequency component is present in voltage.	Does not eliminate switching noise as switching frequency component is present in voltage.
Size (with respect to overall drive size)	100%	15-50% (depending upon the drive power size)	5-15% (depending upon the drive power size)

Voltage Drop (with respect to DC bus voltage)	4-10%	0.5%	0%
Maximum Cable Length	With Compliance to EMC standards		
	For screened cable: 300m For unscreened cable: 150m.	For screened cable: 150m;	For Screened cable: 150m with frame size A, B, C, 300m with frame size D, E, F For unscreened cable: 300m
	Without Compliance to EMC standards		
	Up to 150m	For screened cable: 150m	-

2.6.2 Active Filtering Technique

It is well known that the CM voltage induced due to the operation of the PWM inverter, depends on the speed of the drive. Under low-speed range, the lower modulation index results in higher RMS of the CM voltage. Indeed, the traditional filters, mainly the sinewave and the dV/dt filter, are ineffectual in suppressing the CM voltage since they are designed to operate at 50-60Hz and to suppress the voltage stress at the machine terminals. Moreover, due to the magnetic saturation at the low speed, the performance of the CM filters deteriorates as compared to the analytical analysis. Therefore, a method is required which can alleviate the CM voltage over a wide speed range, especially for the drives with frequent start and stop operations.

Considering the requirements of CM voltage suppression, especially at low speed, Ogasawara *et.al.* [131] propose an active common-noise canceller (ACC) as illustrated in Figure 2.14. It consists of a CM transformer whose secondary winding is impressed by a compensating voltage, whose amplitude is the same but with opposite polarity as the CM voltage produced by the inverter. As a result, the CM voltage is eliminated. The CM voltage is impressed on the secondary winding using a couple of transistors connected in a push-pull emitter follower arrangement. The emitter follower circuit excites the secondary winding by the pseudo-CM voltage generated by the star connected capacitors. The other terminal of the secondary winding is connected to the mid-point of the DC link which impedes the flow of DC current. The combination of the emitter follower circuit along with the star connected capacitors and the CM transformer is referred to as ACC. The emitter follower circuit and the capacitors act as a voltage-controlled voltage source, as it excited the secondary winding with the CM voltage of reverse polarity. Moreover, the voltage gain of this combined circuit is unity, alongside the high input impedance and low output impedance. Because the four windings are tightly coupled, the secondary winding induces a CM voltage on the primary winding with opposite polarity, offsetting the inverter's CM voltage. The results illustrate a notable suppression of the CM voltage, shaft voltage and the ground return current even at low speed. However, the ACC is ineffective in suppressing the voltage stress at the machine terminals.

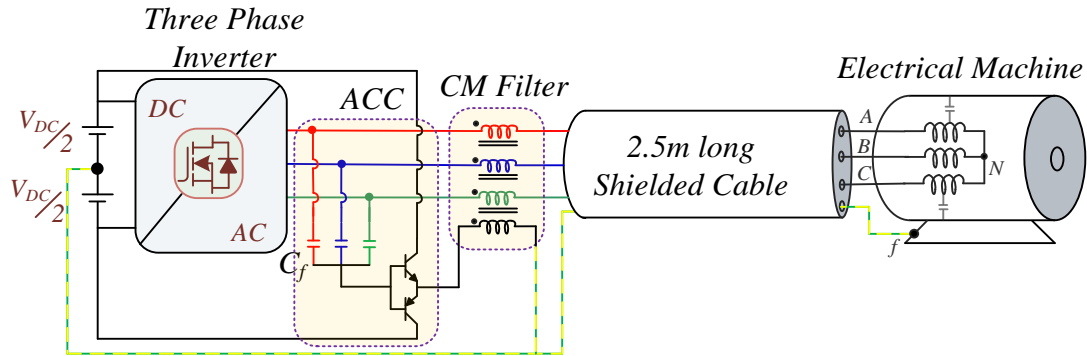


Figure 2.14: Schematic of VSI-fed drive with active common-noise canceller circuit connected at the inverter terminals.

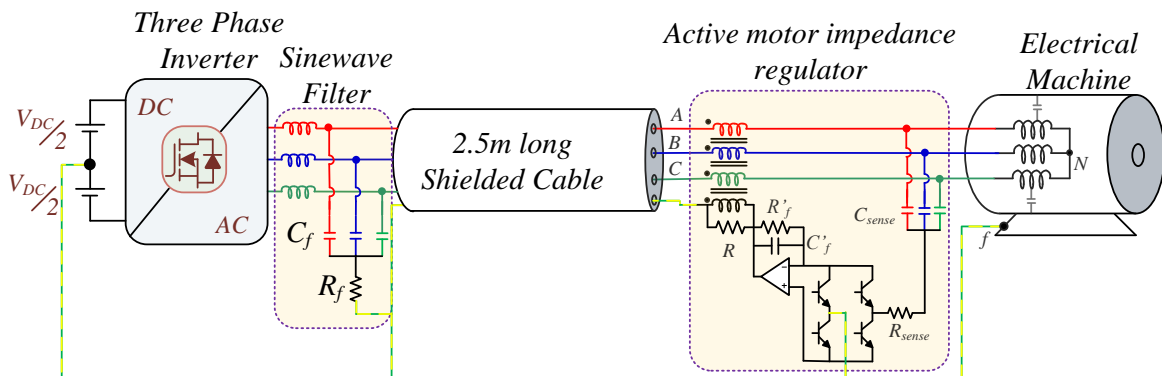


Figure 2.15: Schematic of VSI-fed drive with sinewave filter connected at the inverter terminals and an active motor impedance regulator is connected at the motor terminals.

In yet another study [132], an active motor impedance regulator (IR) is used in series with the machine, which regulates the machine impedance by the active circuit with the flexible gain adjustment. Notably, the IR is installed at the motor terminals as illustrated in Figure 2.15. For suppressing the voltage at the motor terminals, a conventional sinewave circuit is used. The IR circuit consists of three parts; star connected capacitor used for sensing the CM voltage at the machine terminals, op-amp based amplifier circuit and a CM transformer. The CM voltage sensed using the capacitor circuit is amplified and inverted using the amplifier circuit. The amplified and inverted output is impressed on the primary winding using the secondary winding of the CM transformer. The performance of the IR circuit is heavily reliant on its feedback control. The feedback control architecture ensures the immediate alteration of the output signal if any changes are observed in the sensed CM voltage. Needless to say, the output voltage rating of the op-amp must be as high as the CM voltage, as this will aid in assuring the CM transformer's unity turn ratio, resulting in a compact and low-cost transformer. Additionally, the slew rate, bandwidth and the ability to drive capacitive load must be optimised to ensure faster response time, larger gain and stronger driving capability. The

experimental results illustrate that the proposed combination of the sinewave filter and the IR circuit attenuates the peak-to-peak CM voltage by 88% at the rated frequency and 68% at the low frequency range (1-20Hz). Comparatively, if only the sinewave filter is used, the peak-to-peak CM voltage is reduced by 47% at the rated frequency and 30% at the low frequency range. Certainly, the combination of the traditional filters with the CM filter mitigates the voltage stress at the machine terminals alongside the CM voltage which aid in reduction in the ground return current, conducted and radiated EMI, and bearing current and shaft voltage.

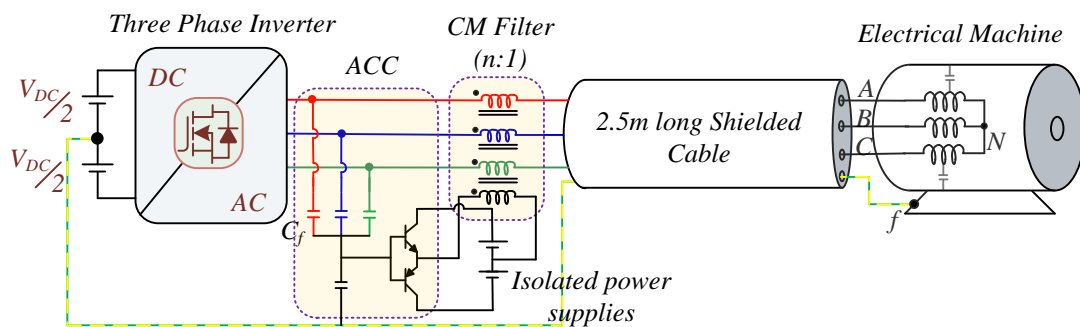


Figure 2.16: Schematic of VSI-fed drive with active common-noise canceller (ACC) realised using isolated power supplies and connected at the inverter terminals.

In the aforementioned solutions, the active amplifier circuit (op-amp or push-pull amplifier) is excited by the CM voltage. Thus, for safe operation, the voltage rating of the amplifier circuit must be higher than the DC link voltage. In general, the op-amp or the transistors with high voltage rating, high slew rate and bandwidth in the range of MHz are less common. Nevertheless, this problem can be solved by adjusting the turns ratio of the CM transformer [133] as illustrated in Figure 2.16, wherein, the voltage rating of the active amplifier circuit can be reduced by factor n using a CM transformer of turns ratio $n:1$. However, simultaneous use of two voltage systems is not recommended. Furthermore, the active filtering technique does not suppress the voltage stress at the machine terminals in solitary.

These aforementioned solutions are effective in attenuating the voltage stress at the machine terminal, along with the reduction in HF ground return current and the bearing current. However, the efficacy of the filters depends on the slew rate of the voltage pulse. Also, the passive magnetic elements of the filter restricts its effectiveness at light load conditions. During, the light load condition, the phase currents are peaky which results in the magnetic saturation of the core. Furthermore, the size of the expensive filter components restricts the realisation of high power density converters. Although, the filters alleviates the voltage stress at the machine terminals, its impact on the voltage stress within the winding is unknown,

particularly under the high slew rate voltage pulse excitation. Therefore, the voltage distribution within the winding is established in the following investigation, and its influence under various passive filters is investigated.

2.7 Summary

Overall, the existing modelling methods represent the HF behaviour of the machine winding and have developed an understanding of voltage distribution under HF PWM voltage excitation. However, the modelling methods have shortcomings in representing the following:

- *Frequency dependent parameters:* The majority of the modelling methods, especially in the time domain, have computed the parameters analytically, wherein, the resistance is computed analytically without considering the proximity effect. Some of the methods have calculated the capacitance without accounting for the fringing effect, thereupon calculating the inductance using the principle of duality with an implicit assumption that the speed of electromagnetic wave within the winding is constant. Only a few methods have calculated the parameters by computing the energy stored in an electrostatic and magnetic field using FEM. One of the advantages of this method is its potential to calculate the frequency dependency of the parameters. Therefore, the following study follows this method [38] to calculate the frequency dependent parameter.
- *Explicit representation of the frequency dependent mutual couplings:* To the best of the authors' knowledge, no methods have represented the frequency dependent mutual coupling between the turns explicitly. All methods in time-domain, except [38] have ignored the frequency dependent representation of the mutual couplings. In [38], the mutual couplings parameters are added to self parameters with an implicit assumption that the capacitive current during excitation is negligible. Therefore, the following study will aim to develop a method for explicit representation of the frequency dependent mutual coupling in the time domain.
- *Voltage stress characterisation under PWM voltage excitation:* In past studies, voltage stress is characterised under single voltage pulse excitation in solitary. However, in the service field, the machines are excited using a PWM inverter, wherein, all the three phases are excited simultaneously. As a result, the authors have gone to considerable length to formulate a method for representing the frequency

dependent parameters explicitly which will characterise the voltage distribution within the winding under PWM voltage excitation

- *Voltage stress suppression at the neutral point*: The modelling method proposed in this study finds excessive voltages stress at the neutral point in addition to the well-known voltage stress at the machine terminals. No studies so far, have bespoke the voltage stress at the neutral point, as the studies have characterised the voltage distribution under a single voltage pulse in isolation. Consequently, the voltage mitigation measure is focused on the voltage stress at the machine terminals. Therefore, the following study will formulate a mitigation measure for the voltage stress at the neutral point.

Chapter 3: Modelling High Frequency Behaviour of Shielded Cable

3.1 General

The cables are an essential part of the VSI-fed drive system and it plays a vital role in transmitting power from the VSI to the machine. Before the advent of semiconductor devices, cables were used to feed at line frequency. However, at the line frequency excitation, the control and operations of the drive were limited to the applications where the speed of the drive is constant. The semiconductor devices based VSI overcome the shortcomings by utilizing their indiscernible gravimetric and volumetric power densities. These characteristics encourage adopting a fast slew rate and high switching frequency for better controllability, which makes the VSI fed drives more prominent in the applications such as industrial processes and automation, electrification of transport, renewable energy generations, and household appliances.

Although the VSI-fed drives have advantages such as smooth start-stop operation, fast acceleration or de-acceleration, speed reversal, increased power factor and better efficiency, there are inimical effects due to the fast slew rate of the voltage pulses of the VSI. When the fast slew rate voltage pulse travel through the cable, HF voltage oscillations occur at the machine terminal which causes voltage overshoot. In addition, the HF CM voltage engendered from the VSI produces HF CM current to earth, primarily determined by the capacitance between the winding and the core of the machine. In the cable with the protective earth (PE) wire, the CM current flows through it which causes EMI with the nearby electronic equipment, interference with the ground fault protection system in industrial facilities and induces HF bearing current especially in the high power motors leading to its bearing failure. Also, the CM current flowing through the phase wires leaks due to capacitive coupling between the phase wires and the PE wire.

These harmful effects occur primarily at HF due to the parasitic impedance of the cable and the machine. Under line frequency excitation, these effects are minimal, as the parasitic impedance is less dominant at low frequency. Therefore, the analysis of these harmful effects requires a suitable model of the cable, which is representative and of good fidelity over a wide range of frequencies. This chapter explains the modelling of the HF behaviour of the cable and its validation, which will be used in the following chapters to study the effect of HF voltage excitation in the VSI-fed drives.

3.2 Multi-Conductor Transmission Line Model

The voltage pulses emitted by the VSI and propagating through the cable correspond to electromagnetic waves propagating through parallel conductors with uniform circular-cylindrical cross-sections along the length. Therefore, the cables are uniform lines, which acts as a wave-guiding structure. Generally, the conductors are enveloped by circular-cylindrical dielectric insulation whose permeability (μ_c) and permittivity (ϵ_c) are constant and are independent of the position in space, as illustrated in Figure 3.1. Hence, the cables are said to constitute conductors in a homogeneous medium. The velocity, ϑ_c , of propagation of the waves on the conductor is equal to that of the medium, in which they are immersed and is expressed as [134],

$$\vartheta_c = \frac{1}{\sqrt{\mu_c \epsilon_c}} \quad (3.1)$$

Therefore, the cables with 3 phase conductors and one protective earth wire can be considered as a uniform, homogeneous, MCTL. The voltage pulse impinging the line terminals induces an electromagnetic field around the conductor, which has a TEM structure. The fundamental assumption of the TEM structure is that the electric field intensity $\vec{E}(x, y, z, t)$ and the magnetic field intensity $\vec{H}(x, y, z, t)$ in the space surrounding the conductor lie in a plane (x, y) transverse to line axis (z -axis), as illustrated in Figure 3.2. The important consequence of the TEM field structure, which relates it to the voltage exciting the cable is,

- The voltage between the conductors and the current flowing through it can be uniquely defined, although the fields are varying with time.

- The sum of the current through the conductors at any cross-section is zero. This infers that the reference conductors, herein is protective earth wire, is the return for the remaining three conductors.

However, in practice, the net current through the cross-section may not be zero. The presence of nearby conductors or metallic structures or distant sources such as radar transmitters or the television and radio transmitters may induce extra currents, also known as EMI. Therefore, shielded cable is used to reduce this effect.

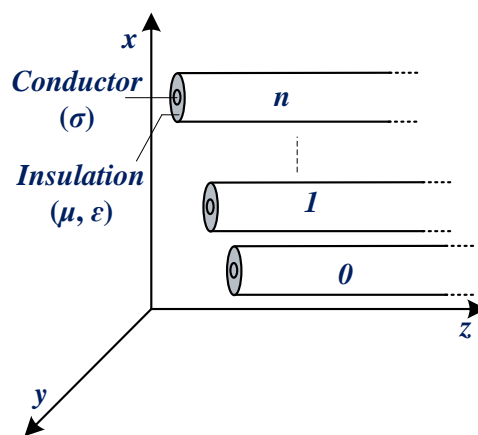


Figure 3.1: Multi-conductor transmission line embedded in homogeneous medium.

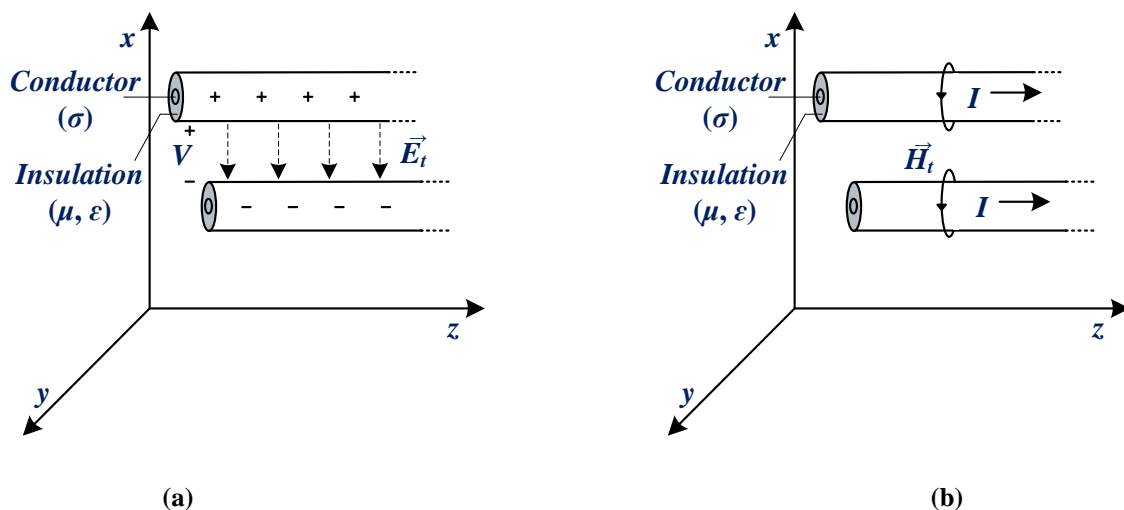


Figure 3.2: Transverse electromagnetic field structure in a multi-conductor transmission line representing (a) electric field intensity, (b) magnetic field intensity.

If the voltage pulse impinging cable terminals induces electric field intensity $\vec{E}_t(x, y, t)$ and the magnetic field intensity $\vec{H}_t(x, y, t)$ in the space surrounding the conductor in a transverse

plane (x, y) perpendicular to the axis of its propagation (z) , then using Maxwell's equation [134],

$$\nabla \times \vec{E}_t = -\mu \frac{\partial \vec{H}_t}{\partial t} \quad (3.2a)$$

$$\nabla \times \vec{H}_t = \sigma \vec{E}_t + \varepsilon \frac{\partial \vec{E}_t}{\partial t} \quad (3.2b)$$

The del (∇) operator can be resolved in two components as, (∇_t) in the transverse plane and (∇_z) in the z -direction [134], where,

$$\nabla_t = \hat{a}_x \frac{\partial}{\partial x} + \hat{a}_y \frac{\partial}{\partial y} \quad (3.3a)$$

$$\nabla_z = \hat{a}_z \frac{\partial}{\partial z} \quad (3.3b)$$

where, \hat{a}_x , \hat{a}_y , and \hat{a}_z are the unit vectors in the direction of their respected axes. Using (3.2-3.3),

$$(\nabla_t + \nabla_z) \times \vec{E}_t = \nabla_t \times \vec{E}_t + \nabla_z \times \vec{E}_t = -\mu \frac{\partial \vec{H}_t}{\partial t} \quad (3.4a)$$

$$(\nabla_t + \nabla_z) \times \vec{H}_t = \nabla_t \times \vec{H}_t + \nabla_z \times \vec{H}_t = \sigma \vec{E}_t + \varepsilon \frac{\partial \vec{E}_t}{\partial t} \quad (3.4b)$$

On solving (3.4),

$$\hat{a}_z \times \frac{\partial \vec{E}_t}{\partial t} = -\mu \frac{\partial \vec{H}_t}{\partial t} \quad (3.5a)$$

$$\hat{a}_z \times \frac{\partial \vec{H}_t}{\partial t} = \sigma \vec{E}_t + \varepsilon \frac{\partial \vec{E}_t}{\partial t} \quad (3.5b)$$

$$\nabla_t \times \vec{E}_t = 0 \quad (3.5c)$$

$$\nabla_t \times \vec{H}_t = 0 \quad (3.5d)$$

From (3.5a-3.5b), the electric and the magnetic field are orthogonal. Also, (3.5c-3.5d) illustrates that the electric and magnetic fields in a space around the conductor satisfy static distribution in the transverse plane. Alternatively stated, the electric and magnetic fields in the transverse plane are identical to that of DC excitation, even though they are time-dependent. This implies that the transmission line parameters such as per-unit length capacitance, inductance and conductance can be determined in the transverse plane using independent excitation, which simplifies their determination.

3.2.1 Transmission Line Parameters

The transverse electric field induces transverse conduction current through the lossy medium due to its conductivity (σ). This effect can be represented by a section of conductor of length (Δz) using a conductance (g). For a uniform homogeneous conductor, this effect is distributed uniformly along its length. Therefore, if the section of the conductor of length (Δz) has total conductance G , then the per-unit length conductance (g) is expressed as [134],

$$g = \lim_{\Delta z \rightarrow 0} \frac{G}{\Delta z} \quad (3.6)$$

wherein, the transverse current ($\Delta I_g(z,t)$) is expressed as [134],

$$I_g(z,t) = g \Delta z V(z,t) \quad (3.7)$$

Similarly, the charged conductors separated by the lossy insulated medium forms capacitance through which the displacement current ($\Delta I_c(z,t)$) flows. This effect is uniformly distributed along the line. If the section of conductor of length (Δz) has total capacitance C , then the per-unit length capacitance (c) is expressed as [134],

$$c = \lim_{\Delta z \rightarrow 0} \frac{C}{\Delta z} \quad (3.8)$$

wherein, the displacement current ($\Delta I_c(z,t)$) is expressed as [134],

$$I_c(z,t) = c \Delta z \frac{\partial V(z,t)}{\partial t} \quad (3.9)$$

Intuitively, the current flowing through the phase conductor and returning from the PE wire produces magnetic field intensity (\vec{H}_t) in the transverse plane. Due to the conductor permeability (μ), the magnetic field intensity causes field density (\vec{B}_t) which induces magnetic flux (Ψ_t) in the transverse plane. This magnetic flux will have an associated inductance which is uniformly distributed along the length. If a section of the line of length (Δz) has total inductance L , then, the per unit length inductance (l) is expressed as [134],

$$l = \lim_{\Delta z \rightarrow 0} \frac{L}{\Delta z} \quad (3.10)$$

The per-unit length inductance (l) is the ratio of transverse magnetic flux per-unit length penetrating the loop between the conductors and the current (I) flowing through it as [134],

$$l = \frac{\Psi_t}{I(z, t)} \quad (3.11)$$

This will produce a voltage drop ($V_l(z, t)$) across the conductor, which is expressed as [134],

$$V_l(z, t) = l \Delta z \frac{\partial I(z, t)}{\partial t} \quad (3.12)$$

For a homogeneous medium surrounding the uniform transmission lines, these parameters are related as [134],

$$lc = \mu \epsilon \quad (3.13a)$$

$$gl = \sigma \mu \quad (3.13b)$$

$$\frac{g}{c} = \frac{\sigma}{\epsilon} \quad (3.13c)$$

The aforementioned discussion is valid for the perfect conductor, wherein, the conductivity of the conductors is assumed infinity. Practically, the conductors have finite conductivity, so-called imperfect conductors. The current flowing through the imperfect conductors induces a non-zero electric field (\vec{E}_z) along with the propagation, thereby, violating the fundamental assumption of the TEM field structure. The net electric field is the sum of the electric field in the transverse direction and the z -direction. However, so long as the transmission lines act as a guided wave structure, these losses must be small. This is referred to as a quasi-TEM structure.

If the section of conductor of length (Δz) has total resistance R , then the per-unit length resistance (r) is expressed as [134],

$$r = \lim_{\Delta z \rightarrow 0} \frac{R}{\Delta z} \quad (3.14)$$

3.2.2 Transmission Line Equation

Thus lumped parameter circuit of the electrically small section (Δz) representing the per-unit resistance (r), inductance (l), conductance (g) and capacitance (c) for a n conductor cable is represented in Figure 3.3 (a), and the total cable length is represented as a continuum of these as illustrated in Figure 3.3 (b). The protective earth conductor is assumed reference conductor carrying return current of n -conductor cable and is denoted by '0'. The current flowing through protective earth conductor at instance t in section z is represented as $I_0(z, t)$, whereas, the current in the i^{th} conductor is represented as $I_i(z, t)$. Similarly, the i^{th} conductor voltage measured with respect to the protective earth conductor in section z at instant t is represented as $V_i(z, t)$.

Using Kirchhoff's law gives [134],

$$V(z + \Delta z, t) - V(z, t) = -r\Delta z I(z, t) - l\Delta z \frac{\partial I(z, t)}{\partial t} \quad (3.15a)$$

$$I(z + \Delta z, t) - I(z, t) = -g\Delta z V(z + \Delta z, t) - c\Delta z \frac{\partial V(z + \Delta z, t)}{\partial t} \quad (3.15b)$$

Dividing both sides by Δz and applying limit $\Delta z \rightarrow 0$ yields the transmission line equation [134],

$$\frac{\partial V(z, t)}{\partial z} = -rI(z, t) - l \frac{\partial I(z, t)}{\partial t} \quad (3.16a)$$

$$\frac{\partial I(z, t)}{\partial z} = -gV(z, t) - c \frac{\partial V(z, t)}{\partial t} \quad (3.16b)$$

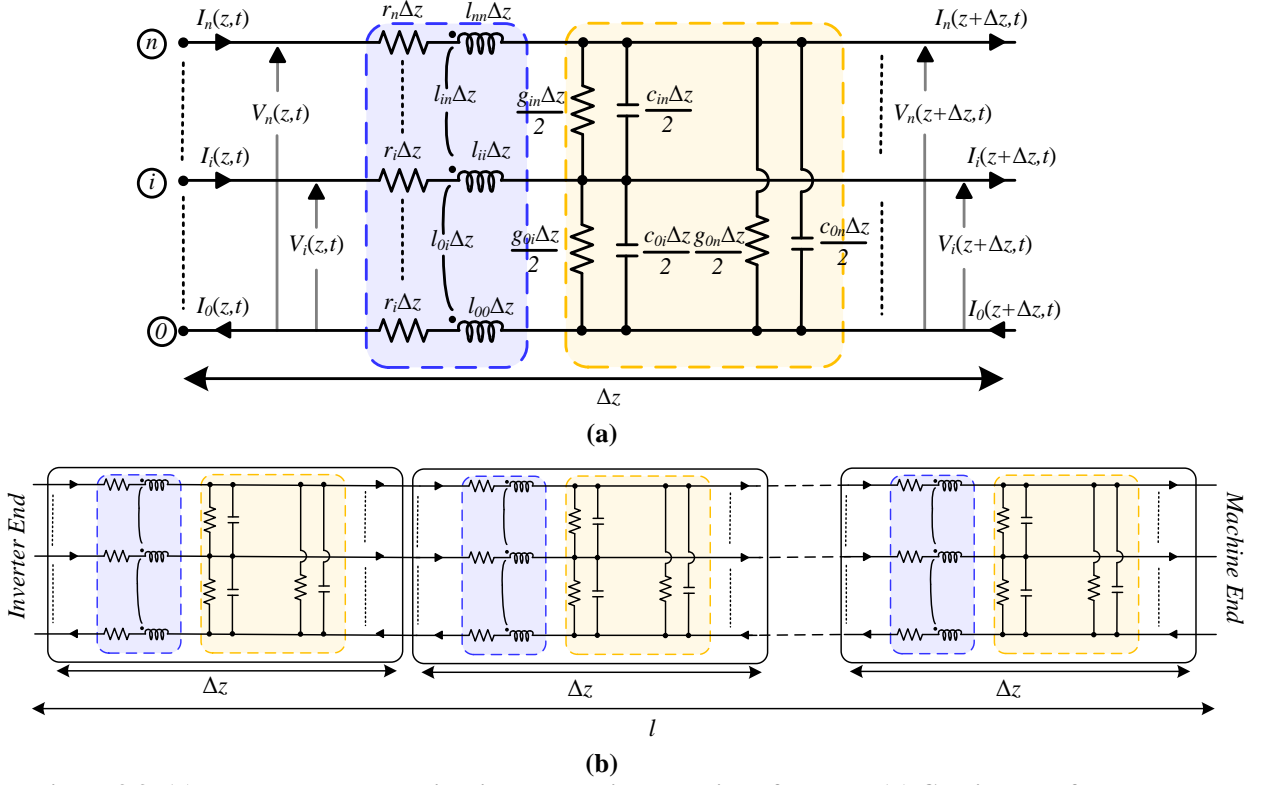


Figure 3.3: (a) lumped parameter circuit representing a section of a cable, (b) Continuum of lumped parameter circuit used for cable model

The TEM field structure can be analysed in two important domains, the time-domain and the frequency-domain. The equations in (3.16) represent the TEM field structure in the time-domain. The frequency-domain differential equation can be derived by replacing the time derivative with $j\omega$ as [134],

$$\frac{d\hat{V}(z, \omega)}{dz} = -r\hat{I}(z, \omega) - jl\omega\hat{I}(z, \omega) \quad (3.17a)$$

$$\frac{d\hat{I}(z, \omega)}{dz} = -g\hat{V}(z, \omega) - jc\omega\hat{V}(z, \omega) \quad (3.17b)$$

where, $I(z, t) = I\cos(\omega t + \theta(z)) = \hat{I}(z, \omega)$ and $V(z, t) = V\cos(\omega t + \theta(z)) = \hat{V}(z, \omega)$. Thus, the first order coupled partial differential equation in the time-domain is represented as an ordinary differential equation in the frequency-domain, thereby, the solution becomes simpler.

3.2.3 Time-Domain vs Frequency-Domain Solution

So far, the per-unit parameters of the transmission line are assumed constant throughout the length of the conductor. However, these parameters vary with the frequency of excitation. For perfect conductors, wherein, $r = 0$, the current will reside on the surface of the conductor. For imperfect conductors, at low frequency, the current is uniformly distributed over the conductor's cross-section. But at HF, due to induced eddy currents, the current is pushed towards its surface within the order of a skin depth (δ), which is represented as [134],

$$\delta = \frac{1}{\sqrt{\pi f \mu \sigma}} \quad (3.18)$$

Thus, with the increase in the excitation frequency (f), the per-unit resistance ($r(\omega)$) will increase at the rate of \sqrt{f} . Similarly, when the current is uniformly distributed over the conductor cross-section at low frequency, some of the magnetic flux lie internal to the conductor, which entails internal inductance (l_i). With increasing frequency, the current moves towards the surface of the conductor, thereby the internal inductance decreases at the rate of \sqrt{f} . Thus, the internal inductance is frequency dependent. The total per-unit length inductance of the conductor ($l(\omega)$) is the sum of the inductance due to internal flux and the constant external flux. As a result of it, the per-unit inductance is frequency dependent.

The effective conductivity of the medium surrounding the conductors is primarily due to the bond charges in the dielectric. Therefore, the conductivity (σ) is frequency dependent, thereby, the per-unit conductance ($g(\omega)$) is frequency dependent. Similarly, the relative permittivity of the dielectric (ϵ_r) varies with frequency, although mildly. Therefore, the per-unit length capacitance ($c(\omega)$) depends on the frequency. Thus, with the frequency dependent parameters, (3.17) transforms as [134],

$$\begin{aligned} \frac{d\hat{V}(z, \omega)}{dz} &= -r(\omega)\hat{I}(z, \omega) - j\omega l(\omega)\hat{I}(z, \omega) \\ &= -\hat{z}(\omega)\hat{I}(z, \omega) \end{aligned} \quad (3.19a)$$

$$\begin{aligned} \frac{d\hat{I}(z, \omega)}{dz} &= -g(\omega)\hat{V}(z, \omega) - j\omega c(\omega)\hat{V}(z, \omega) \\ &= -\hat{y}(\omega)\hat{V}(z, \omega) \end{aligned} \quad (3.19b)$$

where, $\hat{z}(\omega) = r(\omega) + j\omega l(\omega)$ is the per-unit length impedance and $\hat{y}(\omega) = g(\omega) + j\omega c(\omega)$ is the per-unit length admittance. The solution to (3.19) in frequency-domain presents no difficulty, as the equation is solvable at each frequency by calculating the per-unit parameters at that frequency and incorporating them as a constant for that frequency of excitation. However, in the time-domain, solving the time-domain equation (3.16) involves inverse Fourier transform and convolution. Firstly, the frequency dependent parameter is transformed into the time-domain using the inverse Fourier Transform as [85],

$$z(t) = \frac{1}{2\pi} \int_{-\infty}^{\infty} \hat{z}(\omega) e^{j\omega t} d\omega \quad (3.20a)$$

$$y(t) = \frac{1}{2\pi} \int_{-\infty}^{\infty} \hat{y}(\omega) e^{j\omega t} d\omega \quad (3.20a)$$

Later, the time-domain inverse Fourier transform is used in (3.16) with the convolution (*) to get the time-domain transmission line equation with the frequency dependent parameters as,

$$\begin{aligned} \frac{\partial V(z,t)}{\partial z} &= -z(t) * I(z,t) \\ &= -\int_0^t z(\tau) I(z,t-\tau) d\tau \end{aligned} \quad (3.21a)$$

$$\begin{aligned} \frac{\partial I(z,t)}{\partial z} &= -y(t) * V(z,t) \\ &= -\int_0^t y(\tau) V(z,t-\tau) d\tau \end{aligned} \quad (3.21b)$$

Thus, in comparison to the frequency-domain, where, the per-unit parameters can be easily incorporated in the transmission line equation, the time-domain solution presents three computational challenges, (1) obtain the time-domain inverse Fourier transform of the frequency dependent parameters, (2) perform the convolution, and (3) solve the first-order coupled partial differential equation.

Despite the computation complexity, the time-domain solution is advantageous in determining the response to the physical signals. Generally, the physical signals are in the time-domain, which can be used to get the voltage and current along the transmission line without

the transformation to the frequency-domain. However, in the frequency-domain, the physical signal must be decomposed into its spectral component using Fourier series, and then the voltage-current relationship is solved for each frequency. Later, the time-domain solution is obtained using an inverse Fourier transform. This approach is expedient for considering the frequency-dependent parameters and the mutual coupling in the HF model. However, such an approach is inappropriate for the application of fast varying signals and studies of system behaviour, consisting of other components, such as inverter, possible filter, cable, etc. Albeit the simple form of transmission line equation in the frequency-domain, the inclusion of the mutual parameters between the conductors increases the computation complexity. One of the possible solutions to it is modal transformation [86], which diagonalise the impedance matrix and exterminate the mutual coupling terms. Consequently, the frequency dependence of the mutual inductive coupling engenders frequency dependent modal transformation matrix, which increases further complexity.

In practice, electromagnetic fields are distributed throughout space. If the TEM field structure's largest dimension is less than the wavelength of the shortest wave of the field, the EM effects can be lumped into the circuit elements as in lumped circuit theory and represent the conductors as lumped equivalent circuits. These equivalent circuits can be further solved by circuit theory, thereby avoiding the solution to the transmission line equations. The transmission line equations, which views the cable as distributed parameter structure, can be extended to lumped circuit analysis technique to solve the electrically large structures. Therefore, in the following sections, the cable is represented as a series connected lumped parameter equivalent circuit, which represents the distributed nature of the parameters. Further, the lumped parameter circuit is used to calculate the voltage response at the cable end when it is excited with the high slew rate voltage pulse.

3.2.4 Equivalent Circuit Representation

The major advantage of the lumped circuit is that the voltage and current distribution within a transmission line can be analysed without solving the transmission line equation. The approximation of lumped circuit representation for a TEM field structure is applied to a circuit whose largest dimension is electrically smaller than the shortest wavelength (λ_{min}) of the TEM field around the conductor. The shortest wavelength in the field induced due to the voltage pulse excitation is expressed as [39],

$$\lambda_{\min} = \frac{\mathcal{G}}{f_{\max}} \quad (3.22)$$

where, \mathcal{G} is the velocity of the TEM wave within the cable, and f_{\max} is the maximum frequency component in the spectrum of the voltage excitation. The spectral amplitude [135] of the voltage pulse illustrated in Figure 3.4 (a), with slew rate (t_r), amplitude V_{DC} , and duty ratio D is shown in Figure 3.4 (b). As illustrated, the spectral amplitude remains constant until the first corner frequency ($f_{sw}/\pi D$), which depends on the switching frequency (f_{sw}) of the voltage pulse. Later, the spectral amplitude reduces gradually at the rate of 20dB/decade until the second corner frequency ($1/\pi t_r$). Thereafter, the spectrum rolls off at the rate of 40dB/decade. The second corner frequency depends on the slew rate, thereby, the voltage pulse with a fast slew rate has significant spectral content until higher frequency. Although according to the Fourier series, the spectral content spreads to infinite frequency, it is impossible to include all of them in the analysis. As a rule of thumb, it is assumed that to reasonably reconstruct the voltage pulse with the same slew rate, pulse width and magnitude, the spectral components up to three times the second corner frequency is sufficient [135]. Hence, the maximum frequency of the spectrum is expressed as [41],

$$f_{\max} = \frac{3}{\pi t_r} \quad (3.23)$$

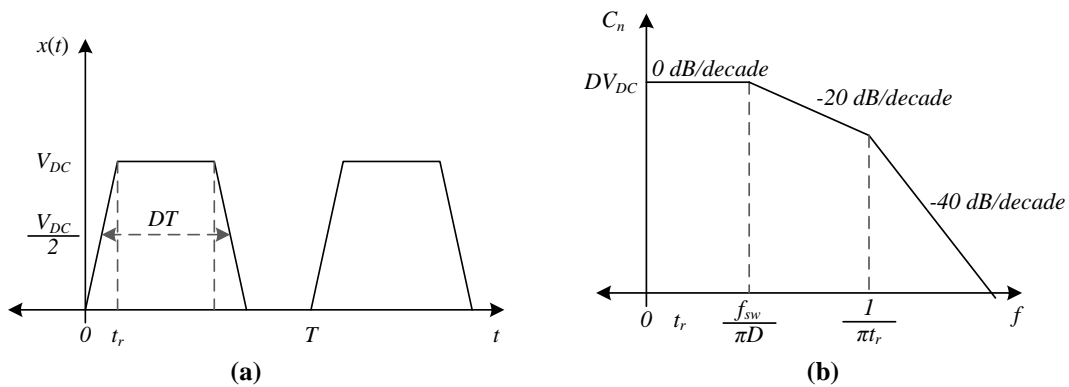


Figure 3.4: (a) A periodic pulse train representing the output of the PWM inverter, (b) Spectral spread of the pulse train.

Thus, the voltage pulse with a steep slew rate has a wide spectral spread. With the recent semiconductor technology, the typical slew rate of the IGBT based drives is 200ns, whereas, the SiC based drives can switch within 20ns [136]. Consequently, with the SiC based drives,

the voltage overshoot and the EMI will be high. To keep the cable model representative of the HF excitation arising due to the fast slew rate, the modelling process assumes the maximum slew rate of the voltage pulse, that is, 20ns. The largest dimension of the TEM field structure, herein, a section of the cable (Δl), must be smaller than the shortest wavelength such that at least 20 sections of the cable can be accommodated within the wavelength [39], which is expressed as,

$$\Delta l = \frac{\lambda_{\min}}{20} = \frac{9 \times \pi \times t_r}{20 \times 3} \quad (3.24)$$

The relative permittivity of the conductor insulation of the cable considered in this study is 2.8. Therefore, using (3.23), for a voltage pulse of slew rate 20ns, the length of cable represented by each lumped circuit is,

$$\Delta l = \frac{1}{\sqrt{\epsilon\mu}} \frac{\pi \times t_r}{20 \times 3} = 0.1877m \quad (3.25)$$

Thus, for a voltage pulse of slew rate 20ns, the lumped parameter circuit should represent the maximum cable length of 0.1877m. Generally, the cable length (l_c) is larger than the length of the smaller section (Δl). Therefore, the lumped circuit is iteratively repeated to represent the whole length of the cable. The lumped circuit is also known as a cell since it represents a section of the wire. The lumped equivalent circuit can be represented in two ways, the lumped-Pi structure or the lumped-T structure as shown in Figure 3.5. These structures represent a section of the cable and are named after the structure they represent. In the lumped-Pi circuit, the shunt parameters are divided into two equal parts, which are represented on either side of the series parameter. In the lumped-T structure, the series parameters are equally divided into two and represented on either side of the shunt parameters. The series parameters include the frequency dependent resistance and inductance of the conductor and the mutual coupling between them, whereas, the shunt parameters includes capacitive coupling between the conductors in concern, i.e., the partial capacitance. Both the structure represent the behaviour of the TEM field structure unless the length of the structure represented by each unit cell is greater than the shortest wavelength of the excitation. In this study, the lumped-Pi structure is adopted.

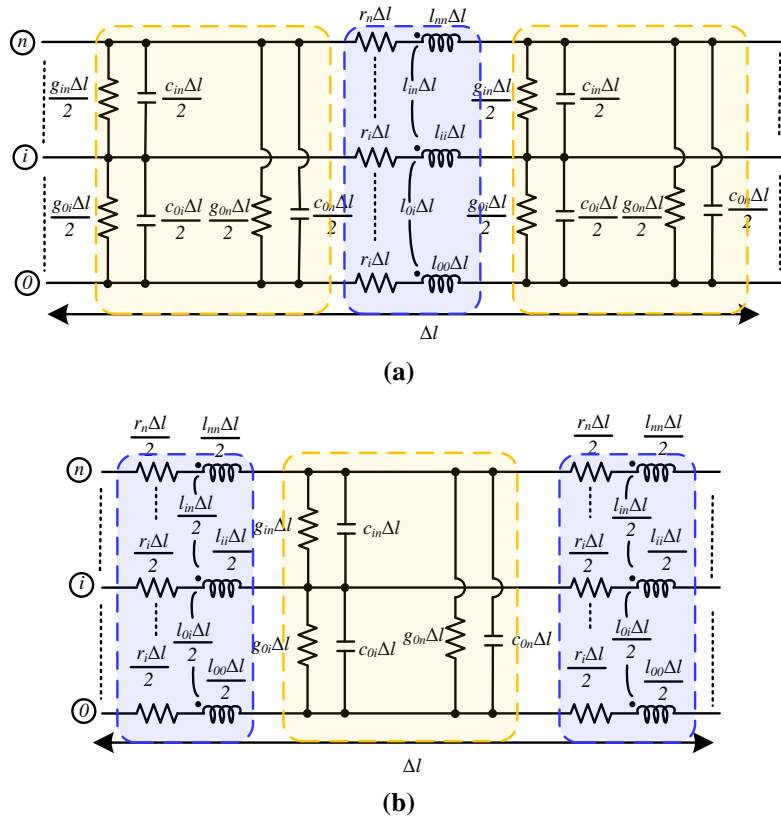


Figure 3.5: Lumped parameter circuit representing a section of cable called cell; (a) lumped-Pi circuit, (b) lumped-T circuit

Each section represents Δl length of the cable and is repeated N ($N = l/\Delta l$) times to represent the full length of the cable. The lumped circuit represent series impedance, that is, inductance and resistance of the conductor, and the shunt impedance such as capacitive coupling between the conductors and the dielectric loss. As emphasised previously, these parameters are frequency dependent. One of the ways to encompass the frequency dependency is to have a set of lumped parameter circuits each representing the cable for a single frequency excitation. Thus, to calculate the voltage at the cable ends as a response to the voltage pulse, the lumped parameter circuit is assumed linear time-invariant system, thereby, the response is the sum of the response of the cable due to the spectral content of the voltage pulse. Figure 3.6 summarises the process to calculate the response to the voltage excitation, in which the voltage pulse is decomposed into its spectral component and is fed to their respective circuits representing the cable behaviour at that frequency. Later, the response of the circuit is used to transform in time-domain using an inverse Fourier transform. However, this method is cumbersome, as to reasonably reconstruct the response to the voltage excitation, a large set of the circuit is required each representing the cable behaviour over a specific frequency. As a result, to find the

response over a voltage excitation of fast slew rate, the lumped parameter circuit is discretely defined over a wide range of frequency, which requires a large set of lumped parameter circuits.

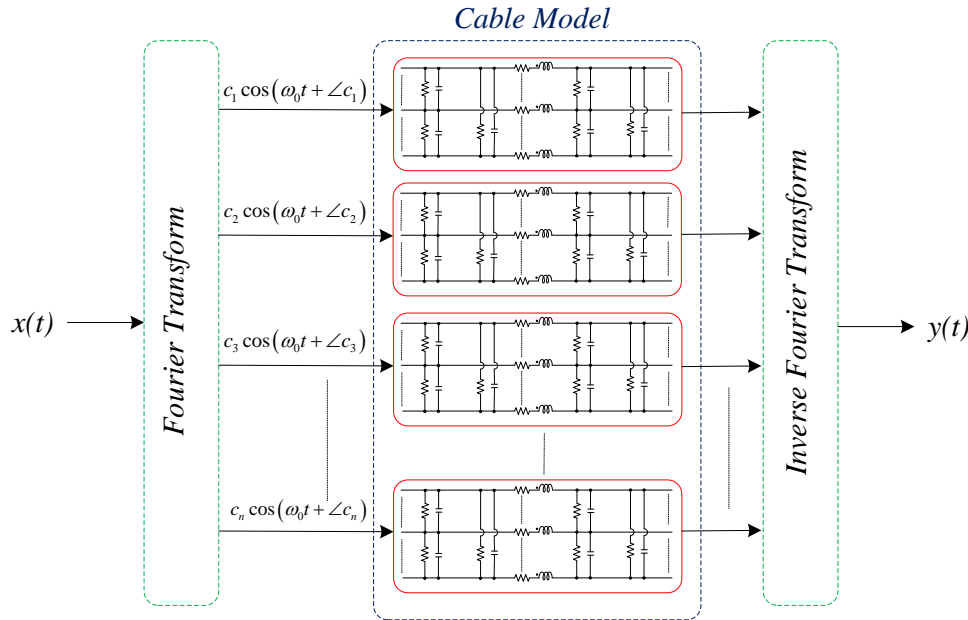


Figure 3.6: Schematic of the method to obtain the time-domain response of a lumped parameter transmission line circuit.

In another approach, the frequency response of the parameters is approximated as a linear combination of the frequency independent parameters. The key advantage of this method is that it incorporates the frequency dependency of the parameter into a single circuit. As a result, the frequency dependent behaviour of the cable parameters is represented by a single circuit. This technique is used in this study and is thoroughly detailed in the following section.

3.3 Computation of Model Parameters

As emphasised in section 3.2, the fundamental principle of the TEM field structure is; the electric and magnetic field surrounding the conductors resides in the plane transverse to the direction of propagation. In addition, the fields are orthogonal and satisfy static distribution in the transverse plane. In essence, the electric and magnetic fields are identical in structure to those for the DC excitation, although they vary in time. This has two major implications:

- The voltages and currents that are ordinarily defined for excitation, can be specified uniquely in the 2D transverse plane, although the fields vary in time.
- The transmission line parameters such as per-unit length resistance, inductance capacitance and inductance can be deduced using separate excitation which simplifies their determination.

Therefore, by computing, the energy stored in the static electric field arising from the potential difference between the conductors, the capacitance between the conductors separated by the dielectrics can be determined. Similarly, by computing the energy stored in the magnetic field surrounding the conductors arising due to the current flowing through it under different frequencies of excitation, the frequency dependent resistance and inductance can be deduced.

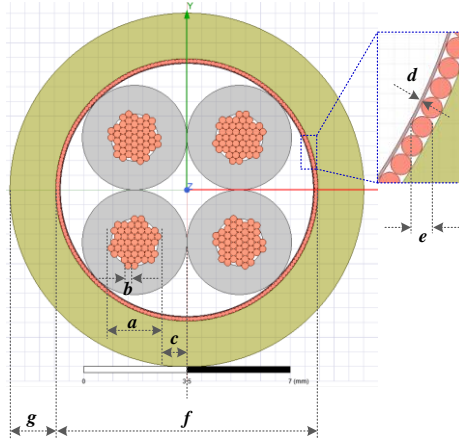


Figure 3.7: Schematic diagram of the cross-section of 4-wire shielded cable

Table 3.1: Parameters of shielded cable

Parameter	Value
Conductors	4
Conductor Diameter (a)	1.784 mm
No. of Strands/Conductor	40
Strand Size (b)	30 AWG
Thickness of core insulation (c)	0.9 mm
Permittivity of core insulation	2.8 F/m
Thickness of aluminum sheath (d)	0.02 mm
Diameter of braid strand (e)	0.14 mm
Inner diameter of jacket insulation (f)	9 mm
Thickness of jacket insulation (g)	1.5 mm
Permittivity of jacket insulation	4 F/m

Herein, ANSYS[®] Maxwell [137] is used for computing the electric and magnetic fields surrounding the conductor. ANSYS[®] Maxwell is an electromagnetic field solver, which computes the electromagnetic field distribution using the FEM [138]. Firstly, a 2-D geometry of the cable cross-section along with the material properties is defined which is illustrated in

Figure 3.7. The detailed specification of the geometry and material properties of the cable cross-section is defined in Table 3.1. The cable used in this analysis is shielded and braided 4-wire, 2.5m long cable. The shielding and braids are used for electromagnetic shielding and providing strength to the cable. The conductor's strands are not individually insulated, in contrast to the litz wire.

Later, the electrostatic field solver and the eddy current solver is used to calculating the capacitance, and the resistance and inductance of each conductor respectively. The solver discretises the geometry into FE mesh simply called mesh and computes the field at the nodes. Thus, mesh plays an important role in the field solution. Its resolution should be higher in the region where the field gradient is high. Due to the eddy current and proximity effects, at HF excitation, the current is pushed towards the surface of the conductor. Consequently, at the surface, the field gradient is high, thereby, it is recommended to restrict the edge length of the mesh to one-third of the skin depth at the highest frequency of interest. The parameters of the cable are calculated up to 60MHz. So the edge length is restricted to $2.81\mu\text{m}$. By way of example, Figure 3.8 (a) illustrates the magnetic field distribution of the 2-D geometry of the cable cross-section and Figure 3.8 (b) shows the corresponding meshing. Notably, the edge length of the mesh close to the surface of the conductor and at the interface of the cable dielectric and the aluminium foil is small as the field changes more rapidly. The mesh in other regions is kept coarse, as the field gradient is low. In addition, to resolve the curved surfaces into a fine mesh, surface approximation mesh operation [137] is used, wherein, the maximum spacing between the edge and true curved geometry is restricted to one-third of the skin depth. Also, the maximum surface normal deviation is set to one-third of the skin depth.

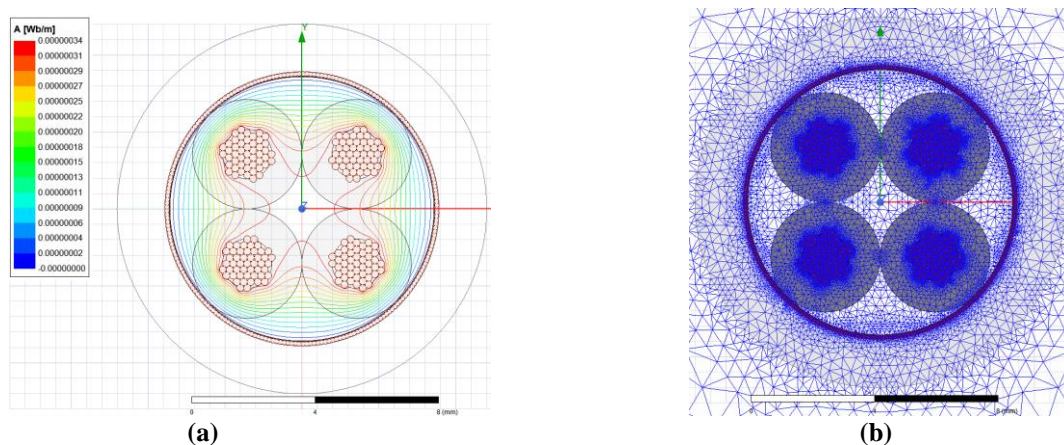


Figure 3.8: Conductor cross-section representing (a) the magnetic field distribution, (b) Meshing used to calculate the frequency dependent parameters.

While solving the geometry using FEM, defining boundary conditions plays a vital role. The boundary conditions control the electric or magnetic field behaviour at the planes of symmetry, periodicity or the edges of the problem region. While calculating the capacitance using an electrostatic solver, the protective earth conductor and the conductive shield is assumed reference conductor, and each phase conductor is excited sequentially by 1V. The edge of the problem region is opted as balloon boundary type, which allows the electric field to vary such that the voltage fringe at the edge. During the calculation of the resistance and inductance, eddy-current solver is used in which the vector potential at the edge of the problem is set to zero. It is generally used for magnetically isolated structures. The eddy-current solver solves the time varying electromagnetic field arising due to sequential excitation of each conductor by a current source of 1A at each frequency of interest, which is comprehensively discussed in section 3.3.2.

3.3.1 Capacitance Calculation

The capacitance between the conductors is determined by solving the static electric field surrounding the conductors using ANSYS[®] Maxwell. Due to the bond charges, the losses in the surrounding dielectric medium are frequency dependent. In addition, the relative permittivity of the dielectric medium decreases with the frequency, although mildly. The capacitance is a measure of energy stored (W_e) in the electrostatic field which arises due to potential differences as [137],

$$W_e = \frac{1}{2} CV^2 \quad (3.26)$$

where, C is the capacitance and V is the potential difference between the conductors. Maxwell's electrostatic field solver determines the energy by solving the static electric field for a given charge distribution. The solver determines the electric scalar potential $\phi(x,y)$ within the defined geometry of the cable for a given charge distribution ($\rho(x,y)$) using the FEM as [137],

$$\nabla \cdot (\epsilon_r \epsilon_0 \nabla \phi(x, y)) = -\rho \quad (3.27)$$

After calculating the electric scalar potential, the solver computes the electric field ($\vec{E}(x,y)$) and the electric flux ($\vec{D}(x,y)$) using Faraday's law and Gauss law as,

$$\vec{E}(x, y) = -\nabla\phi(x, y) \quad (3.28a)$$

$$\vec{D}(x, y) = \varepsilon_r \varepsilon_0 \vec{E}(x, y) \quad (3.28b)$$

The solver computes the electric field and the flux by sequentially exciting each conductor by 1V with respect to the remaining conductor. Further, using (3.28), the energy stored between two conductors i and j is expressed as [137],

$$W_{ij} = \frac{1}{2} \int_{\Omega} \vec{D}_i \cdot \vec{E}_j d\Omega \quad (3.29)$$

where, D_i is the electric flux when the conductor i is excited by 1V and the E_j is the electric field when the conductor j is excited. Using (3.26) and (3.29), the partial capacitance (C_{ij}) between the conductor is deduced. During the analysis, the PE wire is assumed as a reference conductor. For the cable with n phase conductors along with a PE wire, the solver provides the capacitance as a $n \times n$ matrix which gives the relationship between the charge and the voltage as [137],

$$\begin{bmatrix} Q_1 \\ \vdots \\ Q_i \\ \vdots \\ Q_n \end{bmatrix} = \underbrace{\begin{bmatrix} \sum_{\substack{i=0 \\ i \neq 1}}^n C_{1i} & \cdots & -C_{1j} & \cdots & -C_{1n} \\ \vdots & \ddots & & & \vdots \\ -C_{j1} & & \sum_{\substack{i=0 \\ i \neq 1}}^n C_{ji} & & -C_{jn} \\ \vdots & & & \ddots & \vdots \\ -C_{n1} & \cdots & -C_{nj} & \cdots & \sum_{\substack{i=0 \\ i \neq n}}^n C_{ni} \end{bmatrix}}_{\text{Self-Capacitance Matrix}} \begin{bmatrix} V_1 \\ \vdots \\ V_i \\ \vdots \\ V_n \end{bmatrix} \quad (3.30)$$

where, Q_i and V_i is the charge and voltage of conductor i with PE wire as a reference, C_{k0} is the partial capacitance between the conductor k and the PE wire, and C_{ij} is the partial capacitance between the i^{th} and j^{th} conductor. The diagonal element of the matrix is called self-capacitance which is the sum of the partial capacitances from one conductor to all the conductors, whereas, the off-diagonal element is the mutual capacitance between the two conductors. Each diagonal element represents the charges induced on one conductor when 1V is applied to that conductor

and 0V is applied to the remaining. The off-diagonal elements represent the charges induced on another conductor when 1V is applied to that conductor. For instance, for a 3-phase cable, if 1V is applied to conductor 1 with respect to the remaining conductors, then the capacitance matrix is,

$$\begin{bmatrix} Q_1 \\ Q_2 \\ Q_3 \end{bmatrix} = \begin{bmatrix} \sum_{\substack{i=0 \\ i \neq 1}}^3 C_{1i} & -C_{12} & -C_{13} \\ -C_{21} & \sum_{\substack{i=0 \\ i \neq 2}}^3 C_{2i} & -C_{23} \\ -C_{31} & -C_{32} & \sum_{\substack{i=0 \\ i \neq 3}}^3 C_{3i} \end{bmatrix} \begin{bmatrix} 1 \\ 0 \\ 0 \end{bmatrix} = \begin{bmatrix} C_{10} + C_{12} + C_{13} \\ -C_{21} \\ -C_{31} \end{bmatrix} \quad (3.31)$$

where, the first element is the sum of partial capacitance per unit length between conductor 1 and the remaining conductors. The second element represents the charge induced on conductor 2, when 1V is applied to conductor 1 and 0V is applied to conductor 2. Thus, the partial capacitance matrix can be deduced from the self-capacitance matrix as [137],

$$\begin{bmatrix} C_{10} & C_{12} & C_{13} \\ C_{21} & C_{20} & C_{23} \\ C_{31} & C_{32} & C_{30} \end{bmatrix} = \begin{bmatrix} \sum_{i=1}^3 C_{1i} & -C_{12} & -C_{13} \\ -C_{21} & \sum_{i=1}^3 C_{2i} & -C_{23} \\ -C_{31} & -C_{32} & \sum_{i=1}^3 C_{3i} \end{bmatrix} \quad (3.32)$$

where, c_{ij} is the elements of the self-capacitance and mutual-capacitance matrix deduced in (3.30). Using the 2-D cable model illustrated in Figure 3.7, the partial capacitances of the 1m long cable is,

$$C = \begin{bmatrix} 43.89 & 37.72 & 20.28 \\ 37.72 & 25.61 & 37.36 \\ 20.28 & 37.36 & 43.93 \end{bmatrix} pF/m \quad (3.33)$$

3.3.2 Inductance and Resistance Calculation

The frequency dependent resistance and inductance of the cable is determined using the eddy current field solver of ANSYS® Maxwell. The solver determines the time varying magnetic field induced in the transverse plane by the time-varying current through the conductor. The solver computes the eddy current by solving for magnetic vector potential (\vec{A}) and the electric scalar potential $\phi(x,y)$ using (3.34) as [137],

$$\nabla \times \frac{1}{\mu} (\nabla \times \vec{A}) = (\sigma + j\omega\epsilon) (-j\omega\vec{A} - \nabla\phi) \quad (3.34a)$$

$$I_T = \int_{\Omega} (\sigma + j\omega\epsilon) (-j\omega\vec{A} - \nabla\phi) d\Omega \quad (3.34b)$$

where, μ is the absolute magnetic permeability, ω is the angular frequency of current excitation, σ is the conductivity of the conductor, ϵ is the absolute permittivity, Ω is the conductor cross-section, and I_T is the total current flowing through the conductor. The conductor current in (3.34b) can be resolved into the following components,

- The current from the external source (I_s) [137],

$$I_s = - \int_{\Omega} \sigma \nabla \phi d\Omega \quad (3.35)$$

- The induced eddy current (I_e) induced due to time-varying magnetic field in the transverse plane [137],

$$I_e = - \int_{\Omega} j\omega\sigma A d\Omega \quad (3.36)$$

- The displacement current (I_d) induced due to time varying electric field [137],

$$I_d = - \int_{\Omega} j\omega\epsilon (-j\omega A - \nabla\phi) d\Omega \quad (3.37)$$

Notably, the $j\omega$ term in the eddy current and displacement current expression indicate that they are a function of frequency and increases with increasing frequency. Using the magnetic vector potential (\vec{A}) deduced from (3.34), the magnetic field density (\vec{B}) and magnetic field intensity (\vec{H}) is determined as [137],

$$\nabla \times \vec{A} = \vec{B} \quad (3.38a)$$

$$\vec{B} = \mu \vec{H} \quad (3.38b)$$

The solver sequentially injects 1A current to one conductor with the remaining unexcited, and calculates the resistance and the inductance of the conductor. It breaks the impedance matrix calculation into two parts. First, it solves for the inductance matrix and then for the resistance matrix. Later, it combines the inductance and resistance matrix to calculate the impedance matrix. To compute the inductance of the current loop, the solver calculates the average energy stored in the time-varying field as [137],

$$W_{AV} = \frac{1}{4} \int_V (\vec{B} \cdot \vec{H}) dV \quad (3.39)$$

where, V is the conductor volume. If the current injected into the conductor is $I = I_0 \cos(\omega t + \theta)$, the average energy stored in the field is also expressed as [137],

$$W_{AV} = \frac{L}{4} \cdot \frac{1}{2\pi} \int_0^{2\pi} I_0^2 \cos^2(\omega t + \theta) d\omega t \quad (3.40)$$

Using (3.39-3.40), the inductance of the conductor is [137],

$$L = \frac{4W_{AV}}{I_0^2} \quad (3.41)$$

Similarly, the mutual inductance between two conductors i and j can be deduced using the flux linkage between the two conductors because of the excitation of one of them as [137],

$$L_{ij} = \frac{\Psi_{ij}}{I_0} \quad (3.42)$$

where, Ψ_{ij} is the flux linking the j^{th} conductor due to excitation of the i^{th} conductor. For calculating the resistance, the solver calculates the ohmic loss (P) in the conductor using (3.39) as [137],

$$P = \frac{1}{2\sigma} \int_V (\vec{J} \cdot \vec{J}) dV \quad (3.43a)$$

$$P = \frac{I_0^2}{2} R \quad (3.43b)$$

where, \vec{J} is the current density within the conductor, and I_0 is the peak current through the conductor. Similarly, the mutual resistance between the two conductors can be deduced using (3.44) as [137],

$$P_{12} = \frac{1}{2\sigma} \int_V (\vec{J}_1 \cdot \vec{J}_2^*) dV \quad (3.44a)$$

$$P_{12} = (I_{01} \cdot I_{02}^*) R_{12} \quad (3.44b)$$

where, J_1 and J_2 are the current density of conductor 1 and 2 respectively, and I_{01} and I_{02} are the peak current through the conductor. The mutual resistance between the conductors can be interpreted physically as the copper loss arising due to interaction between the electric field produced by the current excitation of one conductor (I_{01}) with the current density of the another conductor (\vec{J}_1).

As the cable is comprised of 4 conductors, the impedance matrix is a 4×4 matrix. Notably, the eddy current and the displacement current are frequency dependent, thereby, the current distribution across the conductor cross-section varies with frequency. Consequently, the impedance matrix is different at a different frequency. For characterizing the variation, the impedance matrix is calculated at 11 different frequencies, 50Hz, 1kHz, 10kHz, 100kHz, 1MHz, 10MHz, 20MHz, 30MHz, 40MHz, 50MHz, and 60MHz. Illustratively, the self-inductance and the resistance of the unit length of phase A conductor deduced by the solver is illustrated in Figure 3.9.

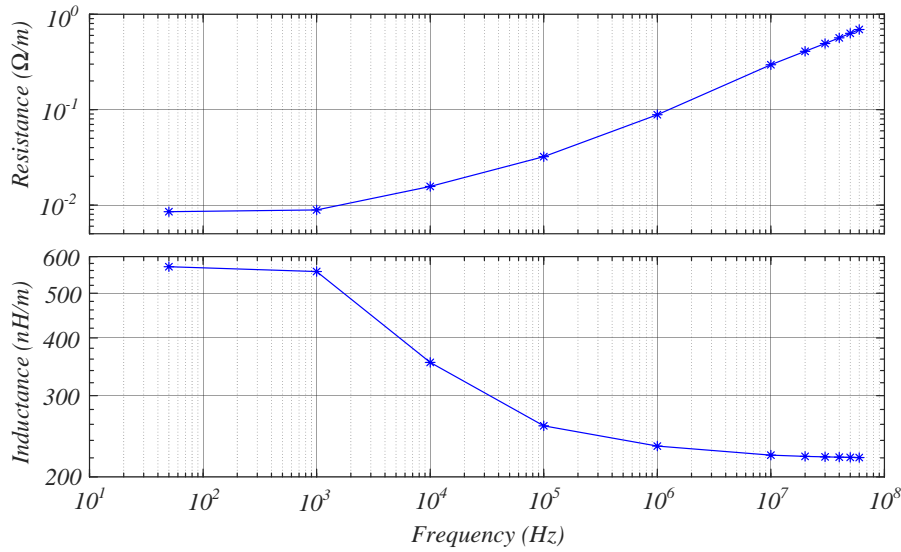


Figure 3.9: Frequency dependent self-impedance of phase A conductor computed using FEM.

The cable with the imperfect conductors has finite conductivity. Thus, at low frequencies, instead of current residing on the surface, it is distributed uniformly across the cross-section. As a result, the magnetic flux also lies within the conductors. At higher frequency, the internal flux induces eddy current which pushes the current towards the conductor surface leading to a decrease in effective cross-section. Therefore, the resistance increases with the increasing frequency. As the current is pushed towards the surface of the conductor, the internal flux reduces. Therefore, the inductance displays the reverse trend. In addition, the external magnetic field in proximity to the current also changes the current distribution which changes the resistance and inductance of the conductor. As evinced, the resistance remains constant until 1kHz and increases exponentially thereafter. Similarly, the inductance at low frequency is the sum of the inductance due to internal and external flux. However, above 1kHz, the internal inductance decreases which are reflected as a roll-off in the inductance. This variation is represented using high-frequency circuit in MATLAB[®] and is validated experimentally by measuring the impedance using a vector network analyzer (BODE 100).

3.4 Representation of Frequency Dependent Parameters

The frequency dependency of the parameters calculated in the previous section must be taken into account for effective cable modelling. These variations can be realised using a Ladder circuit [139]. The Ladder circuit is a combination of frequency independent passive elements which approximate the variation in cable parameters due to frequency. For realising this, the series impedance combination of resistance and inductance is used, also known as the RL-

Ladder circuit. Similarly, for realising the frequency dependent shunt parameters, the combination of resistance and capacitance is used which is called as CG-Ladder circuit.

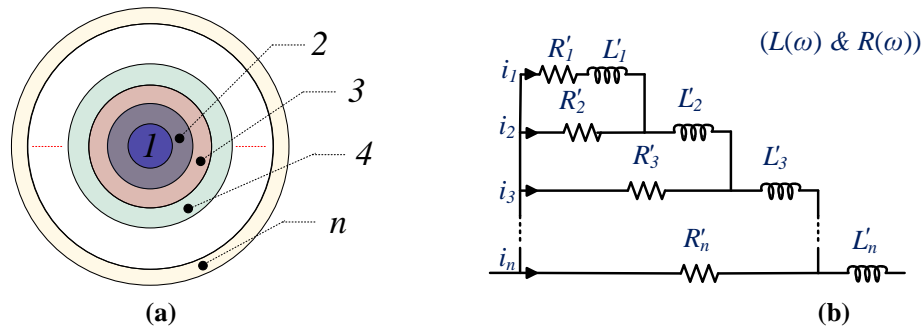


Figure 3.10: (a) Cross-section of a phase conductor divided into the annular region; (b) Ladder circuit representing the impedance of each annular region.

The physical significance of the RL-Ladder circuit can be explained for the cable model. Conceptually, the cable conductors can be approximated as an infinite shunt connected concentric annular regions as shown in Figure 3.10 (a). Each region has its resistance due to the finite conductivity of the conductors and can be represented using a resistor. The inductance of each region depends on the flux linked by the current through that region. For instance, the current flowing through the innermost region will be linked by the flux produced by all the regions and the flux external to the conductor, whereas the current flowing through the region close to the surface will only be linked by the flux in that region and the flux external to the conductor. Therefore, the impedance of the innermost region, marked as 1, is represented by R'_1 and L'_1 in the Ladder circuit representing the impedance of the conductor in Figure 3.10 (b), and the current i_1 flowing through it is the same as the current flowing through R'_1 and L'_1 . As the current i_1 is linked to the flux in region 2, the current through the inductor L'_2 representing the inductance due to the flux in region 2, is the sum of i_1 and i_2 . As a result, each branch of series connected resistor and inductor represent the impedance of the annular region. Thus, the order of the Ladder circuit is the same as the regions within the conductor. The current through all the regions is linked to the external flux. Also, the flux in the region adjacent to the surface is linked to the currents in all of the regions. Therefore, in the circuit representation, the inductance due to these flux linkages is represented using an inductor L'_n through which the entire current flows.

The parameters of the Ladder circuit are calculated using Vector Fitting (VF) [140]. VF is a state equation approximation method, which is applied in the frequency-domain and approximates the state equation of the system by locating its dominant poles and residues over

an observed domain. In complex frequency-domain, the complex frequency response of the system ($f(s)$) is expressed as a sum of the residues (r_n) over first-order poles (p_n) as [140],

$$f(s) \approx \sum_{n=1}^N \frac{r_n}{s - p_n} + d + se \quad (3.45)$$

where, d and e are optional. In the time-domain this corresponds to an impulse response that is, a superposition of damped sinusoids as [140],

$$h(t) = \sum_{n=0}^N r_n e^{p_n t} \quad (3.46)$$

For calculating the parameters of the RL-Ladder circuit, which represents the series impedance ($Z(\omega)$) of the conductor, the frequency response is expressed as [140],

$$Z(\omega) = R(\omega) + j\omega L(\omega) \quad (3.47)$$

where, $R(\omega)$ and $L(\omega)$ are the frequency dependent resistance and inductance of the conductor. In Laplace domain, (3.47) is expressed as,

$$Z(s) = R + sL \quad (3.48)$$

Using VF, for an m^{th} order Ladder circuit, the impedance is approximated as [140],

$$Z(s) \approx \underbrace{\sum_{n=1}^m \frac{r_n}{s - p_n}}_{1/Y(s)} + d + se \quad (3.49)$$

Thus, using (3.49), the sum of the inductance (L'_m) of the region close to the conductor surface and the inductance due to external flux is e H. The remaining term can be represented as an admittance ($Y(s)$) which can be further approximated as a rational function using VF as [140],

$$Y(s) \approx \underbrace{\sum_{n=1}^m \frac{r_n}{s - p_n}}_{1/Z'(s)} + se + d \quad (3.50)$$

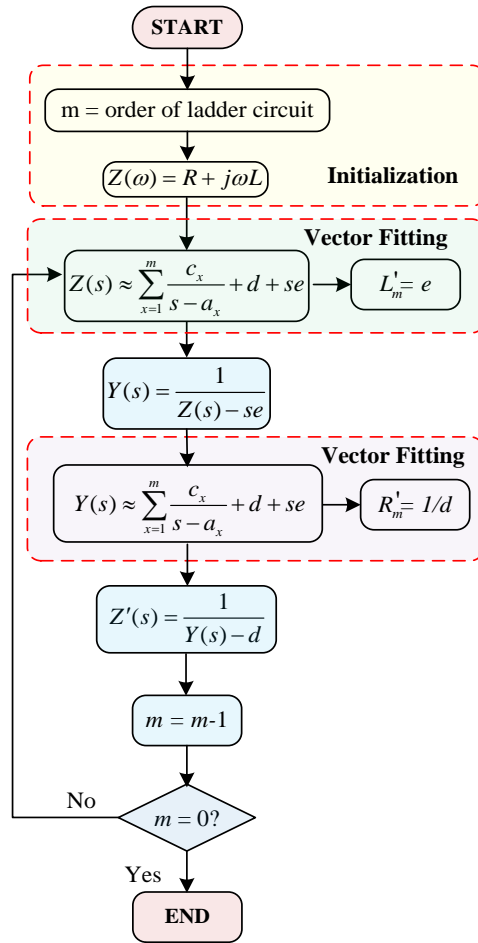


Figure 3.11: Proposed procedure for the development of the Ladder circuit using vector fitting.

The constant term (d) in (3.50) represents the conductance ($1/R'_m$) of the Ladder circuit. Henceforth, using (3.49-3.50) and repeating the aforementioned process, the other parameters of the Ladder circuit can be calculated which is summarised in Figure 3.11. By way of example, the frequency dependent self-impedance of the phase A conductor calculated in section 3.3 is used to synthesize a 6th order Ladder circuit using the process in Figure 3.11 and is illustrated in Figure 3.12 (a). The Ladder circuit represents a cell of the model. The parameters of the Ladder circuit is shown in Table 3.2. Under HF voltage excitation, the current density moves towards the conductor's surface owing to induced eddy current, resulting in increased impedance of the innermost area. Similar behaviour can be seen in the Ladder circuit, wherein, the L'_1 representing the inductance of the innermost region is maximum. As a result, the Ladder circuit represents the frequency dependency of the impedance due to the induced eddy currents. The frequency response of the Ladder circuit is illustrated in Figure 3.12 (b), demonstrating its conformity with the FE calculated impedance.

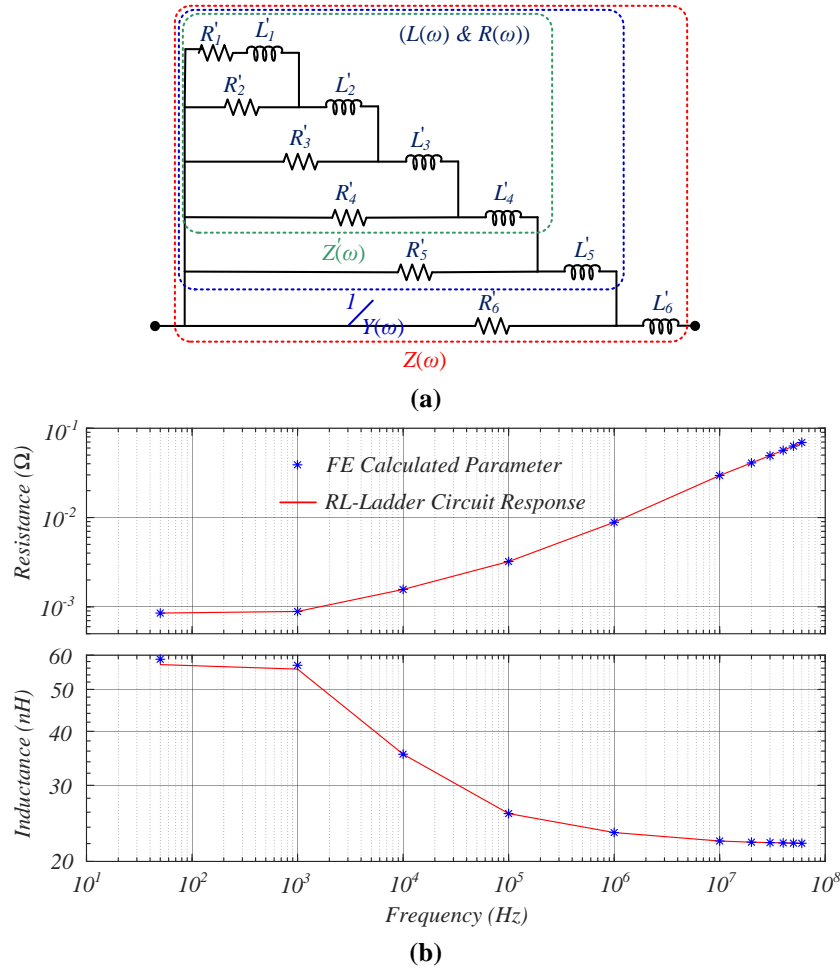


Figure 3.12: Time-domain circuit representing frequency dependent series impedance of phase A conductor, (a) RL-Ladder circuit, (b) Frequency response of the RL-Ladder circuit.

Table 3.2: Parameters of RL-Ladder circuit representing the impedance of phase A conductor

i	1	2	3	4	5	6
$R'_i (m\Omega)$	1.82	3.00	5.30	14.80	41.69	102.19
$L'_i (nH)$	95.78	15.85	2.69	1.02	0.42	21.93

Similar to the RL-Ladder, for representing the frequency dependent dielectric losses and the permittivity of the insulation, CG-Ladder is used, wherein, the principle of duality is followed. The resistance is replaced by the conductance and the inductance is replaced by capacitance. By way of example, Figure 3.13 (a) depicts a 6th order Ladder circuit, and Figure 3.13 (b) represents its frequency dependence admittance. The parameters of the CG Ladder are calculated following the process illustrated in Figure 3.11 and the principle of duality. Similar to the RL-Ladder circuit, the admittance and hence, the capacitance of branch 1 is the lowest which makes the current flow through the last branch. Thus, the RL and CG Ladder circuit closely follows the redistribution of the current and, as a result, the frequency dependency of

the parameters. The variation in capacitance and conductance of the dielectric medium illustrated in Figure 3.13 is mild. Compared to the inductance, where it decreases by 60% at HF, the decrease in capacitance is merely 6.82%. In addition, the resistance representing the dielectric loss is large as compared to the series resistance of the conductor. Although, this variation can be represented using the CG Ladder, but with a substantial increase in computation time and resources. Therefore, for a simplified model without losing accuracy, this variation is neglected, and the dielectric is represented as a lossless medium with constant capacitance.

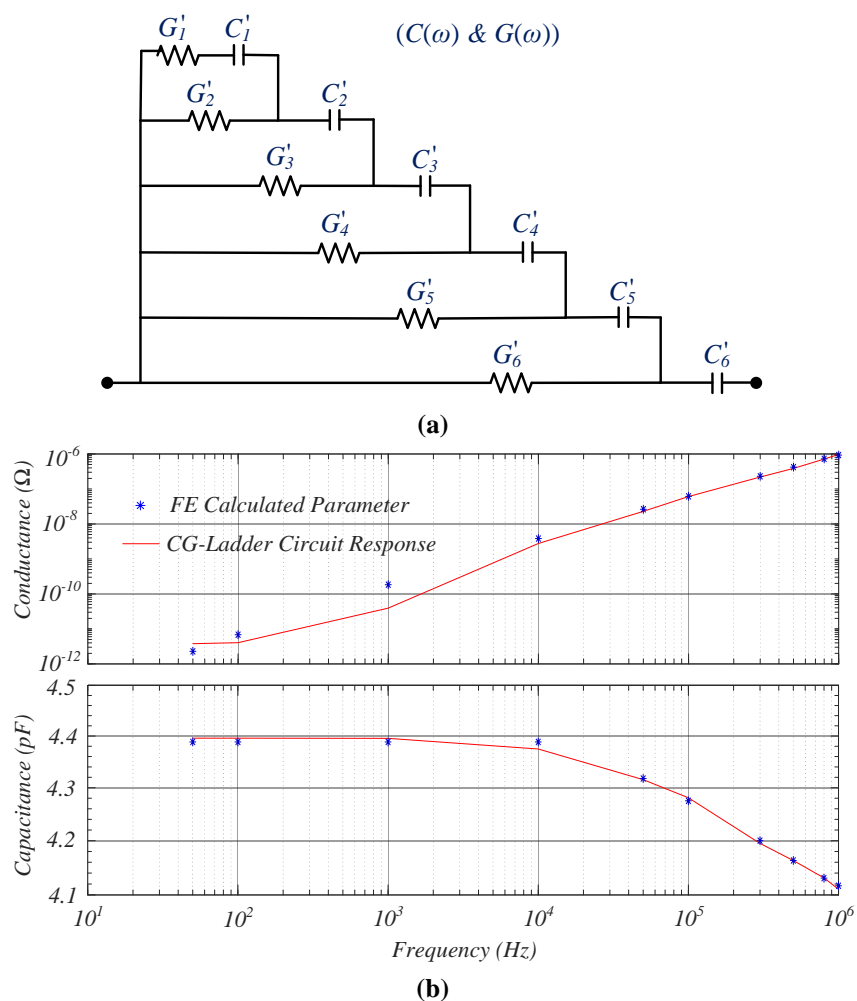


Figure 3.13: Time-domain circuit representing frequency dependent shunt impedance, (a) CG-Ladder circuit, (b) Frequency response of the CG-Ladder circuit.

Notably, though the RL and CG Ladder circuits realise the frequency dependency of the cable parameters, their parameters themselves are frequency independent. Thus, the Ladder circuit can be used in the time-domain lumped parameter circuits to incorporate the frequency dependent parameter.

3.5 Representation of Mutual Resistive and Inductive Coupling

The frequency dependent impedance matrices extracted from the ANSYS® Maxwell in section 3.3.2 represents the series impedance of the cable conductor. The diagonal elements represent the self-resistance and the self-inductance, whereas the off-diagonal element represents the mutual coupling between the two conductors. Due to the skin and proximity effect, the resistance and inductance are non-linear functions of frequency. To accurately reproduce the voltage response of the cable, the frequency dependence of the parameters must readily be incorporated. As emphasised in the previous section, the frequency-dependent impedance can be easily incorporated in the time-domain lumped parameter circuit using an RL-Ladder circuit. The self-impedance is represented simply by connecting the RL-Ladder circuit in lieu of the frequency dependent resistance and inductance, as illustrated in Figure 3.14. However, the representation of the frequency dependent mutual coupling is demanding. In an approach, the inclusion of the mutual coupling is possible by analysing the spectral content of the excitation individually. The excitation is resolved into its spectral content using the Fourier series and each frequency component is analysed individually. Later, inverse Fourier Transform is used to convert the response from the frequency-domain to the time-domain. Consequently, multiple lumped circuit representing the cable for a specific frequency is required. As a result, if the slew rate of the excitation pulse is high, then the spectral component of the excitation will be spread over the wide frequency range, thereby large set of lumped parameter circuits is required. In another approach, the modal transformation [86] is used, which diagonalise the impedance matrix and eliminate the mutual coupling term. However, the frequency dependence of the mutual inductive coupling engenders a frequency-dependent modal transformation matrix, which increases further complexity.

Without explicitly employing either the modal transformation, convolution, Fourier transform, or multiple circuits representing cable behaviour at different frequencies, all of which involve computational complexity, the mutual coupling can be incorporated in the lumped parameter circuit more accurately, yet lucidly, by employing a current controlled voltage source. Due to mutual coupling between conductor i and k , the i^{th} conductor voltage can be mathematically expressed as;

$$V_i = \underbrace{\left(R_{ii}(\omega) I_i + L_{ii}(\omega) \frac{dI_i}{dt} \right)}_{V_{ii}} + \sum_{\substack{k=1 \\ i \neq k}}^N \underbrace{\left(R_{ik}(\omega) I_k + L_{ik}(\omega) \frac{dI_k}{dt} \right)}_{V_{ik}} \quad (3.51)$$

where, I_i is the i^{th} conductor current, $R_{ii}(\omega)$ and $L_{ii}(\omega)$ are the frequency dependent self-resistance and self-inductance of i^{th} conductor, and $R_{ik}(\omega)$ and $L_{ik}(\omega)$ are the frequency dependent mutual-resistance and mutual-inductance between conductor i and k . The first term (V_{ii}) in (3.51) represents the i^{th} voltage across i^{th} conductor due to self-impedance. The second term (V_{ik}) in (3.51) represents the conductor voltage due to mutual coupling between i^{th} and k^{th} conductor. The voltage drop due to self-impedance can be easily realised using a RL-Ladder circuit.

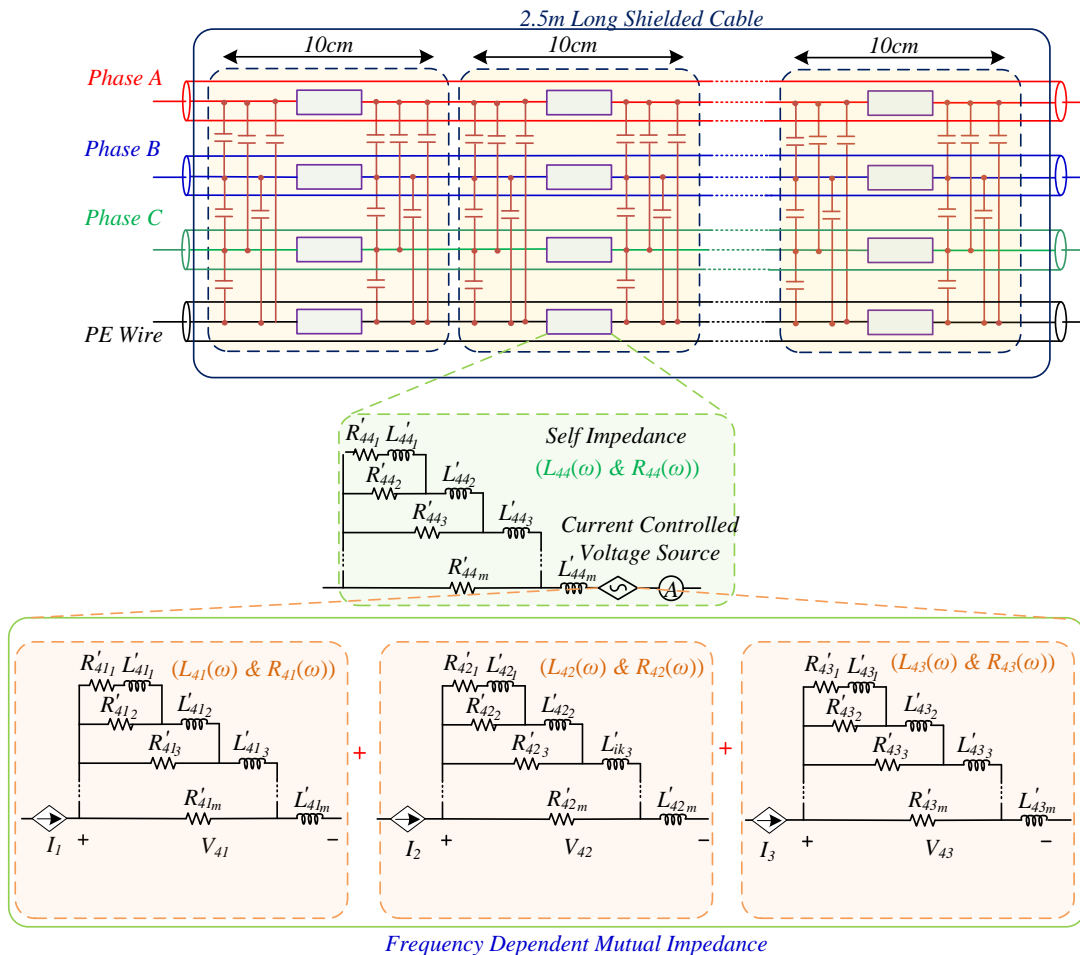


Figure 3.14: HF model of the cable using lumped parameter circuit connected in continuum.

For representing the voltage drop due to mutual impedance a current controlled voltage source is used. For instance, the voltage drop across the i^{th} conductor due to the current in k^{th}

conductor (I_k) is calculated by injecting the current I_k through a Ladder circuit representing the mutual coupling between the conductors i & k . It should be noted that the time derivative for inductive voltage has been implicitly represented by the inductive elements of the circuit. Similarly, the voltage drop due to mutual coupling with the other conductors is calculated and then added together to represent the current controlled voltage source. Thus, for N number of cable conductors, 1 Ladder circuit is used to represent the self-impedance and $N-1$ Ladder circuits are used to represent mutual coupling with the remaining $N-1$ conductors. Herein, the cable has 4 conductors. So, for representing each conductor, 4 Ladder circuit is required. One of them is used to represent the self-impedance and the remaining three is used to represent the mutual coupling between the other three conductors. By way of example, in Figure 3.14, the impedance of a unit cell of the PE wire is illustrated, wherein, one Ladder circuit is used to represent the self-impedance $R_{44}(\omega)$ and $L_{44}(\omega)$, and a current dependent voltage source is connected in series to represent the mutual coupling between the remaining three conductors. The dependent voltage source represents the total voltage drop across the Ladder circuit representing the mutual coupling with the phase conductors when the phase current is injected into them.

3.6 Experimental Validation

The HF model is intended to investigate the potential problem of the voltage overshoot at the load terminals. When the fast slew rate PWM voltage pulse propagates through the cable, it engenders HF voltage oscillations at the load end. Therefore, it is necessary to validate the model over the wide frequency range. These voltage oscillations arise because of the parasitic impedance of the cable in the CM and DM path. As a result, comparing the CM and DM impedance of the cable with the experimental measurement is a common practice to validate the model. This ensures that the model represents the distributed parasitic impedance of the cable over the wide frequency range. Further, the voltage oscillations at the load end can be validated by exciting the cable using a PWM inverter. These methods are adopted for validation in the following section.

3.6.1 Common-Mode and Differential-Mode Impedance Validation

For the validation of the CM and DM impedance of the cable model, the CM and DM impedance of the model is compared with the experimental measurement. The impedance is measured experimentally using an OMICRON Lab manufactured Bode 100 impedance

analyser over a frequency range of 1kHz to 50MHz. Figure 3.15, illustrates the experimental rig used for the impedance measurement, wherein, the 2.5m long shielded cable is connected to the impedance analyser which is connected to the PC for data acquisition and post-processing. The schematic of impedance measurement is illustrated in Figure 3.16. For comparison, the impedance of the model is predicted in the MATLAB[®]/Simscape environment. The prediction is made between 1Hz to 100MHz.

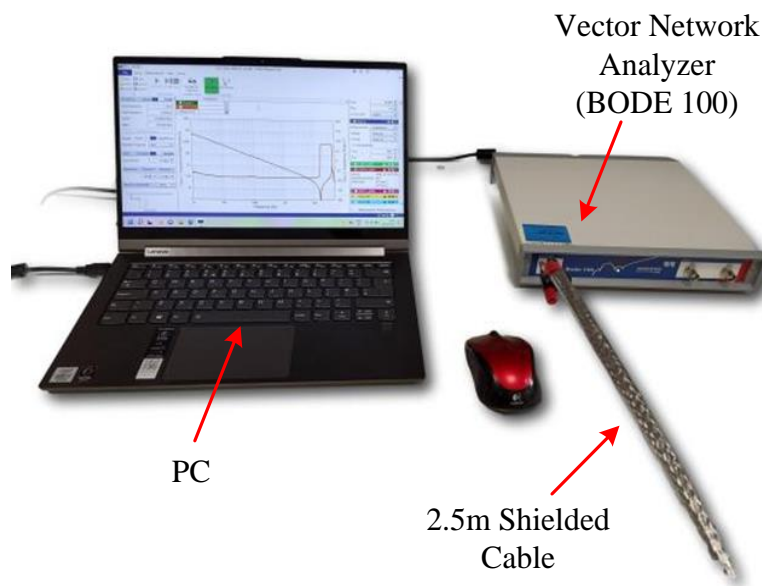


Figure 3.15: Experimental rig used for measuring the CM and DM impedance of the cable.

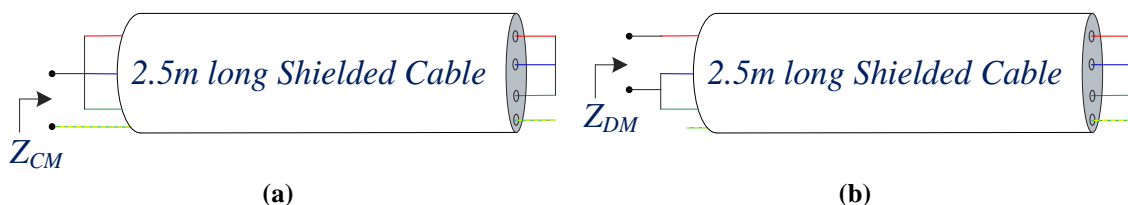


Figure 3.16: Schematic of experimental measurement of common-mode and differential-mode impedance.

Figure 3.17 compares the measured and the predicted impedance of the cable. As elucidated, the CM impedance of the model conforms with the measurement with a minor deviation above 30MHz. The capacitive coupling between the phase wires and the PE wire is dominant until 1st anti-resonance frequency ($f_{ar_{c(1)}}$), thereafter, it displays multiple resonances. The 1st anti-resonance frequency of the model best fits the measurement. The voltage at the load terminals oscillates at this frequency, due to its low impedance. Thus, the voltage wave travelling through the cable endure oscillations for a longer period. The significance of the anti-resonance frequency over the voltage oscillations is comprehensively discussed in chapter 5.

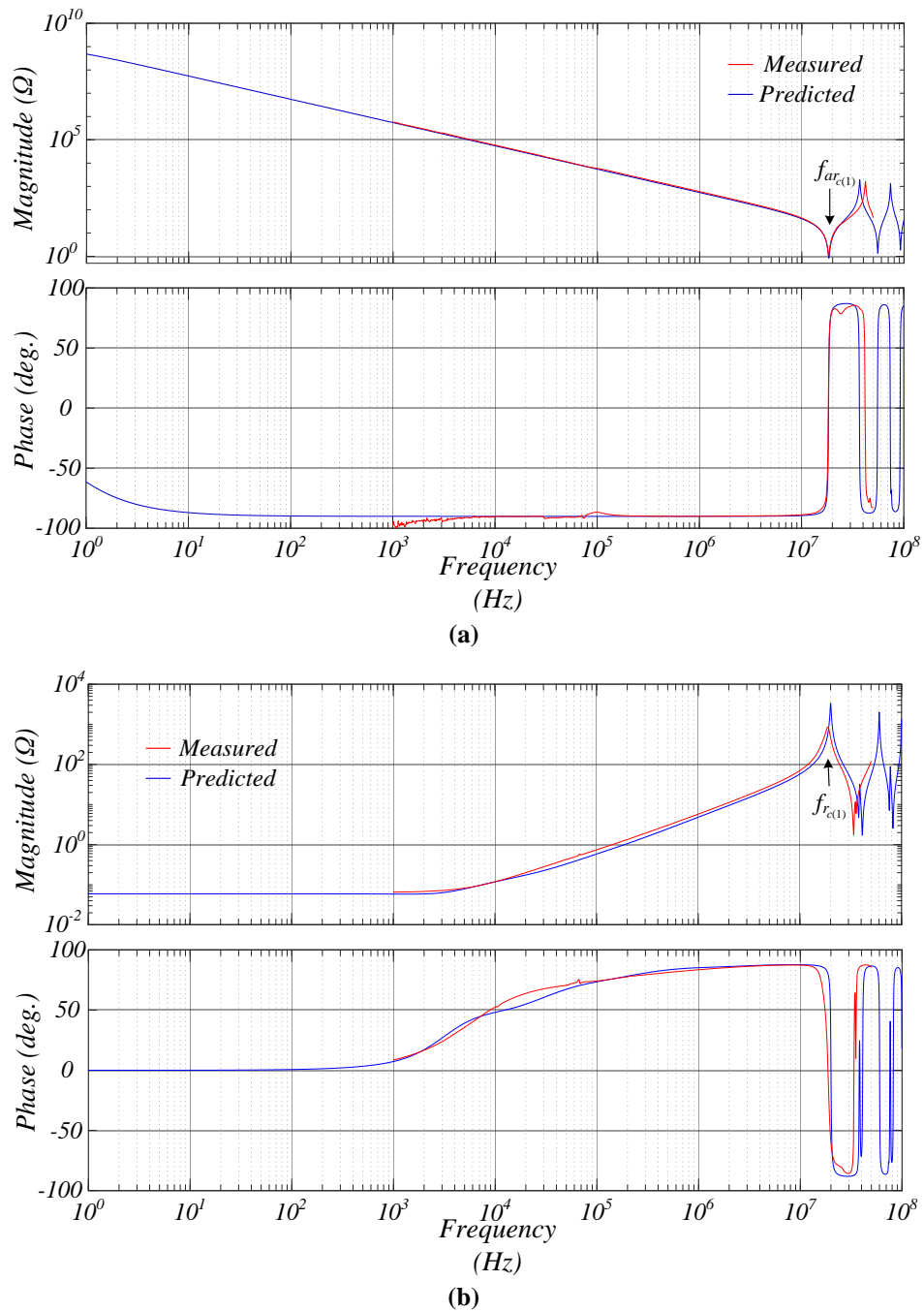


Figure 3.17: Impedance comparison between experimental measurement and prediction; (a) Common-mode impedance, (b) Differential-mode impedance.

The measured DM impedance of the cable and the prediction of the model is compared in Figure 3.17 (b). The cable behaves like a resistive element until 1kHz, thereafter, turns inductive until 20MHz. Beyond 20MHz, the cable exhibits multiple resonances. The model best fits the cable with minor deviations. When the cable impedance resembles resistive characteristics, the predicted impedance conforms with the measurement. Between 10kHz and 20MHz, in which the inductive characteristics are dominant, the predicted inductance is less

than the measurement. Although the 1st resonance frequency ($f_{ar_{c(1)}}$) is close, the predicted impedance is higher than the measurement.

Small differences, however, exist due to a number of uncertainties in the modelling process. Majorly, the material properties, such as permittivity and permeability, used in the FE analysis may differ slightly from those in the machine. The uncertainty in the geometrical dimension of the cable also plays a role. In addition, the adjacent strand of each conductor is assumed shorted with each other, i.e., the contact resistance between the strands is ignored. Consequently, the resistance and the inductance of the conductor may differ slightly. The difference in the resonance (f_{r_c}) and anti-resonance frequency (f_{ar_c}) except the first are majorly affected by the mutual inductive and capacitive coupling between the conductors. In addition, the impedance of the connection between the impedance analyser and the cable is considerable at HF. Although, this impedance is offset during calibration before measurement.

3.6.2 Time-domain Validation

The time-domain cable model can be validated by comparing the voltage at the load end with the experimental measurement when the model is excited by PWM voltage pulse measured experimentally. The PWM voltage pulse is fed through a SiC MOSFET based three-phase inverter. The SiC MOSFET is a CREE manufactured C2M0040120 with 1200V rated voltage and 60A rated drain current. During the experiment, as illustrated in Figure 3.18, the three phase wires of the cable are connected to the three-phase inverter output and the PE wire is connected to the mid-point of the DC link. At the load end, three star connected 640 Ω resistance are connected to the phases and the PE wire is floating. The experimental rig used for the validation is illustrated in Figure 3.19. To ensure minimum parasitic impedance of the load, that is, the load is resistive over a wide range of frequency, a thick film chassis-mounted resistor (BDS2A100330RK) is used. The three phase voltage at the inverter terminal is measured using two Teledyne Lecroy manufactured 400 MHz bandwidth, 2000V, HVD3220 high voltage active differential probes and one Teledyne Lecroy manufactured 100 MHz bandwidth, 1400V, ADP305 high voltage active differential probe. The voltage at the load end is measured using an ADP305 high voltage active differential probe across phase A terminal and the PE wire. The measured voltage is captured using a Teledyne Lecroy manufactured 4 channel, 4GHz bandwidth WavePro404HD high-definition oscilloscope. The voltages are captured at 10GSa/s sampling frequency. Later, the MATLAB[®]/Simscape based cable model is excited using the

measured three phase voltage and the predicted load voltage is compared with the experimental result.

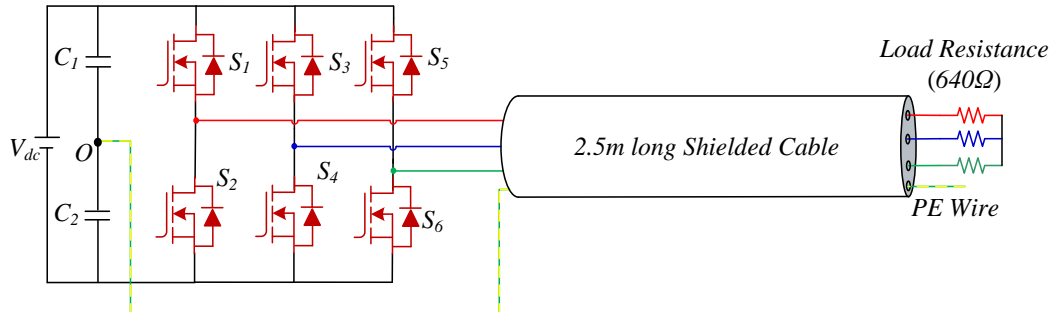


Figure 3.18: Schematic diagram of the experimental rig used for the validation of cable model.

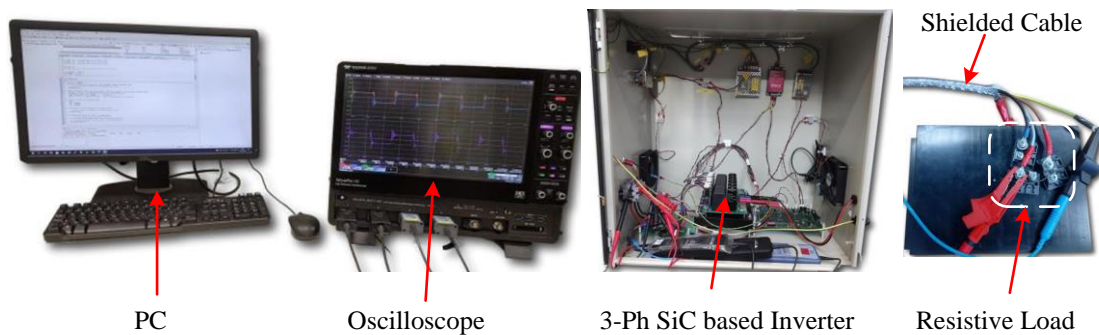


Figure 3.19: Experimental rig used for the time-domain validation of the cable model under PWM voltage pulse excitation.

The comparison between the load voltages is illustrated in Figure 3.20 (a) and the enlarged view of a switching event is illustrated in Figure 3.20 (b). During the experiment, the DC link voltage is 200V, the rise time is 60ns, the switching frequency is 40kHz and the modulation index is 0.1. The results are illustrated in pu, wherein, the base voltage is DC link voltage. As elucidated, the inverter output voltage is oscillatory and oscillates at 9.87MHz. These are the effects of the parasitic impedance of the inverter. In response to the oscillatory voltage pulse, the load end voltage also oscillates at 9.87MHz. Notably, the predicted load end voltage conforms with the measurement. Both oscillates at 9.87MHz, though, the peak-peak oscillation is less in prediction. Thus, the cable model represents the behaviour of the cable over a wide frequency range and can be used to predict the voltage stress at the load end.

In Figure 3.20 (b), although phase B is switched 1μs after phase A, the voltage starts rising since the phase A switching. The rise in voltage is due to capacitive coupling between the phases. Generally, the peak voltage stress at the load end depends on the DC link voltage, the slew rate of the voltage pulse, dwell time between the switching of the phases, cable length and

its material properties. The physical cause of these factors, especially the phase coupling and the dwell time between the switching of the phases is comprehensively studied in chapter 5. Furthermore, the consequences and the remedies to the voltage stress is discussed in chapter 6.

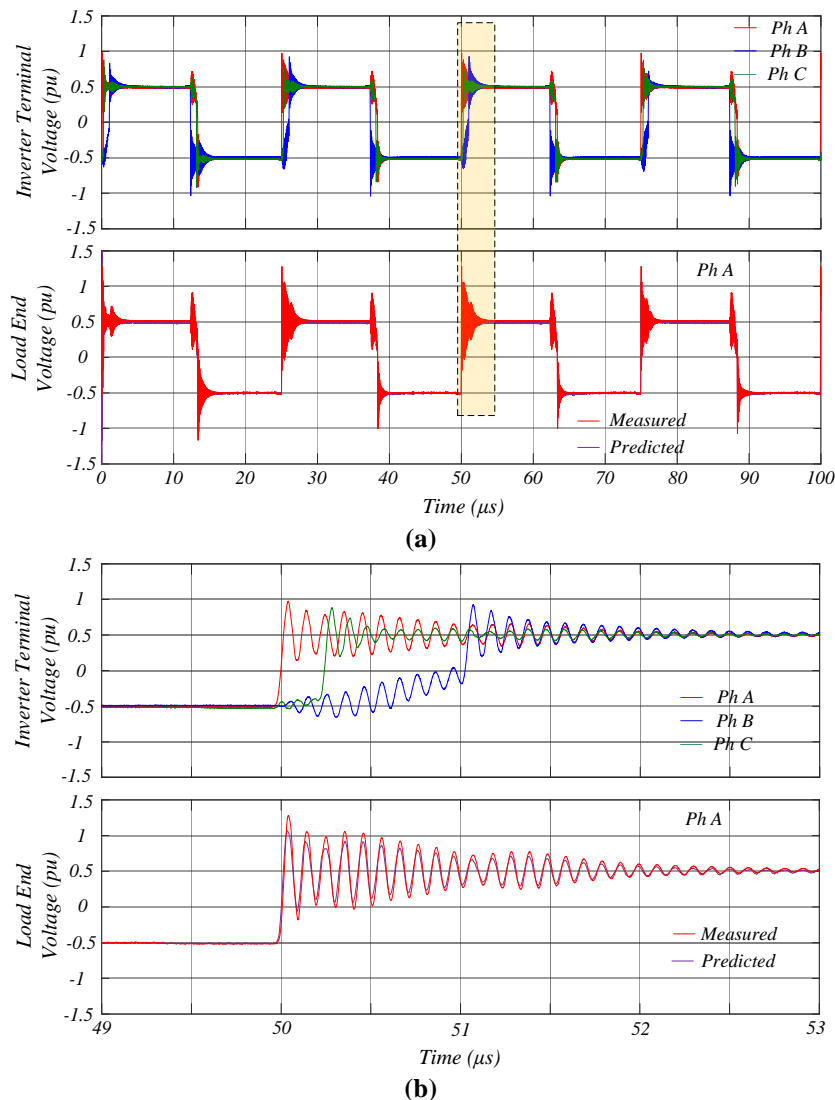


Figure 3.20: Experimental validation of cable model under PWM voltage excitation with 200V DC link voltage, 40kHz switching frequency, and 60ns rise time; (a) Load end voltage comparison, (b) Load end voltage over one switching instant.

3.7 Summary

In this chapter, an MCTL model for studying the HF behaviour of cable under PWM excitation is proposed. The proposed model employs lumped parameter circuit to represent the distributed impedance. These parameters are calculated using FEM and are frequency dependent. The resistance increases and the inductance decreases with increasing frequency as a result of induced eddy current and proximity effect. Similarly, the dielectric loss is frequency

depend due to bond charges and the permittivity decreases with increasing frequency. However, the variation in the capacitance and the conductance is minimal. Therefore, the dielectric is represented as a constant capacitance. For representing the frequency dependent resistance and inductance, Ladder circuit is used. The Ladder circuit reproduce the frequency response of the impedance with frequency independent parameters. By virtue of it, the frequency dependent impedance can be realised in time-domain analysis. The mutual impedance between the conductors can be realised using convolution, Fourier transform, or modal transformation. However, these methods requires enormous computation time and resources. The mutual impedance can be incorporated in the lumped parameter circuit more accurately, yet lucidly by using current controlled voltage source. Herein, a lumped parameter transmission line circuit is proposed in which the mutual coupling between the conductors is considered using a current controlled voltage source which injects a voltage equivalent to the voltage drop across the mutual impedance. Thereby, the mutual coupling between the conductors can be realised lucidly.

The proposed model is validated by comparing the measured and predicted CM and DM impedances. The results show that the predicted impedance conforms with the measurement. Minor differences exist especially beyond 1st anti-resonance frequency of the cable ($f_{ar_{c(1)}}$) in CM impedance and the impedance magnitude at the resonance peaks (f_{r_c}) in DM impedance. These differences exist due to the uncertainties in the modelling process, such as tolerance in the dimensions and the material properties of the cable.

Furthermore, the voltage stress at the load end is predicted using the proposed mode. The predicted voltage stress shows conformity with the measured stress. Hence, the proposed model can be used to study the inimical effects of the fast slew rate voltage pulse travelling through the cable. The model can be used to study the CM current which causes EMI with the nearby equipment. In addition, the model can be utilised to study the effect of the inverter parasitic impedance especially the coupling between the phases on the load end voltage stress. The physical cause of these factors is comprehensively discussed in chapter 5.

Chapter 4: Modelling High Frequency Behaviour of Machine Winding

4.1 General

The propagation and reflection of the TEM waves within the electric drive emanating from the high slew rate PWM voltage pulse can be rendered using the HF models. These models are effective in understanding innumerable undesirable issues such as (1) voltage overshoot at the machine terminal [14-19] leading to the potential reduction of the insulation lifetime, (2) CM HF ground return current escaping through the capacitive coupling between the winding and the core of the machine causing conducted EMI in the electric power system [141]. They also provide a basis for assessing radiated EMI [26] and bearing current as shaft earthing current flowing through the shaft to the grounded driven machinery, or as capacitive discharge current, if the driven machinery is not grounded while the machine core is connected to the ground [23-25] [142-143]. To address these detrimental consequences, an HF model of the overall drive is necessary.

In the previous chapter, the HF behavioural model of the power cable is discussed, wherein, the cable is represented as a MCTL model. The modelling of the cable is simple in the way that the cable conductors are surrounded by homogeneous insulation material. However, in the case of the machine winding, insulated electrical steel lamination sheets surround the conductors embedded in the slot region while part of the winding in the overhang region is exposed to the ambient condition. In addition, the electrical steel used as a core is ferromagnetic material having non-linear magnetic properties, i.e., the permeability depends on the magnetic flux density. The magnetic properties of the ferromagnets are often described using the curve of magnetic induction (\vec{B}) against external magnetizing force (\vec{H}) and the slope is defined as the permeability. Due to the magnetic saturation, the permeability of the material varies non-linearly. As a consequence, the permeability of the material changes subjected to the operation condition of the machine. Additionally, the magnetic induction lags behind the magnetizing force subjected to HF magnetization cycle, which is referred to as magnetic hysteresis. Thus,

the magnetic behaviour is represented as complex permeability representing the hysteresis effect. As a result, a modified modelling approach is required to account for the TEM wave propagation through a non-homogeneous medium. In this chapter, HF modelling of the machine winding is discussed, accounting for the non-linearity such as non-homogeneous and non-linear medium, imperfect conductors, frequency dependent properties of the medium and conductor, and the losses in the medium.

4.2 Comparison between Power Cable Model and Machine Winding Model

The MCTL model represents the propagation of TEM wave structure through a medium. Akin to the power cable, machine winding can be represented using the MCTL model over a broad range of frequencies. The voltage wave exciting the cable induces orthogonal electric and magnetic fields in the transverse plane and constitutes TEM field structure. In other words, no component of the electric and magnetic field is in the direction of the wave propagation. The velocity of the wave structure depends on the material properties of the medium surrounding the conductors, which is expressed as [41],

$$v = \frac{1}{\sqrt{\mu\varepsilon}} \quad (4.1)$$

where, μ and ε are the permeability and permittivity of the medium surrounding the conductor. The permeability of the medium is often expressed relative to the free space as $\mu = \mu_0\mu_r$, where, μ_0 is the permeability of free space and μ_r is the relative permeability of the medium with respect to the free space. Similarly, the permittivity of the medium is expressed relative to the free space as $\varepsilon = \varepsilon_0\varepsilon_r$, where, ε_0 is the permeability of free space and ε_r is the relative permeability of the medium with respect to the free space. In the case of the power cable, the velocity of the TEM wave structure depends on the properties of the insulation surrounding the conductors. Generally, the relative permeability of the insulation is equal to 1, and the relative permittivity (ε_r) varies between 2.5 - 4. As a result, the velocity of the TEM wave within the power cable is approximately half of the speed of light.

Nevertheless, the TEM wave propagation through the machine winding is like the power cable, with a non-linear medium surrounding the machine winding. The conductors embedded within the slot are surrounded by the laminated sheets of electrical steel, whereas a part of the conductors in the overhang region is surrounded by the ambient condition in which the machine

is exposed. Therefore, the velocity of the TEM wave structure inside the slot is different from the velocity in the overhang region, which invalidates the basic assumption of unique velocity in a medium. However, the transmission line equation can be applied if the two sections are considered independently.

Further, the medium surrounding the cable conductors is isotropic, i.e., its properties are the same in all the directions. However, the electrical steel surrounding the conductors within the slot is anisotropic. The electrical steels are classified into two sections based on their processing: non-oriented electrical steel and grain oriented electrical steel [144-146]. The non-oriented electrical steels have linear properties in all directions. The grain oriented has strong crystallographic properties. This type of electrical steel undergoes a recrystallization process that enhances grain structure resulting in better magnetic properties in the rolling direction of the sheets. The magnetic field density increases by 30% in the rolling direction with 5% reduction in magnetic saturation [146]. Thereby, the grain oriented electrical steel is an anisotropic material with higher permeability in the rolling direction. The permeability of the electrical steel in the direction of propagation of the TEM wave induces magnetic field lines outside the transverse plane, thereby, violating the assumption that the magnetic and electric field exists in the transverse plane. In electrical machines, however, non-oriented electrical steels are commonly used.

In the power cable, the conductors are surrounded by insulating materials. However, in the machine winding, the electrical steel surrounding the conductors is conductive. The time-varying flux induced by the time-varying conductor current induces an eddy current in the core. Although the eddy current in the core is restricted by the thin insulated laminated sheets, it is considered at high frequencies when the skin depth is less than half of the laminate thickness. Consequently, the induced eddy current opposes its cause, resulting in a significant increase of resistance and decrease of the inductance with increasing frequency and incurs additional losses known as hysteresis and eddy current losses. The model must be modified to incorporate this loss.

The electrical steel surrounding the conductors in the slot regions has non-linear magnetic properties. The B-H characteristics of the steel used in the following analysis and the non-linear variation of the permeability are illustrated in Figure 4.1. Different from the linear material, the permeability depends on the magnetizing force, and hence the operating point of the

machine. The permeability of the material is commonly defined in three ways as illustrated in Figure 4.1; incremental permeability, apparent permeability, and initial permeability. The slope of the line tangent to the B-H curve at the operating point is called incremental permeability. The slope of the line from the origin to the operating point is called apparent permeability and the slope of the line tangent to the B-H curve at the origin is called initial permeability. Except for initial permeability, the apparent permeability and incremental permeability depend on the operating point. For linear material, all three permeability values are equal. The ANSYS[®] Maxwell [137] used for calculating the inductance of the winding uses apparent permeability to calculate the flux linkage as a function of the independent variable since it changes with the current as of the material properties changes. Thus, the calculated inductance is the apparent inductance which depends on the operating point.

The ANSYS[®] Maxwell [137] follows two step procedure to calculate the apparent inductance:

- A non-linear magnetostatic solution is initiated with the specified turn currents. This specifies the permeability of each mesh element since the degree of saturation varies throughout the slot geometry.
- This specified permeability is further used in a linear solution for generating an inductance matrix. The resulting values are apparent inductance, which varies with the specified turn current operating point as the material properties changes.

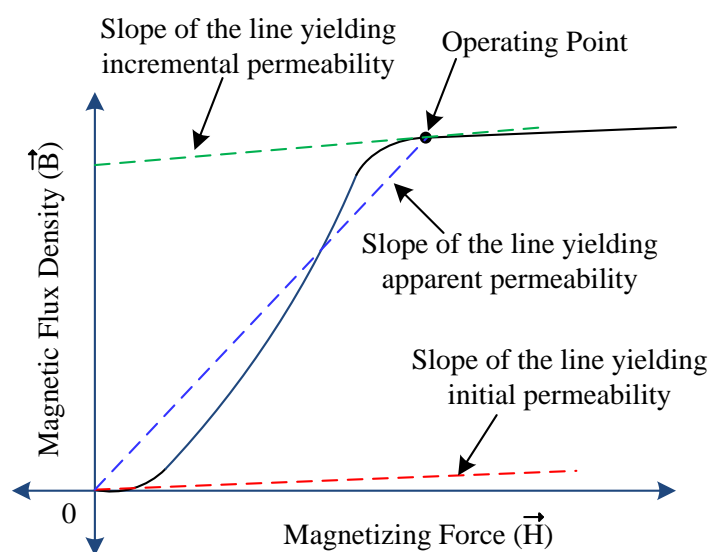


Figure 4.1: B-H curve of the electrical steel representing non-linear magnetic properties.

In the power cable, four conductors arranged symmetrically constitute the medium for TEM waves. Four continuum of lumped parameter circuit representing a small section of the cable conductor, magnetically and electrostatically coupled together forms the cable model. However, in the case of the machine winding, continuum of lumped parameter circuits representing a small section of a winding are magnetically and electrostatically coupled. Generally, the turn conductors embedded in the same slots are represented by lumped parameter circuits and are magnetically and electrostatically coupled together. Further, if the two phases of the winding share the same slot, akin to the cable, the continuum of the circuit representing each phase is mutually coupled. In consequence, modelling machine winding is more complex with mutual resistive and inductive coupling between the turns, coils and phases.

In consequence, the MCTL model of the stator winding is a special case of the cable model wherein,

- The surrounding medium is non-homogeneous and non-linear. Thus, the TEM wave propagates at two different velocities, one within the stator slot and the other in the overhang region.
- Unlike cable, the surrounding medium is conductive. Therefore, the effect of induced eddy current in the core must be accounted.
- Different from the cable, the lumped parameter circuit representing sections of the same phases of the winding are mutually coupled. Therefore, the lumped parameter circuit cannot be repeated without change.

However, there are similarities which can be inherited from the cable model for modelling the stator winding:

- The dielectric loss and the permittivity variation with the frequency is marginal. So, the capacitive coupling between the conductors can be represented purely as capacitance.
- The frequency dependent inductance and resistance of turn can be represented using a Ladder circuit with frequency independent parameters.
- The mutual resistive and inductive coupling between the conductors can be represented using current controlled voltage source.

In the following section, an MCTL model of the stator winding is discussed representing its behaviour over a broad range of frequencies. The modelling procedure begins by inheriting the similarities of the cable model and then offers changes to incorporate the complexity in the machine winding.

4.3 Multi-Conductor Transmission Line model

Similar to the cable, the MCTL model of the machine winding is a continuum of the lumped parameter circuit, due to its advantage of solving the current and voltage distribution using circuit simulation. The approximation of the lumped parameter circuit representation for a MCTL model is applicable if the length of the winding represented as a lumped parameter circuit, also called a cell, is electrically less than the shortest wavelength (λ_{min}) of the TEM wave. In other words, the space variation of the electromagnetic field within each cell along the direction of travel is negligible. Thus, the shortest wavelength depends on the maximum frequency (f_{max}) component of the impinging voltage wave, which is expressed using (3.22-3.23) as [41]

$$\lambda_{min} = \frac{\mathcal{G}\pi t_r}{3} \quad (4.2)$$

where, \mathcal{G} is the velocity of the TEM wave in the medium, and t_r is the rise time of the voltage pulse. In general, due to the permeability of the core and the permittivity of the insulation, the propagation speed of the TEM wave within the winding is about a quarter of the speed in free space (c) [134]. To validate this fact, the propagation delay within the phase winding of the machine under study is measured experimentally by exciting one of the phase winding by a single voltage pulse. The propagation delay is measured as the dwell time between the voltage pulse at the phase terminal and at the neutral point. The measured dwell time is 300ns, and the approximate length of the phase winding is 28.82m. Thus, the propagation speed within the winding is 96m/ μ s, which is moderately higher than a quarter of the speed of an electromagnetic wave within free space. As discussed in chapter 3, the frequency spectrum of fast slew rate voltage pulse spreads over a wide range. Also, its deleterious effect is more pronounced under a fast slew rate voltage pulse. Therefore, to keep the machine winding model representative of the HF excitation arising due to the fast slew rate, the modelling process assumes the maximum slew rate of the voltage pulse, which is 20ns. Thus, the shortest wavelength of the wave engendered by a voltage pulse of rise time 20ns is 1.57m. The lumped

parameter circuit representing a section of the winding must be less than 1.57m. As a general principle, for the model to be representative at HF, at least 5 sections should be accommodated within the shortest wavelength. Therefore, the length of the winding represented by each lumped parameter circuit is less than 314mm.

Herein, an 8-pole, 60 kW PMSM [29] adapted to Toyota Prius vehicle is used whose stack length (l) is 50.8mm and overhang length (l_{ov}) on each side is 113mm. Thus, the length of a turn, which is twice the sum of stack length and overhang length, is less than 314mm. Hence, each turn of the winding can be represented as lumped parameter circuit and each turn model is connected in sequence to form a coil model. The machine under study has 11 turns/coil. Thus, 11 lumped parameter circuits are connected in series along with the frequency dependent mutual coupling between them to form a coil model.

The lumped parameter circuit using Lumped-Pi or Lumped-T circuit as elemental section are illustrated in section 3.2.4. In an additional Lumped- Γ circuit, the shunt impedances are connected to one side of the series impedance, which has the benefit of realising with fewer elements. Therefore, the lumped parameter circuit used for the modelling, unlike cable, is a lumped- Γ circuit with the shunt impedance connected on one side of the series impedance, as illustrated in Figure 4.2. The series impedance comprising frequency dependent resistance and inductance represent the turn resistance and inductance, whereas the capacitance between the turns and between the turn and core is represented using a capacitor. Each part of the cable depicted as a cell in the cable model is neither electrostatically nor magnetically connected; nonetheless, the phase conductors of the same section are mutually coupled. In the machine winding, however, the turns embedded in the same slot are coupled together. As a result, the circuits representing the turns in the same slot are connected in series and are mutually coupled. This makes the model more complex. The Figure 4.2 illustrates the continuum of lumped- Γ circuit representing one turn, to form a coil. The figure depicts the capacitance between the i^{th} turn and the core as C_{i0} , the capacitance between the i^{th} and k^{th} turn as C_{ik} and the resistance and inductance of i^{th} turn as R_{ii} and L_{ii} and the mutual resistive and inductive coupling between the i^{th} and k^{th} turn as R_{ik} and L_{ik} . It is worth noting that, the resistive and inductive parameters are frequency dependent. The frequency dependent characteristics, like the cable, are represented using a Ladder circuit.

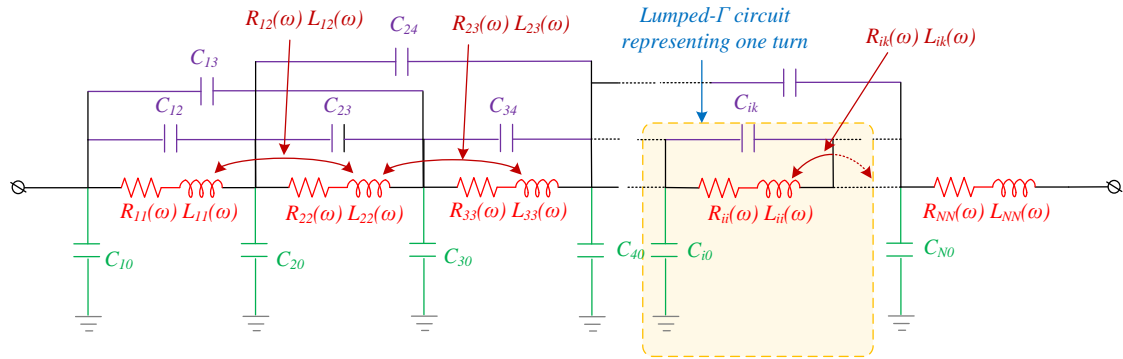


Figure 4.2: Continuum of lumped- Γ circuit representing MCTL model of the stator winding.

4.3.1 Computation of Model Parameters

The fundamental principle of the TEM wave is, that the electric and magnetic fields are orthogonal and satisfy static distribution in the transverse plane. This implies that the transmission line parameters can be deduced more readily using separate excitation. Like the cable, the parameters are determined using ANSYS[®] Maxwell [137]. The parameter estimation is a two-step process:

- First, a 2-D geometry of the stator cross-section along with the material properties is defined, as illustrated in Figure 4.3. The detailed specification of the geometry and material properties of the cable cross-section is defined in Table 4.1. The stator winding is a three-phase, single layer winding with 8 coils per phase (N_c) and 11 turns per coil (N_t). Therefore, each phase is spread across 16 slots. Each turn comprises 12 parallel conductors that are denoted by T_j , where j is the turn number as depicted in Figure 4.3. As a result, each slot has 132 conductors. In the random wound winding, determining the exact location of the turn conductor is difficult. Therefore, the distribution of the turn conductors within the slot is assumed symmetrically arranged and is the same for all the slots. Each turn has 12 parallel conductors.
- Further, the capacitive coupling is calculated using an electrostatic field solver and the resistance and inductance of each conductor are calculated using an eddy current solver.

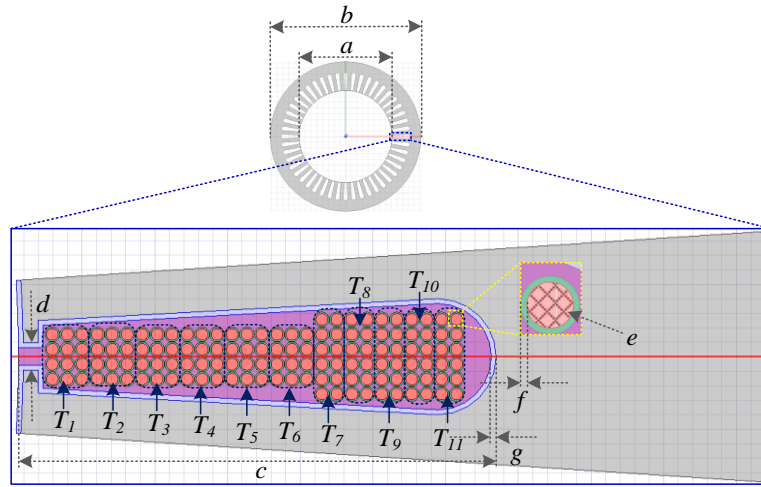


Figure 4.3: Schematic diagram of the cross-section of a stator slot of the stator winding.

Table 4.1: Stator dimensions [29] and properties of insulation.

Parameter	Value
Dimension of the Stator Slots	
Inner stator diameter (a)	161.9 mm
Outer stator diameter (b)	264 mm
Stack length	50.8 mm
Depth (c)	30.9 mm
Slot opening (d)	1.88 mm
Parameters of the Stator Winding	
Number of slots	48
Series coils/Phase (N_c)	8
Parallel circuits/Phase	0
Turns/Coil (N_t)	11
Parallel Strands per turn (N_p)	12
Wire size (e)	20AWG
Resistance/Phase	0.77 Ω
Insulation Parameter of the Stator Winding	
Thickness of turn insulation (f)	0.025 mm
Permittivity of turn insulation	3.5 F/m
Permittivity of main-wall insulation	3.5 F/m
Thickness of ground-wall insulation (g)	0.35 mm
Permittivity of ground-wall insulation	3.5 F/m

The time varying current through the conductor embedded in the slots induces magnetic flux lines, which penetrate the core. The flux lines produce eddy current due to the core conductivity, resulting in eddy current loss in the core. To minimise the loss, the core is manufactured as stacked thin insulated sheets, which prevents the induction of eddy current. However, if the thickness (t) of the sheet is larger than twice the skin depth (δ), small eddy current loops will be induced. As a result, the induced eddy current opposes its source, i.e., the eddy current restricts the penetration of the magnetic flux induced by the conductor current. The skin depth depends on the core permeability (μ), conductivity (σ) as frequency (f) of excitation as [134],

$$\delta = \sqrt{\frac{1}{\pi f \sigma \mu}} \quad (4.3)$$

At HF of excitation, the skin depth is small. Thus, above the frequency where twice the skin depth is less than the thickness of the insulated sheet, an eddy current is induced. The induced eddy current inhibits the magnetic flux from penetrating the core, acting as a flux barrier. In consequence, the high permeability of the stator core confines the HF components of the magnetic field within a single tooth-slot region [37-38][112][147].

A similar phenomenon can be seen in the rotor core. For a semi-closed slot, the leakage flux into the air gap is quite small, and the induced eddy current in the rotor core or magnets acts as a flux barrier [37-38][112][147]. Due to the air gap and the high permeability of the rotor core, the HF flux linkage between the stator and the rotor is the least.

Hence, a single slot model is used without the rotor for the development of the proposed model. For the experimental validation, the machine without the rotor is used. Figure 4.4 (a) depicts the stator of the PMSM [29] used in the study, which is extracted from the overall machine structure.

While building a suitable model for form-wound windings using measurement is simple, creating a model for random-wound windings is challenging. In the random wound winding, determining the exact location of the turn conductor is difficult. In [147], cut-open electrical machines are used to determine the location, however, the cut-open machines are often unavailable. The probability distribution function (PDF) is used in [148] to predict the location of the conductors, however, it requires experimental measurements which necessitate the

stator's availability. Therefore, this method cannot be adopted during the design stage. For a simplified approach, the conductors are assumed symmetrically arranged as illustrated in Figure 4.3. In consequence, uncertainty in the estimation of turn-to-turn capacitance and inductance matrices can be observed, however, differences in the turn-to-core capacitance will be less. As a result, at HF, differences in the CM and DM impedance between the measurement and prediction will be large, wherein, the effect of turn-to-turn capacitance dominates. At LF, the turn-to-core capacitance dominates, hence, the difference is less. Also, the turn inductance depends on its location. This variation is influential under HF excitation. With the turn distribution illustrated in Figure 4.3, the inductance of the turn closest to the slot opening is 105nH at 1MHz, while the inductance of the turn in the middle of the slot is 200nH and at the slot end is 230nH. As a result, the turn distribution is crucial for the impedance measured at HF excitation.

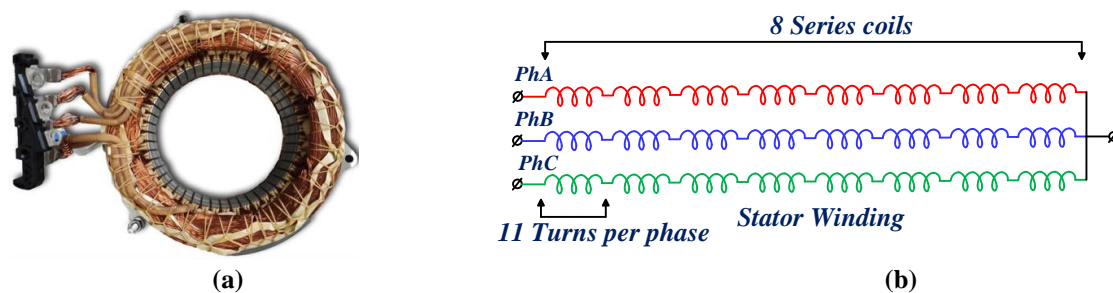


Figure 4.4: Stator winding [29] of the 60kW PMSM employed in Toyota Prius electric vehicle.

4.3.1.1 Capacitance Calculation

The capacitance between the turn conductor and between the turn conductors and the core is determined by solving the static electric field surrounding the conductors using ANSYS[®] Maxwell [29]. These capacitive couplings vary between the slot and in the overhang region. In the slot region, the turns are in proximity to the core. However, in the overhang region, the turn conductors are separated from the core, as illustrated in Figure 4.5. Although the capacitive coupling with the core can be determined by solving the static electric field in 3-D geometry, to ease the parameter calculation, without involving complex computational resources and time, this capacitive coupling is ignored. The capacitive coupling within the slot region is determined by solving the static electric field using the 2-D single slot model. Akin to the cable, the electrostatic field solver is used to calculate the capacitances. The capacitance calculation is comprehensively discussed in section 3.1.5.

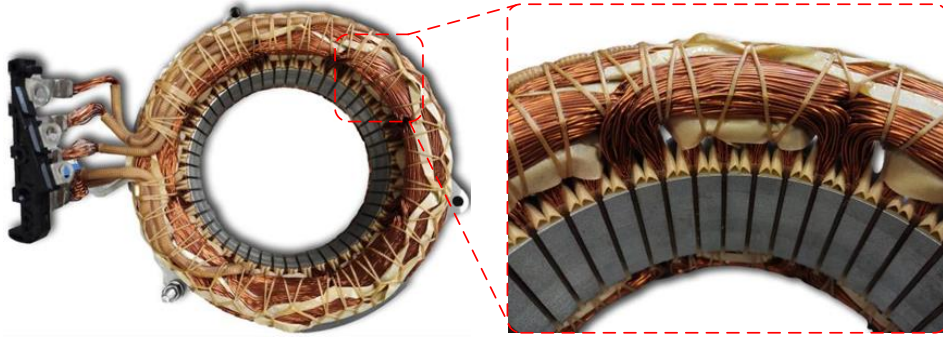


Figure 4.5: Overhang region of the winding representing the separation between the core and the winding.

The winding under study is a single layer winding with 8 coils per phase (N_c), 11 turns per coil (N_t) and 12 parallel conductors/turn (N_p), as illustrated in Figure 4.4 (b). Therefore, 11 groups of conductors with 12 conductors in each group are embedded in one slot. Each group of 12 conductors are considered as one side of a turn and is excited simultaneously to calculate the capacitance. The core is assumed as a reference. For calculating the capacitance matrix, the solver excites each turn sequentially by 1V with respect to the remaining turns. In the end, the solver provides the self-capacitance matrix with elements c_{ij} which represents the self-capacitance per unit length between the conductor i and j . From the self-capacitance matrix, the capacitive coupling between the conductors and, conductors and core is calculated using (3.28) as [137],

$$\begin{bmatrix} C_{slot_{10}} & \cdots & C_{slot_{111}} \\ \vdots & \ddots & \vdots \\ C_{slot_{110}} & \cdots & C_{slot_{111}} \end{bmatrix}_{11 \times 11} = \begin{bmatrix} \sum_{i=1}^{11} c_{1i} & \cdots & -c_{111} \\ \vdots & \sum_{i=1}^{11} c_{2i} & \vdots \\ -c_{111} & \cdots & \sum_{i=1}^{11} c_{11i} \end{bmatrix}_{11 \times 11} \quad (4.4)$$

The diagonal elements ($C_{slot_{ii}}$) of the capacitance matrix represents the capacitive coupling between the i^{th} turn conductors and the core, whereas the off-diagonal elements ($C_{slot_{ij}}$) represent the capacitive coupling between the i^{th} and j^{th} turn conductors.

Generally, during the manufacturing process, the core and winding assembly is impregnated with resins to ensure electrical insulation between the conductors and the structural integrity. Hence, the dielectric properties of the resins greatly influence the capacitive coupling between the turn conductors. As the conductors within the slot region and in the overhang region are

impregnated with the resins, the capacitive coupling between the turn conductors in both the regions is the same. Therefore, the turn-to-turn capacitance per unit length in the overhang region is considered the same as the slot region. Thus, the turn-to-turn capacitance (C_{ovij}) in overhang region between turn i and j is deduced as [38],

$$C_{ovij} = \frac{l_{ov}}{l_{stack}} C_{slotij} \quad (4.5)$$

where, l_{stack} is stack length and l_{ov} is the overhang length on each side. Herein, the stack length is 50.8mm and the average overhang length on each side is 113mm. So, the capacitance between the turn conductors in the overhang region is 2.22 times the capacitance in the slot region. Notably, the diagonal elements of the capacitance matrix (C_{ovii}) representing the capacitance in the overhang region is zero, as it is ignored.

In general, the turns are divided in 4 parts, two embedded within the slots and the remaining two on either side in the overhang region. Therefore, the total capacitance (C) of a turn is expressed as [38],

$$C = 2(C_{slot} + C_{ov}) \quad (4.6)$$

where, C_{slot} is the capacitance matrix representing the capacitance between the turns in slot region and C_{ov} is the capacitance matrix representing the capacitance between the turns in overhang region. Equation (4.6) represents the capacitance coupling of the turns in the machine winding. It is assumed that the distribution of the conductors in every slot is the same. So, the capacitance matrix for each coil of the phases is assumed same.

4.3.1.2 Inductance and Resistance Calculation

The frequency dependent inductance and resistance are calculated differently from the cable. In cable, the conductors are surrounded by a homogeneous dielectric medium with zero conductivity. However, in the machine winding, the conductors embedded within the slots are surrounded by the thin conductive sheets of insulated electrical steel. Different from the cable, the core is conductive. Although the core is made of laminated sheets, the HF flux lines penetrating the core induce an eddy current, which restricts its cause. As a result, when excited at HF, the core acts as a flux barrier confining the flux lines inside the slot region [37-38][112][147]. Because the skin depth is greater than the sheet thickness, the laminated sheets

behave as an insulating material during LF excitation. Therefore, the laminated sheets are more effective in alleviating eddy current induction at LF than HF excitation. In addition, the laminated core is a non-linear lossy ferromagnetic material. The non-linear variation of the permeability of the core depends on the magnetic flux density within it which is accounted for using the B-H curve. As a result, the apparent permeability is used as a representation of the material property at the operating point, as described earlier.

The parameters may be computed accurately using a 3-D geometry of the slot, wherein, the laminated sheets can be defined with non-linear magnetic properties. However, it will increase the computational resources and time significantly. One way to avoid complex computation is to assume zero conductivity of the core [38]. This assumption will not make difference in the parameters at LF excitation, as the laminated core acts as insulating material. However, this assumption will largely affect the predicted inductance at HF. In the real scenario, the absence of a flux line within the core will significantly reduce the inductance. However, when the conductivity of the core is assumed zero, the inductance predicted at the HF will be large. In the same vein, the predicted resistance will be less than the actual resistance. Furthermore, with zero conductivity, the induced eddy cannot be realised, and so the core losses cannot be represented.

The aforementioned problems can be dealt with lucidly, yet practically by adding an additional resistance across the turn impedance in the lumped parameter circuit [38]. This resistance is a representation of hysteresis and eddy current losses and will impart the same effect as with the conductive core. The resistance in parallel will reduce the effective inductance of the turn at HF with an increase in resistance. The design of the resistance is discussed comprehensively at a later stage in section 4.3.1.3.

The frequency dependent inductance and resistance of the turn conductors embedded in the slot are determined the same as the cable. The eddy current field solver of ANSYS® Maxwell [137] is used for parameter extraction. The solver sequentially injects 1A current to one group of conductors with the remaining unexcited and calculates the resistance and the inductance of the group. It breaks the impedance matrix calculation into two parts. First, it solves for the inductance matrix and then for the resistance matrix. Later, it combines the inductance and resistance matrix to calculate the impedance matrix. The diagonal elements of the matrix represents the self-impedance of the turn conductor, whereas the off-diagonal elements

represent the mutual coupling between the turn conductors. It is noteworthy that, the resistance and inductance are frequency dependent. Consequently, the impedance matrix is different at different frequencies. For characterizing the variation, the impedance matrix is calculated at 7 different frequencies, 50Hz, 100Hz, 1kHz, 10kHz, 100kHz, 1MHz, and 10MHz.

Due to the skin and proximity effect, the current distribution across the cross-section of the conductor changes with frequency. With the increasing frequency, the eddy current induced within the conductor shifts the current density towards the surface [134]. As a result, the resistance of the conductor increases. The inductance of the conductors is composed of the flux linkage within the conductor and external to the conductor. At HF, due to redistribution of current density, the flux linkage internal to the conductors reduces, which reduces the inductance of the conductor. However, in the real scenario, an additional reduction is imparted by the induced eddy current in the core. This additional reduction is accounted for in the lumped parameter circuit by a resistor connected in parallel with the turn impedance.

4.3.1.3 Core loss resistance calculation

In the previous section, while determining the turn parameters, the lamination effect of the core is realised by assuming zero conductivity of the core. However, the assumption doesn't hold at HF excitation, where the induced eddy current in the core restricts the penetration of the flux lines within the core. As a result, the predicted inductance of the turns is higher than the actual inductance. In addition, the assumption of zero conductivity ignores the eddy current loss in the core. The laminated cores can be modelled analytically as in [144-145], wherein the current and magnetic field intensity vector are restricted in an orthogonal axis, thus reducing the problem to one-dimensional analysis.

To account for the difference, a lucid, yet practical way is to add a resistor across the turn impedance. This resistance is often called core loss resistance (R_e). An empirically defined curve [149] between the core loss resistance and the stator outer diameter is used to find the resistance. The outer diameter of the stator used in this analysis is 16.19 cm [29]. Using the curve, therefore, the core loss resistance per phase is 2 k Ω . With 11 turns per coil (N_t) and 8 series coils per phase (N_c), the core loss resistance per turn is 22.73 Ω . Figure 4.6 illustrates the comparison between the impedance of a turn conductor with and without the resistance. Illustratively, a 22.73 Ω resistance is connected across the turn impedance for core loss representation.

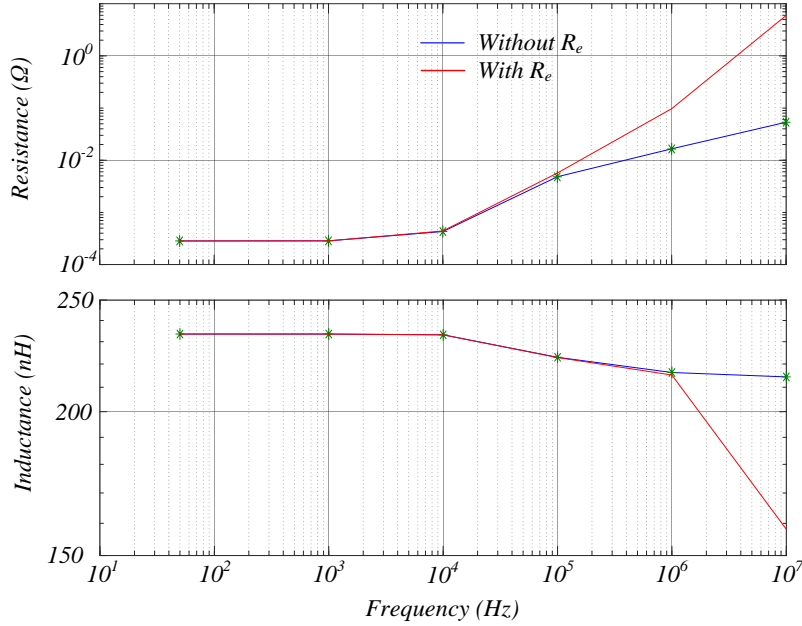


Figure 4.6: Frequency dependent impedance of turn 1 with and without core loss resistance.

The effect of the resistance is similar to the effect of the induced eddy current at HF excitation. The induced eddy current makes the core as flux barrier which reduces the inductance of the conductors. In the same vein, adding an additional resistor reduces the inductance of the conductor at HF excitation without affecting the impedance in the LF region.

4.3.1.4 Overhang inductance calculation

The winding inductance in the overhang region is assumed constant and equally distributed among the turns. This assumption is based on the experimental evidence presented in [147]. Every section of the winding was separated in [147], and the impedance of the end winding was measured using a customised jig to keep the end winding section in place. The analysis predictably reveals that the inductance in the overhang region is much smaller than that in the slot region and is close to constant. The inductance is calculated [38] from (4.7) as,

$$L_{ovT} \cong k_r \cdot \frac{1}{N} \cdot \left(\mu_0 N_t^2 \cdot \left(\frac{2}{P} \right) \cdot \lambda_b \cdot l_{ov} \right) \quad (4.7)$$

where, k_r accounts for the reduction in inductance due to skin effect, P is the number of pole-pairs, N_t is the total number of turns per phase, λ_b is geometry coefficient ($\lambda_b \approx 1.5$) and l_{ov} is the length of turn in the overhang region. Herein, $k_r \approx 0.3$, and L_{ovT} calculated from (10) is $2.8\mu\text{H}$.

4.3.2 Representation of Frequency Dependent Parameters

Representing the frequency dependent parameters is the same as the cable model. The Ladder circuit is used to realise the frequency dependency of the parameters. The fundamental feature of the Ladder circuit is its frequency independent characteristics, which permit its usage in time-domain analysis for representing frequency dependent parameters. For realising the series impedance of a turn, the RL Ladder circuit is used. The physical significance of the circuit is comprehensively discussed in section 3.4. The parameters of the Ladder circuit are evaluated using VF [140]. VF is a state equation approximation method, which is applied in the frequency-domain and approximates the state equation of the system by locating its dominant poles and residues over an observed domain. By way of example, the VF represents the i^{th} turn impedance (Z_{ii}) as [140],

$$Z_{ii}(s) = R_{ii} + sL_{ii} \approx \underbrace{\sum_{n=1}^m \frac{r_n}{s - p_n}}_{1/Y(s)} + d + se \quad (4.8)$$

A flowchart explaining the method for evaluating the Ladder circuit parameters is illustrated in Figure 4.7, wherein, the parametrization of mutual impedance (Z_{ik}) between i^{th} and the k^{th} turn is depicted. For evaluating the self-impedance parameter of i^{th} turn, the same flowchart can be followed with $i = k$. For instance, the frequency response of the 6th order Ladder parameter calculated using the flowchart is illustrated in Figure 4.8. The frequency response of the Ladder circuit conforms with the parameter evaluated using FEM. Thus, the Ladder circuit can be employed for representing the frequency dependent behaviour of the turns.

4.3.3 Representation of Mutual Resistive and Inductive Couplings

Akin to the cable, the mutual resistive and inductive coupling between the conductors can be represented using current controlled voltage source. The turn voltage (V_i) due to its impedance and mutual coupling between the i^{th} turn and the k^{th} turn is expressed as,

$$V_i = \underbrace{\left(R_{ii}(\omega) I_i + L_{ii}(\omega) \frac{dI_i}{dt} \right)}_{V_{ii}} + \sum_{\substack{k=1 \\ i \neq k}}^{N_t} \underbrace{\left(R_{ik}(\omega) I_k + L_{ik}(\omega) \frac{dI_k}{dt} \right)}_{V_{ik}} \quad (4.9)$$

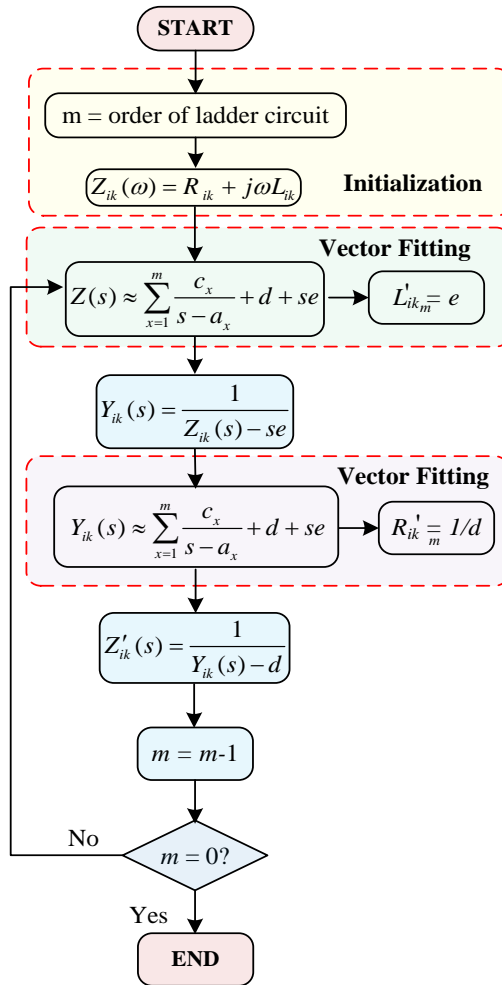


Figure 4.7: Proposed procedure for the development of the Ladder circuit using vector fitting [144].

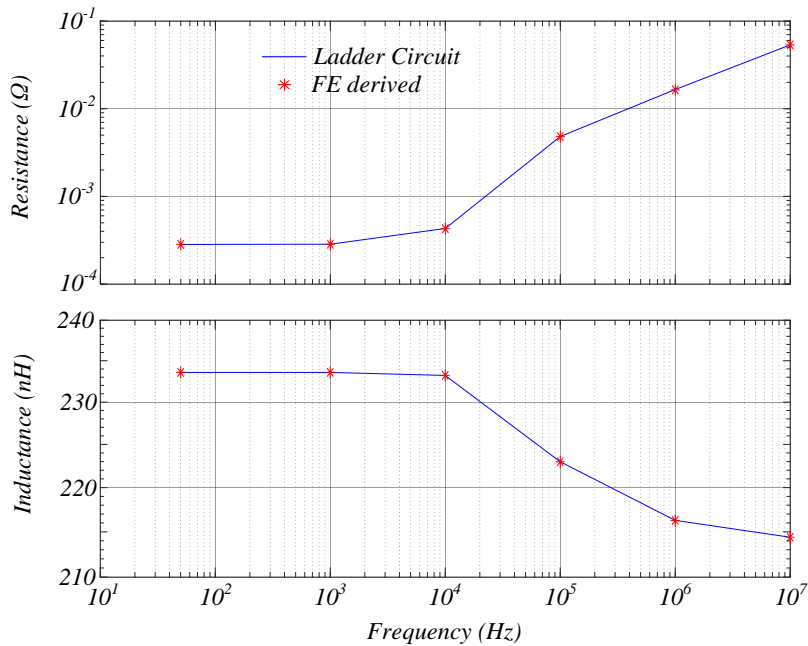


Figure 4.8: Frequency response of 6th order Ladder circuit representing the self-impedance of turn 1 of line end coil.

where, N_t is the number of turns per coil, R_{ii} and L_{ii} are the self-impedance of i^{th} turn, R_{ik} and L_{ik} are the mutual couplings between turns i and k , I_i is the i^{th} turn current and I_k is the k^{th} turn current. In (4.9), the first term (V_{ii}) represents the turn voltage due to self-impedance whereas, the second term (V_{ik}) represents the voltage due to mutual coupling. A current controlled voltage source can be used to represent the turn voltage due to mutual coupling, the same as the cable. For instance, the voltage drop across the i^{th} turn due to the current in k^{th} turn (I_k) is calculated by injecting the current I_k through a Ladder circuit representing the mutual coupling between the turn i & k . Similarly, the voltage drop due to mutual coupling with the other turns is calculated and then added together to represent the current controlled voltage source. Thus, for N_t number of turns per coil, 1 Ladder circuit is used to represent the self-impedance and $N-1$ Ladder circuits are used to represent mutual coupling with the remaining $N-1$ turns. As a result, the N number of the Ladder circuit is required for representing the impedance of 1 turn in the lumped parameter circuit. Thus, for representing a coil, N^2 Ladder circuit is required. By way of example, the machine under study has 11 turns/coil (N_t) and 8 coils per phase (N_c). So, 8×11^2 Ladder circuit is required for the exact representation of the lumped parameter circuit of one phase. Figure 4.9 illustrates the lumped parameter circuit of one phase winding. Each turn model is represented using the following components:

- One Ladder circuit representing the self-impedance of each turn (R_{ii} & L_{ii}).
- $N-1$ Ladder circuit representing the mutual coupling between the turns embedded in the same slot (R_{ik} and L_{ik}). Each Ladder circuit is excited by the turn current, and the total voltage drop is represented as current controlled voltage source.
- $N-1$ current controlled current source exciting $N-1$ Ladder circuit representing the mutual couplings.
- I ammeter measuring current of the turn.
- I current controlled voltage source representing turn voltage due to mutual coupling.
- Overhang inductance representing the inductance of the part of the turn in the overhang region. (L_{ovT}).
- Core loss resistor (R_e) representing the core losses due to induced eddy current in the core. The resistor is connected across the series combination of the overhang inductance, the Ladder circuit representing self-impedance and the current controlled voltage source.

- A Capacitor (C_{i0}) representing capacitive coupling between the turn and the core.
- Capacitors (C_{ik}) representing capacitive coupling between the i^{th} and k^{th} turn.

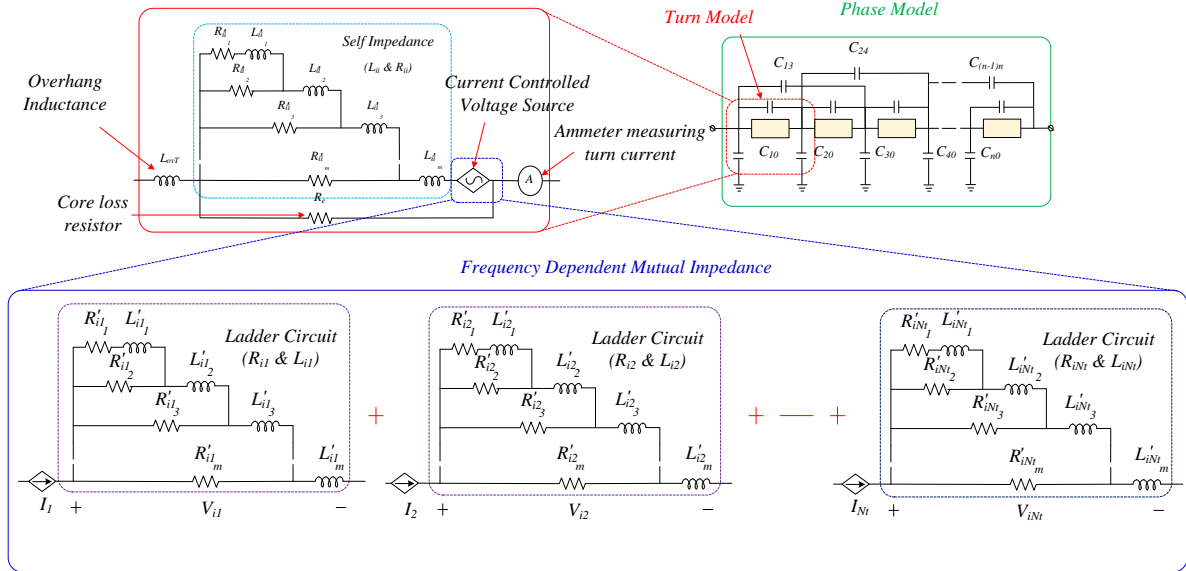


Figure 4.9: Lumped parameter model of a phase winding representing the frequency dependent self-impedance with explicit representation of the mutual coupling between the turns.

The other two phases of the winding are similarly represented and connected in a star to represent the star connected three phase winding. Certainly, this method involves great complexity, computational time, and resources. However, the mutual couplings between the turns can be defined explicitly in the time-domain analysis without the use of modal transformation, Fourier transform, convolution, or multiple lumped parameter circuits representing the winding under a single frequency of excitation. For realising the TEM wave propagation, which characterises the voltage stress at a different location in the machine winding, the proposed lumped parameter circuit is proficient. It can also be used to assess the CM current engendered due to the fast slew rate of voltage pulse causing EMI with the nearby electronic equipment. In the example considered, being a single layer winding, the mutual coupling exists in the conductors of the same phase. However, the concept can also be extended to account for the mutual coupling of a double layer winding where the conductors in a slot carry currents in two different phases separated by phase insulation.

The mutual coupling can be represented in a simplified way by using one Ladder circuit per turn instead of $N-1$. For instance, Figure 4.10 represents the mutual coupling between the 1st turn and the remaining 10 turns of the 1st coil, wherein, the mutual resistive and inductive coupling between the turns are comparable to each other. If the mutual coupling between the

turns are same, say, $R_{i1} = R_{i2} = \dots = R_{iN-1} = R_{im}$ and $L_{i1} = L_{i2} = \dots = L_{iN-1} = L_{im}$ the turn voltage can be expressed mathematically as,

$$V_i = \underbrace{\left(R_{ii}(\omega) I_i + L_{ii}(\omega) \frac{dI_i}{dt} \right)}_{V_{ii}} + \underbrace{R_{im}(\omega) \sum_{\substack{k=1 \\ i \neq k}}^N I_k + L_{im}(\omega) \sum_{\substack{k=1 \\ i \neq k}}^N \frac{dI_k}{dt}}_{V_{ik}} \quad (4.10)$$

Notably, instead of N , (4.9) can be realised with only two Ladder circuits, one for representing self-impedance ($R_{ii}(\omega)$ & $L_{ii}(\omega)$) and the other for representing the mutual coupling between the turns ($R_{im}(\omega)$ & $L_{im}(\omega)$). Thus, if the mutual parameters are assumed same and equal to the average of the mutual parameters, as illustrated in (4.11), the mutual coupling can be realised using the 2 Ladder circuit. Hence, the lumped parameter model can be made simpler and faster using the simplified mutual representation.

$$R_{im}(\omega) = \frac{1}{N-1} \sum_{\substack{k=1 \\ i \neq k}}^N R_{ik} \quad (4.11a)$$

$$L_{im}(\omega) = \frac{1}{N-1} \sum_{\substack{k=1 \\ i \neq k}}^N L_{ik} \quad (4.11b)$$

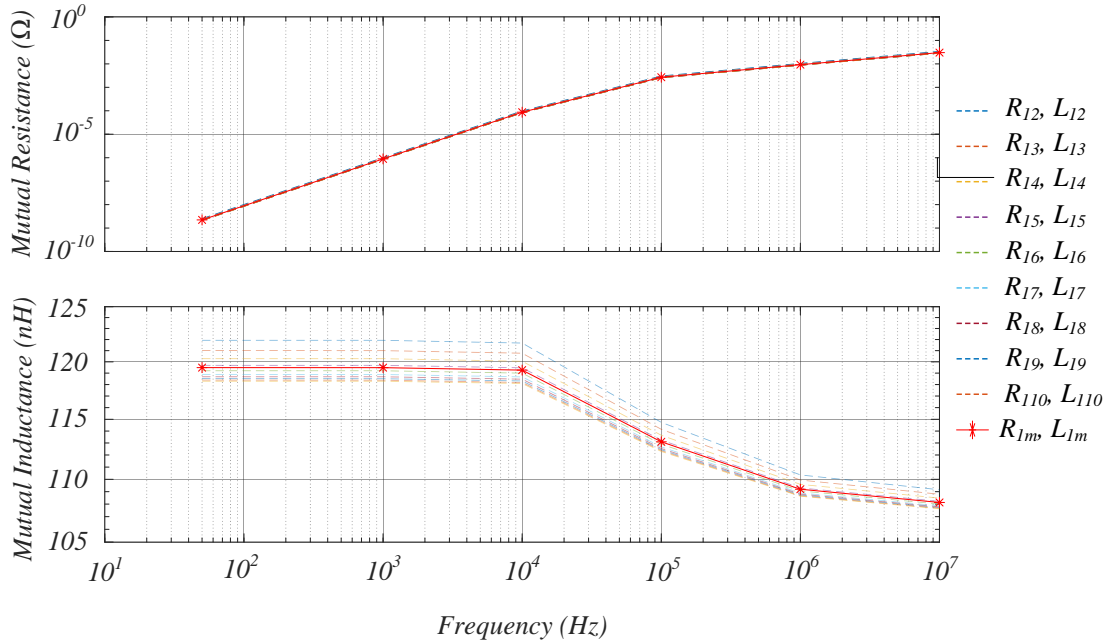


Figure 4.10: Mutual resistive coupling between turn 1 and the remaining 10 turns embedded in the same slot.

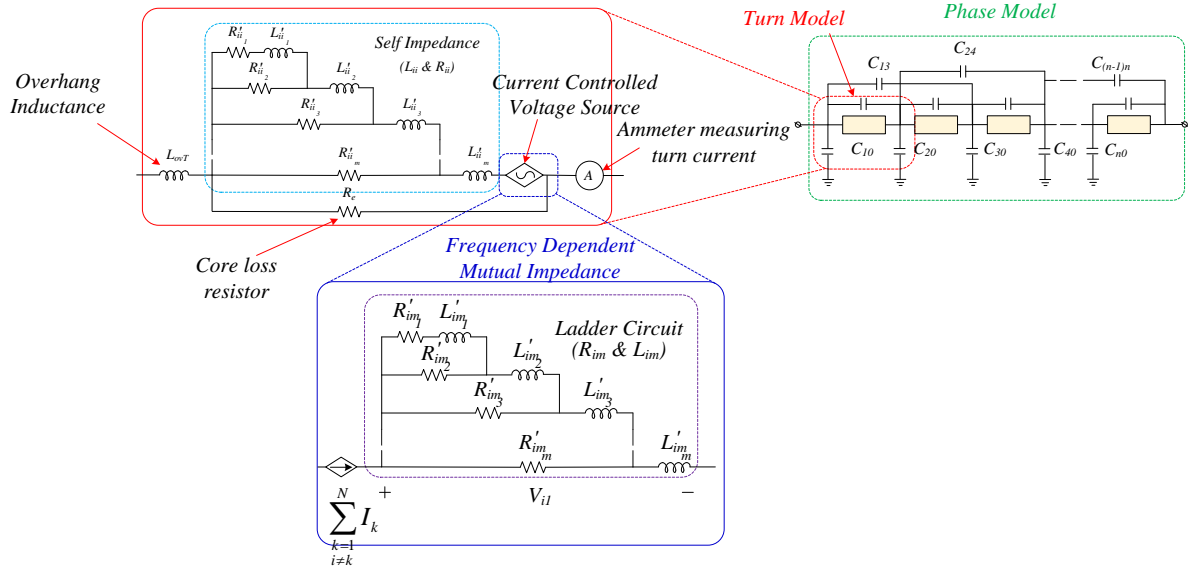


Figure 4.11: Lumped parameter model of a phase winding representing the frequency dependent self-impedance with a simplified representation of the mutual coupling between the turns.

The average mutual coupling between turn 1 and the remaining turns is illustrated in Figure 4.10. The difference between the parameters and the average is majorly in the inductance at the LF region where the impedance of the winding is low. At HF the difference is marginal, and the simplified representation of the mutual coupling can be used without losing accuracy. The lumped parameter circuit employing simplified mutual representation is illustrated in Figure 4.11. Different from the explicit representation of the mutual coupling, this method uses two Ladder circuits per turn.

Each turn model comprises the following components:

- One Ladder circuit representing the self-impedance of each turn (R_{ii} & L_{ii}).
- 1 Ladder circuit representing the average mutual coupling between the turns embedded in the same slot (R_{im} and L_{im}). The Ladder circuit is excited by the sum of the turn current embedded in the same slot, and the voltage drop across it is represented as current controlled voltage source.
- 1 current controlled current source exciting 1 Ladder circuit representing the average mutual coupling.
- 1 ammeter measuring the current of the turn.
- A current controlled voltage source representing turn voltage due to mutual coupling.
- A core loss resistor (R_e) representing the core losses due to induced eddy current in the core. The resistor is connected across the series combination of the overhang

inductance, the Ladder circuit representing self-impedance and the current-controlled voltage source.

- Overhang inductance representing inductance of the part of the turn in the overhang region. (L_{ovT}).
- A capacitor (C_{i0}) representing capacitive coupling between the turn and the core.
- Capacitors (C_{ik}) representing capacitive coupling between the i^{th} and k^{th} turn.

To summarise, the HF model of the machine is developed from the machine design parameters without its physical availability. Using the design parameters, slot geometry and the location of the turns within the slot are defined in ANSYS[®]. Further, the partial capacitance matrix, inductance and resistance matrix are calculated in the ANSYS[®] environment. The frequency dependent inductance and the resistance matrix are then used to calculate the ladder circuit parameters, which is summarised in Figure 4.12. Later, a MCTL model of the machine illustrated in Figure 4.11 is developed in the MATLAB[®] environment. The MATLAB[®] based implementation of the MCTL of the stator winding is comprehensively discussed in the appendix. Furthermore, using the linear analysis of the control system toolbox of MATLAB[®], the model is analysed in the frequency domain to calculate the CM and DM impedance. For ascertaining the impact of the PWM voltage pulse impinging machine terminals, time domain analysis is used. The aforementioned modelling process of the machine is summarised in Figure 4.12.

In the following section, the efficacy of the proposed lumped parameter circuit is comprehensively illustrated. Later, a comparison between the frequency response of the model with the explicit and simplified representation of the mutual coupling is depicted, wherein, a marginal difference is seen in the HF region.

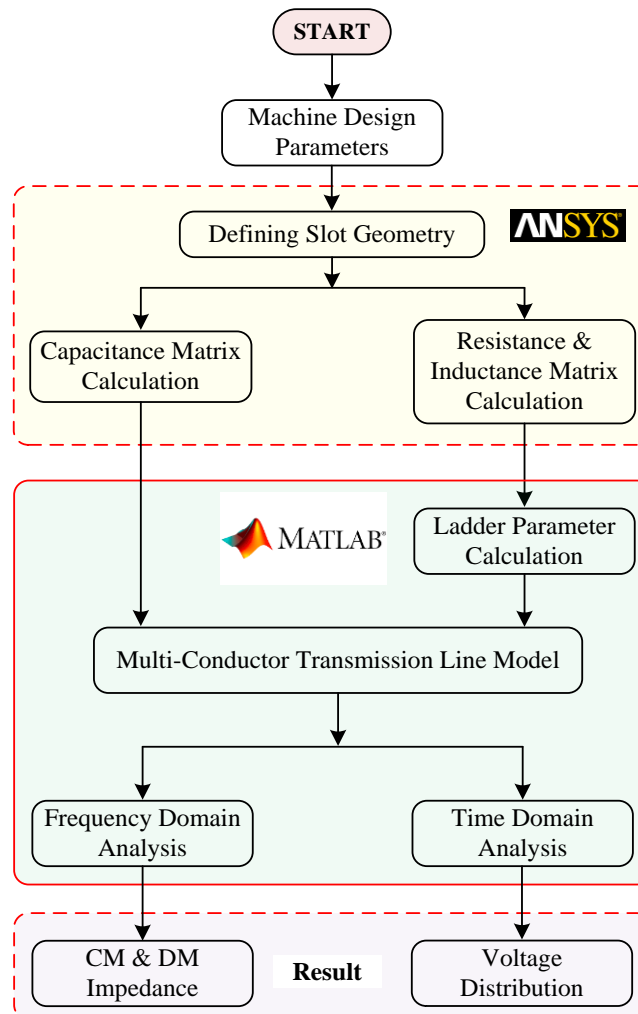


Figure 4.12: Flowchart representing the HF modelling of the machine winding.

4.4 Experimental Validation

The main aim of the model is to assess the voltage distribution within the winding under high slew rate voltage pulse excitation. Because only the terminal ends of the winding are accessible in the field scenario, monitoring the voltage stress at key locations within the winding is challenging. It is only possible if a model representing the winding is available and must be representative over the wide frequency range. Comparing the CM and DM impedance of the model with the experimentally measured impedance is a widely accepted practice to validate the model. This ensures that the impedance rendered to the CM and DM current is representative of the actual scenario. Comparing the voltage stress at the terminal end and the star neutral is another way to validate the model in time-domain. Once the model is validated, the voltage distribution within the winding can be predicted with great confidence. In the following section, the CM and DM impedance of the model is compared with the experimental

measurement. Later, the voltage stress at the terminal end and at the neutral point is compared to validate the model in time-domain. The key characteristics of the voltage stress are discussed thereafter.

4.4.1 Common-Mode and Differential-Mode Impedance Comparison

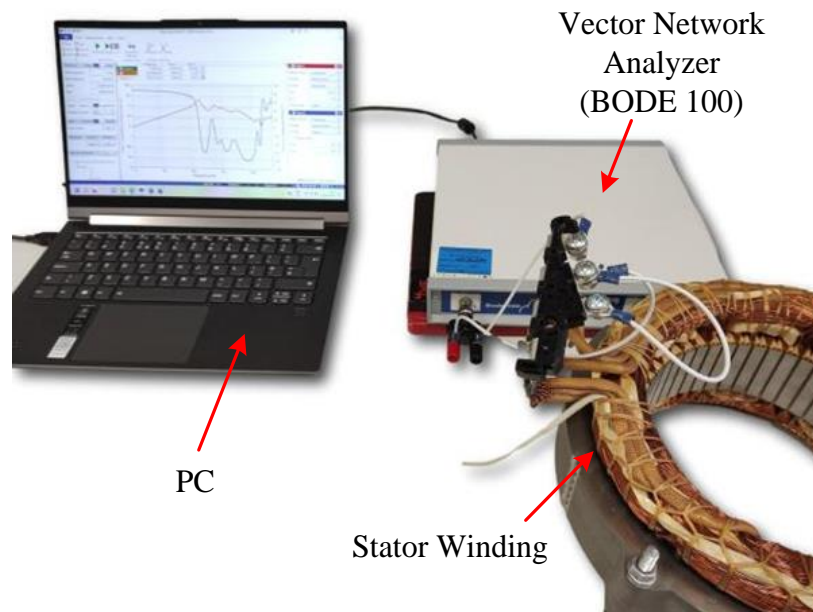


Figure 4.13: Experimental rig used for measuring the CM and DM impedance of the stator winding

For the model validation in the frequency domain, the CM and DM impedance of the model is compared with the experimental measurement. The impedance is measured experimentally using an OMICRON Lab manufactured Bode 100 impedance analyser over a frequency range of 1kHz to 50MHz. Figure 4.13, illustrates the experimental rig used for the impedance measurement, wherein, the machine winding is connected to the impedance analyser which is connected to the PC for data acquisition and post-processing. The schematic of impedance measurement is illustrated in Figure 4.14. For comparison, the impedance of the model is predicted in the MATLAB[®]/Simscape environment. The prediction is made in the same frequency range as the measurement. Similar to the experimental measurement, the predicted CM impedance is measured between the shorted three phase terminals and the core of the machine, whereas, the DM impedance is measured between one of the phase terminals and the shorted remaining two terminals. These predictions are made using the linear analysis of the control system toolbox of MATLAB[®].

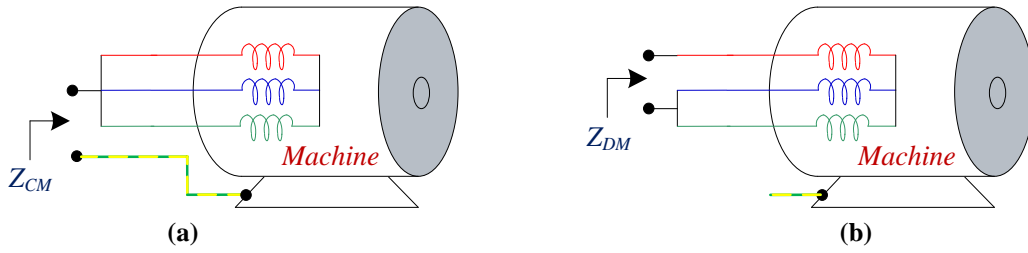


Figure 4.14: Experimental impedance measurement of the stator winding under study, (a) schematic of the CM impedance measurement, (b) schematic of the DM impedance measurement.

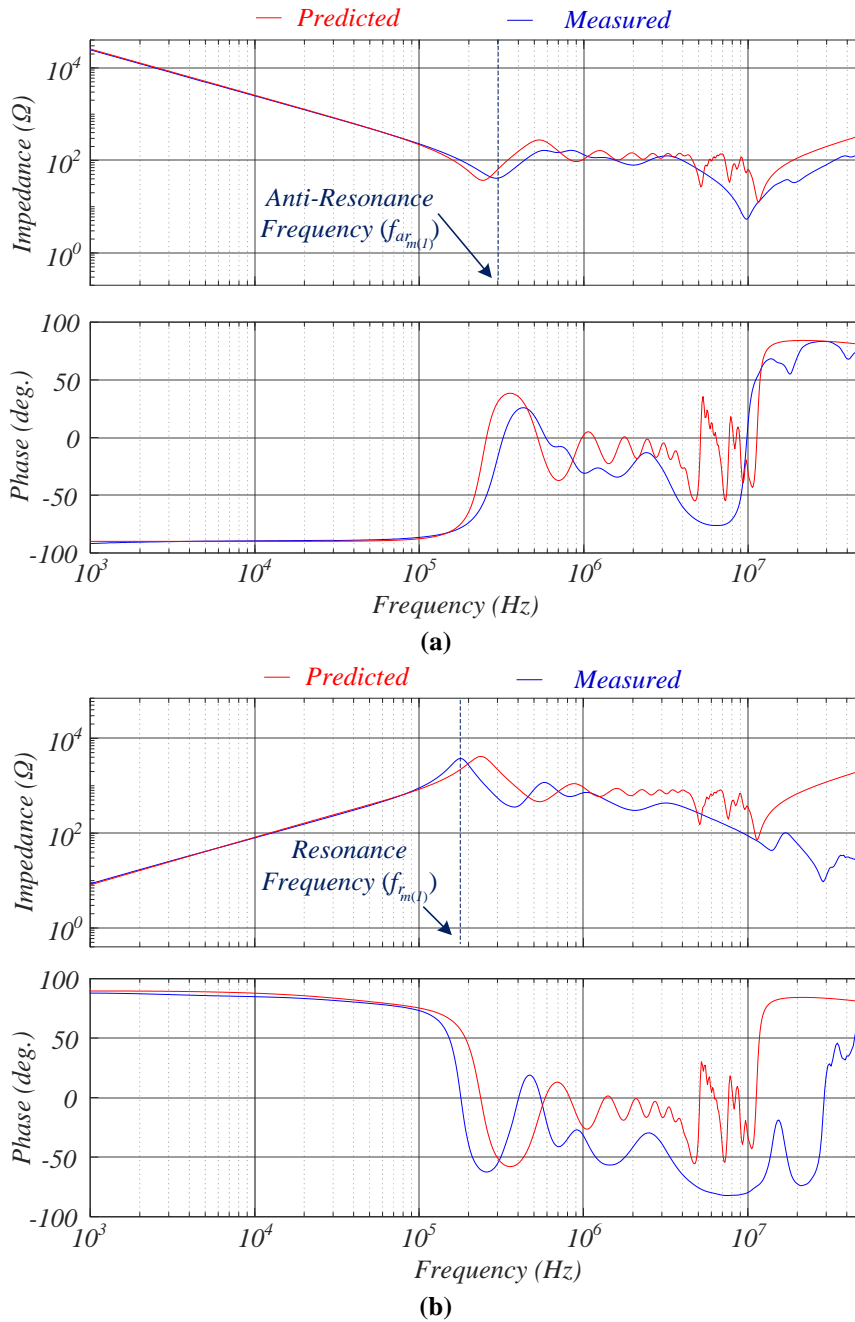


Figure 4.15: Comparison between the predicted and measured impedance (a) CM impedance, (b) DM impedance.

Figure 4.15 compares the measured and predicted CM and DM impedances of the stator winding. As is evident, the predicted impedance with mutual coupling is in close agreement with the experimental measurement. This confirms that the proposed model is a close representation of the actual stator winding. The low frequency impedance of the proposed model best fits the experimentally measured impedance. However, the drawback of the proposed model lies in its large computational time and resources.

In the CM impedance, the model exhibits anti-resonance frequency ($f_{ar_{m(1)}}$) at 227kHz compared to the measured anti-resonance at 287.32kHz. Similarly, in the DM impedance, the model exhibits resonance frequency ($f_{r_{m(1)}}$) at 234.4kHz, whereas the measured resonance frequency is 179.7kHz. Beyond the resonance and anti-resonance frequency small differences, however, exist due to several uncertainties in the modelling process. First, in a random wound machine, the exact locations of conductors are unknown, and the assumption has to be made for the conductor layout in the FE computations. This would inevitably affect the capacitive and magnetic couplings, as they are position dependent. The effects of core loss and the overhang inductance are estimated, and they may also introduce a small discrepancy.

Further, it is assumed that the hysteresis loss within the core under HF excitation is marginal, therefore, it is not represented in the model. The overhang region is represented using an inductor, which ignores its frequency dependence parameter. In addition, the mutual coupling between the coils of the same phase as well as the different phases in the overhang region is ignored. Indeed, the mutual coupling can be calculated using a 3-D model of the overhang region, which further increases the complexity. These mutual coupling, especially the capacitive coupling can be measured experimentally which requires open neutral winding. In addition, the material properties, such as permittivity and permeability, used in the FE analysis may also differ slightly from those in the machine.

In [112], a HF model ignoring the mutual coupling between the turns is proposed. To demonstrate the potential of the mutual coupling considered in the proposed model, the CM and DM impedance of an MCTL model ignoring the mutual coupling is compared with the proposed model and is illustrated in Figure 4.16. Predictably, the model [112] that ignored the mutual coupling, has low DM impedance at low frequency. Also, the model exhibits multiple resonance and anti-resonance which is not present in the experimental measurement. Principally, the impedance offered by the winding without the mutual coupling at resonance

and anti-resonance frequency is low. In essence, the model [112] has high quality factor which implies it resonates with higher amplitude and narrow bandwidth. However, in the measured impedance, the resonance characteristics at resonance and anti-resonance frequency are less prevailing.

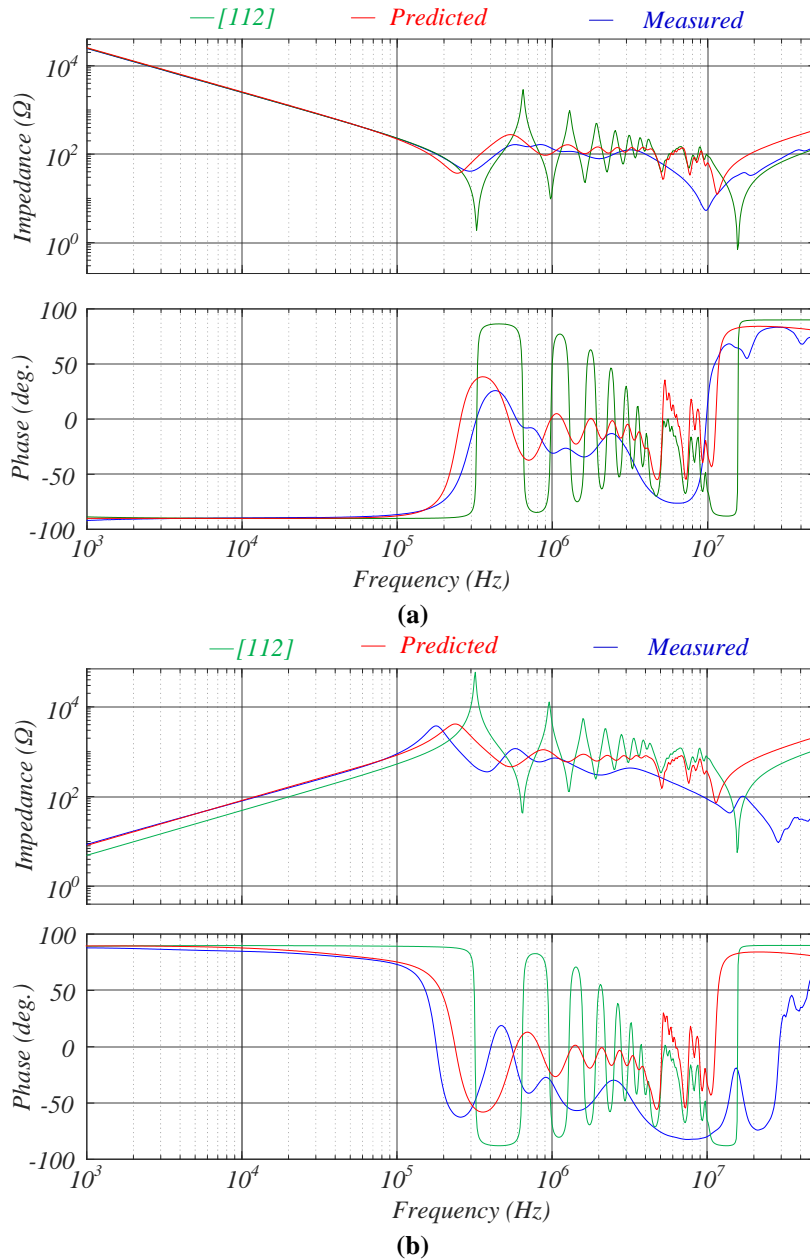


Figure 4.16: Effect of mutual coupling on the impedance (a) CM impedance, (b) DM impedance.

In [37], only the first five turns are represented as a transmission line cell and the rest are modelled as lumped parameters. The first anti-resonance frequency ($f_{ar_{m(1)}}$) in CM impedance (see Figure 4.17 (a)) and first resonance frequency ($f_{r_{m(1)}}$) in DM impedance (see Figure 4.17 (b)) are predominantly influenced by the turn self-inductance and the turn-to-core capacitance.

As only the capacitance of the first five turns is considered, the capacitive effect of the winding is not fully represented, consequently, it shifts towards a higher frequency. Also, the turn self-inductance and the resistance are independent of frequency and the parameters are calculated at 5 MHz frequency. However, due to skin and proximity effects, these parameters are a function of frequency. Therefore, the DM impedance in Figure 4.17 (b) of the model is very low as compared to the experimentally measured impedance until 2MHz.

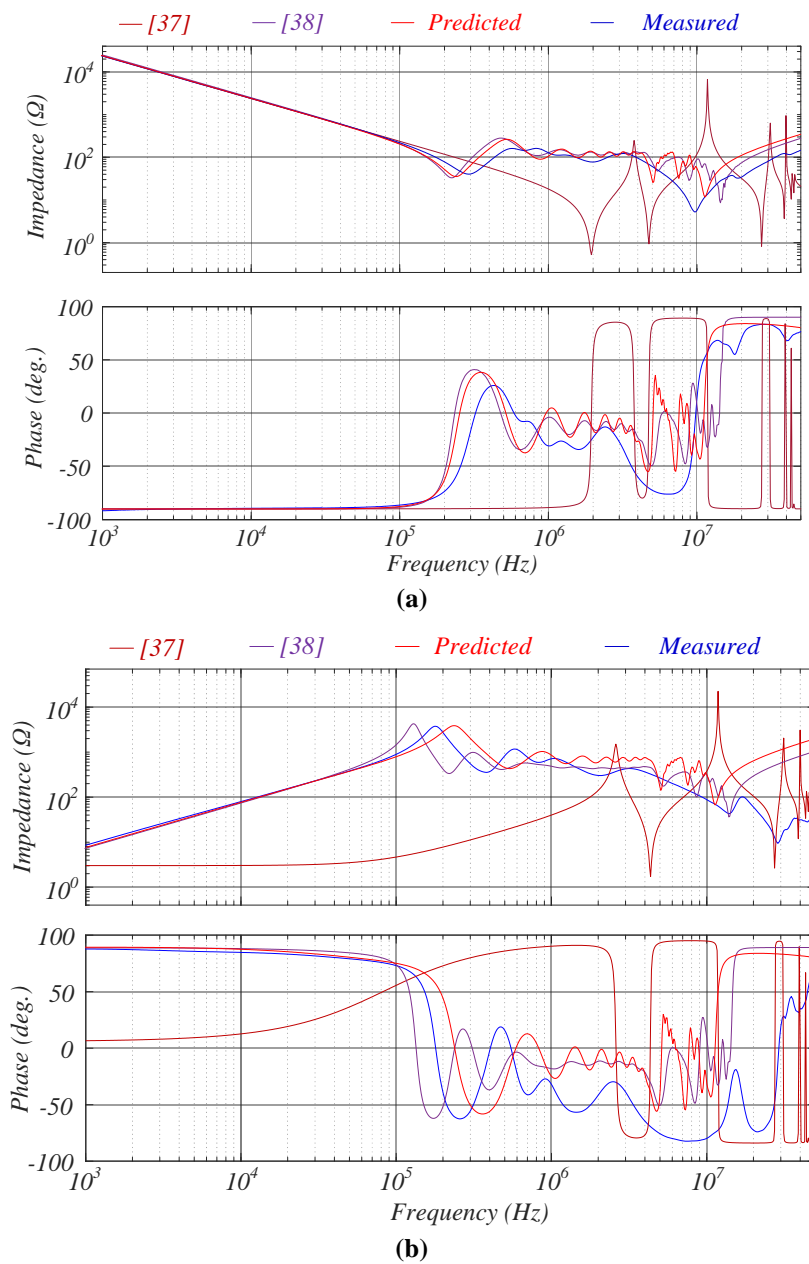


Figure 4.17: Comparison between the methods to include mutual coupling in the model, when only the first 5 turns are modelled with rest turns are represented by lumped circuit [37], and mutual-impedance is added to the self-impedance [38]. (a) CM impedance, (b) DM impedance.

In [38], the frequency dependent parameters of the turn are represented as Ladder circuits. However, the method assumes that the current through each turn of a coil is the same, which allows to include the mutual impedance of the turn into the self-impedance. Hence, the CM impedance in Figure 4.17 (a), and DM impedance in Figure 4.17 (b) are close representative of the experimentally measured impedance. However, this approach cannot be used to model the phases windings which shares the same slot, mainly in double layer winding.

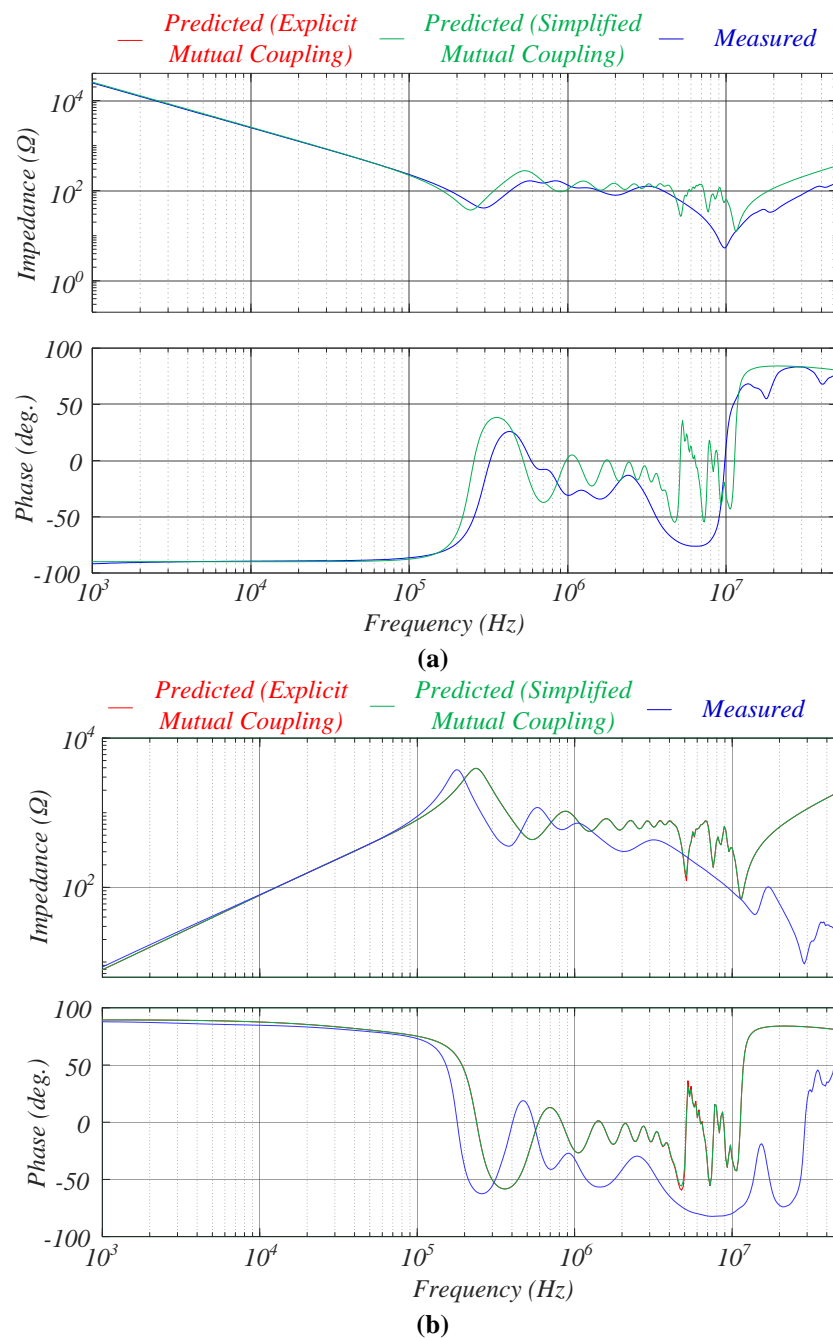


Figure 4.18: Comparison of the impedance of the model between explicit and simplified representation of the mutual coupling, (a) CM impedance, (b) DM impedance.

In Figure 4.18, the CM and DM impedance of the model with an explicit and simplified representation of the mutual coupling is compared. It is noteworthy that, both the models exhibit similar impedance with marginal differences in the DM impedance. The CM impedance of both model is the same. Henceforth, the simplified model can be used to represent the HF behaviour of the stator winding without losing accuracy.

4.4.2 Time-domain Validation

The time-domain lumped parameter model can be validated by comparing the voltage at the terminal end and at the star-neutral point of the three-phase winding with the experimental measurement under PWM voltage pulse excitation. Under the experimental condition, the PWM voltage pulse is fed through a SiC MOSFET based three-phase inverter. The SiC MOSFET is a CREE manufactured C2M0040120 with 1200V rated voltage and 60A rated drain current. During the experiment, as illustrated in Figure 4.19, the three phase wires of the cable are connected to the three-phase inverter output and the PE wire is connected to the mid-point of the DC link. The shield is connected to the enclosure of the inverter. The enclosure is further connected to the ground of the power supply. At the machine end, the three phase terminals of the cable are connected to the three phase terminals of the winding and the PE wire is connected to the core of the machine. The shield of the cable is connected to the machine enclosure. The experimental rig used for the validation is illustrated in Figure 4.20. The phase A voltage at the inverter terminal and at the machine terminal is measured using two Teledyne Lecroy manufactured 400 MHz bandwidth, 2000V, HVD3220 high voltage active differential probes and one Teledyne Lecroy manufactured 100 MHz bandwidth, 1400V, ADP305 high voltage active differential probe is used to measure the voltage at the neutral point. All the voltage measured at the inverter terminal is measured with respect to the mid-point of the DC link and the voltage measured at the machine terminal is measured with respect to the core. The measured voltage is captured using a Teledyne Lecroy manufactured 4 channel, 4GHz bandwidth WavePro404HD high-definition oscilloscope. The voltages are captured at 10GSa/s sampling frequency. Later, the MATLAB[®]/Simscape based machine model connected with the cable model developed in chapter 3, is excited using a high slew rate PWM voltage pulse and the voltage is measured in the same way as the experiment for comparison. In the MATLAB[®]/Simscape based environment the inverter model used for the excitation is assumed ideal, i.e., the PWM voltage pulse is assumed to vary linearly at the rising and the falling edge.

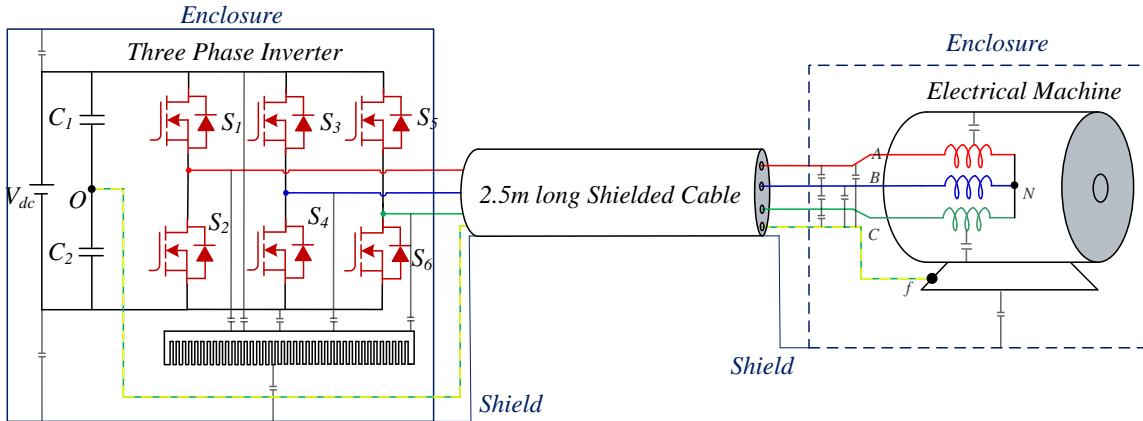


Figure 4.19: Schematic representation of the stator winding fed by a SiC MOSFET based inverter through a 2.5m long shielded cable.

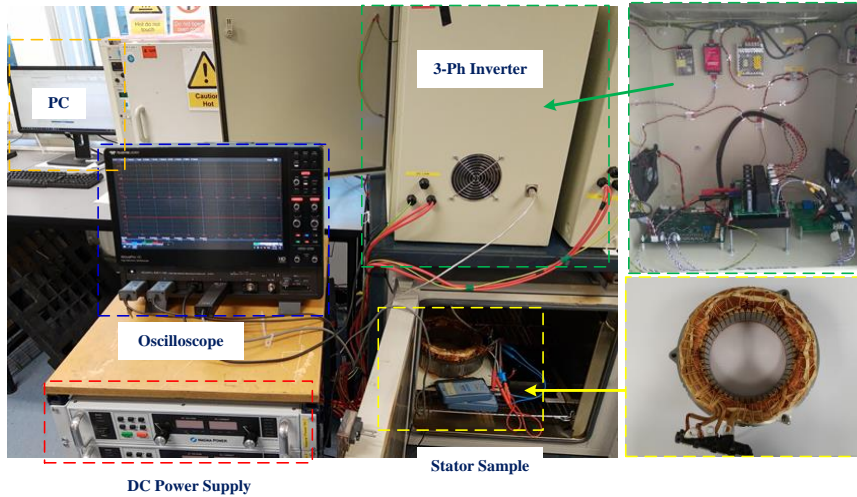


Figure 4.20: Experimental rig illustrating Toyota manufactured stator sample fed by 3-phase MOSFET based inverter through 2.5 m shielded cable.

Figure 4.21 illustrates a comparison between the predicted and the measured voltage stress. Under the experimental condition, the coils of the winding are inaccessible. The coil voltage can be measured if the winding is unwound and then rewound with the taps. In consequence, this method will no longer be indicative of the infield scenario. As a result, only the voltage at the terminal ends and at the neutral point is measured. During the experiment, the DC link voltage is 550V, the rise time is 20ns, the switching frequency is 40kHz and the modulation index is 0.1. As illustrated in Figure 4.21 (a), the voltage stress can be characterised using two modes of oscillation. The HF voltage oscillations are pronounced at the terminal end, and the LF oscillations are distinctly visible at the neutral point. The HF voltage oscillations correspond to the 2nd anti-resonance frequency ($f_{ar_{(c+m)(2)}}$) of the combined cable and the machine winding whereas, the LF voltage oscillations correspond to the 1st anti-resonance frequency ($f_{ar_{m(1)}}$) of

the stator winding. Also, the peak voltage stress occurs at the neutral point of the winding, instead of the line end coil.

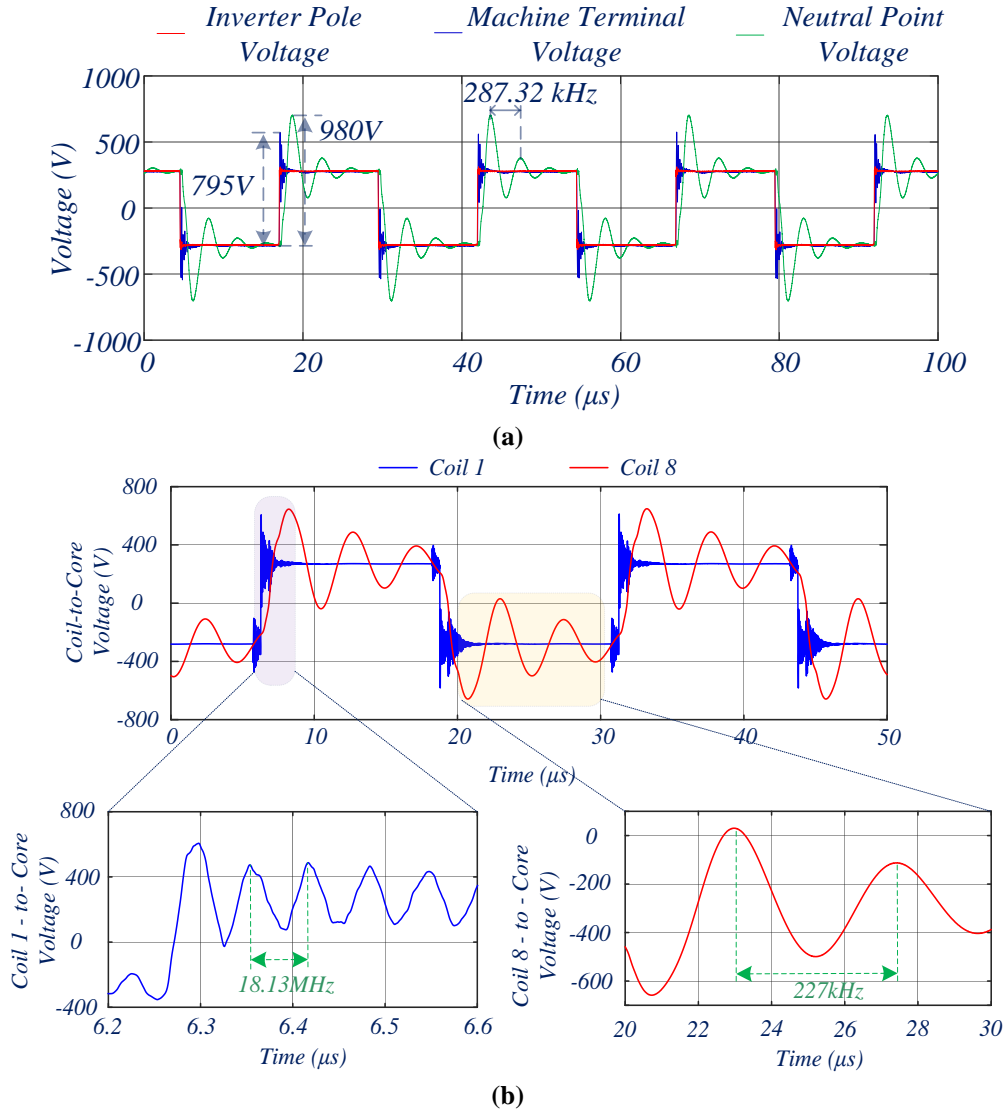


Figure 4.21: Coil-to-core voltage under PWM voltage excitation, 500V DC link voltage, 20ns rise time and 40kHz switching frequency (a) Measured, (b) Predicted.

Figure 4.21 (b) shows the predicted machine terminal voltage and the neutral point voltage under inverter operation at 0.1 modulation index, 550V DC link voltage, 20ns rise time and 40kHz switching frequency. Similar to the measurement, the voltage at the machine terminal oscillates at the 2nd anti-resonance frequency ($f_{ar_{(c+m)(2)}}$) of the combined cable and the machine winding. In addition, the neutral point voltages oscillate at 227kHz, which is the first anti-resonance frequency ($f_{ar_{m(1)}}$) of the stator winding in the CM impedance. Further, in contrast to the literature [90-112] [37-39], the peak voltage stress when the modulation index

is low occurs across the coil close to the neutral point. Therefore, special attention is required for light load operation while designing the insulation of the coil close to the neutral point.

Although the measured and the predicted voltage stress oscillates at their corresponding anti-resonance frequency, the oscillation frequencies are different. This is due to differences in the anti-resonance frequency. By way of example, the measured neutral point voltage stress oscillates at 287.32kHz, whereas, the predicted voltage stress oscillates at 227kHz. This occurs as a result of differences in 1st anti-resonance frequency as is illustrated in Figure 4.15 (a). Albeit the peak voltage stress at the neutral point is comparable, the oscillations damp quickly in the measured voltage stress, in the wake of increased damping at the anti-resonance frequency.

The predicted voltage stress and the oscillation frequency are consistent with the measured one. Therefore, the proposed lumped parameter behavioural model of the stator winding is representative of the experimental condition. As a result, the model can be used to predict the voltage distribution within the machine winding.

Generally, the peak voltage stress depends on the DC link voltage, the slew rate of the voltage pulse, dwell time between the switching of the phases, cable length and its material properties. The physical cause of these factors, especially the dwell time between the switching of the phases is comprehensively studied in chapter 5. Furthermore, the consequences and the remedies to the voltage stress is discussed in chapter 6.

4.5 Summary

This chapter proposes an MCTL model for studying the HF behaviour of the machine windings under PWM excitation. The proposed model can be used in the design stage without its physical availability as it is based on the machine geometry and the material properties. For representing the TEM wave propagation, a continuum of lumped- Γ circuit is used which represents a section of the winding whose length is less than the shortest wavelength of the TEM wave. Thereby, each turn is represented as lumped- Γ circuit. The parameters of the lumped- Γ circuit represent the physical parameters of the turns such as capacitive coupling between the turns, capacitive coupling between the turn and core, resistance and inductance of the turn, and the mutual resistive and inductive coupling between the turns.

Notably, the resistive and inductive parameters of the circuit are frequency dependent. These parameters are incorporated in the time-domain solution without using modal transformation, convolution, or Fourier transform in a simple and lucid, yet representative way using the Ladder circuit. The Ladder circuits approximate the frequency responses of the impedance using frequency independent parameters, allowing time-domain modelling.

The major contribution of the proposed model lies in the modelling of the mutual resistive and inductive coupling between the turns. The proposed model includes the mutual coupling between the turns within the slot using a current-controlled voltage source in the time-domain. In the example considered, mutual coupling exists in the conductors of the same phase. However, the concept can also be extended to account for the mutual coupling of a double layer winding where the conductors in a slot carry currents in two different phases.

The model is validated by comparing the CM and DM impedances of the model against the measurement. The results illustrate the conformity between the two. Further, the model is validated in time-domain by comparing the voltage stress at the machine terminal and at the neutral point. The comparison illustrates that the key characteristics in predicted and measured voltage stress are the same. Thus, the proposed model is representative of the actual machine. In both cases, the voltage stress is characterised by two oscillations; one corresponds to the 2nd anti-resonance frequency ($f_{ar_{(c+m)(2)}}$) of the combined cable and the machine winding occurring at the machine terminal, whereas the other corresponds to the 1st anti-resonance frequency ($f_{ar_{m(1)}}$) of the machine winding occurring at the star neutral point. Several key findings can be derived using the HF behavioural model of the cable and the machine windings. The model can be used to establish voltage distribution within the machine winding, which is difficult to measure as only the terminal ends and the neutral point is accessible. In addition, the model can be used to study the detrimental effect of the high slew rate PWM voltage pulse, thereby helping in developing mitigation strategies. In chapter 5, the key locations within the winding under maximum voltage stress are identified and the mitigation measures are proposed in chapter 6.

There are, however, small differences exist between the measured and the predicted results. The differences occur as a result of the assumptions made while developing a simple, lucid, yet representative model. The location of the turns is assumed distributed uniformly, as cut-open machine is required to deduce the exact location of the turns. Further, the hysteresis loss

in the core is represented as a resistive element across the turn model. To reproduce the lamination effect, the conductivity of the core is assumed zero. However, a lossy resistive element representing the eddy current loss in the core is connected across each turn model. Later, a lumped inductor is used as a representation of the overhang inductance.

The accuracy of the model can be increased further by replacing the assumptions with accurate representations. Although determining the exact location of the turns in a random wound machine is impractical, it is possible in the form wound machine. The hysteresis loss in the core can be accounted for by assuming non-linear complex permeability of the core which may be available from the manufacturers. The laminate effects of the core can be realised using a three-dimensional slot model, where the core is defined as a stack of insulated electrical steel. Herein, the conductivity of the core must be defined to reproduce the induced eddy currents. Additionally, using the three-dimensional slot model, the frequency dependent overhang inductance of winding can be determined. However, extending the analysis to three-dimensional model will increase the computational time and resources. These computational challenges can be overcome by using the homogenised material property of the winding. These methods are comprehensively discussed in Chapter 7 and can be followed for future work.

Chapter 5: Voltage Distribution under PWM Voltage Excitation

5.1 General

Prediction of the voltage distribution within the stator winding due to pulse-width modulated voltage impinging at the machine terminals is prevalent in literature. For this purpose, the state-of-art work employs a HF model to understand the voltage distribution. Majorly, the studies illustrate that the voltage distributes non-uniformly within the winding, with peak voltage stress occurring across the terminal end coil. It has been found that the interturn voltage within the terminal end coil is non-uniformly distributed and the magnitude depends on the slew rate of the voltage pulse impinging the machine terminal, DC bus voltage, and the cable parameters. It is believed that the genesis of the non-uniform voltage distribution lies in the capacitive coupling between the turns themselves and the core. Henceforth, many literatures focused on the first five turns of the winding, wherein, the first five turns are represented using a multi-conductor transmission line model and the remaining are represented as a lumped parameter.

However, herein, it was found that a new oscillatory mode exists in voltage measured across the neutral point and the core of the machine. This oscillatory mode causes overvoltage at the neutral end rather than the terminal end, as previously stated. The voltage stress, indeed, at the terminal end exists whose oscillatory frequency is much higher than the neutral point voltage oscillations.

This chapter provides a thorough examination of the voltage distribution with the winding, which will aid in determining the possible location of voltage stress and comprehending the origin of voltage oscillations at the neutral point. This will help in the development of voltage stress mitigation strategies to minimise premature failure and unexpected downtime.

5.2 Anti-Resonance Phenomenon

Understanding the voltage stress at the machine terminal requires a comprehensive understanding of voltage wave propagation through the cable, which connects the VSI to the

machine. A MATLAB[®]/Simscape based model of a 2.5m long shielded cable, developed in Chapter 4 is illustrated in Figure 5.1, which is fed through a VSI. The VSI is assumed ideal, which implies that the output voltage pulse rises from 0 to V_{DC} linearly with rise time t_r . The PWM voltage pulses travelling through the cable behaves similar to the TEM waves travelling through the transmission lines. Due to wave propagation through the cable and reflection at the machine terminals, the terminal voltage oscillates, whose frequency of oscillation (f_{ar_c}) depends on the propagation delay (t_p) as [116], when the cable loss is neglected,

$$f_{ar_c} = \frac{1}{4t_p} = \frac{1}{4l_c\sqrt{L_cC_c}} \quad (5.1)$$

where L_c and C_c are the per unit length inductance and the capacitance of the cable respectively, and the propagation delay is the propagation time of the voltage wave through the cable, which is expressed as [116],

$$t_p = \frac{l_c}{g_c} \quad (5.2)$$

where, l_c is the length of the cable and g_c is the velocity of the wave propagation through the cable which depends on cable parameters as [116],

$$g_c = \frac{1}{\sqrt{L_cC_c}} \quad (5.3)$$

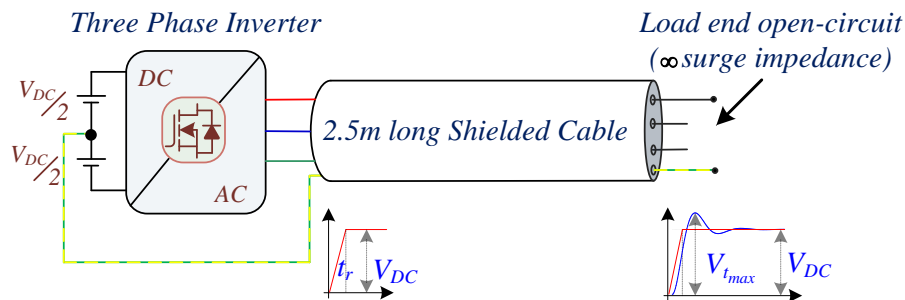


Figure 5.1: An open ended uncharged 2.5m long cable excited through a three phase VSI.

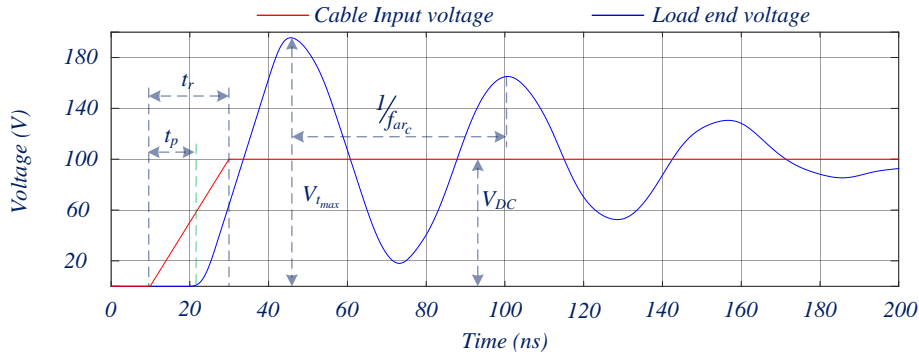


Figure 5.2: Voltage stress at the open end of the cable under single pulse excitation.

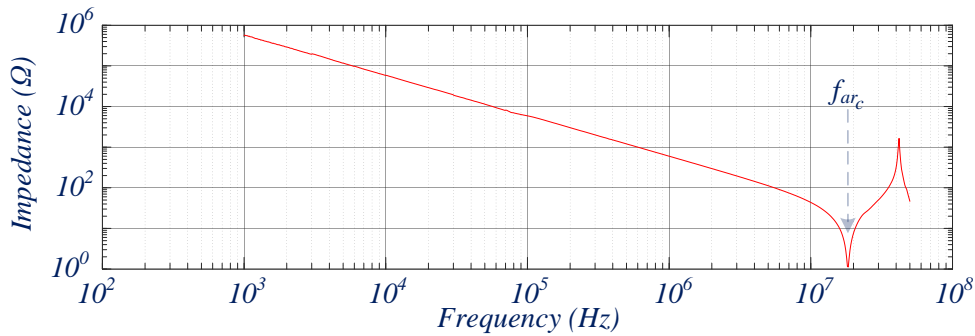


Figure 5.3: CM Impedance of a 2.5m long shielded cable.

As an example, Figure 5.2 illustrates the voltage oscillations measured at the open load end shown in Figure 5.1, when a voltage pulse of magnitude 100V and rise time 20ns impinges the cable input terminals. As elucidated, the load end voltage oscillates at 17.85MHz and the propagation delay measured at the load end is 14ns, which conform to (5.1). Notably, the amplitude of the CM impedance of the cable, illustrated in Figure 5.3, is at a pronounced minima at the frequency, which corresponds to the frequency of oscillation of the load end voltage. This frequency is called anti-resonance frequency ($f_{ar(1)}$) as the impedance reaches a minimum value and the phenomenon is termed as anti-resonance phenomenon.

5.3 Voltage Stress at the Stator Terminal

Similar to the open ended cable as illustrated in the previous section, in a cable connected electrical machine, when a voltage pulse of rise time t_r and magnitude V_{DC} propagates through it, the voltage at the machine terminal is a damped voltage oscillation. This happens as a result of the wave propagation phenomena [116]. The peak of the voltage oscillations (V_{max}) depends on the propagation delay (t_p), rise time (t_r), length of the cable (l_{cable}), and the velocity (v_c) of wave propagation within the cable which is expressed as [116],

$$\frac{V_{t_{\max}}}{V_{DC}} = 1 + \frac{2t_p \times \Gamma}{t_r} = 1 + \frac{2l \times \Gamma}{g \times t_r} \quad \text{for } 2t_p < t_r \quad (5.4a)$$

$$\frac{V_{t_{\max}}}{V_{DC}} = 1 + \Gamma \quad \text{for } 2t_p \geq t_r \quad (5.4b)$$

where, Γ is the reflection coefficient, which depends on the surge impedance of the machine (Z_{0m}) and the cable (Z_{0c}) as [116],

$$\Gamma = \frac{Z_{0m} - Z_{0c}}{Z_{0m} + Z_{0c}} \quad (5.5)$$

The surge impedance of a cable or machine is the ratio of the voltage and the current of a single wave propagating through it. The surge impedance of a lossless medium herein is cable or machine, is expressed mathematically as [116],

$$Z_0 = \sqrt{\frac{l}{c}} \quad (5.6)$$

where, l and c are the per unit length inductance and capacitance of the medium respectively. Thus, the peak voltage stress at the machine terminal depends on the medium parameters and is determined using (5.4-5.6). The length of the cable for which the rise time of the voltage pulse is equal to twice the wave propagation time within the cable is termed as critical cable length ($l_{cable_{cr}}$). Notably, if $l_{cable} > l_{cable_{cr}}$, i.e., $2t_p > t_r$ only the reflection coefficient influences the voltage stress, which is independent of the rise time. In this context, if the surge impedance of the machine is very high i.e., $Z_{0m} \rightarrow \infty$, the reflection coefficient will be 1, in other terms, the voltage stress at the machine terminals will be 2pu. However, if the surge impedance of the machine and the cable are equal, the reflection coefficient will be 0, and no voltage overshoot will be observed at the machine terminals. In such instances, no reflection occurs at the machine terminals.

5.3.1 Condition for Minimum Terminal Voltage Stress

Until now, the voltage stress at the terminal end caused by the single voltage excitation travelling through an uncharged lossless cable has been discussed. However, the cable conductors and the dielectric material separating them incur losses. Due to the losses of the

cable, the voltage stress at the load end of the cable is less than the calculation using (5.4). By way of example, Figure 5.4 shows the voltage stress measured at the open load end using the MATLAB®/Simscape based model as illustrated in Figure 5.1, when a voltage pulse with rise time varying from 20ns to 150ns impinges the cable input terminals. The critical cable length for each rise time is marked in the figure. Evidently, the cable length required to reach 2pu overshoot factor (OF) is larger than the critical cable length due to losses within the cable. The critical cable length is short with a short rise time, therefore the OF reaches 2pu even with a short cable length, as elucidated in Figure 5.4. Illustratively, the corresponding critical cable length for a voltage pulse of rise time 20ns is 1.76m, whereas, for 40ns rise time it is 3.53m. However, due to cable losses, the OF reaches 2pu for a 2.5m long cable instead of 1.76m and 5m instead of 3.53m.

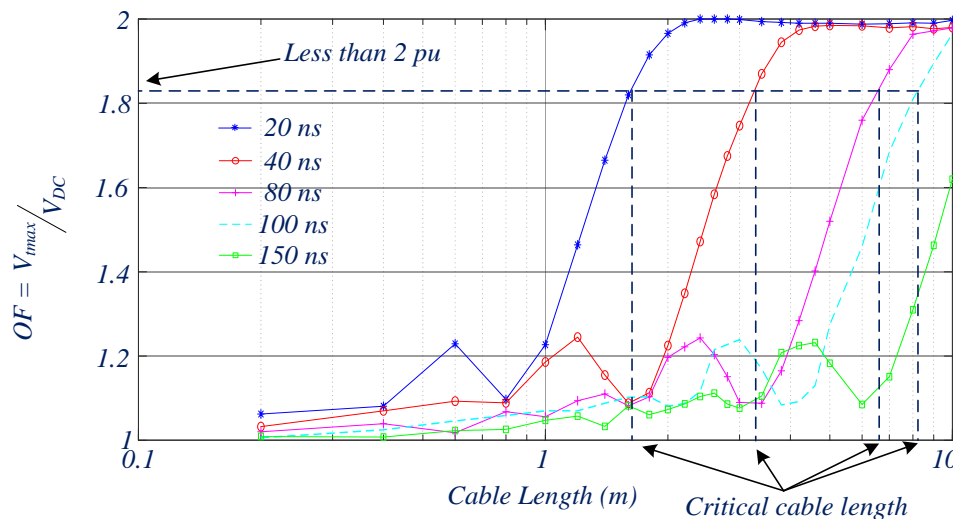


Figure 5.4: Variation of OF w.r.t. cable length for an uncharged cable under single pulse voltage excitation.

Above all, the OF resembles local minima and maxima under different cable lengths. As an example, with 20ns rise time, one local maxima occurs when the cable length is 0.6m and two local minima occur at 0.4m and 0.8m long cable. Similarly, multiple local minima and maxima occur at different rise times. For minimum voltage overshoot, the conditions at which the local minima occur is important. Since these minima occur numerous times with varying cable lengths for a given rise time, it's difficult to comprehend intuitively. However, if the OF is depicted with respect to the ratio of cable length and the critical cable length, as shown in Figure 5.5, a general correlation between these minima and maxima and the rise time can be discerned. Instinctively, all the maxima and minima align together and manifest a

comprehensible relation for maximum and minimum OF. As elucidated, the minimum voltage stress occurs if,

$$t_r = 4kt_p = 4k \frac{l_c}{g_c} = 4kl_c \sqrt{l_c c_c} \quad \forall k = 1, 2, 3, \dots \quad (5.7)$$

where, l_{cable} is the length of cable, l_c and c_c are the per-unit length inductance and capacitance of the cable. Generally, the high voltage stress is avoidable with the long rise time and short cable length. However, upon following the condition in (5.7), the voltage stress can be reduced even with a short rise time and long cable length. As an illustration, the OF measured at the load end is 1.23 if the cable with a propagation delay of 14.16ns is excited by a voltage pulse of rise time 85ns, whereas the OF decreases to 1.1pu if the rise time of the pulse is reduced to 56.67ns. As a result of the slew rate profiling, the voltage stress can be reduced to a minimum.

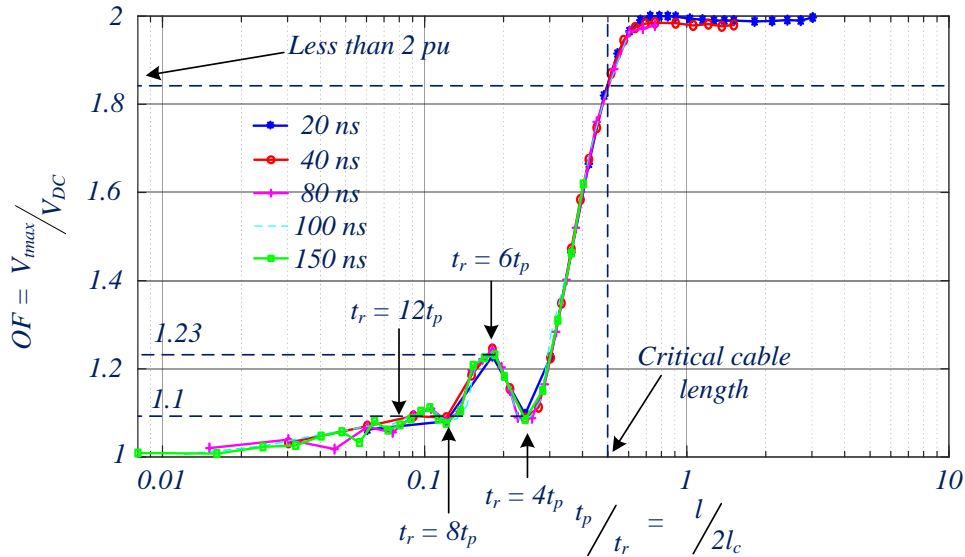


Figure 5.5: Variation of OF w.r.t. ratio of cable length and critical cable length for an uncharged cable under single pulse voltage excitation.

Figure 5.5 also helps in the selection of cable length for the given overshoot limit and the rise time of the voltage pulse. By way of example, if the maximum voltage overshoot allowed is 20%, then

$$\frac{t_p}{t_r} \leq 0.3 \quad (5.8)$$

As a result, if the voltage pulse rise time is 20ns, the maximum permissible propagation delay is 6ns. Because the propagation delay for the 2.5m long cable under study is 14.16ns, the cable length should be less than 1.06m. The IEC standard 60034-25:2014 [15] recommends that the

cable length between the VSI and the machine should be minimum and to avoid the pulse doubling effect, it should be less than the critical cable length. As stated earlier, with cable length equal to critical cable length, the ratio of propagation delay and the rise time is equal to 0.5. In any instance, if the cable length is selected using (5.8), the IEC standard recommendations are followed. As a result, representing the voltage overshoot factor in terms of the ratios of propagation delay and rise time, instead of cable length, is more consistent in determining the ideal cable length for reduced voltage overshoot for a given rise time. This depiction is one of the major contribution of this study.

There are uncertainties involved in the slew rate profiling using (5.7) and the selection of the cable length using (5.8). At first, the cable parameters such as resistance, inductance and capacitance are temperature dependent. However, the variation is more pronounced in the medium-voltage (MV) drives wherein XLPE (Cross-Linked Polyethylene) and PILC (Paper Insulated Lead Covered) cables are used [150]. Therefore, in the MV drive, the propagation delay is temperature dependent and it decreases with the temperature rise [150]. Furthermore, the rise time of the voltage pulse varies with the load current depending upon the parasitic capacitance of the VSI. The positive phase current elongates the fall time, whereas, the negative phase current elongates the rise time [151]. By way of example, [151] illustrates that the phase current and the parasitic capacitance can double the rise time of the voltage pulse. Consequently, the selection of the optimal slew rate and the cable length for minimum voltage overshoot will vary with the temperature. Assuming the uncertainty in the parameters due to the temperature, if the system is designed using (5.7-5.8) at the ambient temperature, the temperature rise will further reduce the voltage overshoot.

5.3.2 Surge Impedance Calculation

In the previous section, voltage stress at the open load end is discussed, wherein, it is independent of the surge impedance as the reflection coefficient is unity and largely depends on the ratio of propagation delay and the rise time. However, when the electrical machine is connected to the cable at the load end, the voltage overshoot is scaled by a factor of the reflection coefficient. As a result, surge impedance becomes an influential parameter in determining the voltage stress.

Estimation of the terminal voltage stress requires surge impedance and hence the medium parameters. The medium parameters depend on its physical dimensions and its material

properties, which are strenuous to calculate. One should have this information with high accuracy to calculate the surge impedance. There are several other methods to calculate the surge impedance. In one of the traditional methods [152], the surge impedance of the cable is measured by exciting it with a single pulse voltage and a purely resistive load is varied until the reflection coefficient at the load end becomes unity. When the reflection coefficient at the load end is unity, the load impedance is equal to the cable surge impedance. This method is empirical and laborious as it involves a repeated change in the load resistance. In addition, the cable must be excited to determine the surge impedance. Besides all, this method is inapplicable to the machine as its windings are either star or delta connected, making the ends inaccessible.

A simple, yet accurate method of determining the surge impedance is using the CM impedance. The CM impedance inherently has the information of the anti-resonance frequency and the capacitance per unit length of the medium, which can be used for surge impedance calculation. Using (5.2-5.3) and (5.6), the surge impedance (Z_0) of the medium is determined as,

$$Z_0 = \frac{t_p}{l_{medium} c} \quad (5.9)$$

where, t_p is the propagation delay, l_{medium} is the length of the medium and c is the per unit length capacitance. By replacing t_p in (5.9) using (5.1), the surge impedance of the medium is,

$$Z_0 = \frac{1}{4 f_{ar} l_{medium} c} \quad (5.10)$$

where, f_{ar} is the anti-resonance frequency of the medium. The product of l_{medium} and c in (5.10) is the total capacitance of the medium, which is the CM capacitance (C_{CM}), measured at low frequency.

By way of example, Figure 5.6 (a) shows the schematic of the CM impedance measurement of the MATLAB®/Simscape based HF shielded cable model developed in chapter 4, wherein, the three phase wires are shorted together at both ends and the impedance is measured between the shorted phases and the fourth wire. During measurements, the shield is floating at both ends. The impedance is measured in the frequency range between 1kHz and 50MHz. The measured impedance is illustrated in Figure 5.6 (b). From the CM impedance, the capacitance

at 10kHz ($C_{@10kHz}$) is 241.11pF and its first anti-resonance frequency ($f_{ar_{c(1)}}$) is 17.71MHz. Thus, the surge impedance of the cable (Z_{0c}) can be deduced as,

$$Z_{0c} = \frac{1}{4 \times 17.71 \times 10^6 \times 241.11 \times 10^{-12}} = 58.54 \Omega \quad (5.11)$$

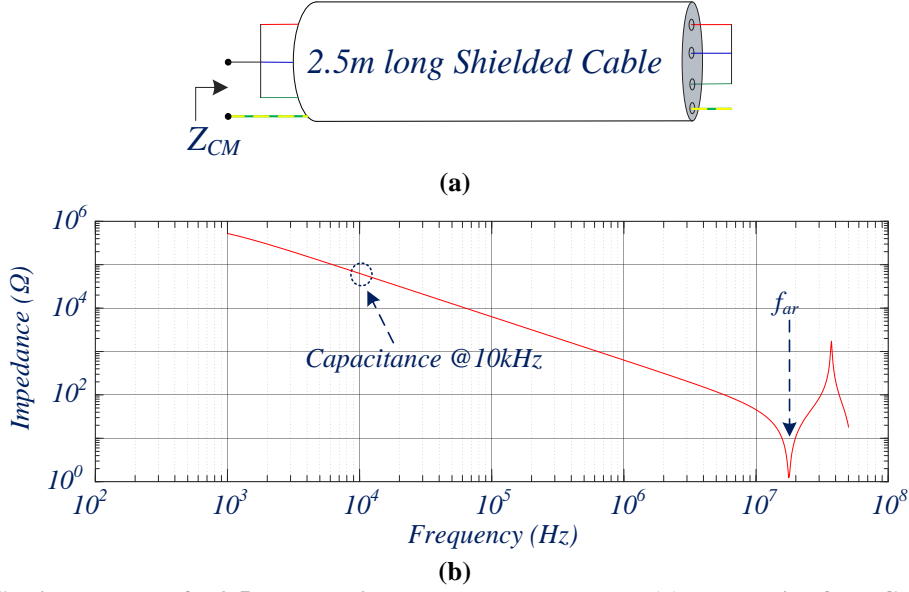


Figure 5.6: CM impedance of a 2.5m long shielded cable under study, (a) schematic of the CM impedance measurement, (b) the measured CM impedance.

Similarly, Figure 5.7 (a) shows the schematic of the CM impedance measurement of the MATLAB[®]/Simscape based HF stator winding model developed in chapter 3, wherein, the three phase terminals are shorted together and the impedance is measured between the shorted phase terminal and the core of the machine. The impedance is measured in the frequency range between 1kHz and 100MHz. The measured CM impedance of the stator winding is illustrated in Figure 5.7 (b). Using the CM impedance, the capacitance at 10kHz ($C_{@10kHz}$) is 5.32nF and its anti-resonance frequency (f_{ar_m}) is 226.84kHz. Thus, the surge impedance of the cable (Z_{0m}) can be calculated as,

$$Z_{0m} = \frac{1}{4 \times 226.84 \times 10^3 \times 5.32 \times 10^{-9}} = 206.99 \Omega \quad (5.12)$$

Thus, the reflection coefficient at the machine terminal may be calculated from (5.5) as,

$$\Gamma = \frac{206.99 - 58.54}{206.99 + 58.54} = 0.56 \quad (5.13)$$

Using (5.1) and the first anti-resonance frequency ($f_{ar_{c(1)}}$) of the cable, the propagation delay of the cable may be deduced as,

$$t_p = \frac{1}{4f_{ar_c}} = \frac{1}{4 \times 17.71 \times 10^6} = 14.12ns \quad (5.14)$$

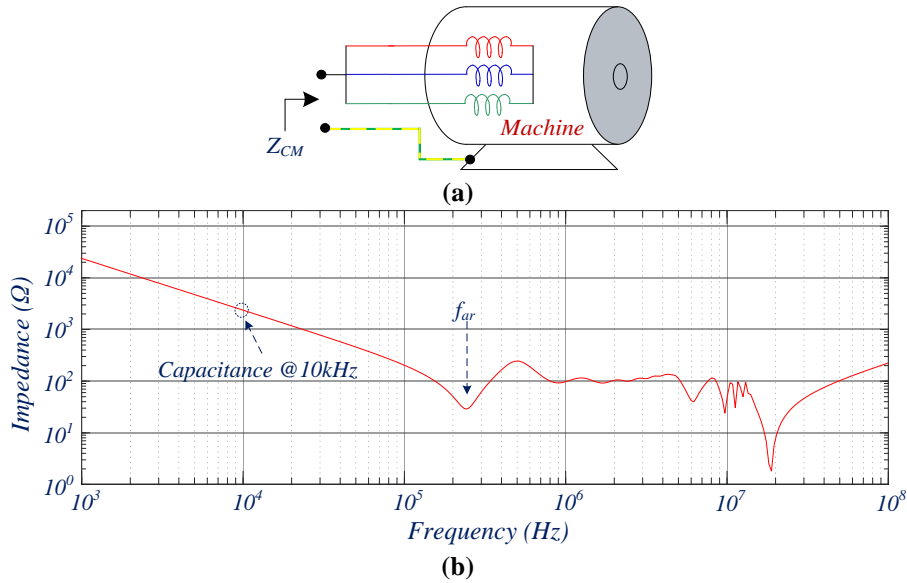


Figure 5.7: CM impedance of the stator winding under study, (a) schematic of the CM impedance measurement, (b) the measured CM impedance.

Hence, when a voltage pulse of 20ns rise time and 550V DC voltage impinges machine terminals, the voltage OF at the machine terminals is determined using (5.4) as,

$$\frac{V_{t_{max}}}{V_{DC}} = 1 + 0.56 = 1.56 \quad (5.15)$$

With 550V DC link voltage, the peak voltage stress at the terminal end may be deduced as,

$$V_{t_{max}} = 1.56V_{DC} = 873.6V \quad (5.16)$$

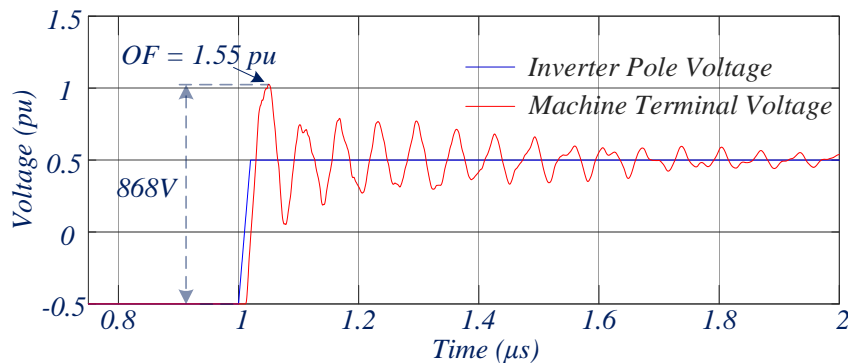


Figure 5.8: Voltage stress at the machine terminal under single voltage pulse excitation.

In Figure 5.8, the terminal voltage measured in response to a voltage pulse is illustrated, wherein, the peak voltage stress complies with the calculation in (5.16). As a result, the peak voltage stress can be determined using the CM impedance, well within the accuracy. The salient feature of this method is, it does not require any voltage excitation. This approach, unlike the previously stated empirically driven method, is based on an analytical solution.

5.3.3 Voltage Stress within Stator Winding under Single Voltage Pulse Excitation

It is well documented in the literature [14-19][37-39][153] that when a single voltage pulse impinges the machine terminal, the voltage distributes non-uniformly, with peak voltage stress across the first few turns of the winding. In the same vein, as illustrated in Figure 5.9, the MATLAB®/Simscape based cable connected machine model is excited with a voltage pulse at phase A terminal with respect to the other two phases, wherein, the coil-to-core voltages are shown in Figure 5.10. The rise time of the voltage pulse is 20ns and the DC link voltage is 550V. The machine has 8 coils per phase (N_c). As shown, the voltages distribute non-uniformly with peak voltage stress at the first coil. The voltage soared to 974V, which is 73.93% higher than the DC link voltage. The coil-to-core voltage of the 1st coil exhibits both high frequency and low frequency modes of oscillation. As compared to HF oscillation in the first coil, other coils oscillate primarily at low frequency with a minimum peak voltage stress across the last coil close to the neutral point. Akin to the cable, the propagation delay is a function of the length of the winding and the wave velocity travelling within it and is a quarter of the time period of the wave oscillation.

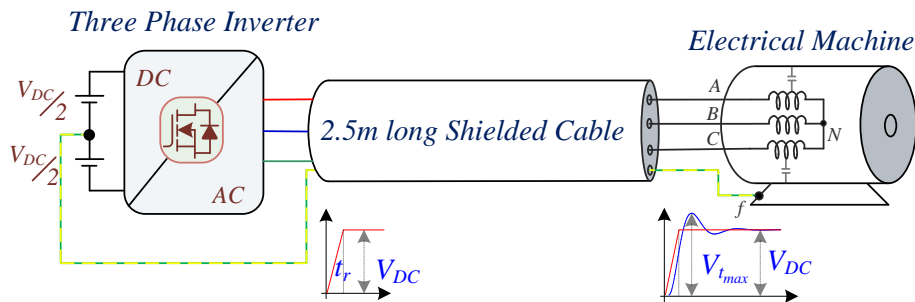


Figure 5.9: Electrical machine under excitation using a three phase VSI through a 2.5 long cable.

The CM impedances of the cable and the stator winding are illustrated in Figure 5.11. It is worth noting that they are of similar characteristics. Both depict anti-resonance behaviour. The stator winding shows the first anti-resonance ($f_{ar_{m(1)}}$) at a relatively low frequency of 227kHz as compared to the second one at 25MHz, whereas, the cable shows multiple anti-resonance

starting from 18.13MHz. Notably, the combined cable and stator winding CM impedance shows two anti-resonances, one aligns with the 1st anti-resonance of the stator winding and the other exists close to the anti-resonance of the cable.

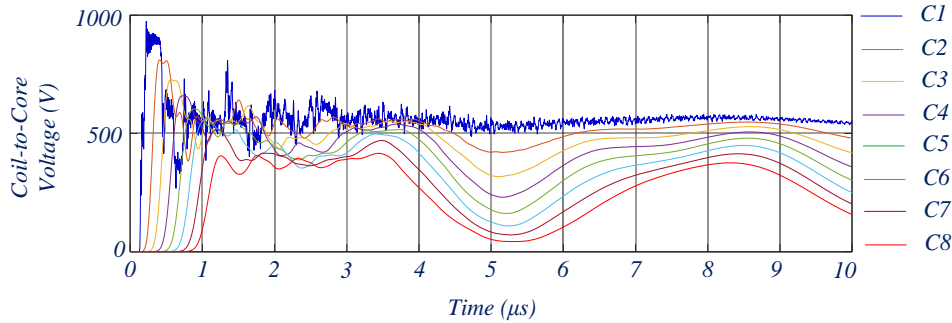


Figure 5.10: Coil-to-core voltage representing voltage distribution within winding under single voltage pulse excitation.

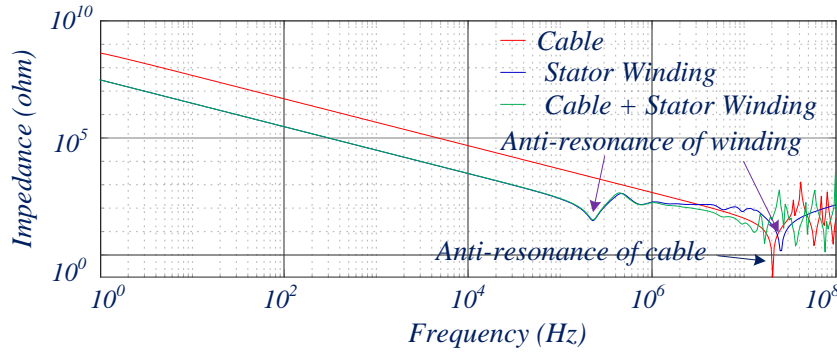


Figure 5.11: Measure CM impedance of the cable, stator winding and the cable connected stator winding.

Due to the high permeability of the core, the per-unit length inductance of machine winding will be lower than that of the cable. Hence, the wave propagation velocity in the machine winding will be lower. Combined with a long winding length the 1st anti-resonance occurs in the winding at a much lower frequency ($f_{ar_{(c+m)(1)}}$). Thereby, the frequency of voltage oscillation within the winding is low as compared to that of the cable. Therefore, hereinafter, the voltage oscillations at the second anti-resonance frequency ($f_{ar_{(c+m)(2)}}$) of the combined cable and stator winding impedance are termed as HF oscillation and the voltage oscillations at the first anti-resonance frequency ($f_{ar_{m(1)}}$) of the stator winding are termed as LF oscillation. It should be noted that in the drive system under study, the cable is relatively short. Therefore the 1st anti-resonant frequency ($f_{ar_{(c+m)(1)}}$) of the cable-machine winding essentially coincides with the 1st anti-resonant frequency ($f_{ar_{m(1)}}$) of the machine winding. Under voltage pulse excitation, the cable and the stator winding offer minimum impedance at their respective anti-resonance frequency, thereby, enduring voltage oscillations. Thus, the voltage wave travelling

through the cable oscillates at the 2nd anti-resonant frequency ($f_{ar_{(c+m)(2)}}$) of the cable-machine winding. Upon reaching the machine terminal, these waves encounter higher inductance due to the high permeability of the core, which restricts their penetration deep into the winding. However, it offers lower impedance to the LF components, thereby; the voltage wave oscillates at LF within it.

5.4 Voltage Stress Distribution within Winding

So far, the voltage stress at the machine terminal due to single voltage pulse excitation travelling through an uncharged cable or cable-winding is discussed, wherein one of the phases is excited by a voltage pulse with respect to the other two phases. Consequently, the voltage stress occurring at the terminal end of the exciting phase is at the maximum and it decreases within the winding. However, this occurs when only one phase is switched. When the machine is in-service, it is fed through a 3-phase VSI wherein, all the three phases are excited simultaneously. To study the influence of the PWM voltage pulses on the voltage distribution within the winding, the MCTL model of the stator winding developed in MATLAB[®]/Simscape is fed by an ideal inverter model. Unlike single pulse voltage excitation, the switching transients emerging from voltage pulses at different phases overlap each other, thereby, the voltage stress redistributes. As is illustrated, Figure 5.12 shows the coil-to-core voltage of phase A under inverter operation at 0.1 modulation index and 40kHz switching frequency. The rise time of the voltage pulse is 20ns and the DC link voltage is 550V. One phase winding of the machine under study consists of 8 series connected coils and each coil has 11 turns. The voltages are measured between the start of the coil and the core (local ground) which are separated by the impregnated resin and the ground-wall insulation. As elucidated, the coil-to-core voltage is characterised by two oscillatory responses. The LF voltage oscillations are pronounced in the coils away from the terminal end, whereas, the HF voltage oscillations are distinctly visible in the 1st coil from the terminal end. Figure 5.13 illustrates the enlarged view of the voltage stress at the first and the last coil from the terminal end, wherein, the voltage oscillations at the 1st coil corresponds to the combined second anti-resonance frequency ($f_{ar_{(c+m)(2)}}$) of the cable and stator winding (18.13MHz) and the voltage oscillations at the last coil correspond to the first anti-resonance frequency ($f_{ar_{m(1)}}$) of the stator winding (227kHz). This occurs because; the cable and the stator winding endure voltage oscillations at their respective anti-resonance frequency. Oddly, the voltage stress at the last coil is greater than the

first coil, whereas, during the single pulse voltage excitation, the voltage across the first coil and the core were maximum. Contrary to the literature [14-19][37-39][153], the peak voltage stress occurs at the last coil, as a result of the superposition of the voltage pulse impinging the machine terminals at different phases. Therefore, special attention is required while designing the insulation of the coil close to the neutral point. The literature studies the voltage distribution within the winding under a single voltage pulse in solitary. Consequently, they concluded that the insulation close to the first coil is most stressed.

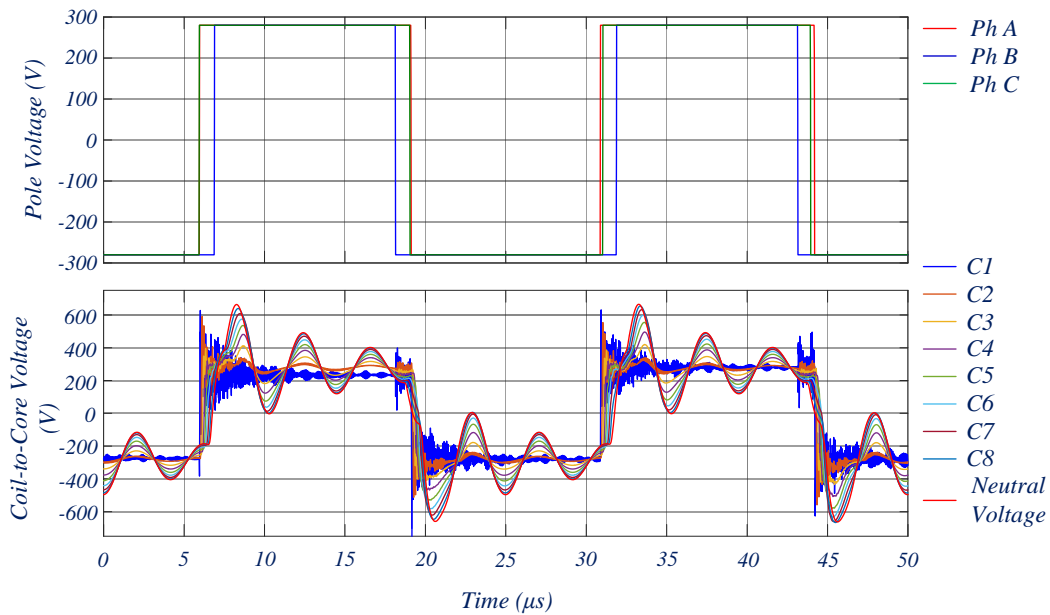


Figure 5.12: Coil-to-core voltage representing voltage distribution within winding at 550V DC link voltage under PWM voltage pulse excitation.

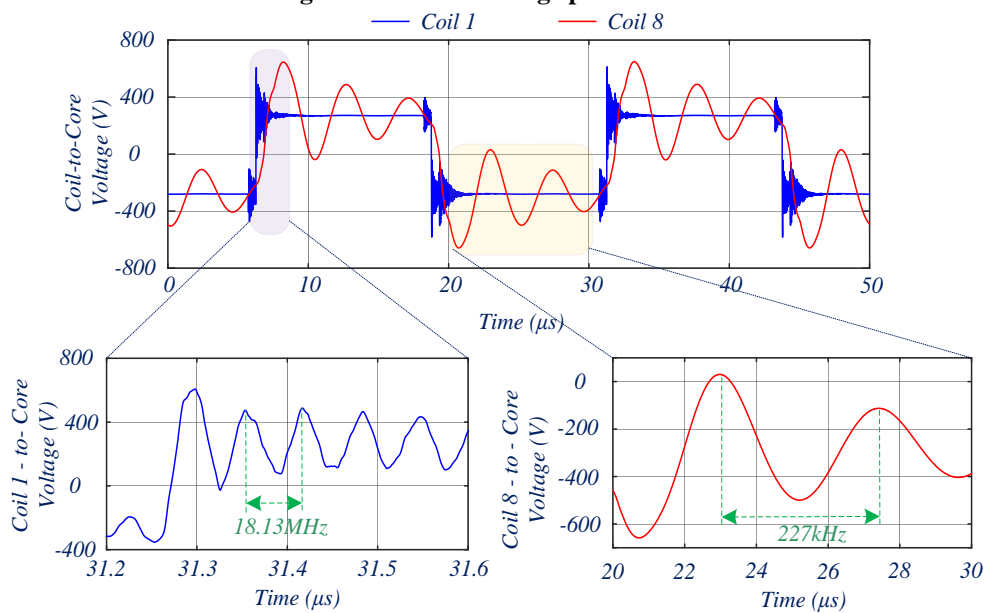


Figure 5.13: Enlarged view of the Coil-to-core voltage for the first and the last coil from the terminal end at 550V DC link voltage under PWM voltage pulse excitation

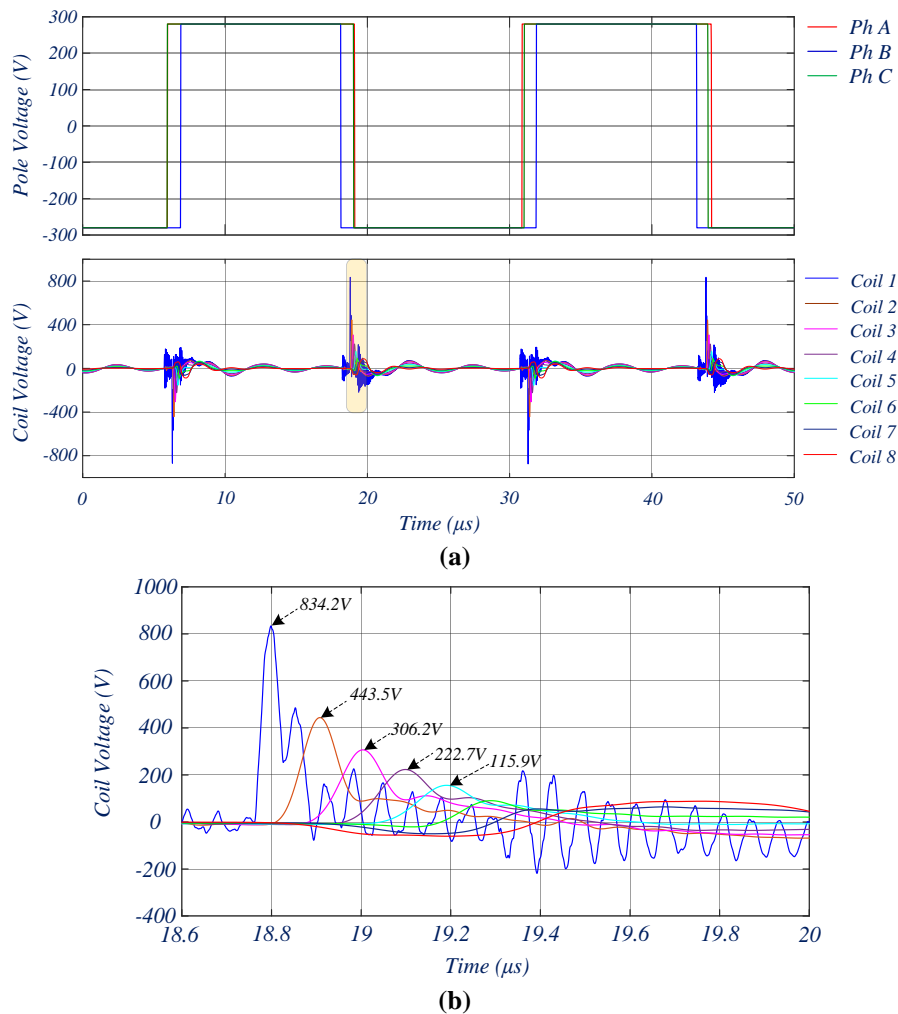


Figure 5.14: Voltage across the coils at 550V DC link voltage under PWM voltage pulse excitation; (a) voltage across 8 coils, (b) enlarged view during a switching event.

Further, Figure 5.14 (a) shows the voltage stress across each coil of phase A and the enlarged view of the voltage stress under a switching event is illustrated in Figure 5.14 (b). The voltage is measured between the start of the first turn and the end of the last turn of the coil. As evident, the voltage distributes non-uniformly within the winding. The peak voltage stress occurs across the first coil, which may rise to 1.52 times (834.2V) the DC link voltage. The peak voltage stress across the next coil is half of the former and decreases rapidly for subsequent coils. In the random wound winding, the location of the turns is not delineated. Consequently, it is likely possible that the first turn and the last turn of the coils are in close vicinity. Under this circumstance, the full coil voltage will appear across the enamel coating separating the two conductors. In the worst case, if it occurs in the first coil, the enamel coating will experience a peak voltage stress of 1.52pu. In addition, the HF voltage oscillations are restricted only to the first coil. The remaining coil voltage oscillates at LF. This is because at HF, the shunt

admittance of the line end coil offers a low impedance path to the HF current, and the series inductive impedance restricts its penetration deep into the rest of the coils.

The phase-to-core and phase-to-phase voltage is illustrated in Figure 5.15, which is measured at the phase terminals. Predictably, the HF voltage oscillations are noticeable in both the traces, which soars the jump voltage between the phase and the core to 840.5V and between the phases to 893.4V. The impregnated varnish and the ground-wall insulation, which separates the turn closest to the terminal end from the core, experience this phase-to-core voltage stress. Similarly, the phase-to-phase voltage is the combined voltage stress occurring across the insulation between the first turn of both the phases and the core. Therefore, the PDIV of the insulation between the first turn and the core must be greater than the peak voltage stress at the terminal, which in the worst case is 2 times the DC link voltage.

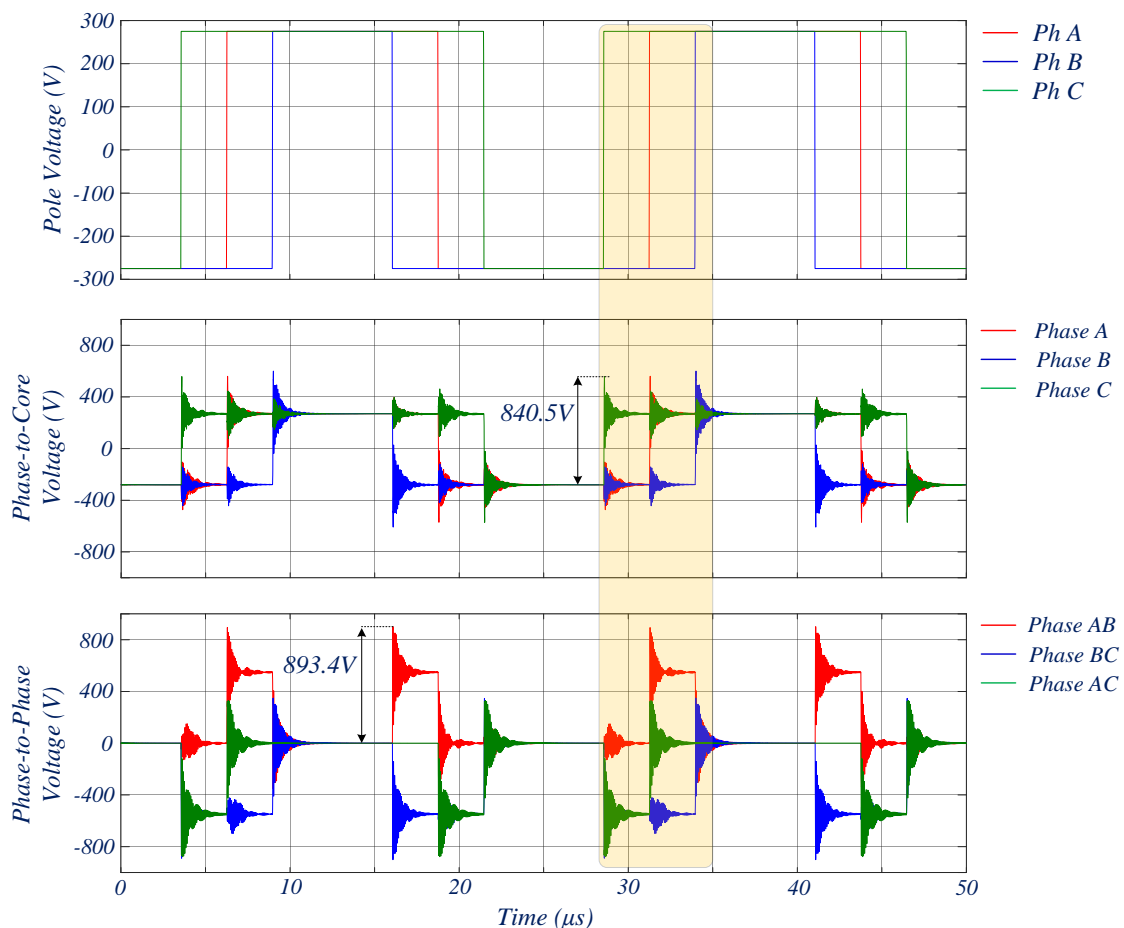
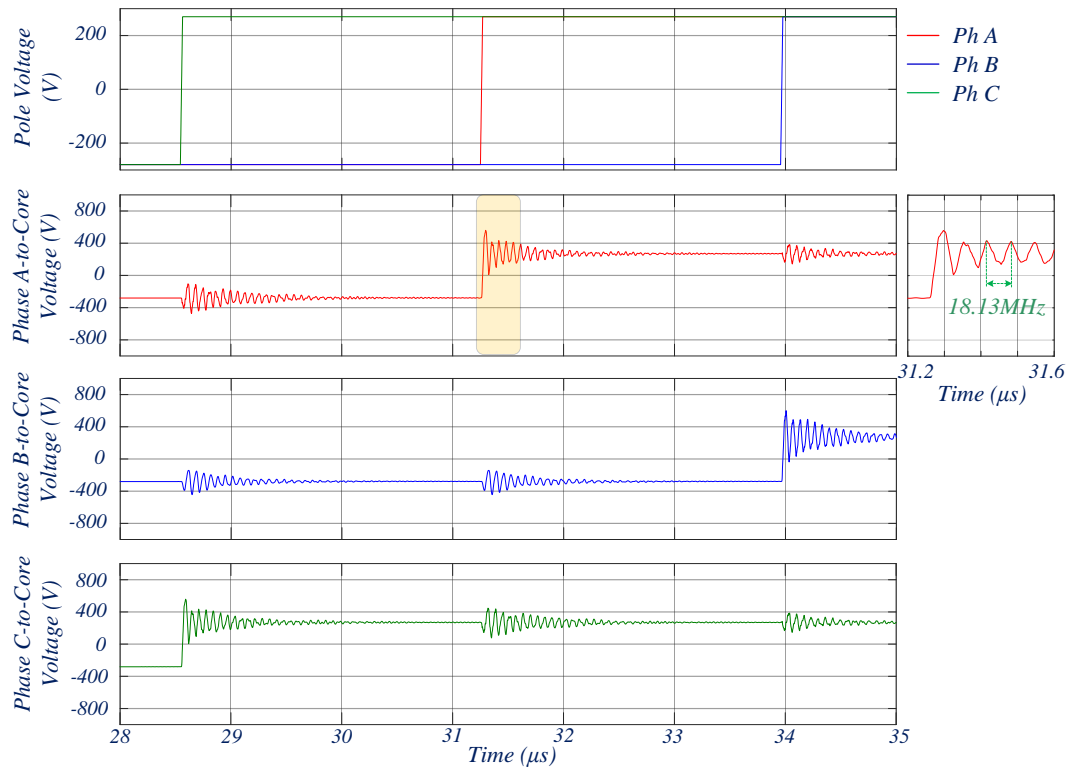
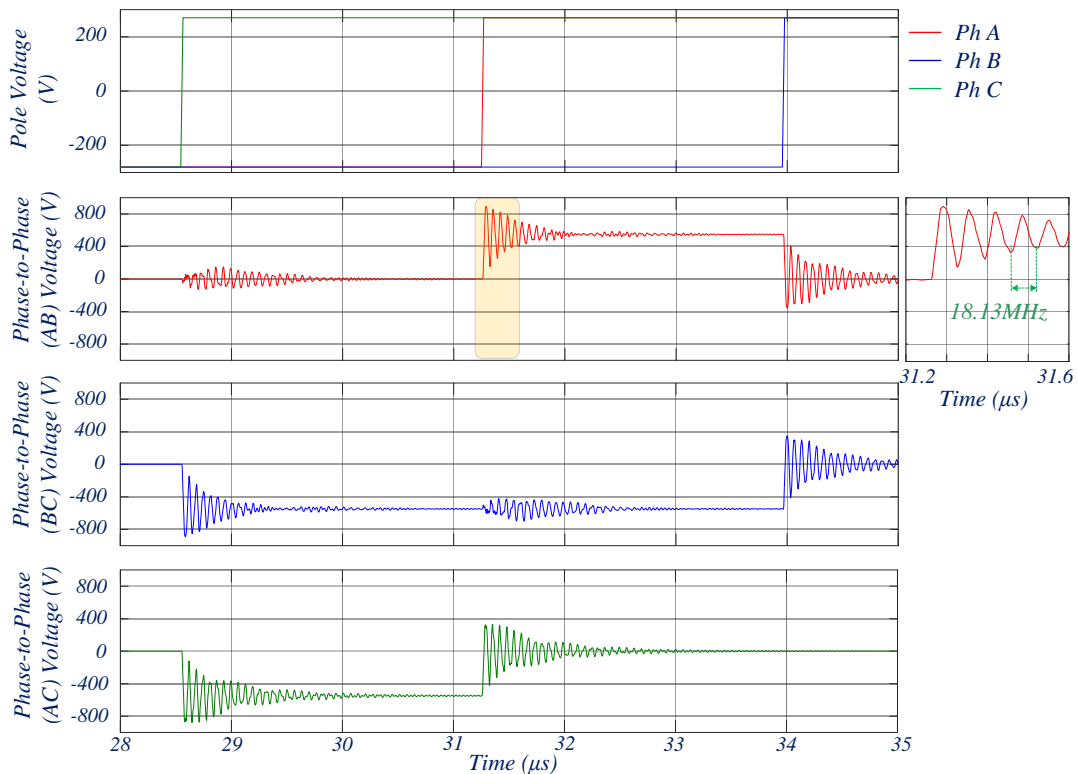


Figure 5.15: Phase-to-core and phase-to-phase voltage measured at 0.5 modulation index, 40kHz switching frequency, 20ns rise time and 550V DC link voltage, under PWM voltage pulse excitation.



(a)



(b)

Figure 5.16: Enlarged view of voltage stress during a switching event under PWM voltage pulse excitation; (a) phase-to-core, (b) phase-to-phase voltage.

The enlarged view of the voltage stress over the switching instant is illustrated in Figure 5.16. As envisaged, the voltages oscillate at 18.13MHz, which is the 2nd anti-resonance frequency ($f_{ar_{(c+m)(2)}}$) of the combined cable and the stator winding. The voltage pulse travelling through the cable encounters minimum impedance at this frequency, thereby, the voltage oscillation is sustained for a longer duration. In addition, the oscillatory response can also be seen in one phase when the other phase is switching, which occurs as a result of the capacitive coupling of both the phases with the core. At the lower modulation index, when the dwell time between the switching of different phases is short, the peak-to-peak voltage oscillations due to switching at different phases may contribute to an increase in the voltage overshoot. This is apparent from Figure 5.13, wherein, the Phase A voltage measured with respect to the core is illustrated. The jump voltage measured at 0.1 modulation index is 895V, which is 54.5V higher than the jump voltage measured at 0.5 modulation index, as illustrated in Figure 5.15. Therefore, the voltage overshoot depends on the modulation index and is more pronounced at the lower modulation.

Similarly, the voltage stress across the first turn of the first coil is maximum as compared to the remaining turns, which is illustrated in Figure 5.17 (a). The figure depicts the voltage stress across the first five turns and the last turn of the first coil of phase A. The enlarged view of the voltage stress under one of the switching events is illustrated in Figure 5.17 (b). As evinced, the voltage distributes non-uniformly within the coil and the peak voltage stress occurs across the first turn with peak stress reaching to 531.4V. Given the conductor distribution within the slot, as illustrated in the appendix, this voltage stress appears across the enamel coating of the four conductors of turns 1 and 2. Although the typical PDIV of the enamel coating of thickness 25 μ m, is 1kV, it decreases with its service lifetime. If the voltage stress exceeds the PDIV of the enamel coating, electric discharge may occur which will deteriorate the insulation composition. Due to the capacitive coupling between the conductors and the core, because of the dielectric properties of the insulation, and the series impedance of the conductor embedded in the slots, the fast slew rate of the voltage pulse distributes non-uniformly. The spectral content of the voltage pulse spreading over the wide frequency range depends on the slew rate of the pulse. If the slew rate (t_r) is fast, spectral content will spread over a wide range up to $1/\pi t_r$ Hz. Also, the series impedance restricts the penetration of the HF voltage oscillations deep into the winding. Thus, the fast slew rate voltage pulse impinging machine terminals aggravates the non-uniform voltage distribution, resulting in increased voltage stress across the

first turn. Illustratively, Figure 5.18 shows the peak voltage stress across the first turn with different slew rates. As envisaged, the voltage stress is higher with the short rise time. Thus, the SiC based VSI converters, capable of rapid switching, leaves an inimical effect on the insulation. The peak voltage stress in IGBT-based VSI converters with a typical rise time of 200ns is 10V, which resembles a uniform voltage distribution, reducing the likelihood of a PD event.

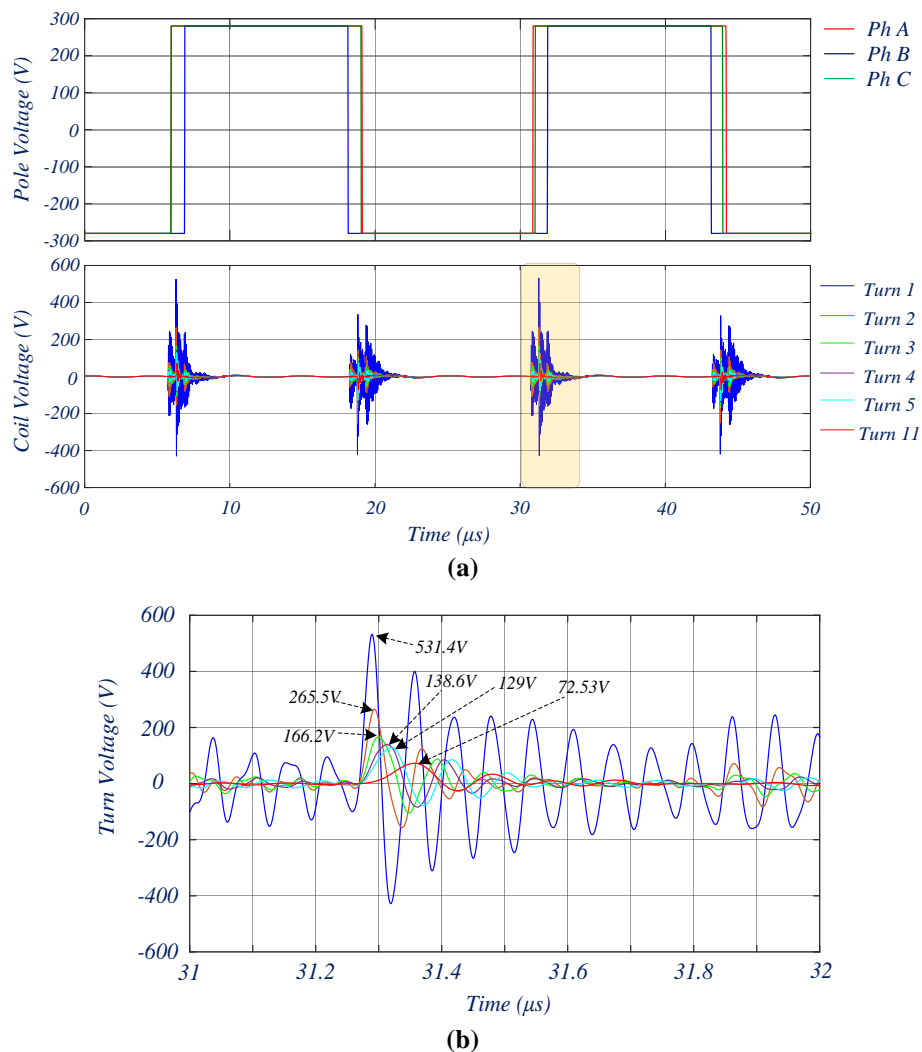


Figure 5.17: Voltage across the turns of the first coil of phase A under PWM voltage pulse excitation; (a) voltage across first five turns and the last turn of the coil, (b) enlarged view during a switching event.

The characteristic difference of the voltage waveforms under PWM excitation results from the superposition of the voltage waves travelling in all three phases, which increases the voltage stress in the insulation close to the neutral point most. The following section investigates the voltage stress distribution and the application of travelling wave theory to predict the voltage stress within the winding is comprehensively discussed.

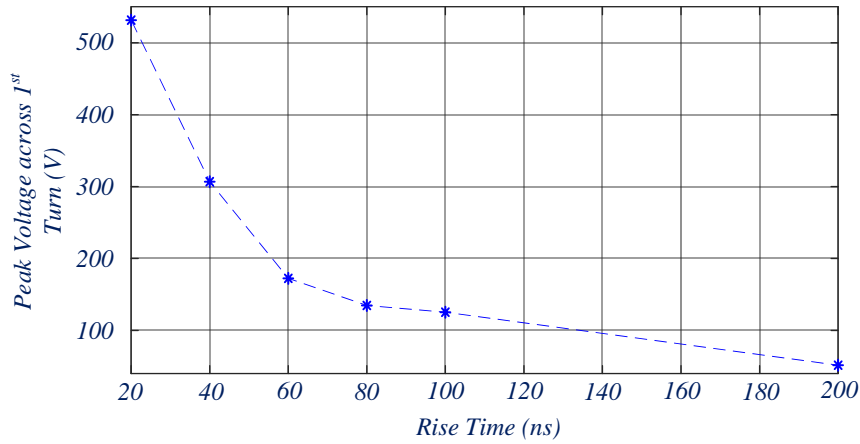


Figure 5.18: Peak voltage across the first turns of first coil of phase A with respect to the rise time under PWM voltage pulse excitation.

5.5 Voltage Stress at the Neutral Point

Notwithstanding the fact that the first few turns are stressed, the previous section shows that at such low modulation index it is the ground wall insulation close to the neutral point, which is most stressed. The studies in the literature [14-19][37-39][153] are limited to the single voltage pulse excitation at one phase with the other two connected to the ground. Therefore, it ignores the voltage distribution due to the transient overlap elicited from the previous excitation as well as excitation at the other two phase terminals. With the absence of voltage excitation at the other two phase terminals, the first coil is most stressed, which is prevalent in literature [14-19][37-39][153] However, the voltage waves impinging different phase terminals superpose each other to engender maximum voltage stress at the neutral point. In the following section, the effect of superposition of voltage wave is comprehensively studied.

5.5.1 Travelling Wave Theory

The PWM voltage excitation is a spectrum of waves impinging the machine terminals. Therefore, the peak voltage stress at the neutral point can be well understood using travelling wave theory.

Consider a uniform string of length l extended in the x -direction, with fixed ends between points a ($x = 0$) and b ($x = l$). Let a sinusoidal mechanical wave travels from a to b , expressed as [154],

$$y(x, t) = Y \sin\left(\omega t - \frac{\omega x}{g}\right) \quad (5.17)$$

where, Y is displacement magnitude from mean position, ω is the angular frequency, g is the velocity of propagation in the x -direction, and t is time. Similarly, another wave travelling in the opposite direction can be expressed as [154],

$$y(x,t) = Y \sin\left(\omega t - \frac{\omega(l-x)}{g}\right) \quad (5.18)$$

The resultant displacement of a particle of the string is the superposition of two waves and is expressed as [154],

$$y(x,t) = 2Y \cos\left(\frac{\omega}{g}\left(\frac{l}{2} - x\right)\right) \sin\left(\omega\left(t - \frac{l}{2g}\right)\right) \quad (5.19)$$

Thus, the particle displacement can be expressed as a standing wave, which is the superposition of two coherent travelling waves, travelling in the opposite direction. From (5.19), the particle at the mid of the string ($l/2$) displaces maximum and the fixed ends remain at the mean position. Thus, the standing waveforms nodes at the ends, and an antinode at the mid of the string, thereby, the string vibrates in a normal mode.

Nevertheless, the mechanical wave travelling along the string can be compared with the voltage waves travelling along with the coils. The PWM voltage wave impinging at machine terminals can be considered as travelling waves, which superposes creating standing waves. As illustrated in Figure 5.11, the damping at the anti-resonance frequency is at a minimum. Thus, upon PWM voltage excitation, the voltage waves oscillating at the anti-resonance frequency endure longer, thereby, the neutral point voltage oscillates at this frequency. Consider a voltage wave of amplitude V_m and oscillating at frequency ω impinges machine terminal at time τ_A , travelling towards neutral point. Corollary to the aforementioned discussion, the wave can be expressed mathematically as,

$$v_{A_{uc}}(x,t) = V_m e^{-\zeta(t-\tau_A)} \sin\left(\omega(t-\tau_A) - \frac{\omega x}{g}\right) \quad (5.20)$$

where, g is the velocity of propagation in the x -direction and ζ is the damping factor representing the damped voltage oscillations. Similarly, the voltage waves impinging phase B and C at time τ_B and τ_C are expressed as,

$$v_{B_{ac}}(x, t) = V_m e^{-\zeta(t-\tau_B)} \sin\left(\omega(t-\tau_B) - \frac{\omega(l-x)}{g}\right) \quad (5.21)$$

$$v_{C_{ac}}(x, t) = V_m e^{-\zeta(t-\tau_C)} \sin\left(\omega(t-\tau_C) - \frac{\omega(l-x)}{g}\right) \quad (5.22)$$

where, l is twice the length of phase winding. Apart from the damped sinusoidal oscillation, the coil-to-core voltage has a DC component that depends on the switching states of the phases. If S_z (where, $z = A, B, C$) represents the switching states of the three phases such that, $S_z = 1$ when the upper switch of phase leg is ON and $S_z = 0$ when the lower switch of phase leg is ON, then, the DC component is represented as;

$$v_{z_{dc}}(x, t) = \begin{cases} \frac{V_{DC}}{6}; & S_z = 1 \\ -\frac{V_{DC}}{6}; & S_z = 0 \end{cases} \quad \forall z = A, B, C \quad (5.23)$$

where, V_{DC} is the DC link voltage. Thus, the voltage at any arbitrary location in the coil with respect to the core is the superposition of the three travelling waves with a DC offset. Notably, in a space vector PWM (SVPWM) technique, $\tau_A - \tau_B$ and $\tau_B - \tau_C$ are the dwell time of the active space vectors, which depends on the switching frequency, modulation index, and phase angle (θ). Therefore, the voltage distribution is a function of the aforementioned factors.

Thus, using (5.20-5.23), the neutral-to-core voltage can be expressed analytically. It is noteworthy that, the analytical model does not account for the overlap of voltage transients elicited from the previous switching event with that of the present switching event. Therefore, (5.20-5.23) must be revised to account for such effects.

5.5.2 Analytical Model of the Neutral Point Voltage Stress

The voltage oscillation at the neutral point is a damped sinusoidal oscillation, which can be approximated as a second order system response. The time domain step response of a second order system with the non-zero initial condition is [154],

$$\begin{aligned}
 y(t) = & Y \left(1 - \sqrt{1 + \left(\frac{\xi}{\omega}\right)^2} e^{-\xi t} \cos \left(\omega t + \tan^{-1} \left(\frac{\xi}{\omega} \right) \right) \right) \\
 & - y_0 \sqrt{1 + \left(\frac{\xi}{\omega}\right)^2} e^{-\xi t} \cos \left(\omega t + \tan^{-1} \left(\frac{\xi}{\omega} \right) + \phi_0 \right)
 \end{aligned} \tag{5.24}$$

where, ξ is the damping factor, ω is the damped frequency of oscillation, Y is the magnitude of undamped sinusoidal oscillation, y_0 and ϕ_0 are initial magnitude and phase. Henceforth, (5.20-5.22) can be transformed using (5.24), to express the damped sinusoidal component of the neutral-to-core voltage (v_N) with the non-zero initial condition as,

$$\begin{aligned}
 v_{A_{ac}}(t) = & \underbrace{v_{A_m} \sqrt{1 + \left(\frac{\xi}{\omega}\right)^2} e^{-\xi(t-\tau_A)} \sin \left(\omega(t-\tau_A) + \tan^{-1} \left(\frac{\xi}{\omega} \right) - \frac{\pi}{2} \right)}_{\text{Forced Response}} \\
 & + \underbrace{v_{A_0} \sqrt{1 + \left(\frac{\xi}{\omega}\right)^2} e^{-\xi(t-\tau_A)} \sin \left(\omega(t-\tau_A) + \tan^{-1} \left(\frac{\xi}{\omega} \right) + \phi_{A_0} - \frac{\pi}{2} \right)}_{\text{Natural Response}}
 \end{aligned} \tag{5.25}$$

$$\begin{aligned}
 v_{B_{ac}}(t) = & \underbrace{v_{B_m} \sqrt{1 + \left(\frac{\xi}{\omega}\right)^2} e^{-\xi(t-\tau_B)} \sin \left(\omega(t-\tau_B) + \tan^{-1} \left(\frac{\xi}{\omega} \right) - \frac{\pi}{2} \right)}_{\text{Forced Response}} \\
 & + \underbrace{v_{B_0} \sqrt{1 + \left(\frac{\xi}{\omega}\right)^2} e^{-\xi(t-\tau_B)} \sin \left(\omega(t-\tau_B) + \tan^{-1} \left(\frac{\xi}{\omega} \right) + \phi_{B_0} - \frac{\pi}{2} \right)}_{\text{Natural Response}}
 \end{aligned} \tag{5.26}$$

$$\begin{aligned}
 v_{C_{ac}}(t) = & \underbrace{v_{C_m} \sqrt{1 + \left(\frac{\xi}{\omega}\right)^2} e^{-\xi(t-\tau_C)} \sin \left(\omega(t-\tau_C) + \tan^{-1} \left(\frac{\xi}{\omega} \right) - \frac{\pi}{2} \right)}_{\text{Forced Response}} \\
 & + \underbrace{v_{C_0} \sqrt{1 + \left(\frac{\xi}{\omega}\right)^2} e^{-\xi(t-\tau_C)} \sin \left(\omega(t-\tau_C) + \tan^{-1} \left(\frac{\xi}{\omega} \right) + \phi_{C_0} - \frac{\pi}{2} \right)}_{\text{Natural Response}}
 \end{aligned} \tag{5.27}$$

$$v_{z_m}(t) = \begin{cases} \frac{V_{DC}}{3}; & S_z = 1 \\ -\frac{V_{DC}}{3}; & S_z = 0 \end{cases} \quad \forall z = A, B, C \tag{5.28}$$

$$v_N(t) = \underbrace{(v_{A_{ac}}(t) + v_{A_{dc}}(t))}_{v_A} + \underbrace{(v_{B_{ac}}(t) + v_{B_{dc}}(t))}_{v_B} + \underbrace{(v_{C_{ac}}(t) + v_{C_{dc}}(t))}_{v_C} \quad (5.29)$$

where, v_{z0} and Φ_{z0} ($z = A, B, C$) is the initial magnitude and the phase of the damped sinusoidal oscillation. Henceforth, (5.25-5.29) can be used to represent the peak voltage stress, i.e. the neutral-to-core voltage within the winding. The voltage oscillations at the three phases expressed in (5.25-5.27) is contributed by two responses, one is the natural response, which occurs solely from the voltage magnitude (v_{z0}), and the phase angle (Φ_{z0}) at the time of the switching and the other is the forced response, which occurs because of the voltage pulses impinging the phase terminals. Consequently, the natural response evinces the voltage oscillations that ensued from the previous switching events whereas, the forced response represents the voltage stress from the current switching event.

5.6 Experimental Validation

To study the voltage distribution within the stator winding due to high slew rate voltage pulses, a SiC MOSFET based three-phase inverter is used. The SiC MOSFET is a CREE manufactured C2M0040120 with 1200V rated voltage and 60A rated drain current. To keep the studies more representative of the infield scenarios, the stator winding under investigation is an 8 pole, 550V (DC link voltage), 60 kW interior PMSM employed in the Toyota Prius hybrid vehicle [29]. The turns and the coils of the winding are not accessible. However, it can be made possible by unwinding and rewinding with the taps. Which will not be representative of the infield scenario. Therefore, for the experimental validation, the terminal voltage and the neutral point voltage is used. The stator winding is fed through a 4 wire cable connected between the inverter and the stator winding. The detailed specification of the stator winding and the cable is outlined in the appendix. The experimental rig used in this study is illustrated in Figure 5.19 and its schematic is illustrated in Figure 5.20.

Generally, during normal operation of the VSI-fed drives, the VSI produces CM voltage with a high slew rate. As illustrated in Figure 5.1, the CM voltage induces CM current, which leaks through the insulation between the core and the winding. To prevent EMI to the nearby equipment, it is necessary to provide a low impedance path to the CM current. This can be achieved by opting TN or IT earthing system. In general, in the electric transport system, IT earthing system is adopted as the supply mains is isolated from the ground. Thereby, it has an

additional advantage of low fault current. In addition, the manufacturers design capacitor based power line filters into the system to decouple the CM current, preventing it from reaching nearby equipment. The power line filters comprise Y capacitors connected between the lines and the local ground to offer a low impedance path to the CM current. Therefore, as illustrated in Figure 5.20, at the inverter end, one end of the protective earth wire is connected to the midpoint of the DC link capacitors acting as a Y-capacitor and the other end is connected to the core of the machine. To illustrate the wave propagation and voltage distribution within the winding, the voltage at the neutral point and the phase A terminal is measured with respect to the core of the machine and is compared with the voltage at the phase A terminal of the inverter output with respect to the mid-point of the DC link. These voltage waveforms are acquired by Teledyne Lecroy manufactured 100 MHz bandwidth, 1400V, ADP305 high voltage active differential probes. Similar voltage oscillations can also be seen in the experimental results illustrated in Figure 5.21. During the experiment, the DC link voltage is maintained at 550V, and a SiC based three phase VSI is used wherein, the switching frequency is 40kHz and the rise time is 20ns which represents its fast switching characteristics.

Akin to the simulation result, the coil-to-core voltage, except the line end coil, oscillates at the 1st anti-resonance frequency ($f_{ar_{m(1)}}$) of the stator winding (287.32kHz). The voltage across the line end coil and the core oscillates at a comparable HF. Also, the peak voltage stress occurs at the last coil of the winding, instead of the line end coil. The peak voltage stress at the machine terminal is 795V, whereas, at the neutral point it is 980V.

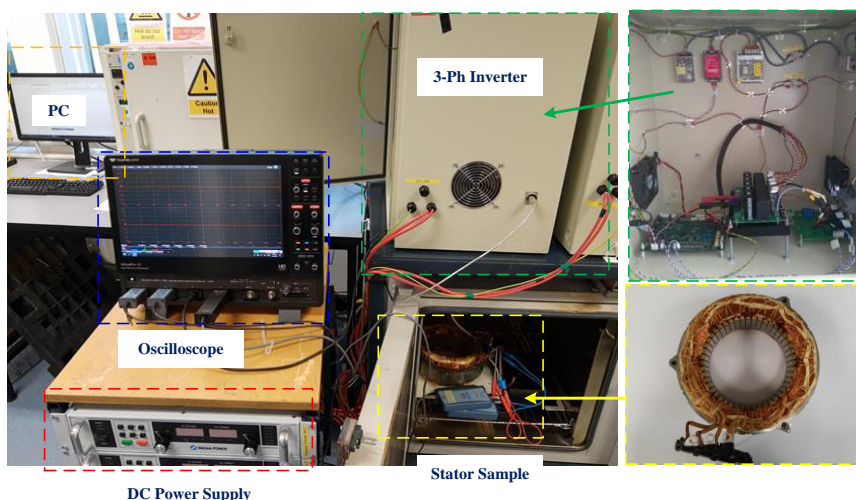


Figure 5.19: Experimental rig illustrating Toyota manufactured stator sample fed by 3-phase MOSFET based inverter through 2.5 m shielded cable.

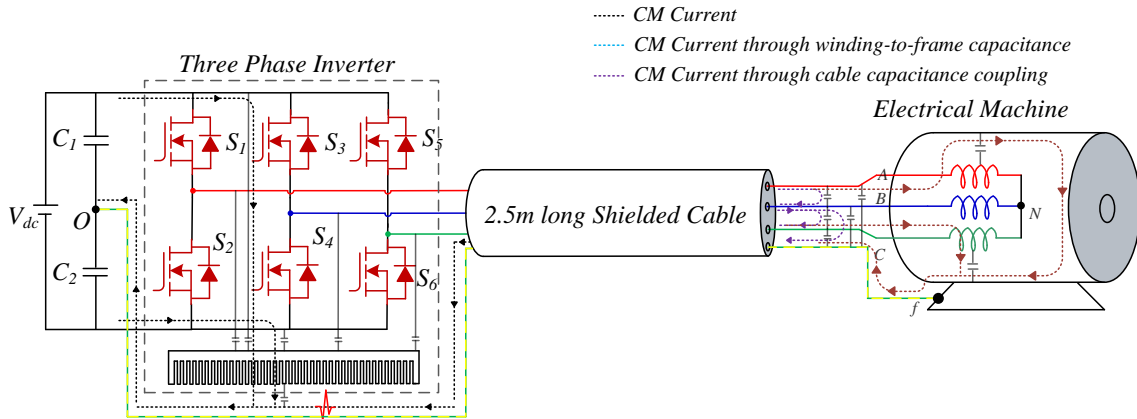


Figure 5.20: Schematic diagram of the 3-phase MOSFET based inverter fed electrical machine through 2.5 m shielded cable.

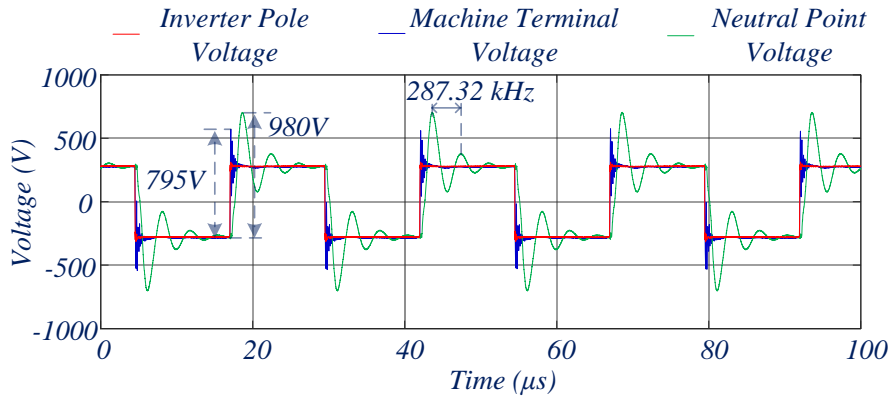


Figure 5.21: Experimentally measured coil-to-core voltage under PWM voltage excitation.

5.6.1 Overshoot Factor Calculation

The voltage overshoot at the machine terminals largely depends on the reflection coefficient which is a function of surge impedance. In section 5.3.2, a simple method based on the CM impedance is discussed to calculate the surge impedance. Figure 5.22 shows the CM impedance of a 2.5m long shielded cable and the stator winding employed in the Toyota Prius hybrid vehicle, measured using the OMICRON Lab manufactured BODE 100 impedance analyser over the frequency range of 1 kHz to 50 MHz. The impedance of the cable is measured across the three phases connected and the potential earth wire with all the three phases shorted together at the load end, as illustrated in Figure 5.6 (a). In the case of the machine, the impedance is measured across the shorted three phase terminals and the core of the machine, as illustrated in Figure 5.7 (a). From the CM impedance, the capacitance at 10kHz ($C_{@10kHz}$) is 269.05pF and its anti-resonance frequency ($f_{ar_{c(1)}}$) is 18.13MHz. Thus, from (5.10) the surge impedance of the cable (Z_{oc}) is 51.24Ω. When the surge impedance is compared to that estimated in section 5.3.2 using MATLAB®/Simscape environment, it is close.

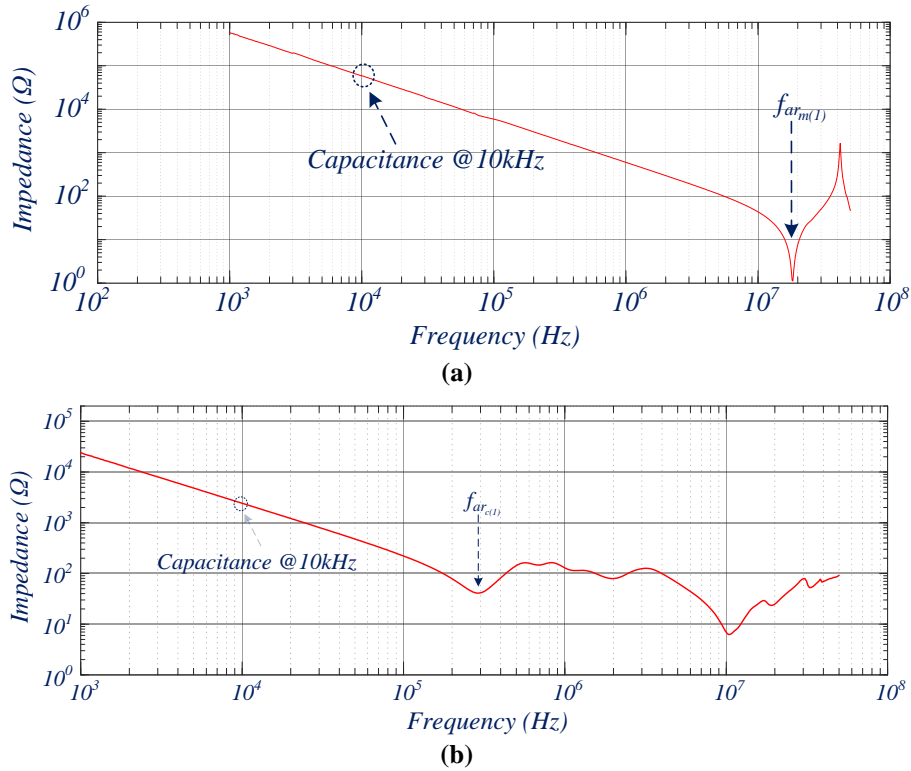


Figure 5.22: Experimentally measured CM impedance of (a) 2.5m long shielded cable, (b) Stator winding used in Toyota Prius hybrid vehicle.

Similarly, from the CM impedance of the machine illustrated in Figure 5.22 (b), the capacitance at 10kHz ($C_{@10kHz}$) is 6.4nF and its anti-resonance frequency ($f_{ar_{m(1)}}$) is 293.06kHz. Thus, using (5.10) the surge impedance of the machine (Z_{0m}) is 133.3Ω. The surge impedance calculated in the MATLAB[®]/Simscape environment is 206.99Ω. The difference in the experimentation and the simulation is due to the difference in the anti-resonance frequency. In the simulation environment, it is 226.84kHz, compared to 293.06kHz in experiments. Thus, from the surge impedance of the cable and the machine, the reflection coefficient at the machine terminal may be determined from (5.5) as 0.445. Using (5.1) and the anti-resonance frequency ($f_{ar_{c(1)}}$) of the cable, the propagation delay of the cable is 13.79ns.

Hence, when a voltage pulse of 20ns rise time and 550V DC voltage impinges machine terminals, the voltage OF at the machine terminals is determined using (5.4) as,

$$\frac{V_{t_{\max}}}{V_{DC}} = 1 + 0.445 = 1.445 \quad (5.30)$$

With 550V DC link voltage, the peak voltage stress at the terminal end is determined as,

$$V_{t_{\max}} = 1.445V_{DC} = 809.2V \quad (5.31)$$

On comparing with the experimentally measured voltage stress illustrated in Figure 5.21, it is marginally less than the calculation. The difference is 1.78%, which owes to the losses within the cable and the machine winding. Thus, the method proposed for calculating the voltage stress at the machine terminal using CM impedance is effective in estimating the voltage stress with high accuracy.

5.6.2 Analytical Model of the Neutral Point Voltage

For using the proposed analytical model (5.25-5.29), experimental measurement of two parameters (ζ and ω) is required, wherein, ζ is the damping factor and ω is the damped frequency of oscillation. When the three phases are effectively switched at the same instant at a very low modulation index with zero initial conditions, the contribution of each phase towards the neutral-to-core voltage will be the same, which enables the measurement of ζ and ω . As an illustration, Figure 5.23 shows neutral-to-core voltage along with the three phase pole voltage measured at 10 kHz switching frequency and 0.01 modulation index. Ω can be measured directly from the waveform, whereas, ζ can be measured using (5.32) as,

$$\zeta = \frac{(\ln(V_1) - \ln(V_2))}{(t_2 - t_1)} \quad (5.32)$$

where, V_1 and V_2 are the neutral-to-core voltages measured at time t_1 and t_2 respectively.

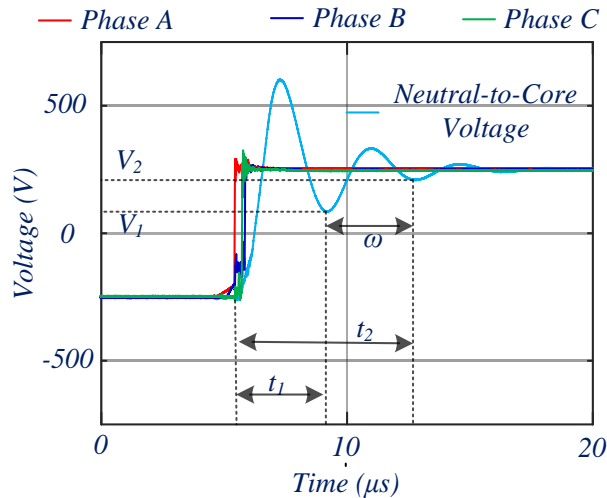


Figure 5.23: Experimental measurement of damping factor (ζ) and damped frequency of oscillation (ω).

Apart from the ω and ζ , the instant of switching (τ_A , τ_B , and τ_C). is required for estimating the voltage stress. In the SVPWM technique, these instants are the instant of intersection between the reference signal and the carrier signal. Figure 5.24, illustrates the switching instant of phase A (τ_A) along with the voltage stress at the neutral point due to the voltage pulse impinging Phase A terminal. At the switching instant, the magnitude (v_{A0}) and the phase (ϕ_0) of the voltage oscillations are recorded which is further used to calculate the natural response. Further, the natural response and the forced response is added together (5.25) to calculate the voltage stress due to the voltage pulse impinging Phase A terminal. Similarly, the voltage stress due to Phase B and C is calculated (5.26-5.27) and using (5.29) the voltage stress is estimated. These calculations are summarised using a flowchart, which is illustrated in Figure 5.25.

The parameters ω and ζ are specific to the cable connected stator winding. Different cables and the stator winding have different impedances. Thereby, the parameters ω and ζ are different. Once the experimental measurement of these parameters is available, the voltage stress at the neutral point can be estimated without exciting the windings.

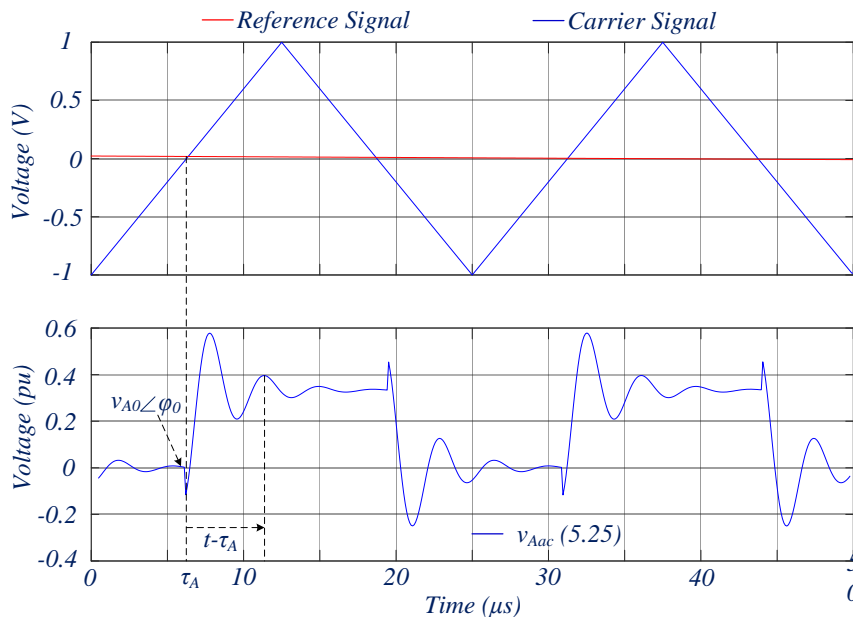


Figure 5.24: Implementation of the analytical model for calculating the voltage stress at the neutral point.

The efficacy of the proposed model is illustrated in Figure 5.26, wherein, the measured neutral-to-core voltage is compared with the analytical model. During the experiment, the SiC based three-phase inverter with 20ns rise time and 100V DC voltage feeds the Toyota Prius hybrid vehicle adapted stator winding through a 2.5m long cable. The voltage is measured at 40kHz switching frequency with varying modulation index between 0.01 and 0.5. Only the

stator winding without rotor is connected to the inverter, which limits the modulation index up to 0.5 for avoiding overcurrent.

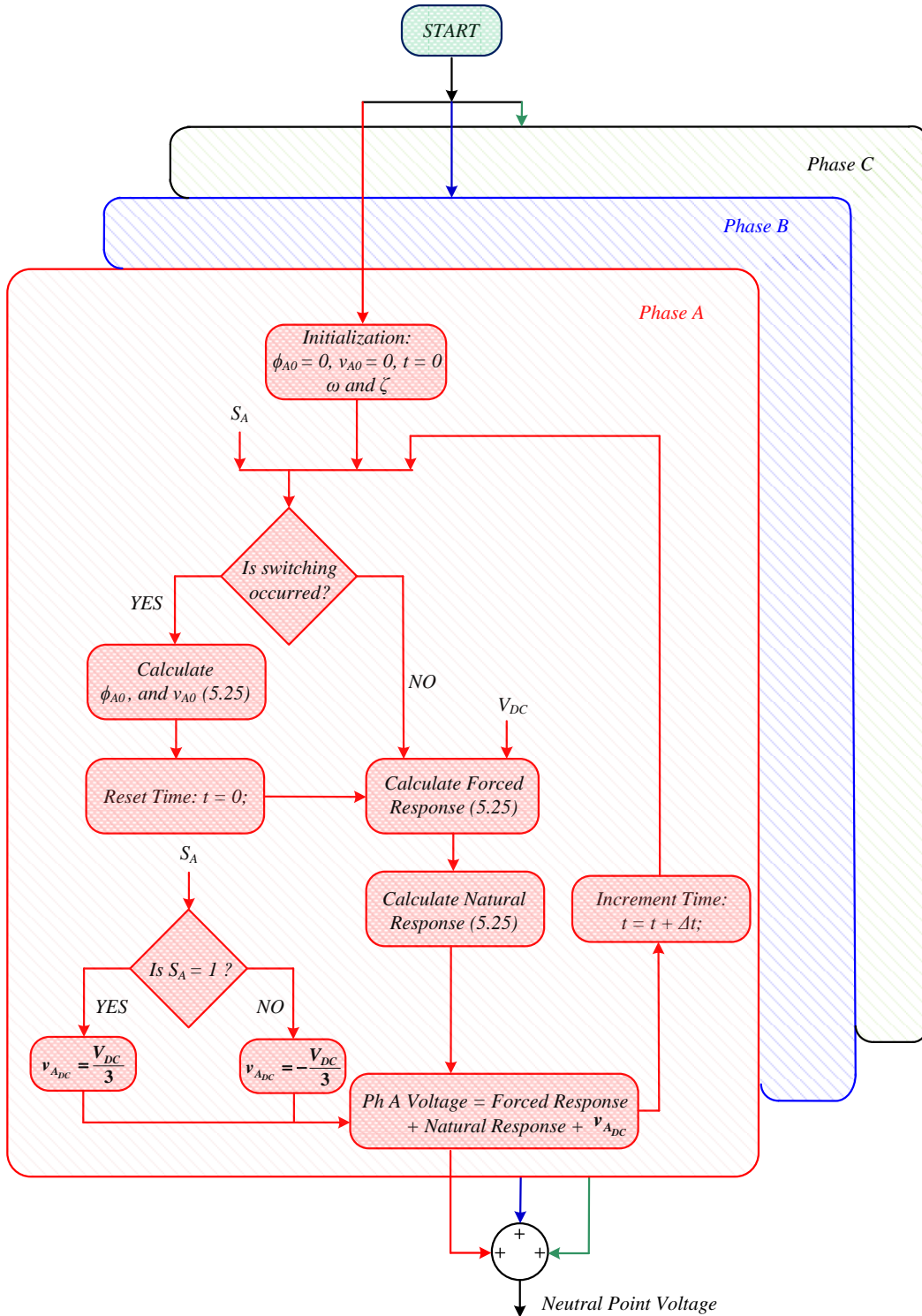


Figure 5.25: Flowchart representation of the analytical model for predicting neutral-to-core voltage.

The damping factor (ζ) and the damped frequency of oscillation (ω) used during the calculation are $3.75 \times 10^5 s^{-1}$ and $1.805 \times 10^6 rad s^{-1}$ respectively. During the experimental validation, the switching instant are calculated using the pole voltage. Instant at which the pole voltage traverse from $+V_{DC}/2$ to $-V_{DC}/2$ or vice-a-versa is considered as the instant of switching. Thus, for the experimental validation, the following measurements are used:

1. DC link voltage (V_{DC}).
2. Pole voltage as an input for calculating instant of switching (τ_A , τ_B , and τ_C).
3. Damping factor (ζ) and damped frequency of oscillation (ω).

It is apparent from Figure 5.26, the proposed analytical model can predict the neutral-to-core voltage under different modulation indexes with great accuracy. Following Figure 5.26, below are the observations on the peak voltage stress at the neutral point:

- The peak-to-peak voltage stress could rise up to 2.5 times DC link voltage with a maximum OF of 1.75pu. Therefore, contrary to the literature [14-19][37-39][153], the location of peak voltage stress is close to the neutral point at low modulation index.
- Under a low modulation index (say 0.01), the peak-to-peak voltage stress is consistent for every switching instant as it is less influenced by dwell time.
- At a higher modulation index, the peak-to-peak voltage stress reduces.
- Under 0.3 and 0.5 modulation index, the peak-to-peak voltage stress varies with dwell time as will be discussed in the subsequent section. Hence, it is high at some switching instant and low at others.

5.6.3 Effect of Dwell Time between Switching Events

As evident, the peak of the neutral-to-core voltage largely depends on the modulation index. At a low modulation index, the peaks are consistent whereas, at high modulation index, the peaks are high at some switching events and low at others. At a low modulation index, the switching events at all three phases occur simultaneously. Therefore, the travelling waves elicited at different phases superpose constructively and engender high voltage stress.

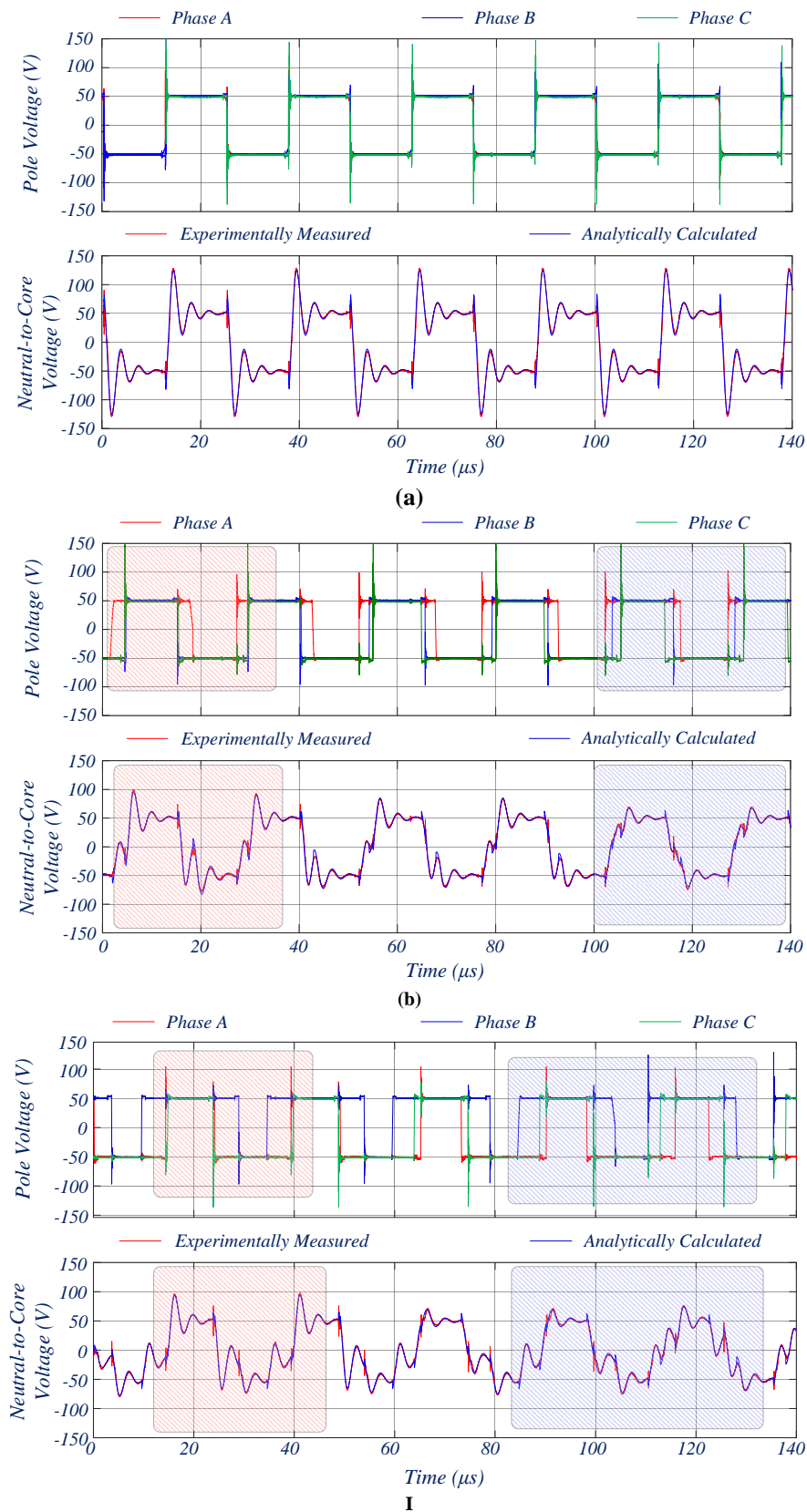


Figure 5.26: Experimental validation of the proposed analytical model at 40 kHz switching frequency and 100V DC link voltage; (a) $m = 0.01$, (b) $m = 0.3$, (c) $m = 0.5$.

Nevertheless, simultaneous switching also occurs at high modulation index but is less likely in all 3 phases. In the regions shaded in red, as illustrated in Figure 5.26, two of the phases switch simultaneously, thereby, the neutral-to-core voltage rises to the DC link voltage. However, in other regions shaded in blue, the different phases switch distantly. Therefore, the neutral point voltage is less than the DC link voltage. In the SVPWM technique, the time difference between the switching of the phases (T_a and T_b) is called active vector time or dwell time, which is expressed as [155],

$$T_a = \frac{\sqrt{3}m}{2f_{sw}} \sin\left(\frac{\pi}{3} - \theta\right) \quad (5.33)$$

$$T_b = \frac{\sqrt{3}m}{2f_{sw}} \sin(\theta) \quad (5.34)$$

where, m is the modulation index, f_{sw} is switching frequency and θ is the angle of reference vector within a switching sector. Under a low modulation index, irrespective of θ , both T_a and T_b are small. Consequently, the switching events arrive simultaneously and the peak voltage stress is at maximum at a low modulation index. Under high modulation index, T_a and T_b depend on both m and θ . Both the dwell times cannot be simultaneously short ($T_a = 0, T_b \neq 0$ if $\theta = \pi/3$ and $T_a \neq 0, T_b = 0$ if $\theta = 0$), i.e., only two phases switch simultaneously. This occurs during the change in the sector of the reference voltage vector, i.e., six times in every fundamental cycle.

When it happens, as marked as the red region in Figure 5.26, the peak of the neutral-to-core voltage reaches DC link voltage. In the regions marked as blue, the dwell time is large, henceforth; the travelling waves elicited at different phases superpose destructively which restricts the neutral-to-core voltage less than the DC link voltage. Further, the experimentally validated analytical model is used to calculate the peak-to-peak voltage stress under modulation index range ($0 < m < 1$) and within one switching sector ($\pi/2 < \theta < 5\pi/6$) which is illustrated in Figure 5.27. As evident, the peak-to-peak voltage stress is maximum under low modulation index as well as, when the two switching events occur simultaneously ($\theta = \pi/2$ and $\theta = 5\pi/6$).

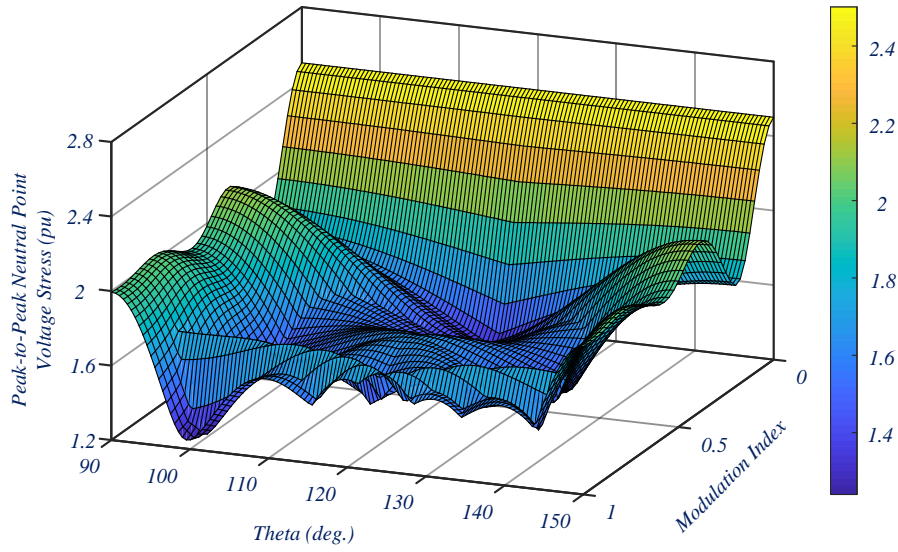


Figure 5.27: Peak-to-peak neutral-to-core voltage expressed in per-unit with respect to the 100V DC link voltage under PWM inverter operation at 40 kHz switching frequency.

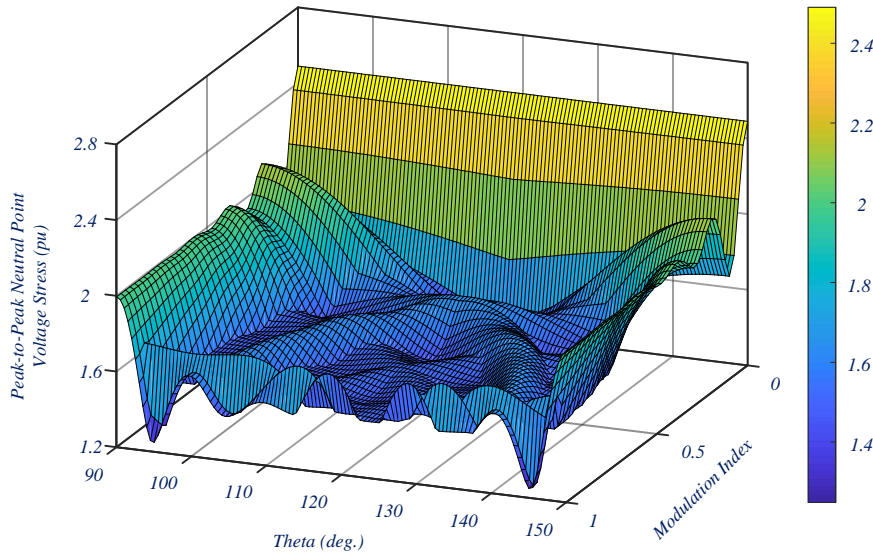


Figure 5.28: Peak-to-peak neutral-to-core voltage expressed in per-unit with respect to the 100V DC link voltage under PWM inverter operation at 20 kHz switching frequency.

5.6.4 Effect of Switching Frequency

The dwell times also depend on the switching frequency. With inverse relation in (5.33-5.34), under low switching frequency, for a given modulation index (m), the dwell times are large. Thereby, with decreased switching frequency (say 20 kHz), the peak-to-peak voltage stress decreases. Figure 5.28 shows the peak-to-peak voltage stress at 20 kHz switching frequency, with varying m and phase angle (θ), wherein, except for the low m and simultaneous phase switching instant ($\theta = \pi/2$ and $\theta = 5\pi/6$), the voltage stress is less as compared to the voltage stress with 40 kHz switching frequency. Upon comparing the voltage stress at the two

switching frequencies (20kHz and 40kHz), the voltage stress envelope spreads in the full range of modulation index (between 0 to 1), in case of 40kHz switching frequency, is compressed to 0.5 modulation index for 20kHz switching frequency. This appears because the dwell time is inversely proportional to the dwell time. Thus, at the low switching frequency, in most of the operating regions, the voltage stress at the neutral point is low.

5.7 Interaction Between the Anti-Resonance Frequency of the Cable and Stator Winding

From the experimental results, it is evident that, at the anti-resonance, the TEM wave endures less damping and hence voltage oscillations sustain for a long period. Therefore, the coil-to-core voltage of the stator winding can be characterised by two oscillatory responses, which depend on the anti-resonance frequencies of the stator winding and cable.

Considering the anti-resonance characteristics, if the first anti-resonance frequency ($f_{ar_{c(1)}}$) of the cable aligns with the first anti-resonance frequency ($f_{ar_{m(1)}}$) of the stator winding, the voltage wave emerging from the inverter will encounter low damping throughout the cable as well as stator winding and consequently oscillate on a single frequency. Also, by increasing the cable length to 163 m, the first anti-resonance frequency ($f_{ar_{c(1)}}$) of the cable is reduced to 287.32 kHz. Under this condition, the voltage wave encounters low damping within the cable and winding, and cause massive coil-to-core voltage stress. This is explicitly illustrated in the following discussion, where the peak-to-peak voltage stress at the neutral point measured with respect to the core is compared with three different cable lengths.

Figure 5.29 (a) illustrates the CM impedance of a 2.5m long cable with first anti-resonance ($f_{ar_{c(1)}}$) at 19.04MHz, a 163m long cable with anti-resonance aligning with the anti-resonance of the stator winding (287.32kHz), and a 180m long cable whose anti-resonance frequency (264kHz) is lower than that of the stator winding. The combined CM impedance of the cable and the stator winding is shown in Figure 5.29 (b), wherein, with 2.5m long cable, the anti-resonance primarily occur at two different frequencies. The LF oscillation at the neutral point occurs due to anti-resonance at 287.32kHz (f_{ar1}) and the HF oscillation at the terminal of the machine oscillates at 2nd anti-resonance frequency (f_{ar2}) which occur at 6.8MHz, as elucidated in Figure 5.29 (b). However, with 163m and 180m long cable, the primarily single anti-resonance frequency (f_{ar3} and f_{ar4}) dominates, thereby, the machine terminal and the neutral point voltage oscillate at the same frequency.

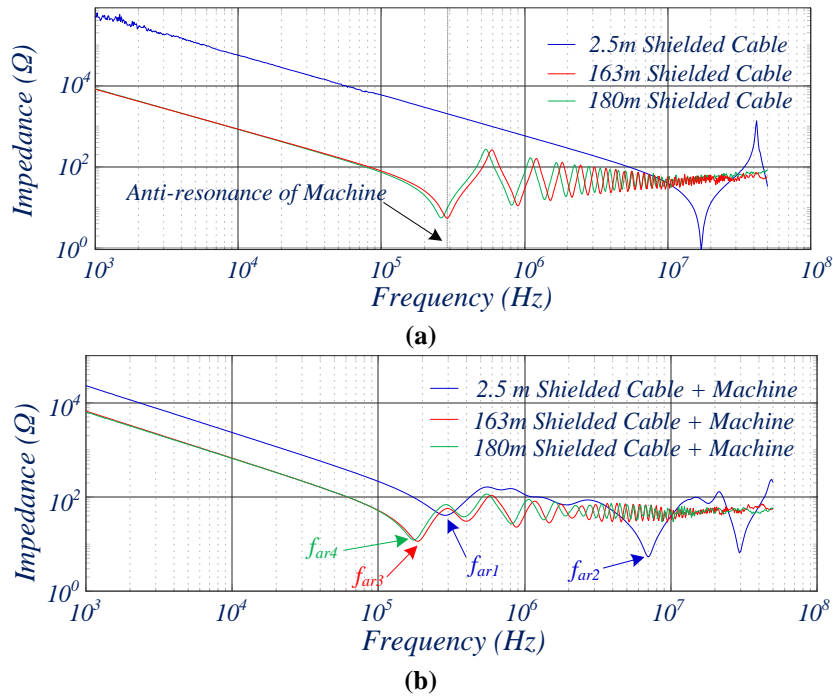


Figure 5.29: Comparison of CM impedance measured experimentally with different lengths of cable; (a) CM impedance of the cable, (b) CM impedance of cable connected to the stator winding.

Due to minimum impedance at f_{ar3} (amongst f_{ar1} , f_{ar3} , and f_{ar4}), the TEM wave travelling within 163m long cable connected winding, undergo minimum damping, resulting in maximum voltage stress at the neutral point. Therefore, the peak-peak voltage stress at the neutral point when the stator winding is excited with a VSI with 300V DC link voltage, as illustrated in Figure 5.30, is 1.167kV as compared to 751V for 2.5m cable and 1.0868kV for 180m cable. Thus, in the worst case scenario, where the cable first anti-resonance frequency ($f_{ar_{c(1)}}$) aligns with that of the stator winding ($f_{ar_{m(1)}}$), the groundwall insulation close to the neutral point undergoes maximum voltage stress (3.9 times DC link voltage). Therefore, to avoid any premature failure of the insulation, the anti-resonance frequency of the cable must not be near the first anti-resonance frequency ($f_{ar_{m(1)}}$) of the stator winding.

The damped voltage oscillations are the key characteristics of the anti-resonance frequency. With a very long cable length, the combined first anti-resonance frequency ($f_{ar_{(c+m)(1)}}$) of the cable and the stator winding shift to a lower frequency range with decreased impedance. Due to reduced impedance, the damping factor of the damped voltage oscillations reduces, resulting in an increase in the peak of the damped voltage oscillation. Using the proposed analytical model, with 163m long cable, the damping factor (ζ) and the damped frequency of oscillation (ω) are $1.6 \times 10^5 \text{ s}^{-1}$ and $1.1435 \times 10^6 \text{ rad s}^{-1}$ respectively. Figure 5.31 shows the comparison

of neutral-to-core voltage between the experiment and the analytical model measured at 40 kHz switching frequency, 100V DC link voltage and 0.1 modulation index. The peak-to-peak voltage stress soars to 3.9 times the DC link voltage, which is 1.56 times higher than the voltage stress with a 2.5m long cable. The peak-to-peak voltage stress at the neutral point under different modulation indexes and over one switching sector ($\pi/2 < \theta < 5\pi/6$) is shown in Figure 5.32. Apparently, the voltage stress is high at the entire operating region as compared with 2.5 long cables, which owes to low ζ .

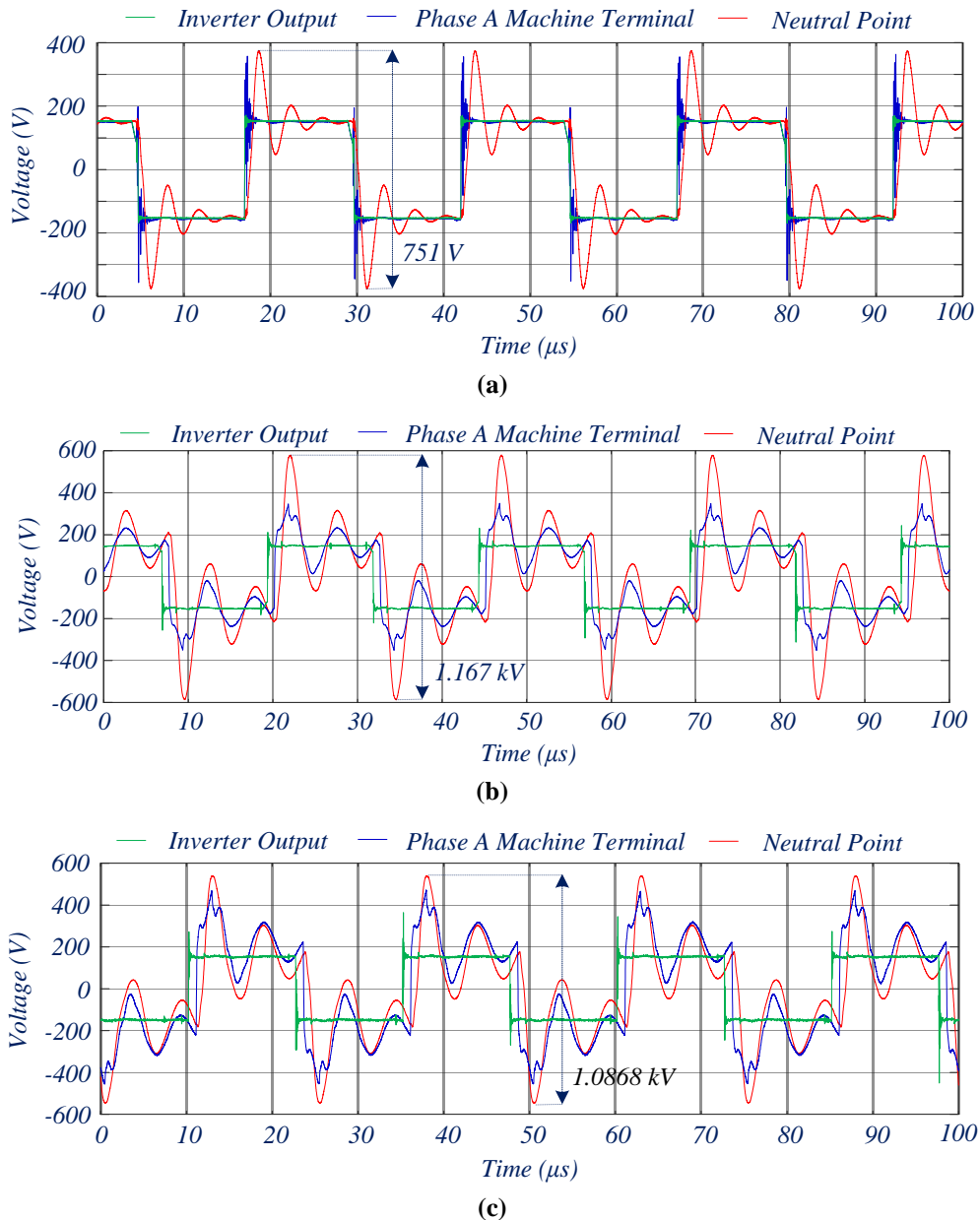


Figure 5.30: Experimentally measured voltage stress at the terminal and at the neutral point of the machine with respect to the core (DC Link voltage = 300 V); (a) when the cable length is 2.5 m, (b) when the cable length is 163 m, (c) when the cable length is 180 m.

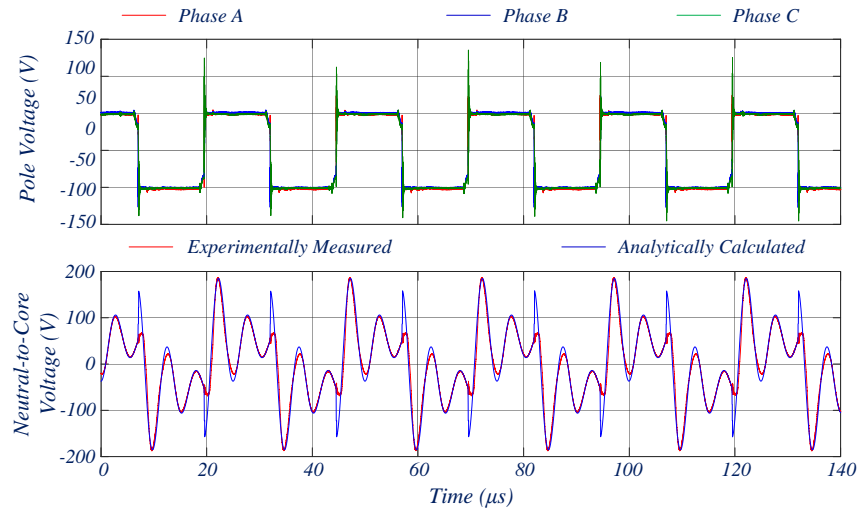


Figure 5.31: Experimental validation of the proposed analytical model at 40 kHz switching frequency with 163m long cable.

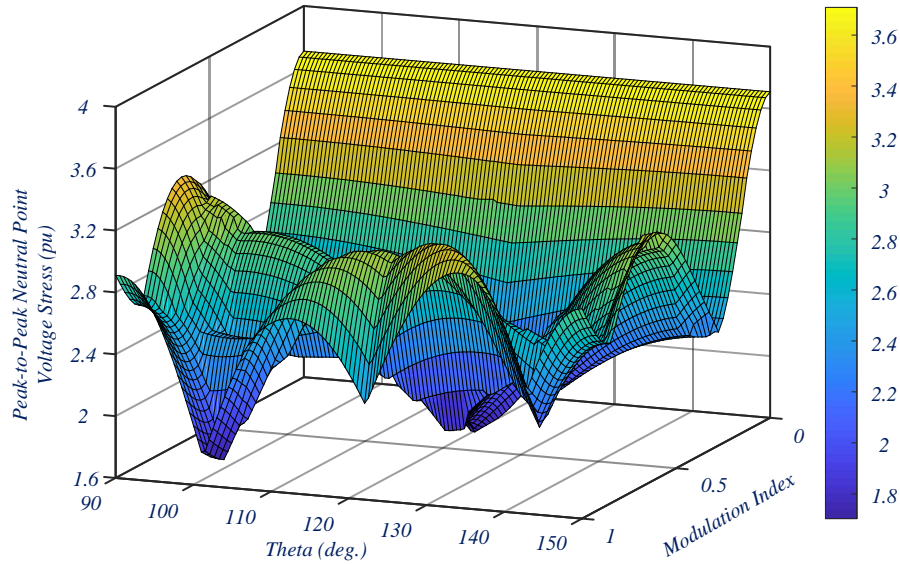


Figure 5.32: Peak-to-peak neutral-to-core voltage expressed in per-unit with respect to the 100V DC link voltage under PWM inverter operation at 40 kHz switching frequency and 163m long cable.

The LF oscillations have not been understood and addressed yet in the literature [14-19][37-39][153][156] owing to two reasons, (1) the use of inappropriate models representing stator winding and, (2) the voltage stress being studied with a single voltage pulse in solitary. Many works of literature [156] have modelled only the line end coil as an MCTL. In addition, they assumed the core as an impenetrable sheet and ignored the core loss. Furthermore, in [37][106] only the first five turns are modelled as Γ - cell and the rest are represented as a single π – cell. In [112], although all the turns are represented as Γ - cell, only single-phase is studied in isolation with the application of a voltage front. These methods fail to represent the wave propagation and reflection phenomenon correctly, consequently, fails to represent the first anti-

resonance frequency ($f_{ar_{m(1)}}$) of the stator winding. The application of a single voltage pulse in isolation leads to travelling waves and consequently, does not result in voltage stress across the coils close to the neutral point.

5.8 Summary

This chapter presents a comprehensive examination of the voltage distribution within the stator winding under PWM voltage pulses excitation. Apparently, the voltage distributes non-linearly within the winding. Under single voltage pulse excitation, the coil close to the terminal is most stressed. However, under PWM voltage pulses excitation, the last coil close to the neutral point is most stressed. Based on the analysis, it has been proclaimed that the voltage distribution is characterized by two oscillatory responses, one at the 2nd anti-resonance frequency ($f_{ar_{(c+m)(2)}}$) of the combined cable and the stator winding and the other at the 1st anti-resonance ($f_{ar_{m(1)}}$) frequency of the stator winding.

Akin to the cable, the TEM voltage waves travels within the stator winding but with a reduced speed due to the high permeability of the core. The voltage waves travelling at a speed corresponding to the 2nd anti-resonance frequency ($f_{ar_{(c+m)(2)}}$) of the combined cable and the stator winding causes voltage stress at the machine terminals. Since the 2nd anti-resonance frequency is in the MHz range, the high permeability of the core restricts the wave from penetrating deep into the winding, and the capacitive coupling between the winding and the core offers a low impedance shunt path to travel. This oscillatory mode engenders peak voltage stress at the terminals. An impedance measurement based method is proposed to calculate the surge impedance, thereby, predict the voltage stress at the terminal ends. Further, based on the cable parameters, an illustration between the OF and the ratio of the cable length and the critical cable length is proposed to facilitate the selection of the optimum rise time and the cable length for the minimum OF.

In addition, the voltage across the coils distributes non-uniformly, with peak voltage stress across the first coil from the terminal end. When the voltage distribution within the coil is observed, it turns out that, voltage stress across the insulation between the first and the second turn is maximum. If the first and the last turn are in close proximity, which may be possible in random wound winding, full coil voltage will appear across the turn insulation. Therefore,

special attention should be paid to ensure that the adjacent turns are only in close proximity while manufacturing.

Further, the results show that the coils close to the neutral point may be most stressed, in contrast with the state-of-art literature, which claims maximum voltage stress at the line end coil. The voltage stress across the coils close to the neutral point occurs due to voltage oscillations at the first anti-resonance frequency ($f_{ar_{m(1)}}$), which is primarily a characteristic of the stator winding. It occurs due to the superposition of travelling voltage waves impinging at the machine terminals

Based on the travelling wave theory, an analytical model is proposed to predict the voltage distribution within the winding under PWM inverter operation. The model accounts for the superposition of switching transients elicited due to the previous switching. In reliance on the model, the peak voltage stress occurs at the low modulation index, wherein, the dwell time between the switching events of the three phases is at a minimum. In addition, at high modulation index, the voltage stress is maximum at the instant of change in the switching sector, which occurs six times in a fundamental cycle. Importantly, the voltage stress increases with the switching frequency and increased cable length.

Furthermore, it is advised to have a short cable length such that the first anti-resonance frequency ($f_{ar_{c(1)}}$) of the cable is not close to the first anti-resonance frequency ($f_{ar_{m(1)}}$) of the stator winding, otherwise, the voltage is stressed across the groundwall insulation may exceed the safety level.

Passive filters are widely accepted in mitigating the voltage stress at the terminal ends of the machine. However, due to the difference in the location of the peak voltage stress, traditional filters cannot be used to mitigate the neutral point voltage stress. A customised passive filter based on the understanding described in this analysis is required to attenuate the voltage oscillations. The voltage stress at the neutral point can be reduced by reducing the dv/dt of the CM voltage. This can be achieved by using multi-level inverters, or modulation techniques that minimise the CM voltage. These solutions to the inimical effect of the voltage stress will be discussed comprehensively in the next chapter.

The finding has a number of implications. First, the existing filtering techniques and standards aimed at limiting dv/dt may not work well. Secondly, since the first anti-resonant

frequency ($f_{ar_{m(1)}}$) of machine windings is relatively low, an increase in PWM frequency is more likely to excite the resonance. Hence, a more effective measure to suppress the oscillation at the machine anti-resonance needs to be developed in order to exploit the fast switching capability of WBG devices.

Chapter 6: Voltage Stress Mitigation Technique

6.1 General

The fast slew rate and high switching frequency voltage pulse impinging at the machine terminals is well known to excite parasitic capacitive coupling, which engenders voltage oscillations. These voltage oscillations stress the machine insulation and may give rise to PD. Long-term exposure to these stresses leads to insulation breakdown in a premature period. In the previous chapter, the machine terminal and the neutral point of the winding have been identified as potential locations of the excessive voltage stress.

The voltage stress at the machine terminal has traditionally been dealt with in various ways. Primarily, changing the system configuration, installing passive filters at the input/output/DC link side, or using multi-level inverters are the ways to mitigate motor terminal voltage stresses. However, the solution to the voltage stress at the neutral terminal is unrecognised. In this chapter, the efficacy of the conventional filters in mitigating the voltage stress at the machine terminal and the neutral point is evaluated. Later, a low cost, retrofit passive filter is proposed to dampen the voltage stress at the neutral point.

6.2 Voltage Stress Mitigation at the Machine Terminals

As discussed in the previous chapter, the voltage stress at the machine terminal has been ascribed to the propagation of voltage waves within the cable. According to the propagation theory [116], the voltage at the interface of the cable and the machine is the superposition of the incident and the reflected wave which depends on the length of the cable (l_{cable}), rise time (t_r) of the voltage wave, the magnitude of the voltage (V_{DC}), propagation delay (t_p), and the velocity of the wave within the cable (\mathcal{G}_c). The time required by the voltage wave to travel through the cable along its length (l_{cable}) is called propagation delay (t_p), which is expressed as [116],

$$t_p = \frac{l_{cable}}{\mathcal{G}_c} \quad (6.1)$$

where, \mathcal{G} is the velocity of wave propagation, which is expressed as [116],

$$g_c = \frac{1}{\sqrt{l_c c_c}} \quad (6.2)$$

where, l_c and c_c are the per unit length cable inductance and capacitance respectively. For instance, when the fast slew rate voltage pulse impinges cable terminals, as illustrated in Figure 6.1, the peak voltage stress (V_{tmax}) at the machine terminal is expressed as,

$$\frac{V_{tmax}}{V_{DC}} = 1 + \frac{t_p \times \Gamma}{t_r} = 1 + \frac{l \times \Gamma}{g \times t_r} \quad \text{for } 2t_p < t_r \quad (6.3a)$$

$$\frac{V_{tmax}}{V_{DC}} = 1 + \Gamma \quad \text{for } 2t_p \geq t_r \quad (6.3b)$$

where, Γ is the reflection coefficient, which depends on the surge impedance of the machine (Z_{0m}) and the cable (Z_{0c}) as [116],

$$\Gamma = \frac{Z_{0m} - Z_{0c}}{Z_{0m} + Z_{0c}} \quad (6.4)$$

Consequently, the voltage stress at the machine terminals depends on the reflection coefficient (Γ), which in turn depends on the surge impedance of the cable (Z_{0c}) and the machine (Z_{0m}). The maximum voltage stress at the terminal could rise to 2 pu which occurs when $\Gamma = 1$, i.e., $Z_{0m} \gg Z_{0c}$. Notably, if $t_p \geq t_r$, the rise time and the cable length no longer affect the voltage stress, thereby, a short rise time and long cable length are two major factors of the voltage overshoot. However, the peak voltage stress can be suppressed if the t_r is long or the cable length is short.

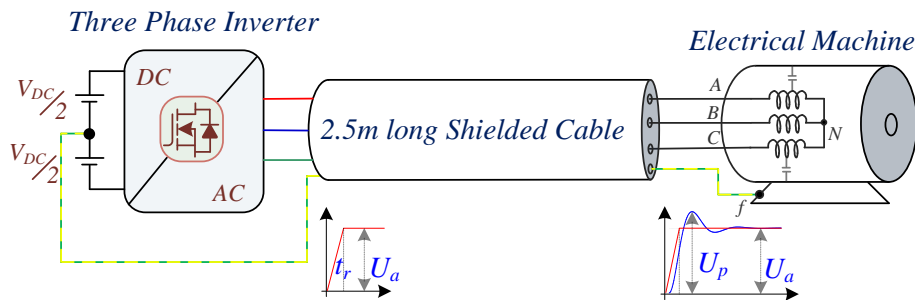


Figure 6.1: Schematic of a Toyota Prius hybrid vehicle employed stator winding fed by a SiC based VSI through a 2.5 long shielded cable.

The voltage stress has been addressed in various ways in literature subjected to the severity in a given situation. In the following section, the measures and their consequences are discussed in detail.

6.2.1 Changing the system configuration

The voltage stress can be suppressed by changing the cable length or the material properties of the cable.

6.2.1.1 Influence of Cable Length

If the cable length (l_{cable}) is longer than the critical cable length ($l_{cable_{cr}}$), the voltage stress doubles at the machine terminal, wherein, the critical cable length (l_c) is the length of the cable at a given rise time (t_r) of the pulse for which, $t_r = 2t_p$ [116]. As a result, shortening the cable length will reduce the overvoltage at the terminal end. Integrated motors are a well-known example for minimum cable length, wherein, the drive electronics and the motors are consolidated within one enclosure. There are additional advantages of the integrated motors, such as improved power density with less number of electronics components, single package installation, cost reduction by 20-40% [157], and integrated cooling can be realised. Although often it is an impractical solution, if the machine is not operated in hostile conditions or far from the inverter, an integrated drive can opt.

6.2.1.2 Influence of Cable Material Properties

The surge impedance of a lossless cable depends on the per unit length capacitance (c_c) and the inductance (l_c) as [116],

$$Z_{0_c} = \sqrt{\frac{l_c}{c_c}} \quad (6.5)$$

Generally, the surge impedance of the cable is much lower than the machine. By way of example, the surge impedance of the 2.5m long shielded cable measured in the previous chapter is 58.54 Ω , whereas, of the machine is 207.0 Ω . For a fast slew rate voltage pulse, from (6.3), the voltage stress depends on the reflection coefficient. Hence, low peak voltage can be attained if the surge impedance of the cable is increased. Selecting a cable with higher dielectric loss or the cables with ferrite rings [15] increases the surge impedance of the cable, which can be opted to suppress over-voltage.

6.2.2 Changing the Inverter Characteristics

The inverter characteristics such as rise time of the voltage pulse, dwell time between the switching of the same or different phases, voltage step at each switching instant plays a vital role in the peak voltage stress at the machine terminals.

6.2.2.1 Increasing Rise time:

Using (6.3a), the voltage stress at the machine terminal can be suppressed by reducing the slew rate of the voltage pulse. This can be achieved by controlling the turn ON/OFF characteristics of the switches of the inverters [158]. Customarily, the slew rate is slowed down by increasing the gate resistance. However, it incurs additional switching losses. One of the prominent ways is employing the soft-switching technique [158], wherein, the voltage and currents are decoupled such that the power loss is nearly zero. In this technique, the slew rate is controlled using resonant circuits, which include 3 resonant inductors and 6 snubber capacitors. The resonant action slows down the rise time of the voltage pulse, thereby; the voltage stress is limited to the 1 pu. The parameters of the resonant circuit, on the other hand, are dependent on the cable specifications and will vary depending on the system. Additionally, it requires 6 auxiliary switches which increases system cost.

6.2.2.2 Preventing Double Pulsing and Cross-Switching

The voltage stress at the machine terminal can exceed 2 pu, even if the cable length is shorter than the critical cable length, when the dwell time between the switching instants in the same phase or two different phases is less than 3τ [59], wherein, τ is the time constant of the cable which is expressed as,

$$\tau = \frac{2l_c}{r_{ac}} \quad (6.6)$$

where, l_c is the per unit length inductance of the cable and r_{ac} is the AC resistance per unit length of the cable conductor at the frequency of concern. Fundamentally, this is because the switching transient caused by the first switching has not decayed down before the next switching takes place, resulting in superposition of two switching transients. This phenomenon is called double pulsing. With a short cable, the frequency of voltage oscillation at the machine terminals is high, which leads to low l_c and high r_{ac} and hence small τ . Thus, a short cable reduces the likelihood of the double pulsing effect. Different modulation schemes have been

proposed in the literature [56-59][159] that account for this criterion of minimum dwell time. The capacitive coupling between the phase conductors also influences the switching transient arriving at different phases leading to excess voltage stress at the machine terminals. This phenomenon is called cross-switching. Likewise, the inductive coupling between phase windings, which are common in most electrical machines will also cause extra voltage stress due cross-switching effect. Avoiding drive operation at a low modulation index, choosing a short cable, and reducing the capacitive and magnetic coupling between the phases are the common measures for the suppression of the voltage stress.

6.2.2.3 Reducing Voltage Step during Switching

Reducing the voltage step during switching is another measure for reducing the voltage stress. One of the prominent solutions is employing a T-type converter [160-163]. In the T-type converter, 3 bidirectional switches are used between the mid-point of the DC link and the mid-point of the phase leg. The bidirectional switch is realised using two switches connected in a common-source configuration. The switch is used to introduce an additional voltage level between the voltage transition from $+V_{dc}/2$ to $-V_{dc}/2$. In the 3-Level T-type converter PWM scheme [161], due to additional voltage levels, the slew rate of the voltage pulse reduces by half. Consequently, the overvoltage at the machine terminal is limited to 1.5 pu. Compared to the 2-Level converter, the switching losses of the 3-Level T-type converter are less as the commutation between the voltage level is halved, whereas, the conduction losses are comparable [160].

The quasi 3-Level T-type converter PWM scheme [162-163] is another alternative wherein, the intermediate voltage level is applied for a brief period. The overvoltage at the machine terminal can be suppressed if the dwell time of the voltage level is adjusted based on the propagation delay and the rise time of the voltage pulse. With this method, the peak voltage stress can be limited to 1.2pu. However, the effective suppression of the voltage is influenced by the variation in rising time during normal operations.

Multi-level inverters such as a 3-Level neutral point clamped converter, cascaded H-bridge converters, or modular multi-level converters can be used to suppress the voltage. The increase in the number of voltage levels resembles the sinusoidal excitation with minimum harmonic content. In addition, reduced step voltage results in low voltage overshoot at the machine.

These aforementioned solutions are effective in voltage stress suppression, but at the expense of the increased number of components, cost, size, and power loss. However, the shortcoming can be offset with their merits in the medium voltage and high voltage drives.

6.2.3 Installing Active/Passive Filters

- Using a reactor [114-115] at the inverter output slows down the slew rate of the PWM voltage pulse. However, the voltage drop across it results in underutilization of DC bus voltage.
- Installing a dV/dt filter [121-122] comprising the inductor, capacitor and resistor limit the slew rate of the PWM voltage pulse resulting in reduced voltage stress at the machine terminal.
- Installing a sinewave filter [116-119] at the inverter output shunts away the HF currents, resulting in sinusoidal voltage at the machine terminals. However, these filters are bulky and costly as compared to the dV/dt filters. The voltage drop across the bulk inductor de-rates the converter. In addition, these filters are not suitable for high dynamic performance.
- Installing the motor termination unit at the motor terminals to match the machine impedance with the cable impedance. However, the studies show that these filters are less effective in suppressing the overvoltage [113].
- The HF ground return current can be suppressed using a CM transformer [124-127][164]. However, the transformer is less effective at low modulation index and low fundamental frequency, particularly when the machine operates under no load, or starts and stops frequently. Under these circumstances, the phase current is no more sinusoidal and the low-frequency distorted phase currents with high peak may cause magnetic saturation resulting in a reduction in filter inductance.
- Active filters [131-133] can be used to mitigate ground return current and the bearing current. However, it requires high power sensing and compensation circuits, which employ high bandwidth power transistors and operational amplifiers.

The aforementioned solutions are effective in attenuating the voltage stress at the machine terminals. However, the excessive neutral point voltage stress, which is discussed in the previous chapter, has not been addressed yet. In the following sections, the competence of the conventional passive filter such as the sinewave filter and dV/dt filter, is examined for voltage

stress mitigation and a low-cost passive retrofit filter is proposed which can be used to attenuate neutral point voltage stress and aids in increasing the lifetime of the insulation.

6.3 Voltage Stress Mitigation using Sinewave Filter

The sinewave filters are mainly installed in the VSI-fed drives to convert the HF square wave voltage pulse into sinusoidal excitation. For better attenuation of the HF voltage pulse, it is advised that the resonance frequency should be an order of magnitude less than the switching frequency (f_{sw}) [118]. However, to avoid resonance with the load, the resonance frequency of the filter should be higher than the fundamental frequency (f_s). Often, a resistor (R_f) is connected in series to dampen the resonance. By way of example, Figure 6.2 shows a sinewave filter connected at the inverter end, wherein, L_f and C_f are the inductance and the capacitance forming a second-order filter.

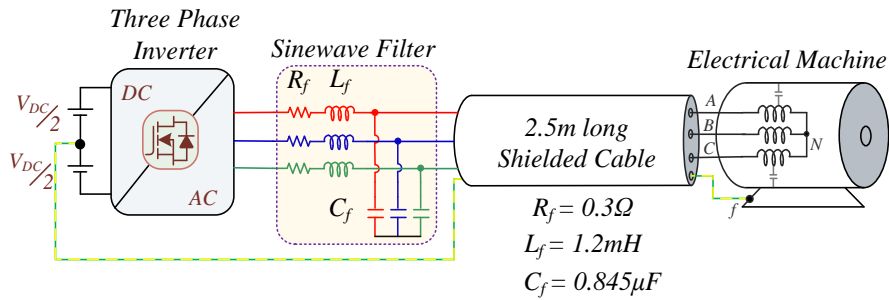


Figure 6.2: Schematic of VSI-fed drive with sinewave filter [118].

For the SiC based VSI fed drive, the L_f is calculated considering the current ripple (Δi) and the voltage drop (v_L) across it, which is expressed as [120],

$$\Delta i = \frac{V_{DC}}{8f_{sw}L_f} \quad (6.7)$$

$$v_L = i \left(\sqrt{R_f^2 + (2\pi f_s L_f)^2} \right) \quad (6.8)$$

where, V_{DC} is the DC link voltage, R_f is the series resistance of the inductor and i is the phase current. The L_f is calculated with the constraints that the maximum voltage drop should be less than 3% and the current ripple should be within 20%.

For better attenuation of the switching transients, the resonance frequency (f_c) of the filter should be an order lower than the switching frequency (f_{sw}). The capacitance can be calculated using the resonance frequency of the filter, which is expressed as [120],

$$f_c = \frac{1}{2\pi\sqrt{L_{eq}C_f}} \quad (6.9)$$

where, L_{eq} is the equivalent inductance which includes cable inductance (L_c), machine leakage inductance (L_m), and the filter inductance and is expressed as,

$$L_{eq} = \frac{L_f \times (L_m + L_c)}{L_f + (L_m + L_c)} \quad (6.10)$$

In the following analysis, using (6.7-6.10), the filter designed in [118] is used, since it is an exemplary representative of the SiC based VSI fed drives which are used in this analysis. Henceforth, the resonance frequency of the filter under study is 5kHz, $L_f = 1.2\text{mH}$, $R_f = 0.3\Omega$, and $C_f = 0.845\mu\text{F}$. The filter connected drive, also illustrated in Figure 6.2, is analysed in a MATLAB® environment with an assumption that the VSI is an ideal voltage source with a pulse rise time equal to 20ns. The DC link voltage is 550V. An HF behavioural model discussed in the previous chapter is used to represent the stator winding connected with the shielded cable.

As illustrated in Figure 6.3, the CM impedance of the filter is compared with those of the cable and machine, and the combined filter, cable, and the machine. The filter resonates (f_{ar_f}) at 5kHz, whereas, the cable connected machine resonates ($f_{ar_{(c+m)(1)}}$) at 227kHz. Due to the low resonance frequency of the filter, the anti-resonance frequency ($f_{ar_{(f+c+m)(1)}}$) of the combined filter, cable, and the machine shifts to 100kHz, with decreased impedance and damping. As a result, the neutral point voltage oscillates at 100kHz, which is illustrated in Figure 6.4. The filter reduces the impedance at the anti-resonance frequency of the combined system, consequently, aggravating the voltage oscillations at the neutral point. However, akin to the literature [116-119], due to increased impedance at frequencies above 1MHz and complete elimination of the 2nd anti-resonant mode ($f_{ar_{(c+m)(2)}}$) of the cable-machine system, the terminal voltage oscillations are damped. Henceforth, the sinewave filters are effective in reducing the voltage stress at the machine terminals but aggravate the stress at the neutral point. Thus, sinewave filters are detrimental to the main-wall insulation in the region close to the neutral point of the machine.

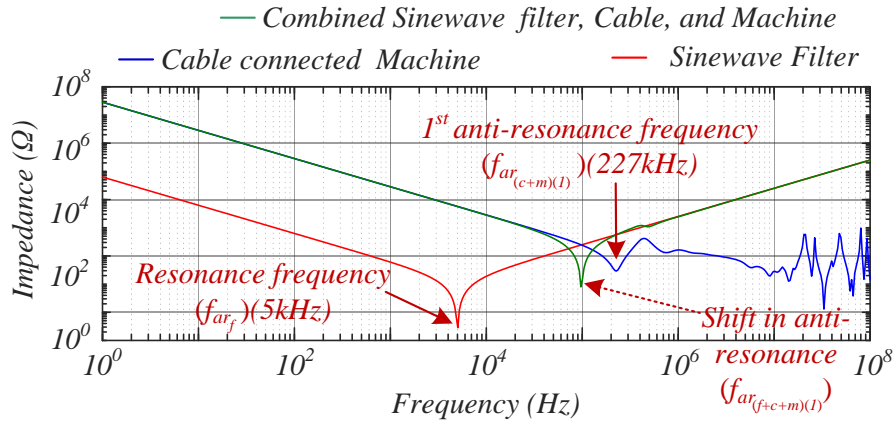


Figure 6.3: CM impedance measurement with sinewave filter.

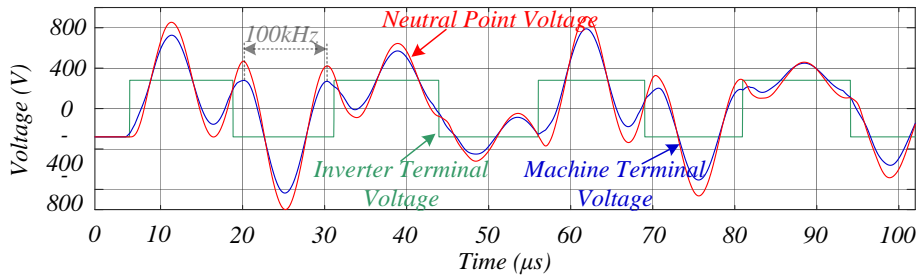


Figure 6.4: Voltage stress within the winding with Sinewave filter.

6.4 Voltage Stress Mitigation using dV/dt Filter

The dV/dt filter limits the slew rate of the voltage pulse impinging the machine terminal [121-122] [165]. The filter increases the rise time of the pulse, thereby, reducing the voltage stress at the machine terminals. The rise time and the DC link voltage of the drive under study is 20ns and 550V respectively. Thus, the dV/dt of the voltage pulse from the VSI is 27.5kV/μs. The dV/dt filter is designed to limit the slew rate to 4kV/μs to meet the NEMA standard MG1-part 31, which is a typical dV/dt of the Si based drive. Illustratively, Figure 6.5 shows the dV/dt filter connected to the SiC based drive at the inverter end.

The combination of inductance (L_f) and capacitance (C_f) forms a second order filter and the resistor (R_f) is used for damping the resonance. The series parameters are designed based on the voltage drop (v_L) across it. If the voltage drop is limited to 1.5% of the rated voltage, then the parameters are deduced as [120],

$$v_L = \frac{i}{\left(\sqrt{R_f^2 + \frac{1}{(2\pi f_s L_f)^2}} \right)} \leq 0.015V_{DC} \quad (6.11)$$

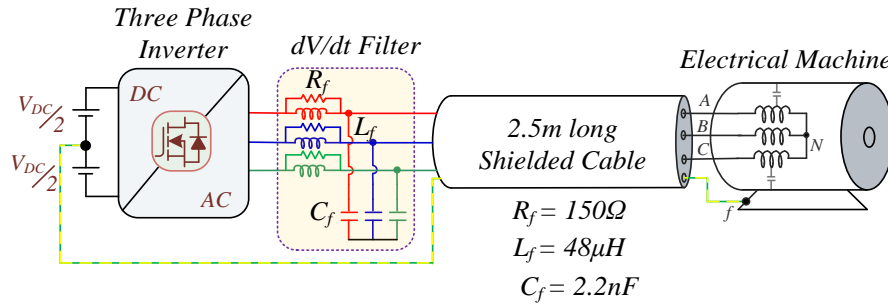


Figure 6.5: Schematic of VSI-fed drive with dV/dt filter [121].

where, i is the phase current and f_s is the fundamental frequency. With 550V DC link voltage and desired 4kV/ μ s slew rate, the rise time at the output of the filter should be 140ns. The product of L_f and C_f represents the one resonant cycle, which is also equal to 4 times the voltage rise time. Thus, L_f and C_f can be expressed as [120],

$$L_f C_f = 4t_r \quad (6.12)$$

The damping resistor decides the damping factor (ξ) of the voltage oscillations. The higher the damping factor, the lesser will be the resistance, and the better will be the damping. Thence, the R_f can be reckoned using (6.13) as [120],

$$R_f = \frac{1}{2\xi} \sqrt{\frac{L_f}{C_f}} \quad (6.13)$$

Using (6.11-6.13), the parameters of the filter can be determined. In the following analysis, the filter designed in [121] is used, since it is an exemplary representative of the SiC based VSI fed drives under study. Henceforth, the parameters of the filter under study are, $L_f = 48\mu\text{H}$, $R_f = 150\Omega$, and $C_f = 2.2\text{nF}$. Compared to the sinewave filter, the inductance and the capacitance of the dV/dt filter is small, owing to the higher resonance frequency (480 kHz), as calculated from (6.9).

For assessing the voltage stress at the machine terminal and at the neutral point, a MATLAB[®] Simulink-based model of dV/dt filter installed VSI-fed drive is used, wherein, the HF behaviour model of the cable connected machine is adapted from the previous chapter. In the model, the VSI is assumed as an ideal voltage source whose output voltage is a rectangular voltage pulse with $t_r = 20\text{ns}$, and magnitude equal to the DC link voltage (550V). The CM impedance of the filter is compared with those of the cable-connected machine, and the combined filter, cable, and machine in Figure 6.6. Compared to the 1st anti-resonance frequency

($f_{ar_{m(1)}}$) (227kHz) of the combined cable and machine, the resonance frequency (f_{ar_f}) of the filter (490kHz), is higher. Therefore, the 1st anti-resonance mode ($f_{ar_{(f+c+m)(1)}}$) of the combined filter, cable, and machine is unchanged. As is result and evident from Figure 6.7, the neutral point voltage oscillations remain undamped. However, due to increased impedance and damping around the 2nd anti-resonance frequency of the combined system, the terminal voltage oscillations are significantly suppressed.

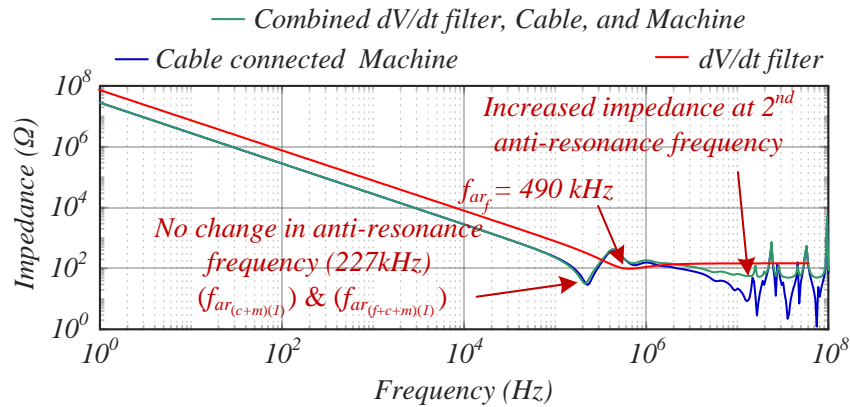


Figure 6.6: CM impedance measurement with dV/dt filter.

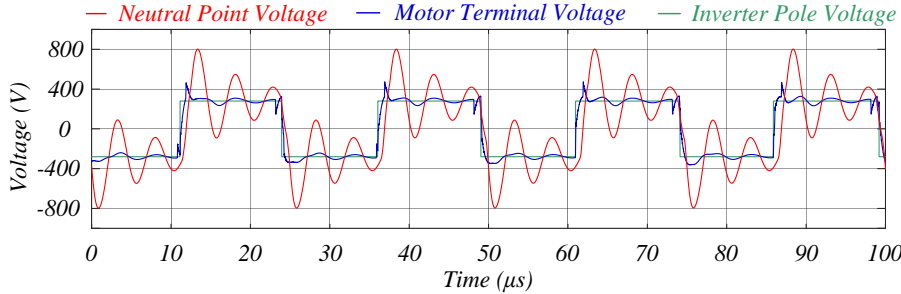


Figure 6.7: Voltage stress within the winding with dV/dt filter.

Although the sinewave and dV/dt filters are competent in attenuating the differential mode voltage oscillations, i.e., the voltage stress at the machine terminal, they are ineffectual in mitigating the voltage stress at the neutral point. These filters offer high impedance and damping at the 2nd anti-resonance frequency with marginal improvement at the 1st anti-resonance frequency. Thus, the voltage oscillations at the neutral point persist even after connecting the filter. The rationale behind the ineffectiveness of the conventional sinewave and dV/dt filter in damping the neutral point, voltage stress is comprehensively discussed in the following section.

6.5 Voltage Oscillations at the Neutral Point

Figure 6.8 shows a VSI-fed drive, wherein, the electrical machine is connected to a VSI through a shielded four-wire cable. At the inverter ends, the cable's protective earth (PE) wire is connected to the mid-point of the DC link, and at the machine end, it is connected to the machine core. It should be noted that in a mains-fed drive, although no direct wire connection is made between the earth and the inverter, a low impedance path to HF CM current exits through the front-end rectifier and earthed neutral point of the feed transformer. In an IT (isolé terre) grounding system, such as those in electrified transport systems, the low impedance path is provided through the Y-capacitors of an EMC filter which is necessary for compliance with relevant EMC standards [166-167]. Conventionally, the neutral point voltage, represented as v_N in Figure 6.8 is the voltage between the star-connected neutral point and the core of the machine. Assuming the machine as a balanced three-phase load, the neutral point voltage in steady-state when HF behaviour of the machine windings is ignored, can be expressed mathematically as,

$$v_N = \frac{v_A + v_B + v_C}{3} \quad (6.14)$$

Where, v_A , v_B , and v_C are the voltages measured at the machine phases with respect to (w.r.t) the machine core. Assuming, the cable as ideal, (6.14) can be transformed as;

$$v_N = \frac{v_{Ao} + v_{Bo} + v_{Co}}{3} \quad (6.15)$$

where, v_{Ao} , v_{Bo} , and v_{Co} are the pole voltages measured w.r.t the mid-point ('o') of the DC link. In the 2-level inverter, the neutral point voltage will be a six-step voltage varying within $\pm V_{DC}/2$, if the VSI is controlled by sinusoidal pulse width modulation (SPWM) or SVPWM technique [155]. In Figure 6.9, this is represented by a blue trace at three modulation indexes.

However, (6.15) holds only if the HF current flowing through the capacitive coupling between the stator winding and the core is neglected. As an illustration, the experimentally measured neutral point voltage (v_N) at the three modulation indexes is represented by a red trace in Figure 6.9. During the experiment, 60kW PMSM is used which is employed in the 2010 Toyota Prius hybrid vehicle [29] and is excited by a SiC inverter with a voltage rise time of 20ns at 40 kHz switching frequency. Evidently, (6.15) fails to represent the HF oscillatory components in the voltage waveform.

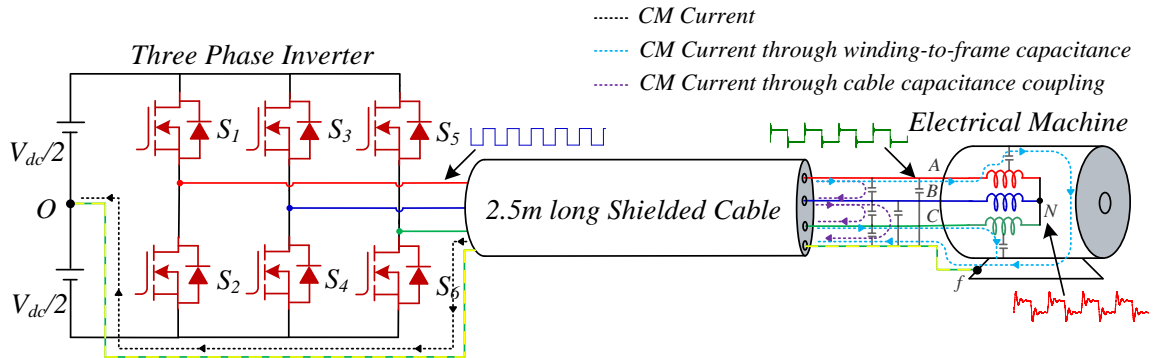


Figure 6.8: Conventional VSI-fed drives, wherein, the electrical machine is connected to the VSI through a 2.5m long shielded cable.

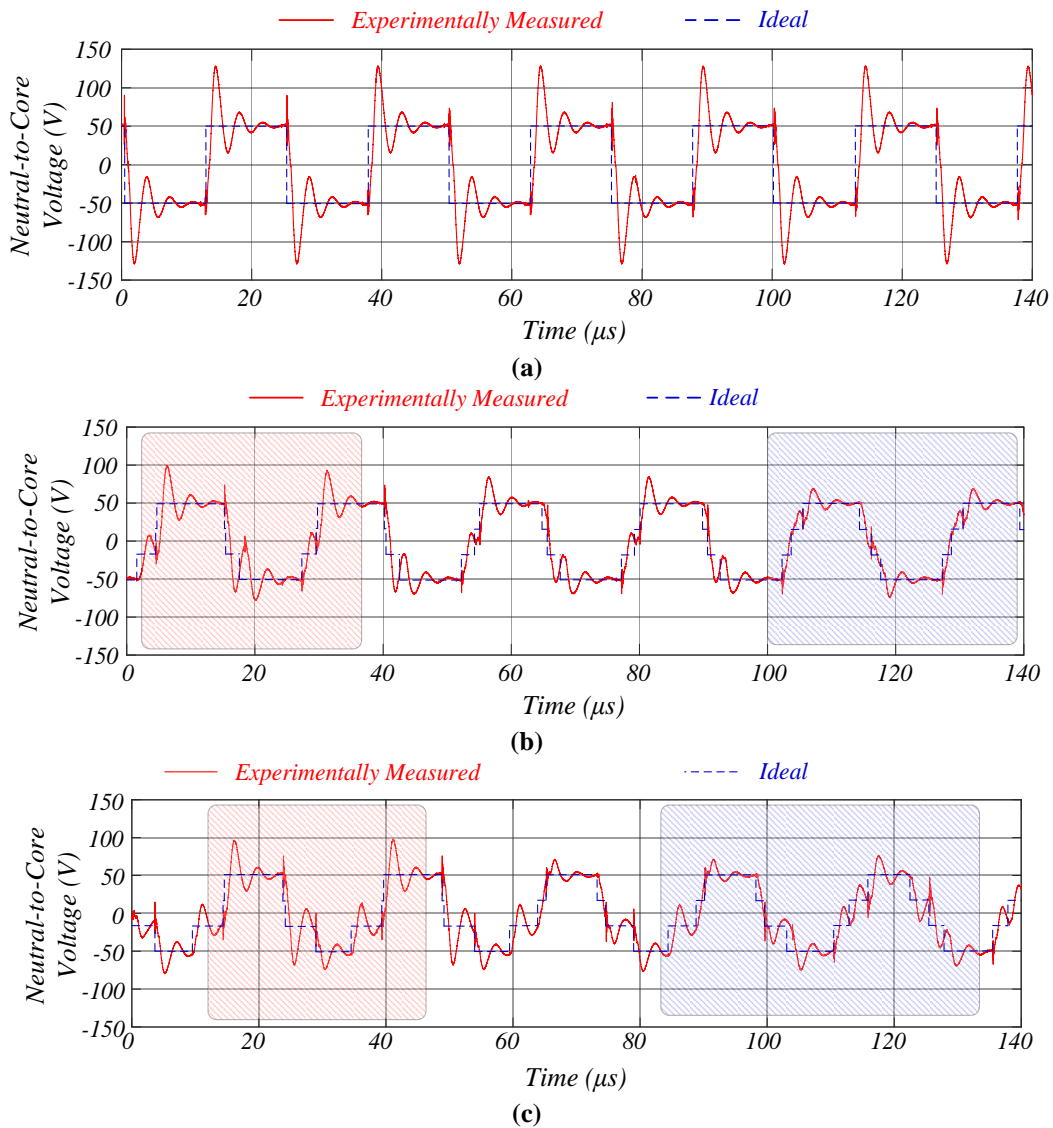


Figure 6.9: Experimentally measured neutral point voltage at three modulation indexes (m); (a) $m = 0.01$, (b) $m = 0.3$, (c) $m = 0.5$.

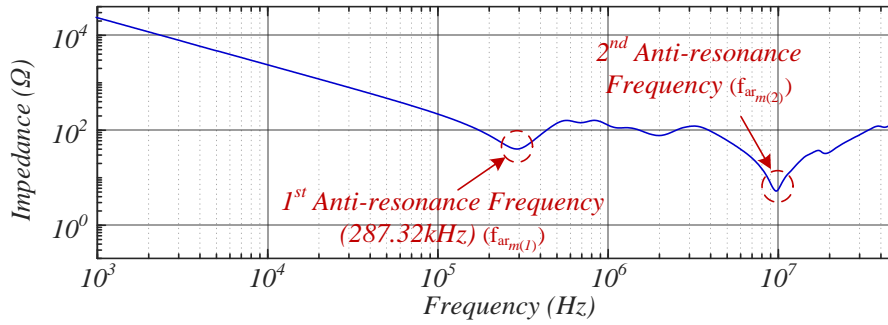


Figure 6.10: Experimentally measured CM impedance of the machine winding.

At a low modulation index ($m = 0.01$), in Figure 6.9, the switching at all three phases occurs simultaneously. Consequently, a consistent large peak can be observed at every switching instant. At higher modulation index ($m = 0.3$ or 0.5), during the red-shaded intervals in Figure 6.9, two of the three phases switches simultaneously, thereby, the voltage peaks are higher as compared to the blue-shaded intervals, wherein, all the three phases switch distinctly. Thus, peak voltage stress depends on the dwell time between the switching events at the phases, which, in Figure 6.9, is a function of the modulation index. The dwell times also vary with the phase angle of the voltage vector periodically in every 60 electrical degrees. This oscillatory mode occurs because of the resonance within the machine winding. Figure 6.10 shows the CM impedance measured at the terminal of the machine, wherein, the 1st anti-resonance frequency ($f_{ar_{m(1)}}$) of the winding is at 287.32kHz, which corresponds to the frequency of the voltage oscillations in the neutral point. The above analysis is discussed comprehensively in [20-21].

Often, it is advised that shortening the cable length reduces the peak voltage stress at the machine terminals [15]. However, the neutral point oscillatory mode is independent of the cable length. Illustratively, Figure 6.11 compares the neutral point voltage measured experimentally between two different cable lengths (l_{cable}), (a) $l_{cable} = 2.5\text{m}$, (b) $l_{cable} = 0.5\text{m}$ at the DC link voltage of 550V, the voltage rise time of 20ns, and switching frequency of 40kHz. In both cases, the neutral point voltage remains undamped.

The solutions proposed in the literature [114-119] [121-122][124-127][164] are aimed at attenuating the voltage stress at the terminal voltage and the resultant CM current while the peak voltage stress at the neutral point has not been addressed. Likewise, passive filters such as line reactors, sinewave filters, dV/dt filters, or, CM choke proposed in the literature are more focused on attenuating the voltage stress at the terminal end of the machine. For effective

attenuation of the CM current, the oscillatory nature of the voltages in machine windings must be understood as it influences the leakage current through the machine insulation.

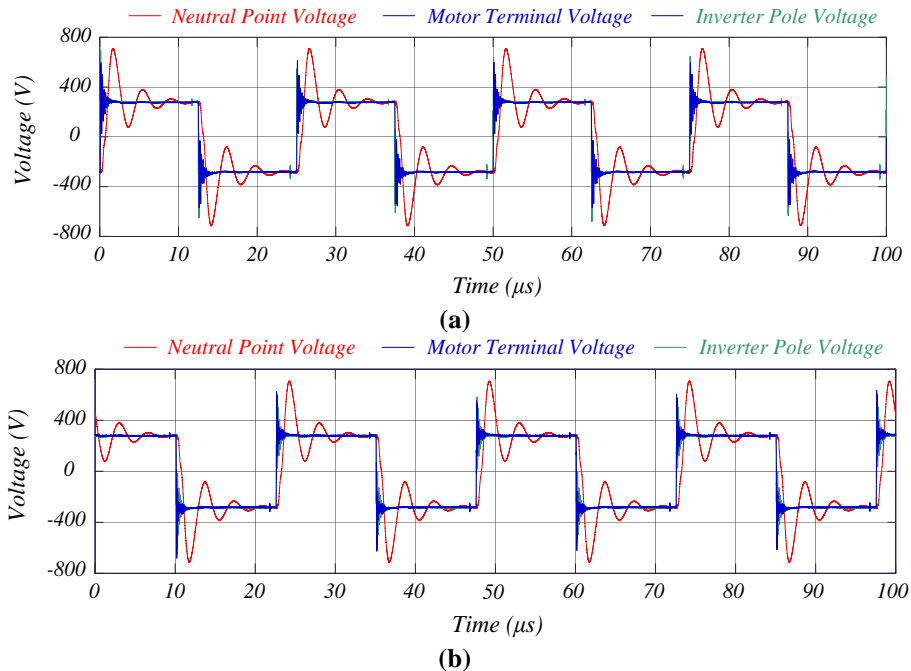


Figure 6.11: Experimentally measured neutral point voltage at different cable length (l); (a) $l = 2.5\text{m}$, (b) $l = 0.5\text{m}$.

As the cause of the voltage stress at the neutral point is now well-understood, an all-embracing analysis is required to investigate a solution that is affordable, less bulky, compact in size, and retrofit so that it can be accepted by the machine manufacturers without any design changes and can be retrofitted to an existing motor in service to extend their lifetime.

6.6 Design of a Low Cost, Retrofit, Passive RC Filter

Being simple, reliable, and cost-effective, passive filtering techniques are widely used in industrial practices. Although passive filters are prominent in suppressing voltage stress at the machine terminal, the neutral point voltage stress remains unaddressed. The oscillatory mode of the voltage causing stress at the neutral point has its genesis in the anti-resonance phenomenon. If somehow, the impedance at the anti-resonance frequency is increased, the oscillation will swiftly dampen. Connecting a resistor across the neutral point and the core of the machine is one of the techniques to do this [168]. By way of example, Figure 6.12 shows the comparison of the CM impedance of the machine with and without a resistor, wherein, a 165Ω resistor is used. As illustrated, the resistor increases the damping at the anti-resonance frequency. However, the impedance at the low frequency is significantly reduced, resulting in

excess CM current flowing through the resistor. Hence such a practice will impede any insulation health monitoring technique based on CM current sensing [169-170].

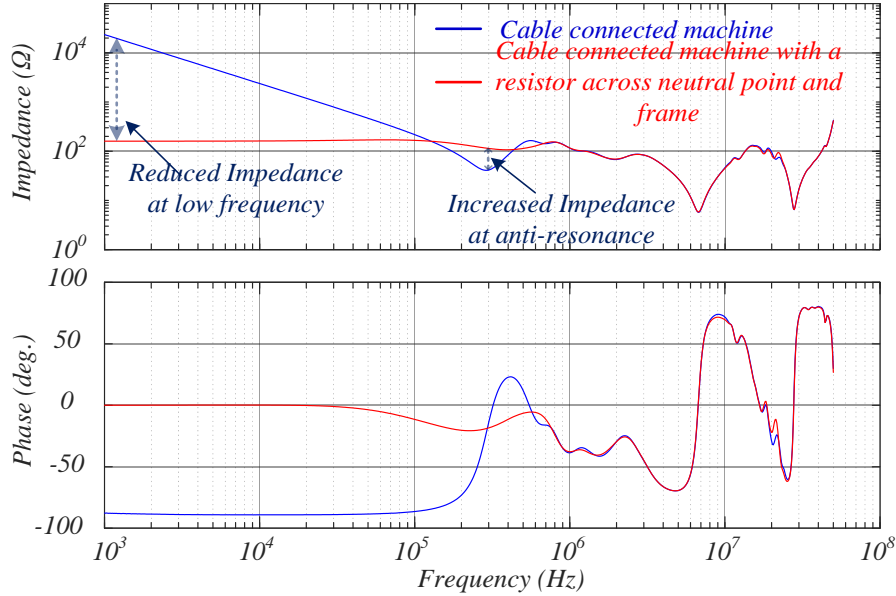


Figure 6.12: Experimental measured CM impedance of the cable connected stator winding with and without a resistor connected across the neutral point and the core of the machine.

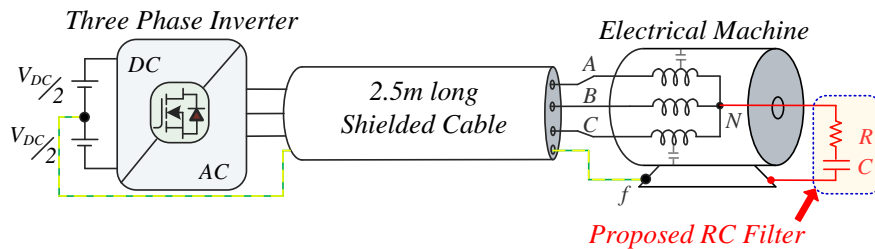


Figure 6.13: Proposed passive filter connected between the neutral point and the core of the machine.

Another possible solution for increasing the damping is a series connected first-order circuit. Figure 6.13 shows the schematic of the proposed passive filter, wherein, a series connected resistance (R) and capacitance (C) are connected between the neutral point and the core of the machine. At the neutral point, the capacitance provides a low impedance to the HF oscillatory voltage, whereas, the resistance dissipates oscillatory energy stored in the capacitor and limits the current through the capacitor. High order filters are possible but this increases circuit complexity. Thus, for simplicity, the proposed filter aids in the attenuation of the neutral point voltage stress with minimum component counts and losses.

As discussed in the previous section, voltage oscillations occur due to the anti-resonance phenomenon. The winding offers low impedance and low damping at the anti-resonance frequency, thereby, resulting in voltage oscillations. These oscillations can be damped by

increasing the impedance and damping at this frequency, which can be achieved using the RC filter.

The parameters of the filters are evaluated based on the measured impedance of the cable connected winding at the first anti-resonance frequency ($f_{ar_{(c+m)(1)}}$). Figure 6.14 shows the schematic of the CM and DM impedance measurements and the measured impedances are shown in Figure 6.15. From Figure 6.15, the CM and DM impedance at anti-resonance frequency is Z_{CM_0} and Z_{DM_0} respectively. These measurements can be perceived using an equivalent Π and T circuit with frequency-dependent parameters, as illustrated in Figure 6.16 (a-b). It is necessary to increase the impedance at the anti-resonance frequency to dampen the voltage oscillations. Let's say, with the filter connected to the machine, the impedance increases by factor k , then, the equivalent T circuit of the filter connected machine can be represented as shown in Figure 6.16 (c). Thus, the filter impedance (Z_{filter}), and hence, the filter parameters can be calculated using (6.3-6.4),

$$Z_{filter} = \frac{1}{\frac{1}{kZ_{CM_0} - \frac{Z_{DM_0}}{2}} - \frac{1}{Z_{CM_0} - \frac{Z_{DM_0}}{2}}} - \frac{Z_{DM_0}}{2} \quad (6.16)$$

$$R_{filter} = \text{real}(Z_{filter}) \quad (6.17a)$$

$$C_{filter} = -\frac{1}{\omega_{far} \times \text{imag}(Z_{filter})} \quad (6.17b)$$

By way of example, from Figure 6.15, the CM and DM impedance of the machine at anti-resonance frequency (ω_{far}) is $40.35 \angle -21.99$ and $247.03 \angle 60.32$ respectively. Using (6.16 - 6.17), the parameters of the filter impedance (Z_{filter}) for increasing the impedance to 100Ω will be $R_{filter} = 159.18 \Omega$ and $C_{filter} = 4.42 \text{nF}$.

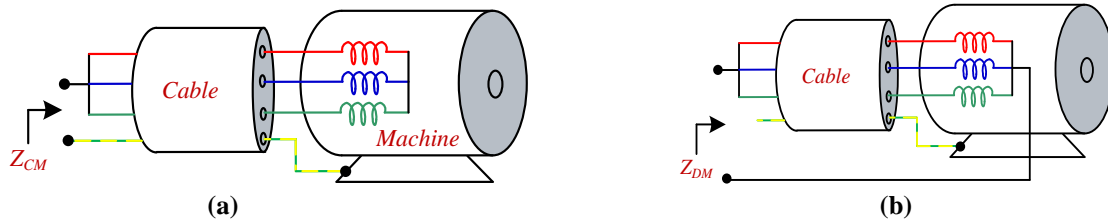


Figure 6.14: Experimental impedance measurements used for filter design (a) CM impedance, (b) DM impedance.

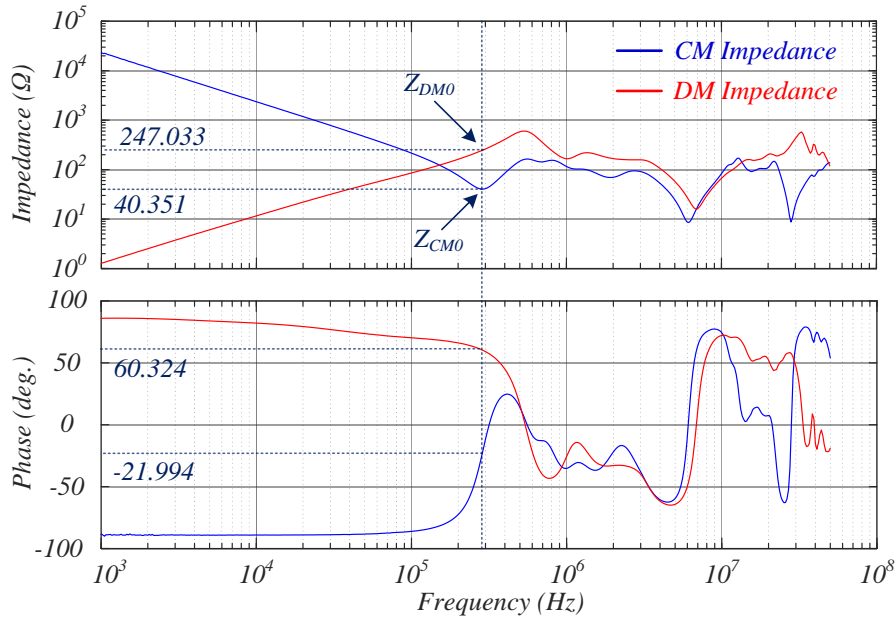


Figure 6.15: Experimentally measured CM and DM impedance of the cable connected machine winding.

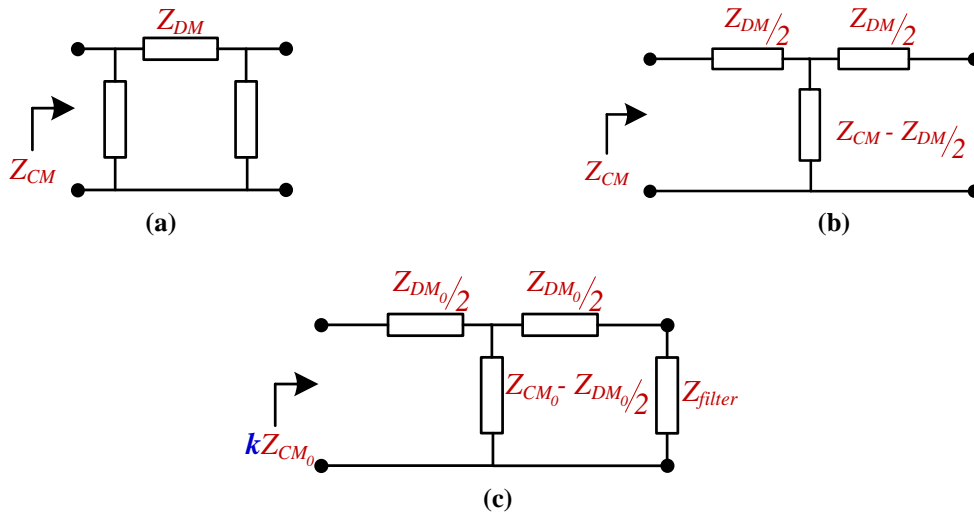


Figure 6.16: Frequency-dependent equivalent circuit of the machine based on CM DM impedance measurement, (a) II circuit, (b) T Circuit, (c) Equivalent circuit with a proposed RC filter.

6.7 Experimental Validation

The effectiveness of the conventional filters in attenuation of the voltage oscillation at the neutral point of a machine winding has been evaluated in sections 6.3 and 6.4, where, it is illustrated that the conventional filter does not alleviate the neutral point voltage oscillation. In the following section, the efficacy of the proposed RC filter designed in the previous section is experimentally evaluated.

The experimental rig developed to analyse the filter performance is illustrated in Figure 6.17, wherein, the filter is installed to a VSI which feeds the stator of a 60kW PMSM machine used

in the 2010 Toyota Prius hybrid vehicle [29]. The cable between the VSI and machine is a 2.5m long shielded LAPP manufactured, whose specification is illustrated in [20]. The VSI is a SiC MOSFET-based inverter with 1200V, 60A C2M0040120 CREE manufactured devices. In the experiments, the voltage at the DC link is 550V and the rise time of the voltage pulse is 20ns.

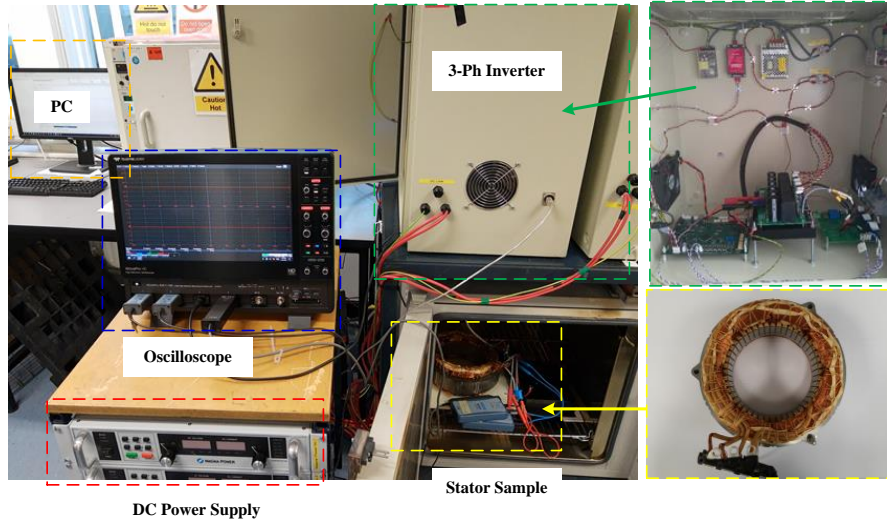


Figure 6.17: Experimental rig under study illustrating Toyota Prius vehicle connected to a three-phase VSI through 2.5m long shielded cable.

The VSI is operated in current control mode with a 40kHz switching frequency. The current control loop adjusts the modulation index in such a way the RMS phase current is 1A and the peak phase current is 10A. The PE wire of the cable is connected to the mid-point of the DC link at the inverter end, and to the machine core at the machine end. During the experiment, 1400V, 100MHz bandwidth ADP305 Teledyne Lecroy high voltage active differential probes are used to measure the Phase A pole voltage, Phase A machine terminal-to-core voltage, and the neutral point-to-core voltage. The CM current is measured using 30A, 50MHz Bandwidth, Teledyne Lecroy CP030 current probe.

6.7.1 Voltage Stress Mitigation using Passive RC Filter

Without any filter connected to the VSI-fed drive, at a low modulation index and 550V DC link voltage, Figure 6.18 shows the measured Phase A pole voltage, Phase A machine terminal-to-core voltage, neutral point-to-core voltage, and the CM current. Notably, the peak-to-peak neutral point voltage is 1.4kV and the CM RMS current is 1.358A with the peak-to-peak current of 14A. The oscillatory modes at the neutral point correspond to the 1st anti-resonance frequency ($f_{ar_{(c+m)(1)}}$) of the combined cable and the machine. The peak-to-peak voltage stress at the machine terminal is 1kV.

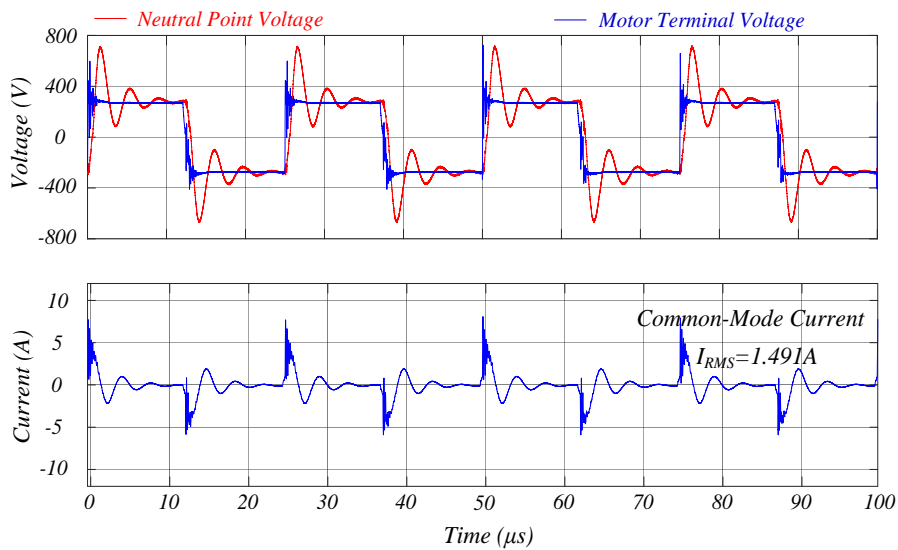


Figure 6.18: Experimentally measured voltage stress within winding when no filter connected to the machine.

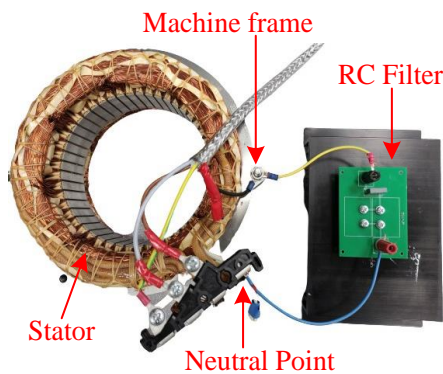


Figure 6.19: Experimental prototype of the proposed RC filter connected to the Toyota Prius hybrid vehicle employed stator winding.

The experimental prototype of the proposed RC filter connected between the neutral and the core of the stator winding is illustrated in Figure 6.19. Compared to the theoretically calculated $R = 159.18\Omega$ and $C = 4.42\text{nF}$, a 4.7nF Vishay manufactured metalised polypropylene film capacitor and two 330Ω , 90W thick film power resistor connected in parallel are used. As illustrated in Figure 6.20, after connecting the filter between the neutral point and the core of the machine, the first anti-resonance frequency shifts to 190kHz with increased impedance. Thereby, the oscillation frequency reduces from 287.32kHz to 190kHz with increased damping. Inevitably, also illustrated in Figure 6.21, the peak-to-peak voltage is reduced substantially from 1.4kV to 903.3V . The loss incurred by the resistor is 67.18W , which is merely 0.112% of the rated power of the machine. The peak-to-peak CM current reduces to 12.37A . The HF oscillation and its magnitude in the CM current depend on the CM voltage experienced by the machine windings. In the regions close to the terminals, the CM voltage

oscillates at HF around the 2nd anti-resonant frequency ($f_{ar(c+m)(2)}$) of the cable-machine while that close to the neutral point oscillates around the 1st anti-resonant frequency ($f_{ar(c+m)(1)}$) of the cable-machine. Thus, with the reduction of the CM voltage at the neutral point, the CM current is also reduced. The experiments are conducted during the light load condition where the CM voltage is the largest as discussed in Chapter 5, which implies that it is the maximum loss that could occur, as the losses decrease with increased loading (modulation index).

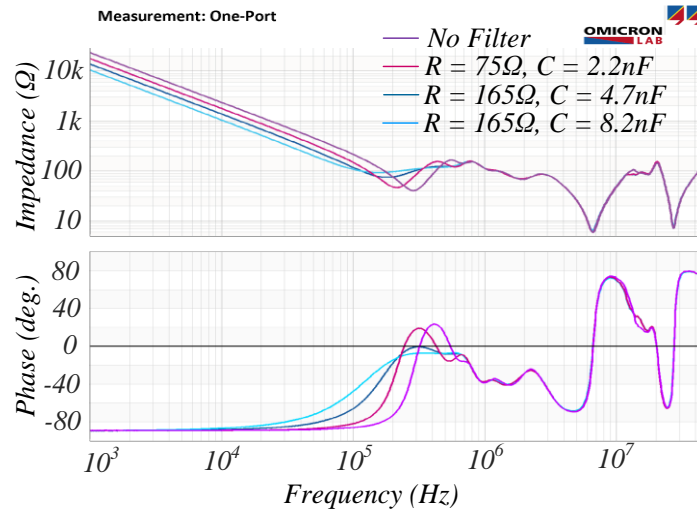


Figure 6.20: Experimentally measured CM impedance with a proposed RC filter.

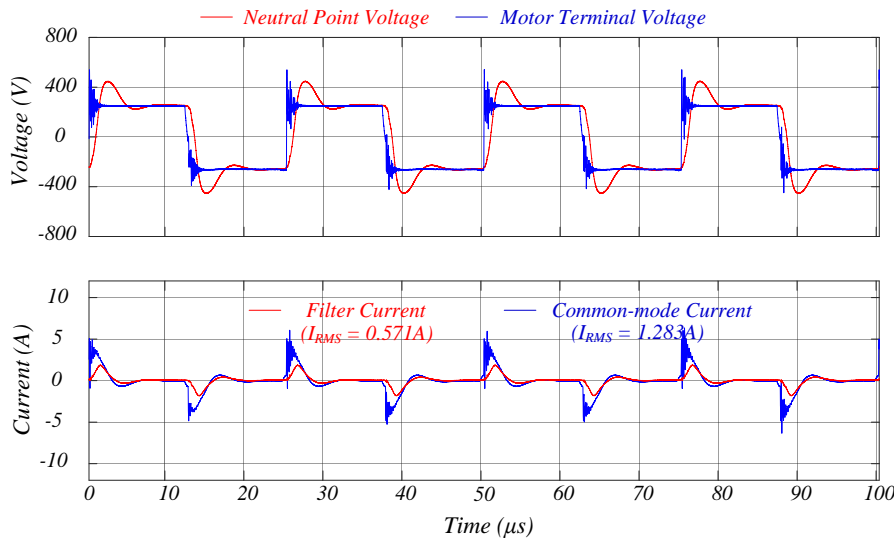


Figure 6.21: Experimentally measured voltage stress within winding with RC Filter, $R = 165\Omega$, $C = 4.7nF$.

6.7.2 Optimum RC Filter Selection

The parameters of the RC filter are influential in the suppression of voltage stress. During experiments, 9 different RC filter parameter combinations were assessed to explore the best solution with less losses. Combination of three different R and C, i.e., $R = 75\Omega$, 165Ω , and

340 Ω , and $C = 2.2\text{nF}$, 4.7nF, and 8.2nF were examined. Evidently, from Figure 6.20, increasing the capacitance to 8.2nF, lowers the anti-resonance frequency to 120kHz, while impedance at anti-resonance increases to 89 Ω . As a result, from Figure 6.22, with these parameters, the peak-to-peak neutral point voltage is reduced to 778V. However, the filter RMS current increases to 0.745A with peak-to-peak current stress of 4.9A, owing to increased losses to 91.58W. If the voltage stress is assumed as the response of the second order system, increased capacitance increases the damping factor of the system, thereby, the settling time increases with reduced voltage overshoot. If the capacitance is decreased to 2.2nF, the peak-to-peak voltage stress soars to 1.194kV. The system behaviour shifts towards the underdamped system with increased voltage overshoot and reduced settling time. However, the RMS current through the filter reduces to 2.93A with a 33.36% reduction in peak-to-peak current. The neutral point voltage can be decreased by increasing the capacitance, albeit at the expense of extra losses.

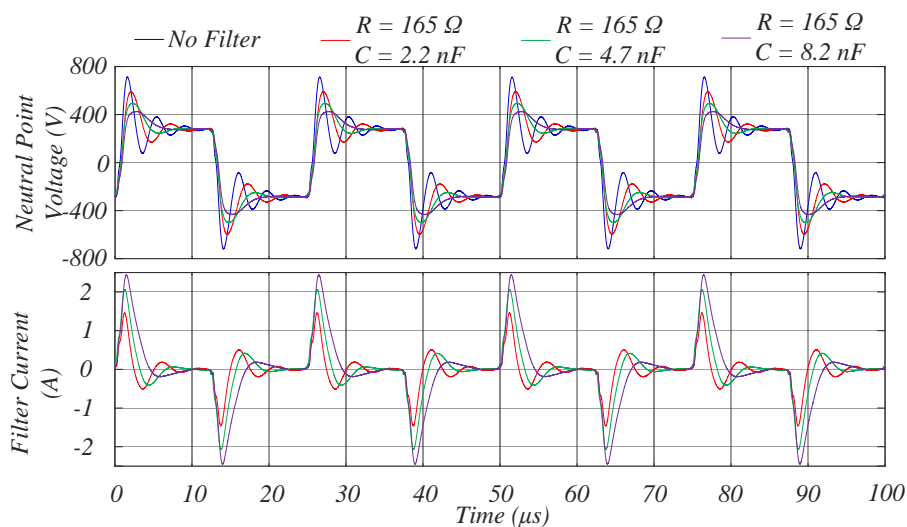


Figure 6.22: Performance of the proposed RC filter with different capacitance.

The resistive losses can be minimised by decreasing the resistance. If the resistance halves, as illustrated in Figure 6.23, the losses reduce by 30.83% (46.94W). However, the peak-to-peak current through the filter increases to 5.03A, with a 38.53% increase in RMS current. In addition, the peak-to-peak voltage stress increases to 1.119kV. The current stress can be reduced by increasing the resistance, let's say, if the resistance is doubled, the peak-to-peak current reduces to 3.04A. However, the filter becomes less effective in suppressing the voltage stress as it increases to 1.024kV with an 11.99% increase in losses. By decreasing the resistance, the oscillatory mode shifts towards an underdamped system. The losses will be minimum if the capacitance and the resistance are reduced. By way of example, when $R = 75$

Ω and $C = 2.2\text{nF}$, the loss reduces to 14.32W . However, as illustrated in Figure 6.24, it makes the filter less effective in damping the voltage stress as the peak-to-peak voltage stress soars to 1.148kV . This occurs as a result of low impedance at anti-resonance frequency which is illustrated in Figure 6.20.

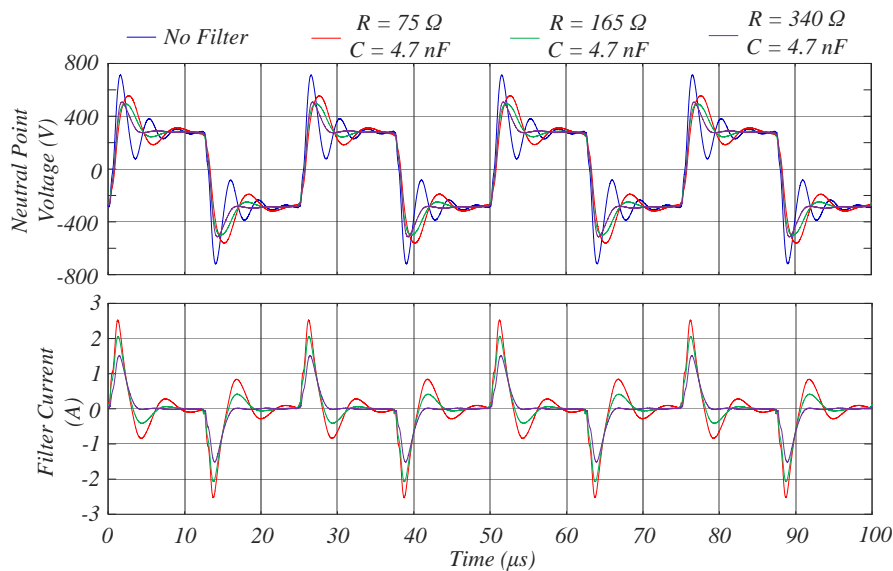


Figure 6.23: Performance of the proposed RC filter with different resistance.

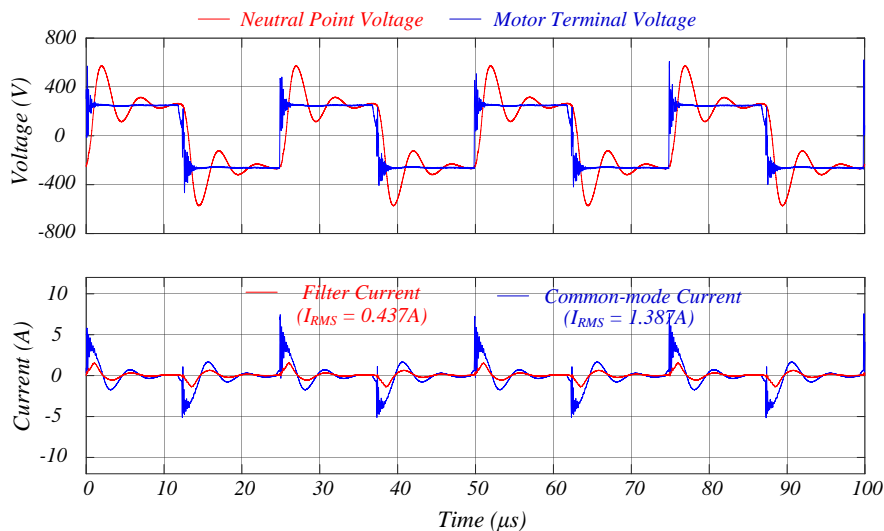
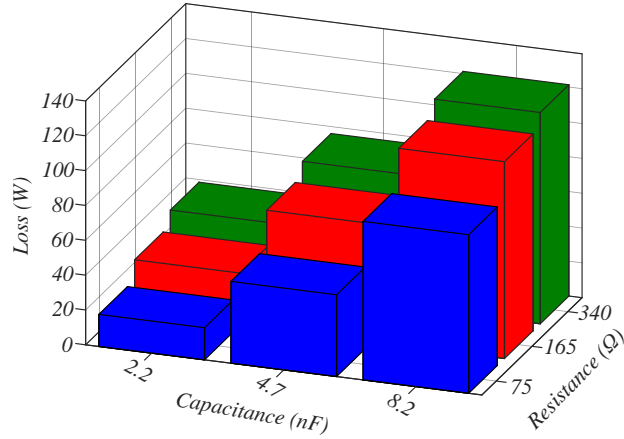


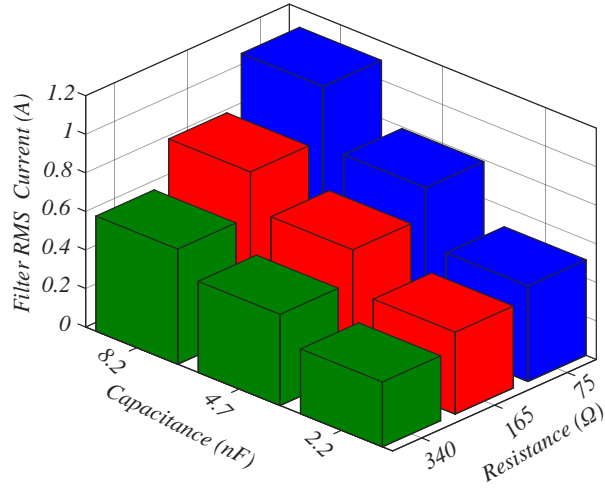
Figure 6.24: Experimentally measured voltage stress within winding with RC Filter ($R = 75\Omega$, $C = 2.2\text{nF}$).

The comparison between the filters against the losses, filter RMS current, and the peak-to-peak neutral point voltage stress is outlined in Figure 6.25. The least voltage stress occurs when $R = 165\Omega$ and $C = 8.2\text{nF}$, conducive to the increased service life of the machine. However, the losses increase to 91.58W . The least loss occurs, when $R = 75\Omega$ and $C = 2.2\text{nF}$. However, with this parameter, the filter is ineffective in damping the voltage oscillations, as the peak-to-peak

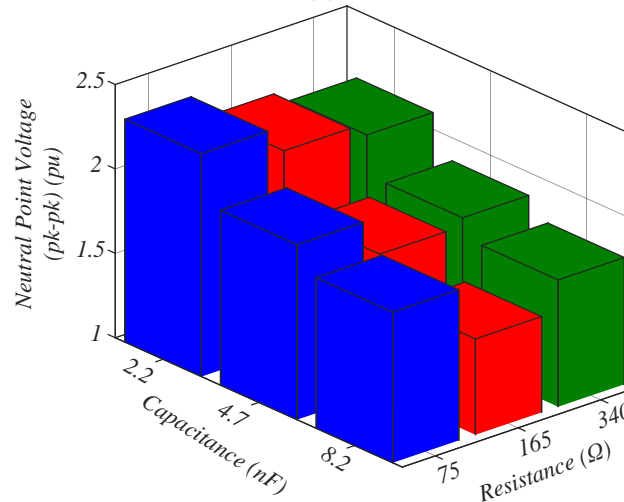
voltage stress reaches 1.148kV. The optimum solution of the filter is with $R = 165\Omega$ and $C = 4.7\text{nF}$, as calculated analytically, wherein the voltage stress is low with lower losses.



(a)



(b)



(c)

Figure 6.25: Comparison between different RC filter w.r.t experimentally measured parameters, (a) Filter loss comparison, (b) Filter RMS current comparison, (c) Neutral point voltage stress comparison

The RC filter is effective in alleviating the voltage stress at the neutral point with low losses. There are several conspicuous advantages of the RC filter listed as follows:

1) Improved service life

Conventional filters are often employed to reduce the terminal end voltage stress, however, it fails to fully damp voltage oscillations at the neutral point. In contrast, the proposed RC filters are effective in reducing the voltage stress across the main-wall insulation close to the neutral point, thereby, reducing the risk of PD and improving service life.

2) Low cost, smaller size, less lossy, and easy to install retrofit solution

The RC filter employs two power resistors and one film capacitor. Therefore, the total cost of the filter is quite low. In addition, the footprints of the R and C are small and compact. As discussed previously, the losses in the RC filter are only 0.112% of the rated power of the motor drive. The installation of the RC filter is relatively simple, as it has only two components and does not require redesigning of the drive system. Thus, it offers a retrofit solution and can be installed on any old motor or any other machine in service where excessive voltage stress at the neutral point is present, to prevent insulation degradation.

3) No magnetic component

The RC filter does not employ any magnetic components, thereby, free from any magnetic losses. In conventional filters, inductors are often used, which not only increases size and weight but also incurs voltage drop and additional losses.

4) No effective voltage drop

Unlike conventional filters, the RC filters are not connected in series with the VSI and the machine. Instead, the filter is connected to the CM circuit. Therefore, a full DC bus can be utilised by the drive.

There are a few disadvantages of the proposed filter, which needs attention and are listed as follows:

1) Difficult installation under hostile environment

If the machine is deployed in a hostile condition, such as under high temperature, high pressure, or high moisture ingress, then cold/heat resistant circuit board and components within high-grade enclosures are required.

2) Accessible neutral point

To install the filter, the neutral point must be accessible, as should be connected across the neutral point and the core of the machine.

6.7.3 Design Modification of dV/dt Filter

The conventional filters are ineffective in attenuating the voltage stress at the neutral point. Indeed, they are efficacious in mitigating the terminal voltage stress, which is explored in detail in the literature [114-119]. However, with an appropriate design when the resonance frequency of the filter is less than the 1st anti-resonance frequency ($f_{ar_{(c+m)(1)}}$) of the cable-winding, a dV/dt filter can partially mitigate the neutral stress at the expense of increased size and cost. When the cable is relatively short, the 1st anti-resonance frequency ($f_{ar_{(c+m)(1)}}$) of the cable-winding is indeed very close to that of the machine winding as has been discussed in Chapter 5.

Figure 6.26 (a) shows the schematic of a dV/dt filter, wherein, L_f and C_f form a second-order filter and R_f is used to damp the resonance. The single phase equivalent circuit is illustrated in Figure 6.26 (b), whose input impedance is expressed as,

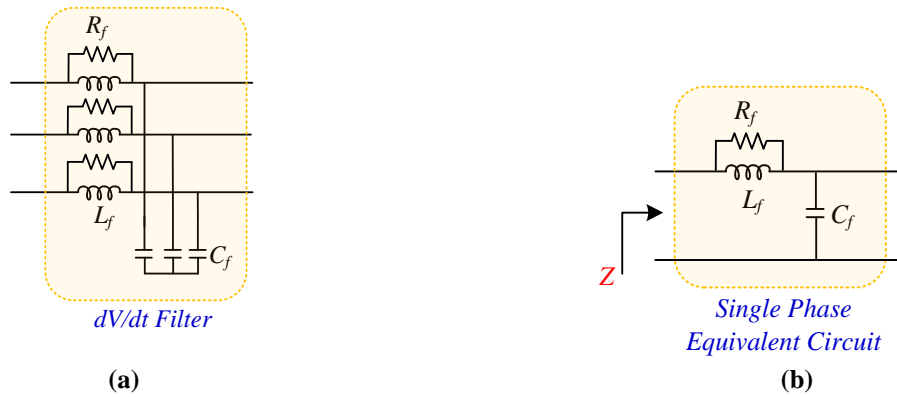


Figure 6.26: Schematic of dV/dt filter, (a) 3-Phase circuit, (b) Single phase equivalent circuit.

$$Z(s) = \frac{\left(\frac{s^2}{1/L_f C_f} + \frac{s}{R_f/L_f} + 1 \right)}{C_f s \left(1 + \frac{s}{R_f/L_f} \right)} \quad (6.18)$$

Thus, the input impedance of the filter has two first order poles at $\omega = 0$ and at $\omega_1 = R_f/L_f$, and one second order zero at $\omega_2 = 1/\sqrt{L_f C_f}$. The damping factor (ζ) of the second order zero is

$$\zeta = \frac{1}{2R_f} \sqrt{\frac{L_f}{C_f}} = \frac{\omega_2}{2\omega_1} \quad (6.19)$$

For a second order zero, low damping at the corner frequency can be avoided if $\zeta \geq 0.5$. Also, $\zeta \gg 0.5$, i.e., $\omega_2 \gg \omega_1$ leads to a larger inductance and low impedance at a frequency greater than the 2nd corner frequency. So, for an optimal design, $\zeta = 0.5$ ($\omega_1 = \omega_2$) is recommended. By way of example, the dV/dt filter discussed in section 4.4 is designed with $\zeta = 0.49$. The first corner frequency of the filter is, $\omega_1 = 498.76\text{kHz}$, and the second corner frequency is, $\omega_2 = 497.35\text{kHz}$. As the corner frequency is higher than the 1st anti-resonance frequency ($f_{ar(c+m)(1)}$) of the cable connected machine (287.32kHz), the filter is ineffective in damping the neutral point voltage stress. If, on the other hand, these two frequencies are placed lower than the 1st anti-resonant frequency ($f_{ar(c+m)(1)}$) of the cable-machine, the dV/dt filter will have an effect on reducing the voltage oscillation at the neutral point.

As an illustration, Figure 6.27(a) shows a Schaffner manufactured dV/dt filter [171] whose schematic is shown in Figure 6.27 (b). The filter is selected appropriately according to the voltage and power rating of the drive under study. As can be seen, the capacitance and inductance of the filter are much greater than those designed according to [121]. The star-connected capacitors at the input end are for suppressing EMI in very-high and ultra-high radio frequency range. Herein, for the sake of simplicity, the input capacitors can be ignored. Thus, the 1st corner frequency of the filter is $\omega_1 = 105.32\text{kHz}$, the 2nd corner frequency is $\omega_2 = 137.16\text{kHz}$ and the damping factor $\zeta = 0.65$.

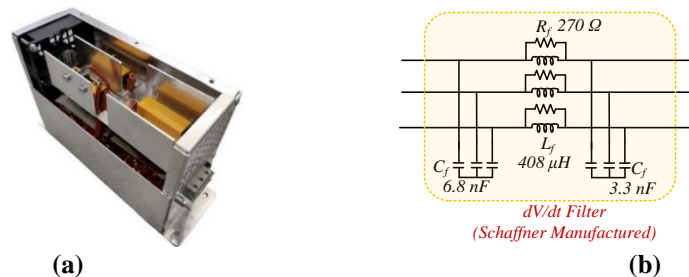


Figure 6.27: Schaffner Manufactured dV/dt Filter [171], (a) Actual filter, (b) Schematic of the filter

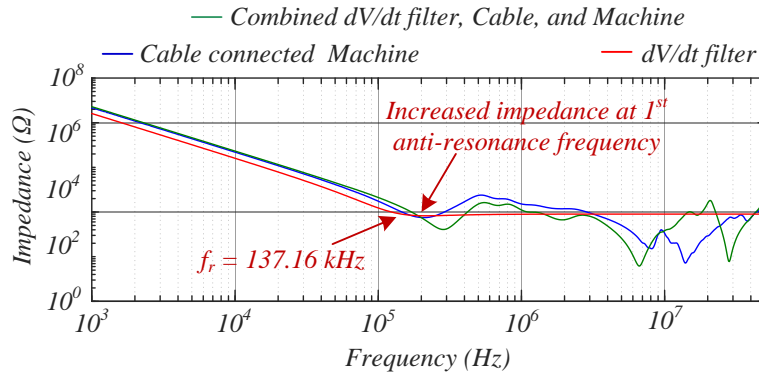


Figure 6.28: Experimentally measured CM impedance with Schaffner manufactured dV/dt filter.

The CM impedance of the cable connected machine, dV/dt filter, and the combined dV/dt filter, cable, and machine is illustrated in Figure 6.28. Evidently, corner frequency of the filter is less than the 1st anti-resonance frequency ($f_{ar_{(c+m)(1)}}$) of the cable connected machine (287.32kHz). Therefore, the filter is effective in increasing the impedance at the anti-resonance frequency. In conclusion, the dV/dt filter is effective in increasing the impedance and damping at the 1st anti-resonance frequency only if,

- The damping factor ζ is greater or equal than 0.5.
- The 2nd corner frequency of the filter is less than the 1st anti-resonance frequency ($f_{ar_{(c+m)(1)}}$) of the cable connected machine.

6.7.4 Effect of Combined dV/dt Filter and Proposed RC Filter

The efficacy of the Schaffner manufactured dV/dt filter is evaluated by connecting it in between the VSI and the cable. Without any filter, the peak-to-peak voltage stress is 1.4kV, which reduces by 17.85% (1.15kV) after connecting the dV/dt filter, as illustrated in Figure 6.29. However, compared to the RC filter, the peak-to-peak voltage stress at the neutral point is 27.31% higher, as are the cost and footprint of the filter, both of which are considerably higher. The dV/dt filter suppresses the terminal end voltage significantly with partial attenuation of the neutral point voltage. In contrast, the proposed RC filter suppresses the neutral point voltage notably with marginal attenuation of the terminal end voltage. The benefits of each are maximised when both the filters are used at the same time. When both the filters are connected, the peak-to-peak neutral point voltage is reduced to 903.3V and the peak-to-peak voltage stress at the machine terminal is reduced to 650V. The voltage overshoot at the machine terminal is reduced to 1.18pu. Therefore, the combination of the dV/dt filter and the

RC filter is the optimum solution for suppressing the peak voltage stress, resulting in reduced chances of premature failure.

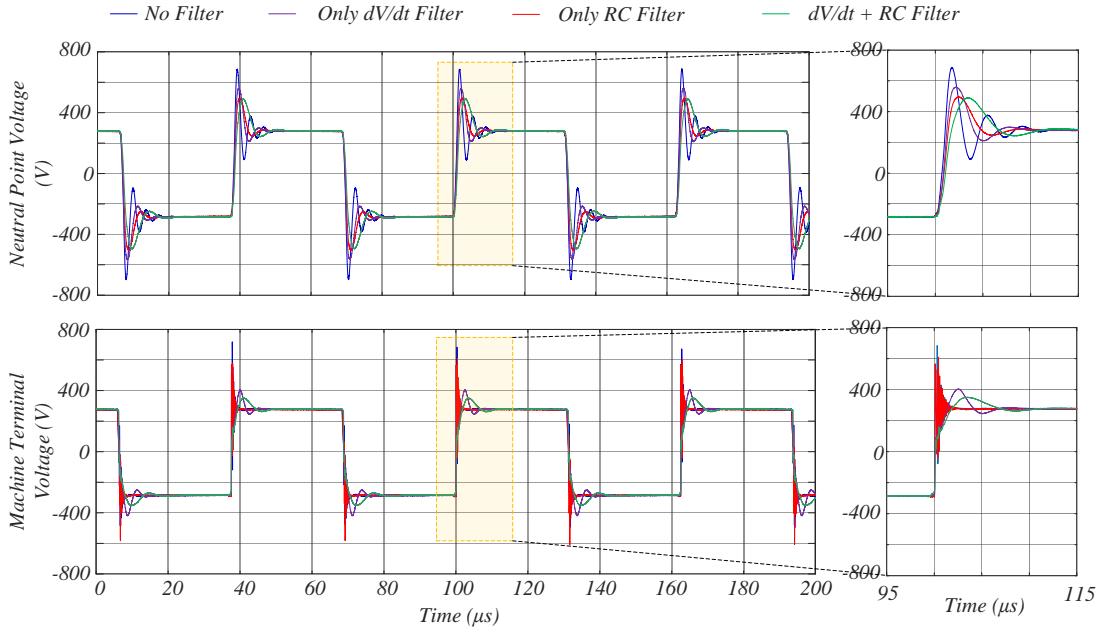


Figure 6.29: Experimentally measured voltage stress within winding with different filters.

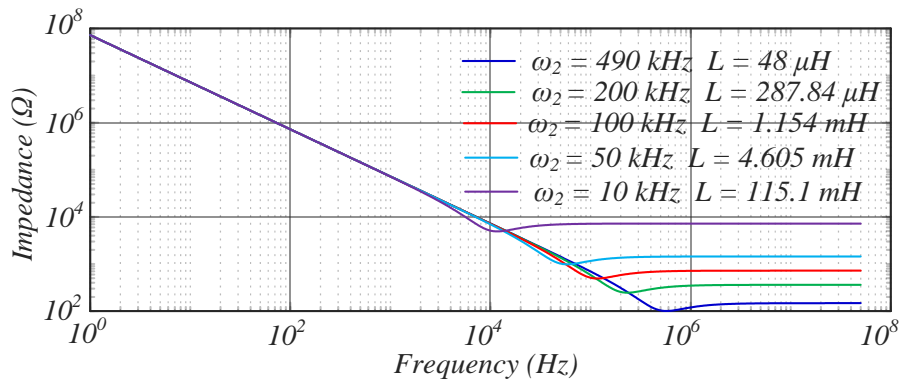


Figure 6.30: Effect of the resonance frequency of dV/dt filter on its CM impedance and filter parameters.

Indeed, for effective voltage stress suppression, the corner frequency of the filter depends on the 1st anti-resonance frequency. If the 1st anti-resonance frequency is low, the filter must be designed such that its 2nd corner frequency is less than the anti-resonance frequency. As a result, the size of the magnetic component of the filter increases. By way of example, Figure 6.30 shows the CM impedance of the dV/dt filter designed at different corner frequencies. Evidently, the inductance, and hence the size of the inductor, increases with the reduction in the corner frequency. However, the lower the 2nd corner frequency, the higher will be the impedance at the anti-resonance frequency, thereby, the better will be the voltage stress suppression. Thus, the benefits of the dV/dt filter come at the expense of increased size, weight, and cost.

6.8 Summary

Despite several studies on the mitigation of voltage stress in VSI-fed drive systems, the excessive voltage stress at the neutral point is one of the least discussed. In this work, a low-cost, passive, retrofit RC filter is proposed to reduce the voltage stress at the neutral point when it becomes excessive.

This study reveals that conventional filters such as sinewave filters are effective in reducing the voltage stress at the machine terminal, however, may aggravate the stress at the neutral point. In the case of the dV/dt filter, it is partially effective in alleviating the stress, unless the resonance frequency of the filter is less than the first anti-resonance frequency ($f_{ar_{(c+m)(1)}}$) of the combined cable and machine. Accordingly, if the anti-resonance frequency of the combined cable and machine is low, say 100kHz, then the resonance frequency of the filter should be lower than 100kHz, which leads to an increase in size, weight, and cost.

The RC filter, proposed here, is effective in alleviating the voltage stress at the neutral point with minimum losses. While designing the RC filter, a trade-off between the voltage stress and the filter losses must be accounted. The voltage stress mitigation capability of the filter can be enhanced but at the cost of increased resistive losses. Contrary, minimizing losses makes the filter less effective in attenuating voltage stress. This study proposes an analytical approach, which is based on impedance measurement, to select the optimum parameters of the filter.

The proposed filter offers a low cost, less lossy, and small size retrofit solution. The resistive power loss in the filter is merely 0.112% of the rated power of the drive. Compared to the RC filter, the conventional filters are more bulky, costly, and large in size. This owes to the absence of any magnetic component in the RC filter.

Chapter 7: Conclusion and Future Work

7.1 General

Transient voltage distribution within the stator winding under PWM voltage excitation has been a contentious subject since the emergence of variable frequency drives (VFDs). Indeed, the short rise or fall time of the PWM voltage pulse has offered better controllability to the drives with increased efficiency. However, as previously mentioned, the short rise or fall time rendered innumerable undesirable issues such as excessive voltage stress within the stator winding, EMI in the nearby equipment and bearing current.

Therefore, a HF model of the cable and the stator winding is developed, herein, to understand and address these detrimental consequences. In the HF model, the cable and the winding are represented as a continuum of lumped parameter circuits also known as a cell. Each cell represents a small section of the cable and the winding respectively. The parameters of the cell are deduced from the finite element analysis (FEA) of two-dimensional geometry of the cable cross-section and the stator slot.

Using the HF model, under PWM voltage excitation, the voltage distribution within the stator winding is established. The results illustrate that the peak voltage stress occurs at two different locations, which can be characterised by two voltage oscillatory modes. The voltage stress at the machine terminal is due to the voltage oscillating at the 2nd anti-resonance frequency ($f_{ar_{(c+m)(2)}}$) of the combined cable and the machine impedance, whereas the voltage stress at the neutral end is due to the 1st anti-resonance frequency ($f_{ar_{(c+m)(1)}}$). The voltage stress at the neutral point, however, which is the key contribution of this study, has not been discussed before. The voltage stress at the neutral point is due to the voltage oscillating at the 1st anti-resonance frequency ($f_{ar_{(c+m)(1)}}$) of the combined cable and stator winding impedance.

Voltage stress at the machine terminal has been addressed in the past. Various industry standards such as NEMA MG 1-2016 [172] and IEC 60034-25:2014 [15] have recommended permissible limits to the peak voltage stress and mitigation measures. The passive filtering

technique is one of the widely accepted mitigation measures, which have been explored in this study.

The finding has a number of implications. The foregoing analysis can be used to identify the potential location of insulation failures, assisting in the diagnosis and prognosis of any unexpected failures. It can also aid in the development of recommendations for the safe usage of VSI in VFDs. These implications and recommendations are comprehensively discussed in the following section.

7.2 Conclusion

The inimical effect of the VSI in the VFDs, especially the voltage stress within the stator winding has been studied so far wherein the HF model of the cable and the stator winding is employed. Using the developed model, voltage stress within the stator winding is characterised and the potential location of excessive voltage stress is identified along with its mitigation technique. The conclusion ensued from the foregoing analysis is listed as follows.

7.2.1 High-Frequency Modelling of Cable

Representation of the propagation and reflection of the TEM voltage wave within the cable is important to characterize the voltage stress at the machine terminals. This can be achieved by solving the transmission line equation. Given the complexity of solving the transmission line equation, the proposed method uses a lumped parameter circuit to realise the TEM wave propagation and reflection within the cable. The lumped parameter circuit is a continuum of cells representing a small section of the cable whose length must be less than the shortest wavelength of the TEM wave. As a result, for a PWM voltage pulse of rise time 20ns, the cell representing a 10cm length of the cable is used.

For an accurate representation of the cable behaviour, the model must encompass the frequency dependent parameters. The frequency dependent parameter can be realised lucidly using the Ladder circuit. The Ladder circuit is a combination of frequency independent passive elements, which approximates the frequency dependent parameters. The parameters of the circuit are deduced using VF, which approximates the state equation of the system by locating its dominant poles and residues over an observed domain. The key advantage of the Ladder circuit lies in its frequency independent parameter. Due to its frequency independence, a single lumped parameter circuit is enough to represent the cable over a wide range of frequencies.

In addition, the frequency dependent parameters of the cable conductors are mutually coupled. Without explicitly employing either the modal transformation, convolution, Fourier transform, or multiple circuits representing cable behaviour at different frequencies, all of which involve computational complexity, the mutual coupling can be incorporated into the lumped parameter circuit practically, yet lucidly, by employing a current controlled voltage and source. The proposed current controlled voltage source is connected in series with the Ladder circuit representing the self-impedance. The voltage source represents the voltage drop across the conductor due to the mutual coupling with the others and represents the mutual coupling explicitly.

7.2.2 High-Frequency Modelling of Stator Winding

The HF model of the stator winding is a special case of the cable model. Like the cable, the stator winding can be represented using lumped parameter circuit. The frequency dependent impedance of turns can be represented using a Ladder circuit and the mutual coupling between them can be represented using current controlled voltage source. Similar to the cable, the dielectric loss and the permittivity variation of the insulation are marginal. Therefore, the capacitive coupling can be represented purely as capacitance.

Howbeit, the medium surrounding the turns is non-homogeneous and non-linear. Due to the magnetic saturation and hysteresis effect, the magnetic properties of the electrical steel surrounding the turns within the slot are non-linear. As a result, the magnetic properties depend on the operating point. The non-linear behaviour of the steel can be realised using B-H curve, often provided by the manufacturers, whereas the core loss due to the hysteresis and eddy current effect can be represented as a resistive element. Unlike cable, the surrounding medium is a stack of insulated conductive steel. Though the laminated steel restricts the eddy current induction at a low frequency of excitation, the induced eddy current under HF excitation restricts the working flux penetrating deep into the steel. In addition, the induced eddy current results in additional core loss, which can be represented as a resistive element.

The induced eddy current inhibits the magnetic flux from penetrating the core, acting as a flux barrier. Thereupon, the high permeability of the stator core confines the HF components of the magnetic field within a single tooth-slot region. Similarly, due to the air gap and the induced eddy current in the rotor core, the HF flux linkage between the stator and the rotor is the least. Consequently, a single slot model is sufficient to compute the HF parameters.

The comparison between the predicted CM and DM impedance of the stator winding illustrates that if the mutual coupling between the turns is ignored, the predicted DM impedance is slightly lower at low frequency. Additionally, the predicted impedance manifests multiple pronounced resonances and anti-resonance frequency which is absent in measurement. The inductive coupling between the turns embedded within the same slot is inevitable. The inductive coupling between the turns contributes to the inductance of the winding and dampens the HF oscillations.

All the turns of the winding must be represented in the HF model. Representing only the first a few turns, say, five turns from the line end as a cell and remaining as lumped frequency independent parameters does not represent the distributed nature and the frequency dependency of the impedance of the winding. As the skin and proximity effect the parameters are frequency dependent and increase with increasing frequency, the DM impedance of the model decrease substantially and exhibits higher resonance and anti-resonance frequency.

Adding the mutual resistive and the inductive coupling to the self-impedance simplifies the model as only one Ladder circuit is required to represent turn impedance. However, this approach cannot be used to model the phase windings, which share the same slot, mainly in double layer winding.

Explicit representation of the mutual coupling using the current controlled voltage source is an accurate representation of the mutual couplings, however, it increases the computational time and resources. By way of example, in a turn-based model, if each coil of the winding has N_t turns, then the N_t^2 Ladder circuit is required to represent the coil. When the turns are embedded within the same slots, the mutual coupling between the turns is similar. Therefore, the mutual coupling can be represented in a simplified way by assuming that the mutual coupling between the turns is the same, which greatly reduces the number of ladder circuits to $2N_t$. In comparison, the impedance between the models with explicit representation and simplified representation is similar. Thus, a simplified representation of the mutual coupling can be used without loss of accuracy.

Generally, the winding turns of the machines in service are inaccessible. Only the terminal ends are accessible. Therefore, the proposed model can be used to identify the potential location of the excessive voltage stress within the stator winding of the machine in service. The HF

model can also be used for the diagnosis and the prognosis of the insulation failures, to avoid unexpected downtime.

7.2.3 Voltage Distribution under PWM Voltage Excitation

As previously mentioned, the HF model of the stator winding connected with the cable model can be used to study the voltage distribution under PWM voltage pulse excitation. Predictably, under single voltage pulse excitation, the voltage distributes non-uniformly within the winding with peak voltage stress occurring across the first few turns from the terminal end. However, under three phase PWM voltage pulse excitation, excessive voltage stress occurs at two different locations. Predictably, one of the locations is the terminal end and the other is the neutral point. Based on the analysis, it is apparent that the voltage distribution can be characterised by two voltage oscillatory modes. One of them oscillates at the 2nd anti-resonance frequency ($f_{ar(c+m)(2)}$) of the cable connected machine impedance causing voltage stress at the terminal end. The second oscillatory mode, which receives the least attention, oscillates at the 1st anti-resonance frequency ($f_{ar(c+m)(1)}$) of the combined cable and stator winding impedance.

The TEM voltage wave travelling in a medium is characterised by its anti-resonance frequency. By way of example, a simple RLC circuit renders minimum impedance at its resonance frequency. Similarly, the cable renders minimum impedance at its anti-resonance frequency. Thus, the TEM wave propagating through the cable reflects between its two ends, resembling a voltage oscillation at the terminals oscillating at the anti-resonance frequency. Consequently, the voltage oscillations at the interface of the cable and the machine correspond to the 2nd anti-resonance frequency ($f_{ar(c+m)(2)}$) of the combined cable and stator winding impedance.

It is noteworthy that the anti-resonance phenomenon has several repercussions. Firstly, the voltage oscillation frequency is characteristic of the anti-resonance frequency. Secondly, the anti-resonance frequency can be characterised by the length of the medium and the speed of the TEM wave within it. Thirdly, the magnitude of the voltage stress can be deduced from the CM impedance and the anti-resonance frequency. Using the CM impedance of the cable and the stator winding, the study proposes a method to compute their surge impedance which is further used to calculate the voltage overshoot factor. Thus, without exciting the drive, the voltage stress at the terminal ends can be estimated.

Contrary to the literature, which claims that the turns close to the terminal end are most stressed, the results illustrate that the turns close to the neutral point may be most stressed at low modulation index or light load. The voltage stress at the neutral point is due to the voltage oscillations at 1st anti-resonance frequency ($f_{ar_{(c+m)(1)}}$) which is primarily a characteristic of the stator winding. It occurs due to the superposition of travelling waves impinging machine terminals. Different to the cable, the voltage stress within the stator winding is characterised by the 1st anti-resonance frequency ($f_{ar_{m(1)}}$). Since the 2nd anti-resonance frequency ($f_{ar_{(c+m)(2)}}$) is in the MHz range, the high permeability of the stator core restricts the penetration of the HF TEM wave deep into the winding and the capacitive coupling between the turns and the core offers a low impedance shunt path to travel.

The voltage stress within the cable and the winding are a result of the superposition of TEM waves elicited from the three phase VSI. Based on the travelling wave theory, the superposition of the waves can be expressed mathematically which aids in predicting the voltage stress. In reliance on the mathematical model, the following conditions result in excessive voltage stress:

- Low modulation index, wherein the dwell time between the switching events at the three phases is short. Consequently, the TEM voltage waves travelling in different phases superpose constructively to cause excessive voltage stress. This phenomenon can also be understood by higher CM voltage at low modulation index.
- At the instant of change in the switching sector, two of the phases switch simultaneously. Thus, TEM voltage wave travelling in the two phases superpose constructively. This condition occurs six times in a fundamental cycle and is unavoidable when the phase angle of the voltage space vector is an integer multiple of 60 electric degrees.
- High switching frequency results in short dwell time between the phases. It is believed that the VSI with recent semiconductor devices capable of switching fast can be operated at a high switching frequency to achieve better controllability, low torque pulsation and low noise. However, the voltage stress at the neutral point raises the limit to this increase. Especially, if the switching frequency is equal or close to the 1st anti-resonance frequency, voltage oscillations within the winding aggravate causing unrestrained voltage stress. Therefore, effective measures need to be developed to

suppress the voltage stress in order to exploit the fast switching capability of the semiconductor devices.

If the 1st anti-resonance frequency ($f_{ar_{c(1)}}$) of the cable aligns with the 1st anti-resonance frequency ($f_{ar_{m(1)}}$) of the winding, especially in long cable, the TEM wave will encounter minimum impedance in both the medium. Thereby, the TEM wave oscillates at the same frequency in both the medium, resulting in excessive voltage stress. The excessive voltage stress results in premature failure of the machine insulation. Therefore, it is of utmost importance to mitigate the stress.

7.2.4 Voltage Stress Mitigation Technique

Several measures are widely accepted for suppressing voltage stress either by changing system configuration or changing inverter configuration or by installing filters. Passive filters is the simplest and cheapest solution for voltage stress suppression. The existing filtering technique either uses a reactor or dV/dt filter to limit the dV/dt of the PWM voltage pulse or the sinusoidal filter which eliminates the HF spectral component of the voltage or installing a motor termination unit to match the machine and cable impedance or by installing CM transformers which limits the CM current.

The aforementioned methods are effective in suppressing the voltage stress at the machine terminals. Generally, the sinewave filters are designed with a low cut-off frequency to restrict the HF spectral component of the PWM voltage pulse which makes the excitation sinusoidal. This reduces the anti-resonance frequency with reduced impedance and hence, the quality factor. Thereupon, the filter is effective in mitigating stress at the terminal end but may aggravate the stress at the neutral point.

The dV/dt filters are partially effective in suppressing the neutral point voltage stress unless the cut-off frequency is higher than the 1st anti-resonance frequency ($f_{ar_{(c+m)(1)}}$) of the combined cable and machine. This implies that the dV/dt filters designed for the drives with low anti-resonance frequency, generally the low voltage drive, must have a low cut-off frequency resulting in the large, bulky, and costly filter. By way of example, the anti-resonance frequency of a 2.83kW, 600V synchronous machine resembles anti-resonance at 100kHz. Thereupon, the cut-off frequency of the filter must be less than 100kHz.

However, a simple RC circuit connected between the neutral point and the core enhances voltage suppression at the neutral point. The RC network increases the impedance at the anti-resonance frequency, thereby increasing the quality factor. As a result, the voltage oscillations at the neutral point are suppressed quickly with less peak voltage stress. This advantage comes at the cost of filter losses. A trade-off exists between the voltage stress and the filter losses which limits the extent of voltage suppression. These losses can easily be dissipated, using the core of the machine. The study proposes an analytical solution based on the impedance measurement to select the optimum parameters for the filter. However, the proposed filter is ineffectual in suppressing the voltage stress at the terminal end. Therefore, the filter is recommended to be used with the conventional filters to attain minimum voltage stress at both locations.

Compared to the conventional filters, the proposed RC filter is a low cost, less lossy, and small size retrofit solution, owing to the absence of any magnetic component. Thus, the machine manufacturer may offer an integrated solution with the RC filter mounted on the core of the machine without any design changes. In addition, the proposed filter can be retrofitted to an existing machine in service to avoid premature failure of the machine insulation.

7.2.5 Guidelines for Safe Use of Electrical Machines under PWM Voltage Excitation:

- Shortening the cable length below critical cable length is an effective measure in suppressing the voltage stress at the terminal ends. The voltage overshoot limit to 20%, if the length of the cable is less than 0.6 times the critical cable length. However, this method is ineffective in suppressing voltage stress at the neutral point.
- Cable with high dielectric loss or with ferrite shielding suppresses the voltage overshoot at the machine terminals. Ferrite shielding is also effective in improving EMC quality.
- Reactors and sinusoidal filters can be used to mitigate terminal voltage stress. However, the low cut-off frequency of the filter aggravates the neutral point voltage stress.
- dV/dt filters are effective in mitigating the voltage stress at the terminals. If designed with a cut-off frequency lower than the anti-resonance frequency of the winding, it is partially effective in suppressing neutral point voltage stress.

- Neutral point voltage stress can be suppressed effectively using the proposed RC filter. The proposed RC filters are also effective in reducing the RMS CM current. The dV/dt filter can be used in conjunction to limit the peak CM current.
- To prevent excessive voltage stress across the insulation close to the neutral point, electric drives running at light load conditions for the most of their operations must use the proposed passive RC filter or multi-level inverters.
- The operating switching frequency of the electric drives must be kept much below the first anti-resonance frequency in order to prevent excessive voltage stress across the insulation near to the neutral point.
- Avoid cable whose anti-resonance frequency is near to the 1st anti-resonance frequency of the winding, otherwise, the peak-to-peak voltage stress could rise to 3.9 times DC link voltage.

7.2.6 Recommendations for the Revision of IEC 60034:25:2014 [15], IEC 60034:18:41 [56], and NEMA MG 1-2016 [172] Standards:

- The standards recognise the voltage stress at the machine terminals, whereas overlook the voltage stress at the neutral point. Hence, the standards should acknowledge its existence.
- The standards suggest that voltage overshoot does not occur if the VSI is integrated into the motor. Short cable length certainly reduces the voltage stress at the machine terminal. However, the voltage overshoot at the neutral point is primarily the winding characteristics. Therefore, shortening the cable length will be ineffective.
- The standards indicate that the voltage pulse with short rise time impinging machine terminals distribute unevenly with peak voltage stress across the first few turns from the line end. Based on the studies, it is advised to revise that the peak voltage stress may also occur at the neutral point which is subjected to the modulation index, switching frequency and the combined cable and stator winding impedance characteristics.
- Various factors act as a catalyst in PD, which is indispensably considered for enhancement of the peak-to-peak operating voltage. The standard IEC 60034:18:41 suggest enhancement factors for the safe use of insulation under different stress category. The standard should revise the enhancement factors by also considering the

peak voltage stress at the neutral point, which could rise to 3.5 times DC link voltage in some adverse conditions.

- The standards use a conventional plot of the overshoot at the machine terminals measured over the cable length at different rise time limited to great than 50ns. As discussed in this thesis, it is more coherent if the overshoot is represented as a measure of the ratio of cable length and critical cable length. This allows voltage overshoot factor to be estimated with any voltage rise time, which can be much lower than 50ns with WBG based switching devices.

7.3 Future Work

Although this thesis comprises a comprehensive study on the voltage stress within the stator winding under PWM voltage excitation and its mitigation measures, some research aspects remain to be studied in future. During HF modelling of the winding, some assumptions are made, which could be considered in detail for further refinement. In addition, HF modelling of the VSI is beyond the scope of this thesis. Representation of the parasitic impedance of the VSI in the present model will fully represent the overall drive, thereby helping in assessing the voltage stress compromising insulation integrity and CM current and the bearing current causing EMI with the nearby equipment. Albeit the investigation on the voltage stress within the winding, its effect on the insulation integrity remained unexamined. In addition, the prognosis of the insulation failure including lifetime assessment would prevent any unexpected downtime, which could be explored in future. The aforementioned aspects also discussed comprehensively in the following section, could be focused on as future research.

7.3.1 High Frequency Model of Stator Winding

The present work is extensively focused on the HF modelling of the cable and the stator winding. Although the cable modelling is meticulously followed, for the sake of simplicity, the stator winding model includes assumptions. These assumptions are listed as follows, which can be reviewed for refinement:

7.3.1.1 Representation of non-linear magnetic properties of core:

Generally, the electrical steel is used as the core of the machine. Electrical steel is an iron alloy tailored to produce enhanced magnetic properties. However, its magnetic properties are non-linear and frequency dependent, especially the magnetic permeability. Although the non-

linear magnetic permeability is represented using B-H curve, its dependency on the frequency of excitation is ignored. At a low frequency of excitation, the magnetizing force is in phase with the magnetic flux density. However, with increased, change in magnetic flux density lags the magnetization force. This variation could be represented using a complex value of permeability. In the present analysis, the non-linear variation in permeability is represented using B-H curve. However, it is assumed real and frequency independent. Any future efforts in modelling could consider the accurate representation of the permeability of the core.

7.3.1.2 Representation of laminated core:

The core of the machine is laminated to restrict the induction of the eddy current which causes eddy current loss. As a result, the conductivity of the core is ignored. However, at a HF of excitation, when the skin depth is less than half of the laminate thickness, the working flux induces an eddy current in the core. In addition, an axial interlaminar displacement current is induced within the core. These induced currents cannot be represented without three-dimensional model of the slot. However, evaluating the parameters using three-dimensional model is strenuous. In the three-dimensional model, the number of mesh elements will increase rapidly which will increase the computational time and resources. This can be overcome if homogenous material properties are assumed.

7.3.1.3 Core Loss model:

In the present model, for the sake of simplicity, the core losses are represented using a resistive element across the turn model. However, it may be represented in detail using frequency dependent complex permeability and accurate representation of the laminated core. However, for the frequency dependent complex permeability, one has to rely on manufacturers and the accurate representation of the laminated core requires three-dimensional slot model with the defined properties of the insulation and the electrical steel.

7.3.1.4 Modelling overhang region:

In the proposed model, the inductance in the overhang region is represented as a lumped inductance which is calculated using a mathematical expression. However, it may be calculated using three-dimension model of a coil. The frequency dependent overhang impedance may be calculated using the impedance of the coil and the impedance of each turn embedded within the slot.

7.3.1.5 Modelling of the rotor core:

As the flux under HF excitation is confined within the slot, the rotor is ignored. However, for the representation of the bearing current, the rotor model is crucial. Hence, the investigation of the HF bearing currents must include the rotor in the proposed model.

7.3.2 High-Frequency Model of the Voltage Source Inverter

The HF modelling of the VSI is important to represent the switching transients, the CM current path, the grounding system, and the parasitic impedance of the snubber circuit. Due to these parasitic impedance, HF voltage oscillations can be observed at the inverter terminal. The rise time of the pulse depends on the switching characteristics and eventually their parasitic inductance and capacitance or any snubber circuits employed. Also, different earth configurations can be realised with the HF model. Therefore, for the comprehensive study of the drives, HF modelling of the VSI is important.

Generally, the model includes the modelling of the semiconductor devices, snubber circuit, and the parasitic elements of interconnections and the DC-link capacitor. On one hand, the physics-based model of the semiconductor device represents the switching dynamics explicitly but is difficult to parameterise such as the physical dimension of the epitaxial layer, the width of the drift region, doping concentration, etc. A behavioural model, on the other hand, is easy to parameterise since the model is represented as an equivalent circuit whose parameters are available from the datasheet and measurements. However, the behavioural model does not represent the transient phenomenon such as the reverse recovery of the anti-parallel diode.

The parasitic elements of the DC link capacitor include equivalent series resistor (ESR), equivalent-series inductance (ESL), and the stray inductance of the conductive connection between the capacitor and the devices. In general, multiple bypass capacitors are used to avoid the influence of the ESL during switching transients. Therefore, these capacitors should be included in the modelling. Parasitic impedance of the snubber circuit is also crucial in the modelling process.

7.3.3 Insulation Integrity and Lifetime Assessment under Voltage Stress

The VSI inverter generates repetitive voltage overshoot which can reduce the insulation lifetime if they exceed its repetitive voltage strength. The risk of insulation damage is more severe with the short rise time of the PWM voltage pulse. The dielectric stress on the insulation

depends on the voltage magnitude, rise time and the frequency of occurrence of the PWM voltage pulse. The upper limit at which the overvoltage becomes detrimental is called PDIV. The PD incites insulation breakdown by causing chemical and mechanical erosion. The short rise time of the PWM voltage pulse aggravates the voltage stress across the turns close to the terminals, which causes an early dielectric breakdown. This could happen well within the PDIV level. These failures remain undetected by the standard dielectric tests performed at 50Hz or 60Hz. At an early stage, the dielectric breakdown results in a turn fault causing localised circulating current, which aggravates catastrophic faults. Organic-based insulation materials used in low voltage machines fail quickly under repeated voltage stress.

Therefore, it is important to study the influence of fundamental frequency, voltage pulse repetition rate, voltage pulse magnitude, jump voltage and rise time on the machine insulation and PD activity over the lifetime of the machine insulation.

Appendix A: Cable Parameters

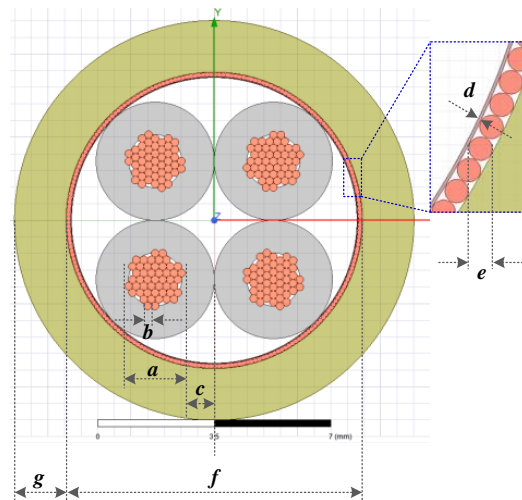


Figure: A.1: Schematic diagram of the cross-section of 4-wire shielded cable

Table: A.1: Parameters of shielded cable

Parameter	Value
Conductors	4
Conductor Diameter (a)	1.784 mm
No. of Strands/Conductor	40
Strand Size (b)	30 AWG
Thickness of core insulation (c)	0.9 mm
Permittivity of core insulation	2.8 F/m
Thickness of aluminum sheath (d)	0.02 mm
Diameter of braid strand (e)	0.14 mm
Inner diameter of jacket insulation (f)	9 mm
Thickness of jacket insulation (g)	1.5 mm
Permittivity of jacket insulation	4 F/m

Appendix B: Stator Winding Parameters

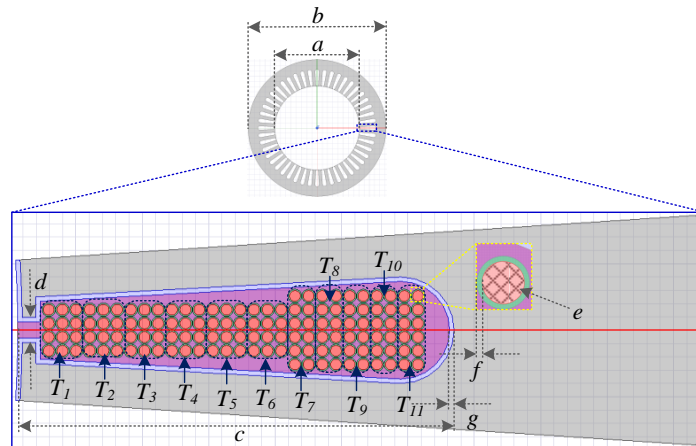


Figure: B.1: Schematic diagram of the cross-section of a stator slot of the stator winding.

Table: B.1: Stator dimensions [29] and properties of insulation.

Parameter	Value
Dimension of the Stator Slots	
Inner stator diameter (a)	161.9 mm
Outer stator diameter (b)	264 mm
Stack length	50.8 mm
Depth (c)	30.9 mm
Slot opening (d)	1.88 mm
Parameters of the Stator Winding	
Number of slots	48
Series coils/Phase (N_c)	8
Parallel circuits/Phase	0
Turns/Coil (N_t)	11
Parallel Strands per turn (N_p)	12
Wire size (e)	20AWG
Resistance/Phase	0.77 Ω
Insulation Parameter of the Stator Winding	
Thickness of turn insulation (f)	0.025 mm

Permittivity of turn insulation	3.5 F/m
Permittivity of main-wall insulation	3.5 F/m
Thickness of ground-wall insulation (<i>g</i>)	0.35 mm
Permittivity of ground-wall insulation	3.5 F/m

Appendix C: MATLAB[®] Based High Frequency Model of the Stator Winding

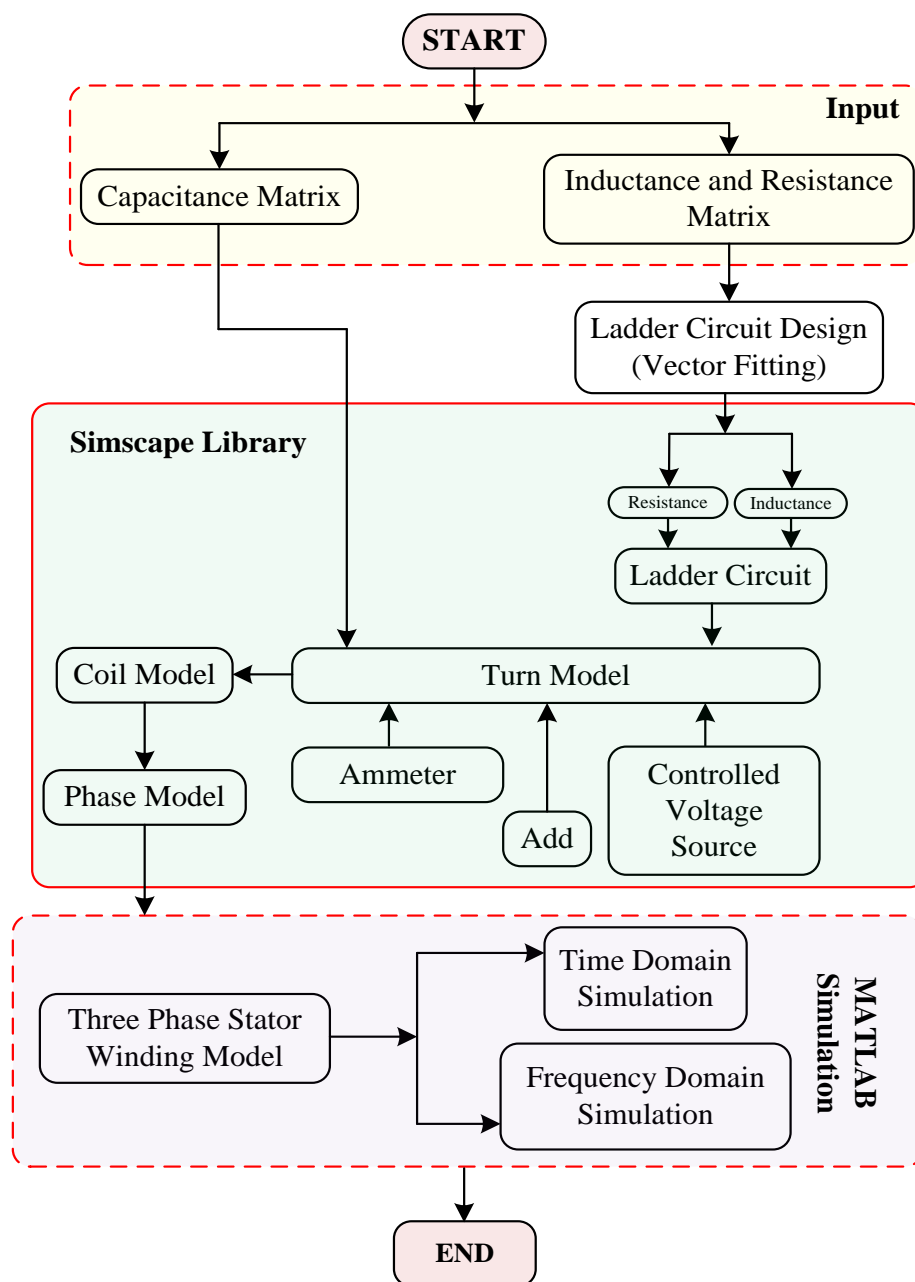


Figure: C.1: MATLAB[®] based high frequency model of the stator winding.

REFERENCES

- [1] The Meteorological Office , “Effects of climate change,” The Meteorological Office, United Kingdom, <https://www.metoffice.gov.uk/weather/climate-change/effects-of-climate-change> (Accessed: May 15, 2022).
- [2] IPCC, “Climate Change 2021: The Physical Science Basis. Contribution of Working Group I to the Sixth Assessment Report of the Intergovernmental Panel on Climate Change,” Cambridge University Press, Cambridge UK, 2021. <https://www.ipcc.ch/report/ar6/wg1/> (Accessed: May 15, 2022).
- [3] National Ocean Service, “2022 sea level rise technical report” National Ocean Service, National Oceanic and Atmospheric Administration, U.S. Department of Commerce <https://oceanservice.noaa.gov/hazards/sealevelrise/sealevelrise-tech-report.html> (Accessed: May 15, 2022).
- [4] G. Madge, “Dashboard highlights urgency of climate action”, The Meteorological Office, United Kingdom, <https://www.metoffice.gov.uk/about-us/press-office/news/weather-and-climate/2021/met-office-climate-dashboard-highlights-the-urgency-of-climate-action> (Accessed: May 15, 2022).
- [5] United Nation Climate Change, “The Paris Agreement,” 2015, https://unfccc.int/sites/default/files/english_paris_agreement.pdf (Accessed: May 15, 2022).
- [6] “National Statistics, 2020 UK greenhouse gas emissions, final figures,” Dept. Business, Energy, Ind. Strategy, United Kingdom, https://assets.publishing.service.gov.uk/government/uploads/system/uploads/attachment_data/file/1051408/2020-final-greenhouse-gas-emissions-statistical-release.pdf (Accessed: May 15, 2022)
- [7] “Transitioning to zero emission cars and vans: 2035 delivery plan,” Dept. for Transport, Office for Zero Emission Vehicles,, <https://www.gov.uk/government/publications/transitioning-to-zero-emission-cars-and-vans-2035-delivery-plan> (Accessed: May 15, 2022).

-
- [8] “The long-term strategy of the United States: Pathways to net-zero greenhouse gas emission by 2050, Nov. 2021”, <https://www.whitehouse.gov/wp-content/uploads/2021/10/US-Long-Term-Strategy.pdf> (Accessed: May 15, 2022).
- [9] National Automotive Board , “Fame India scheme phase II,” Ministry of heavy industries, Government of India, <https://fame2.heavyindustries.gov.in/#>. (Accessed: May 15, 2022).
- [10] “Aircraft technology roadmap to 2050”, International Air Transport Association (IATA), <https://www.iata.org/contentassets/8d19e716636a47c184e7221c77563c93/Technology-roadmap-2050.pdf>. (Accessed: May 15, 2022).
- [11] Alex Avron, About the SiC MOSFET modules in Tesla model 3. PnT power, <https://www.pntpower.com/tesla-model-3-powered-by-st-microelectronics-sic-mosfets/> (Accessed: May 15, 2022).
- [12] “Siemens eAircraft: disrupting the way you fly!” Siemens, <https://www.ie-net.be/sites/default/files/Siemens%20eAircraft%20-%20Disrupting%20Aircraft%20Propulsion%20-%20OO%20JH%20THO%20-%2020180427.cleaned.pdf> (Accessed: May 15, 2022).
- [13] “Auxiliary converter with SiC technology”, Siemens <https://assets.new.siemens.com/siemens/assets/api/uuid:038c7ff6-cccc-4a2e-9a8e-fb6c74b44bf8/mors-b10020-00-7600-folder-auxiliary-converter-sic-300.pdf> (Accessed: May 15, 2022).
- [14] A. H. Bonnett, “Analysis of the impact of pulse-width modulated inverter voltage waveforms on AC induction motors,” *IEEE Trans. Ind. Appl.*, vol. 32, no. 2, pp. 386-392, March-April 1996.
- [15] Rotating electrical machines-Part 25: Guidance for the design and performance of a.c. motors specifically designed for converter supply, IEC 60034- 25:2014, 2014.
- [16] E. Persson, “Transient effects in application of PWM inverters to induction motors,” *IEEE Trans. Ind. Appl.*, vol. 28, no. 5, pp. 1095–1101, Sep./Oct. 1992.

-
- [17] M. Berth, “Electrical stress of the winding insulation of low voltage induction motors fed by pulse converters,” *Ph.D. dissertation*, Dep. Elect. Eng., Dresden Univ. Technol., Dresden, Germany, 1997.
- [18] “Variable speed drives and motors—Motor insulation voltage stresses under PWM inverter operation,” *GAMBICA/REMA*, London, U.K., Tech. Rep., 1st ed., Jan. 2000.
- [19] M. Melfi, J. Sung, S. Bell and G. Skibinski, “Effect of surge voltage risetime on the insulation of low voltage machines fed by PWM converters,” in *Proc. IEEE Industry Applications Conference, 32nd IAS Annual Meeting*, 1997, pp. 239-246 vol.1.
- [20] S. Sundeep, J. Wang and A. Griffio, “Holistic modeling of high-frequency behavior of inverter-fed machine winding, considering mutual couplings in time domain” *IEEE Trans. Ind. Appl.*, vol. 57, no. 6, pp. 6044-6057, Nov.-Dec. 2021.
- [21] S. Sundeep, J. Wang, A. Griffio and F. Alvarez-Gonzalez, “Antiresonance phenomenon and peak voltage stress within PWM inverter fed stator winding” *IEEE Trans. Ind. Electron.*, vol. 68, no. 12, pp. 11826-11836, Dec. 2021.
- [22] Sang Bin Lee, K. Younsi and G. B. Kliman, “An online technique for monitoring the insulation condition of AC machine stator windings,” *IEEE Trans. Energy Convers.*, vol. 20, no. 4, pp. 737-745, Dec. 2005.
- [23] J. M. Erdman, R. J. Kerkman, D. W. Schlegel, and G. L. Skibinski, “Effect of PWM inverters on ac motor bearing currents shaft voltages,” *IEEE Trans. Ind. Appl.*, vol. 32, no. 2, pp. 250–259, Mar./Apr. 1996.
- [24] D. Busse, J. Erdman, R. J. Kerkman, D. Schlegel, and G. Skibinski, “Bearing currents and their relationship to PWM drives,” *IEEE Trans. Power Electron.*, vol. 12, no. 2, pp. 243–252, Mar. 1997.
- [25] D. Busse, J. Erdman, R. J. Kerkman, D. Schlegel and G. Skibinski, “System electrical parameters and their effects on bearing currents,” in *IEEE Transactions on Industry Applications*, vol. 33, no. 2, pp. 577-584, March-April 1997.
- [26] G. L. Skibinski, R. J. Kerkman, and D. W. Schlegel, “EMI emissions of modern PWM ac drives,” *IEEE Ind. Applicat. Soc. Mag.*, vol. 5, pp. 47–81, June 1999.

-
- [27] M. R. Khalid, I. A. Khan, S. Hameed, M. S. J. Asghar and J. -S. Ro, "A Comprehensive Review on Structural Topologies, Power Levels, Energy Storage Systems, and Standards for Electric Vehicle Charging Stations and Their Impacts on Grid," *IEEE Access*, vol. 9, pp. 128069-128094, 2021.
- [28] S. Heydari, P. Fajri, M. Rasheduzzaman and R. Sabzehgar, "Maximizing Regenerative Braking Energy Recovery of Electric Vehicles Through Dynamic Low-Speed Cutoff Point Detection," in *IEEE Transactions on Transportation Electrification*, vol. 5, no. 1, pp. 262-270, March 2019, doi: 10.1109/TTE.2019.2894942.
- [29] M. Olszewski (2011 Mar.). Evaluation of the 2010 Toyota Prius hybrid synergy drive system. Oak Ridge National Laboratory, USA. [Online] Available:<https://info.ornl.gov/sites/publications/files/Pub26762.pdf>.
- [30] J. Azurza Anderson, E. J. Hanak, L. Schrittwieser, M. Guacci, J. W. Kolar, and G. Deboy, "All-Silicon 99.35 % Efficient Three-Phase SevenLevel Hybrid Neutral Point Clamped/Flying Capacitor Inverter," *CPSS Trans. Power Electron. Appl.*, vol. 4, no. 1, pp. 50–61, 2019.
- [31] A. N. Lemmon and R. C. Graves, "Comprehensive characterisation of 10-kV silicon carbide half-bridge modules," *IEEE J. Emerg. Sel. Topics Power Electron.*, vol. 4, no. 4, pp. 1462–1473, Dec. 2016.
- [32] S. Hazra, S. Madhusoodhanan, G. K. Moghaddam, K. Hatua, and S. Bhattacharya, "Design considerations and performance evaluation of 1200-V 100-A SiC MOSFET-based two-level voltage source converter," *IEEE Trans. Ind. Appl.*, vol. 52, no. 5, pp. 4257–4268, Sep./Oct. 2016.
- [33] J. Fabre, P. Ladoux, and M. Piton, "Characterization and implementation of dual-SiC MOSFET modules for future use in traction converters," *IEEE Trans. Power Electron.*, vol. 30, no. 8, pp. 4079–4090, Aug. 2015.
- [34] T. P. Chow, I. Omura, M. Higashiwaki, H. Kawarada, and V. Pala, "Smart power devices and ICs using GaAs and wide and extreme bandgap semiconductors," *IEEE Trans. Electron. Devices*, vol. 64, no. 3, pp. 856–873, Mar. 2017.

-
- [35] A. Bindra, "Wide-bandgap-based power devices: Reshaping the power electronics landscape," *IEEE Power Electron. Mag.*, vol. 2, no. 1, pp. 42–47, Mar. 2015.
- [36] Toyota Global Newsroom. (May 2014). Toyota Develops New Silicon Carbide Power Semiconductor With Higher Efficiency. [Online]. Available: <http://newsroom.toyota.co.jp/en/detail/2656842>.
- [37] G. Suresh, A. Toliyat, A. Rendusara, and N. Enjeti, "Predicting the transient effects of PWM voltage waveform on the stator windings of random wound induction motors," *IEEE Trans. Power Electron.*, vol. 14, no. 1, pp. 23–30, Jan. 1999.
- [38] O. Magdun, S. Blatt and A. Binder, "Calculation of stator winding parameters to predict the voltage distributions in inverter fed AC machines," in *Proc. IEEE International Symposium on Diagnostics for Electric Machines, Power Electronics and Drives (SDEMPED)*, Valencia, Spain, pp. 447-453, 2013.
- [39] Y. Xie, J. Zhang, F. Leonardi, A. R. Munoz, M. W. Degner and F. Liang, "Modeling and verification of electrical stress in inverter-driven electric machine windings," *IEEE Trans. Ind. Appl.*, vol. 55, no. 6, pp. 5818-5829, Nov.-Dec. 2019,
- [40] Yifan Tang, "Analysis of steep-fronted voltage distribution and turn insulation failure in inverter-fed form-wound AC motor," in *IEEE Trans. Ind. Appl.*, vol. 34, no. 5, pp. 1088-1096, Sept.-Oct. 1998.
- [41] D. Han, S. Li, W. Lee and B. Sarlioglu, "Adoption of wide bandgap technology in hybrid/electric vehicles-opportunities and challenges," in *Proc. IEEE Transportation Electrification Conf. Expo. (ITEC)*, 2017, pp. 561-566.
- [42] S. Ozdemir, F. Acar and U. S. Selamogullari, "Comparison of silicon carbide MOSFET and IGBT based electric vehicle traction inverters," in *Proc. International Conf. Electrical Eng. Informatics, (ICEEI)*, Denpasar, 2015, pp. 1-4.
- [43] B. Wrzecionko, D. Bortis and J. W. Kolar, "A 120 °C ambient temperature forced air-cooled normally-off SiC JFET automotive inverter system," *IEEE Trans. Power Electron.*, vol. 29, no. 5, pp. 2345-2358, May 2014.

-
- [44] H. Zhang, L. M. Tolbert, and B. Ozpineci, "Impact of SiC devices on hybrid electric and plug-in hybrid electric vehicles," *IEEE Trans. Ind. Appl.*, vol. 47, no. 2, pp. 912-921, March-April 2011.
- [45] G. C. Stone, K. Boulter, Culber, and Dhirani, "Rotating machine insulation systems" in *Electrical Insulation for Rotating Machines: Design, Evaluation, Aging, Testing, and Repair*, 2nd Ed. New Jersey, NJ, USA, Wiley-IEEE Press, 2014, Chapter-1, pp. 1-46.
- [46] R. H. Rehder, R. E. Draper, B. J. Moore: "How good is you motor insulation system?", *IEEE Electrical Insulation Magazine*, Vol. 12, No. 4, pp. 8-13, July/August 1996.
- [47] "NEMA MW 35-C or M 73-C Class 200 copper - round conductors - polyester/polyamideimide coated magnet wire/winding wire", Essex Ultrashield plus, Superior Essex Inc.
- [48] "Trivoltherm N: For insulation class F or insulation system up to 180⁰C", August Kerpel Soehne GmbH.
- [49] J. Pyrhönen, T. Jokinen and V. Hrabovcová, "Insulation of Electrical Machines," in *Design of Rotating Electrical Machines*, Chichester, UK, John Wiley & Sons, Ltd, 2008, Chapter 8, pp. 429-455.
- [50] "Impregnating materials," Elantas Group, Accessed: 31 May 2022, [Online] Available: <https://www.elantas.com/beck-india/products/electrical-insulation-system/electrical-insulating-varnishes-resins.html>.
- [51] P. Przybylek and H. Moscicka-Grzesiak, "The influence of water content and ageing degree of paper insulation on its mechanical strength," in *Proc. IEEE International Conference on Solid Dielectrics (ICSD)*, 2010, pp. 1-3.
- [52] M. Duval, A. D. Pablo, I. Atanasova-Hoehlein and M. Grisaru, "Significance and detection of very low degree of polymerization of paper in transformers," *IEEE Electrical Insulation Magazine*, vol. 33, no. 1, pp. 31-38, 2017.
- [53] S. Diaham, M. Locatelli and T. Lebey, "Improvement of polyimide electrical properties during short-term of thermal aging," in *Proc. Annual Report Conference on Electrical Insulation and Dielectric Phenomena*, 2008, pp. 79-82.

-
- [54] W. Zhao, W. H. Siew, M. J. Given, Q. Li, J. He and E. Corr, "Thermoplastic materials aging under various stresses," in *Proc. IEEE Electrical Insulation Conference (EIC)*, 2016, pp. 615-618.
- [55] "Thermal-oxidative degradation of polymers" Accessed: 31 May 2022, [Online] Available:
<http://polymerdatabase.com/polymer%20chemistry/Thermal%20Degradation.html>
- [56] Rotating electrical machines-Part 18-41: Partial Discharge free electrical insulation system (Type I) used in rotating electrical machines fed from voltage converters- Qualification and quality control tests, IEC 60034- 18-41:2014, 2014.
- [57] D. Leggate, J. Pankau, D. W. Schlegel, R. J. Kerkman and G. L. Skibinski, "Reflected waves and their associated current [in IGBT VSIs]," *IEEE Trans. Ind. Appl.*, vol. 35, no. 6, pp. 1383-1392, Nov.-Dec. 1999.
- [58] G. Skibinski, R. Kerkman, D. Leggate, J. Pankau and D. Schlegel, "Reflected wave modeling techniques for PWM AC motor drives," in *Proc. Thirteenth Annual Applied Power Electronics Conference and Exposition (APEC)*, 1998, pp. 1021-1029 vol.2.
- [59] R. J. Kerkman, D. Leggate and G. L. Skibinski, "Interaction of drive modulation and cable parameters on AC motor transients," *IEEE Trans. Ind. Appl.*, vol. 33, no. 3, pp. 722-731, May-June 1997.
- [60] M. Kaufhold, "Electrical behavior of the interturn insulation of lowvoltage machines fed by pulse controlled inverters," *Ph.D. dissertation*, Dep. Elect. Eng., Dresden Univ. Technol., Dresden, Germany, 1994.
- [61] O. V. Thorsen and M. Dalva, "A survey of faults on induction motors in offshore oil industry, petrochemical industry, gas terminals and oil refineries," *IEEE Trans. Ind. Appl.*, vol. 31, no. 5, pp. 1186-1196, 1995.
- [62] J. W. Aquilino, "Report of transformer reliability survey - industrial plants and commercial buildings," *IEEE Trans. Ind. Appl.*, vols. IA-19, no. 5, pp. 858-866, 1983.
- [63] G. C. Stone, K. Boulter, Culber, and Dhirani, "Stator failure mechanisms and repair" in *Electrical Insulation for Rotating Machines: Design, Evaluation, Aging, Testing, and Repair*, 2nd Ed. New Jersey, NJ, USA, Wiley-IEEE Press, 2014, Chapter-8, pp. 1-46.

-
- [64] P. Neti, P. Zhang, X. Qi, Y. Zhou, K. Younsi, M. Shah and K. Weeber, "Online detection of endwinding contamination in industrial motors," in *Proc. Electrical Insulation Conference (EIC)*, Annapolis, MD, 2011.
- [65] IEEE Std 43-2006, Recommended Practice for Testing Insulation Resistance of Electric Machinery, American National Standard Institute (ANSI), 2006.
- [66] Grubic, S.; Aller, J.M.; Lu, B.; Habetler, T.G., "A survey of testing and monitoring methods for stator insulation systems in induction machines" in *Proc. International Conference on Condition Monitoring and Diagnosis (ICCMD)*, Beijing, China, 21–24 April 2008; pp. 4127–4136.
- [67] G. C. Stone, R. G. VanHeeswijk, and R. Bartnikas, "Investigation of the effect of repetitive voltage surges on epoxy insulation," *IEEE Trans. Energy Convers.*, vol. 7, pp. 754–760, Dec. 1992.
- [68] L. Egiziano, C. Petrarca, V. Tucci, and M. Vitelli, "Investigation on performances of insulation materials for inverter-fed traction motors," in *Proc. Conf. Electr. Insul. Dielectric Phenomena*, Atlanta, GA, 1998, pp. 564–567.
- [69] L. Egiziano, C. Petrarca, G. Pizzella, V. Tucci, M. Vitelli, and A. Masucci, "Insulation systems for inverter-fed traction motors: A comparison of the behavior of different polyimide-based composites," in *Proc. 8th Europe. Conf. Power Electron. Applicat.*, Lausanne, Switzerland, 1999, paper 487.
- [70] P. Wang, G. C. Montanari, and A. Cavallini, "Partial discharge phenomenology and induced aging behavior in rotating machines controlled by power electronics," *IEEE Trans. Ind. Electron.*, vol. 61, no. 12, pp. 7105–7112, Dec. 2014.
- [71] A. Cavallini, E. Lindell, G. C. Montanari, and M. Tozzi, "Off-line PD testing of converter-fed wire-wound motors: When IEC TS 60034-18-41 may fail?," *IEEE Trans. Dielect. Elect. Insul.*, vol. 17, no. 5, pp. 1385–1395, Oct. 2010.
- [72] R. C. Sheehy, T. R. Blackburn, and J. Rungis, "Accelerated aging of high voltage stator bars using a power electronic converter," in *Proc. IEEE Int. Symp. Elect. Insul.*, Montreal, QC, Canada, 1996, pp. 230–234.

-
- [73] P. Wang, G. Wu, B. Gao, Y. Luo, and K. Cao, "Study of partial discharge characteristics at repetitive square voltages based on UHF method," *Sci. China Tech. Sci.*, vol. 56, no. 1, pp. 262–270, 2013.
- [74] Electrical Insulating Materials and Systems – Electrical Measurement of Partial Discharge (PD) Under Short Rise Time and Repetitive Voltage Impulses, IEC Standard 61934 – TS Ed.1.0, 2011.
- [75] M. Kaufhold, G. Borner, M. Eberhardt and J. Speck, "Failure mechanism of the interturn insulation of low voltage electric machines fed by pulse-controlled inverters," *IEEE Electrical Insulation Magazine*, vol. 12, no. 5, pp. 9-16, Sept.-Oct. 1996.
- [76] J. P. Bellomo, T. Lebey, J. M. Oraison and F. Peltier, "Characterisation of voltage shapes acting on the insulation of rotating machines supplied by inverters," in *Proc. 4th International Conference on Properties and Applications of Dielectric Materials (ICPADM)*, 1994, pp. 792-795 vol.2.
- [77] J. P. Bellomo, T. Lebey, J. M. Oraison and F. Peltier, "Influence of rise time on the dielectric behavior of stator insulation materials," in *Proc. IEEE Conference on Electrical Insulation and Dielectric Phenomena (CEIDP)*, 1996, pp. 842-845 vol.2.
- [78] A. Mbaye, F. Grigorescu, T. Lebey and Bui Ai, "Existence of partial discharges in low-voltage induction machines supplied by PWM drives," *IEEE Trans. Dielectric Electrical Insul.*, vol. 3, no. 4, pp. 554-560, Aug. 1996.
- [79] Weijun Yin, "Dielectric properties of an improved magnet wire for inverter-fed motors," *IEEE Electrical Insulation Magazine*, vol. 13, no. 4, pp. 17-23, July-Aug. 1997.
- [80] Weijun Yin, K. Bultemeier, D. Barta and D. Floryan, "Critical factors for early failure of magnet wires in inverter-fed motor," in *Proc. IEEE Conf. Electrical Insul. Dielectric Phenomena (EIDP)*, 1995, pp. 258-261.
- [81] P. Alger, H. Samson, "Shaft currents in electric machines," *Trans. Am. Inst. Electr. Eng.*, vol. 43, pp. 235–245, 1924.
- [82] P. J. Link, "Minimizing electric bearing currents in ASD systems," *IEEE Ind. Appl. Mag.*, vol. 5, no. 4, pp. 55–66, 1999.

-
- [83] C. Ammann, K. Reichert, R. Joho, *et al.*, “Shaft voltages in generators with static excitation systems-problems and solution,” *IEEE Trans. Energy Convers.*, vol. 3, no. 2, pp. 409–419, 1998.
- [84] S. Bell *et al.*, “Experience with variable frequency drives and motor bearing reliability,” in *Proc. 45th Annual Petroleum and Chemical Industry Conference (PCICON)*, *IEEE Ind. Appl. Soc.*, pp. 253-262, 1998.
- [85] A. V. Oppenheim, A. L. Willsky, *Signal and Systems*, 2nd ed., Prentice Hall Inc. 1996.
- [86] L. M. Wedepohl, H. V. Nguyen and G. D. Irwin, “Frequency-dependent transformation matrices for untransposed transmission lines using Newton-Raphson method”, *IEEE Trans. Power Syst.*, vol. 11, no. 3, pp. 1538-1546, Aug. 1996.
- [87] B. Mirafzal, G. Skibinski, R. Tallam, D. Schlegel, and R. Lukaszewski, “Universal induction motor model with low-to-high frequency-response characteristics,” *IEEE Trans. Industry Appl.*, vol. 43, no. 5, pp. 1233-1246, Sep./Oct. 2007
- [88] O. Magdun and A. Binder, “High-frequency induction machine modeling for common mode current and bearing voltage calculation,” *IEEE Trans. Ind. Appl.*, vol. 50, no. 3, pp. 1780–1790, May/Jun. 2014.
- [89] J. Sun and L. Xing, “Parameterization of three-phase electric machine models for EMI simulation,” *IEEE Trans. Power Electron.*, vol. 29, no. 1, pp. 36-41, Jan. 2014.
- [90] R. Rudenberg, “Performance of travelling waves in coils and windings,” *AIEE Trans.*, vol. 59, pp.1031-1045, 1940.
- [91] T. J. Lewis, “The transient behaviour of ladder networks of the type representing machine and transformer windings,” in *Proc. IEE*, vol. 101, part 2, 1954, pp.541-553.
- [92] V. Lovass-Nagy, P. Rozsa, “Matrix analysis of transient voltage distributions in alternating ladder networks,” in *Proc. IEE*, vol. 110, no.9, 1963, pp.1663-1670.
- [93] B. Heller, A. Veverka, “Surge phenomena in machines,” Iliffe, London, 1968.
- [94] P. G. Parrot, P. G. “Surge voltage distribution in the line end coils of high voltage motor windings,” E.R.A. Report No. 5224, 1968.

-
- [95] K. L. Christiansen, A. Pedersen, "An experimental study of impulse voltage phenomena in a large AC motor," in *Proc. Electrical Insul. Conf.*, 1968, pp.148-150.
- [96] H. R. Johnston, Parsons Peebles Research Division, Internal Report No. RL 79-11, 1979.
- [97] G. N. Petrov, A. I. Abramov, "Overvoltage stresses in the turn insulation of electrical machinery windings during electromagnetic transients," *Electrichestov*, No.7, March, 1954, pp.24-31.
- [98] R.E. Adjaye and K.J. Cornick, "Distribution of Switching Surges in the Line-End Coils of Cable Connected Motors," in *Proc. IEE Electric Power Appl.*, vol. 2, no. 1, pp. 11-21, 1979.
- [99] R. J. Clowes, "Surges in high voltage A.C. motors: Resume of published information up to 1964,". ERA Report 5105, 1967.
- [100] M. T. Wright, S. J. Yang and K. McLeay, "General theory of fast-fronted interturn voltage distribution in electrical machine windings," in *Proc. IEE*, vol. 130, no. 4, pp. 245-256, 1983.
- [101] P. G. McLaren and H. Oraee, "Multiconductor transmission-line model for the line-end coil of large AC machines," in *Proc. IEE*, vol. 132, no. 3, May 1985.
- [102] P. G. McLaren and M. H. Abdel-Rahman, "Modeling of large AC motor coils for steep-fronted surge studies," in *IEEE Trans. Ind. Appl.*, vol. 24, no. 3, pp. 422-426, May-June 1988.
- [103] J. L. Guardado and K. J. Cornick, "A computer model for calculating steep-fronted surge distribution in machine windings," *IEEE Trans. Energy Convers.*, vol. 4, no. 1, pp. 95-101, March 1989.
- [104] J. L. Guardado and K. J. Cornick, "Calculation of machine winding electrical parameters at high frequencies for switching transient studies," *IEEE Trans. Energy Convers.*, vol. 11, no. 1, pp. 33-40, March 1996.
- [105] J. L. Guardado and K. J. Cornick, V. Venegas, J. L. Naredo, and E. Melgoza, "A three - phase model for surge distribution studies in electrical machines," *IEEE Trans Energy Convers.*, vol. 12, no. 1, pp. 24-31, March 1997.

-
- [106] L. Gubbala, A. von Jouanne, P. Enjeti, C. Singh and H. Toliyat, "Voltage distribution in the windings of an AC motor subjected to high dV/dt PWM voltages," in *Proc. IEEE Power Electronics Specialist Conference (PESC)*, vol.1, 1995, pp. 579-585.
- [107] J. M. Martínez-Tarifa, H. Amarís-Duarte and J. Sanz-Feito, "Frequency-domain model for calculation of voltage distribution through random wound coils and its interaction with stray capacitances," in *IEEE Trans. Energy Convers.*, vol. 23, no. 3, pp. 742-751, Sept. 2008.
- [108] Kohji Maki, Hiroki Funato and Liang Shao, "Motor modeling for EMC simulation by 3-D electromagnetic field analysis," in *Proc. IEEE Int. Electric Machines Drives Conf. (IEMDC)*, 2009, pp. 103-108.
- [109] V. Mihaila, S. Duchesne and D. Roger, "A simulation method to predict the turn-to-turn voltage spikes in a PWM fed motor winding," *IEEE Trans. Dielectrics Electrical Insul.* vol. 18, no. 5, pp. 1609-1615, October 2011.
- [110] A. Krings, G. Paulsson, F. Sahlén and B. Holmgren, "Experimental investigation of the voltage distribution in form wound windings of large AC machines due to fast transients," in *Proc. IEEE XXII Int. Conf. Electrical Machines (ICEM)*, 2016, pp. 1700-1706.
- [111] N. Boucenna, F. Costa, S. Hlioui and B. Revol, "Strategy for Predictive Modeling of the Common-Mode Impedance of the Stator Coils in AC Machines," *IEEE Trans. Ind. Electron.*, vol. 63, no. 12, pp. 7360-7371, Dec. 2016.
- [112] J. L. Guardado, J. A. Flores, V. Venegas, J. L. Naredo and F. A. Uribe, "A machine winding model for switching transient studies using network synthesis," *IEEE Trans. Energy Convers.*, vol. 20, no. 2, pp. 322-328, June 2005.
- [113] A. von Jouanne, D. Rendusara, P. Enjeti and W. Gray, "Filtering techniques to minimize the effect of long motor leads on PWM inverter fed AC motor drive systems," in *Proc. IEEE Ind. Appl. Conf. Thirtieth IAS Annual Meeting*, 1995, pp. 37-44 vol.1.
- [114] Han-Jong Kim, Geun-Ho Lee, Cheol-Ho Jang and Jea-Pil Lee, "Cost-effective design of an inverter output reactor in ASD applications," *IEEE Trans. Ind. Electron.*, vol. 48, no. 6, pp. 1128-1135, Dec. 2001.

-
- [115] A. F. Moreira, P. M. Santos, T. A. Lipo and G. Venkataramanan, "Filter networks for long cable drives and their influence on motor voltage distribution and common-mode currents" *IEEE Trans. Ind. Electron.*, vol. 52, no. 2, pp. 515-522, April 2005.
- [116] A. von Jouanne and P. N. Enjeti, "Design considerations for an inverter output filter to mitigate the effects of long motor leads in ASD applications," *IEEE Trans. Ind. Appl.*, vol. 33, no. 5, pp. 1138-1145, Sept.-Oct. 1997.
- [117] D. A. Rendusara and P. N. Enjeti, "An improved inverter output filter configuration reduces common and differential modes dv/dt at the motor terminals in PWM drive systems," *IEEE Trans. Power Electron.*, vol. 13, no. 6, pp. 1135-1143, Nov. 1998.
- [118] P. Mishra and R. Maheshwari, "Design, analysis, and impacts of sinusoidal LC filter on pulsewidth modulated inverter fed-induction motor drive" *IEEE Trans. Ind. Electron.*, vol. 67, no. 4, pp. 2678-2688, April 2020.
- [119] Y. Sozer, D. A. Torrey and S. Reva, "New inverter output filter topology for PWM motor drives," in *IEEE Trans. Power Electron.*, vol. 15, no. 6, pp. 1007-1017, Nov. 2000.
- [120] M. M. Swamy, J.-K. Kang, and K. Shirabe, "Power loss, system efficiency and leakage current comparison between Si IGBT VFD and SiC FET VFD with various filtering options," *IEEE Trans. Ind. Appl.*, vol. 51, no. 5, pp. 3858-3866, Sep./Oct. 2015.
- [121] S. Baek, Y. Cho, B. Cho and C. Hong, "Performance comparison between two-level and three-level SiC-based VFD applications with output filters" *IEEE Trans. Ind. Appl.*, vol. 55, no. 5, pp. 4770-4779, Sept.-Oct. 2019.
- [122] J. He, G. Y. Sizov, P. Zhang and N. A. O. Demerdash, "A review of mitigation methods for overvoltage in long-cable-fed PWM AC drives", in *Proc. IEEE Energy Conversion Congress and Exposition (ECCE)*, Arizona, USA, 2011, pp. 2160-2166.
- [123] Motors and Generators, NEMA MG1-2016 Part 31, 2016.
- [124] S. Ogasawara and H. Akagi, "Modeling and damping of high-frequency leakage currents in PWM inverter-fed AC motor drive systems," *IEEE Trans. Ind. Appl.*, vol. 32, no. 5, pp. 1105-1114, Sept.-Oct. 1996.

-
- [125] Y. Murai, T. Kubota, and Y. Kawase, "Leakage current reduction for a high-frequency carrier inverter feeding an induction motor," *IEEE Trans. Ind. Appl.*, vol. 28, pp. 858–863, July/Aug. 1992.
- [126] M. M. Swamy, K. Yamada and T. Kume, "Common mode current attenuation techniques for use with PWM drives," *IEEE Trans. on Power Electron.*, vol. 16, no. 2, pp. 248-255, March 2001.
- [127] J. Xue, F. Wang, and W. Chen, "A study of motor-end EMI filter on output common-mode noise suppression in DC-fed motor drive system" in *Proc. 28th Annu. IEEE Appl. Power Electron. Conf. Expo. (APEC)*, Indonesia, pp. 1556–1561, Mar. 2013.
- [128] H. Akagi and T. Doumoto, "An approach to eliminating high-frequency shaft voltage and ground leakage current from an inverter-driven motor," *IEEE Trans. Ind. Appl.*, vol. 40, no. 4, pp. 1162-1169, July-Aug. 2004.
- [129] X. Chen, D. Xu, F. Liu and J. Zhang, "A Novel Inverter-Output Passive Filter for Reducing Both Differential- and Common-Mode dv/dt at the Motor Terminals in PWM Drive Systems," *IEEE Trans. Ind. Electron.*, vol. 54, no. 1, pp. 419-426, Feb. 2007.
- [130] R. M. Tallam, G. L. Skibinski, T. A. Shudarek and R. A. Lukaszewski, "Integrated Differential-Mode and Common-Mode Filter to Mitigate the Effects of Long Motor Leads on AC Drives," *IEEE Trans. on Ind. Appl.*, vol. 47, no. 5, pp. 2075-2083, Sept.-Oct. 2011.
- [131] S. Ogasawara, H. Ayano and H. Akagi, "An active circuit for cancellation of common-mode voltage generated by a PWM inverter," *IEEE Trans. Power Electron.*, vol. 13, no. 5, pp. 835-841, Sept. 1998.
- [132] W. Chen, X. Yang, J. Xue and F. Wang, "A Novel Filter Topology With Active Motor CM Impedance Regulator in PWM ASD System," *IEEE Transactions on Industrial Electronics*, vol. 61, no. 12, pp. 6938-6946, Dec. 2014.
- [133] S. Ogasawara and H. Akagi, "Circuit configurations and performance of the active common-noise canceller for reduction of common-mode voltage generated by voltage-source PWM inverters," in *Proc. IEEE IAS Annu. Meeting*, 2000, vol. 3, pp. 1482–1488.

-
- [134] Matthew N. O. Sadiku and S. V. Kulkarni, *Principles of electromagnetics*, 3rd ed., USA, Oxford University Press, 2015.
- [135] D. Han, S. Li, Y. Wu, W. Choi, et al., “Comparative analysis on conducted CM EMI emission of motor drives: WBG versus Si devices,” *IEEE Trans. Ind. Electron.*, vol. 64, no. 10, pp. 8353-8363, Oct. 2017.
- [136] Y. Xu, X. Yuan, F. Ye, *et al.*, “Impact of high switching speed and high switching frequency of wide-bandgap motor drives on electric machines,” *IEEE Access*, vol. 9, pp. 82866-82880, 2021.
- [137] ANSYS Maxwell— Release Version 20.2. “Maxwell help” in ANSYS, Canonsburg, PA, 2020.
- [138] R. D. Cook, D. S. Malkus, M. E. Plesha and R. J. Witt, *Concepts and applications of finite element analysis*, 4th ed., USA, John Wiley & Sons, 2001.
- [139] H. De Paula, D. A. d. Andrade, M. L. R. Chaves, J. L. Domingos, and M. A. A. de Freitas, “Methodology for cable modeling and simulation for high-frequency phenomena studies in PWM motor drives,” *IEEE Trans. Power Electron.*, vol. 23, pp. 744-752, Mar. 2008.
- [140] B. Gustavsen and A. Semlyen, “Rational approximation of frequency domain responses by Vector Fitting,” *IEEE Trans. Power Del.*, vol. 14, no. 3, pp. 1052-1061, July 1999.
- [141] H. Akagi and S. Tamura, “A passive EMI filter for eliminating both bearing current and ground leakage current from an inverter-drive motor,” *IEEE Trans. Power Electron.*, vol. 21, no. 5, pp. 1459–1469, Sep. 2006.
- [142] S. Chen and T. Lipo, “Circulating type motor bearing current in inverter drives,” *IEEE Ind. Appl. Mag.*, vol. 4, no. 1, pp. 32–38, Jan./Feb. 1998.
- [143] T. Plazenet, T. Boileau, C. Caironi and B. Nahid-Mobarakeh, “A comprehensive study on shaft voltages and bearing currents in rotating machines” *IEEE Trans. Ind. Appl.*, vol. 54, no. 4, pp. 3749-3759, July-Aug. 2018.
- [144] A. D. Podoltsev, K. G. N. B. Abeywickrama, Y. V. Serdyuk and S. M. Gubanski, “Multiscale Computations of Parameters of Power Transformer Windings at High Frequencies. Part I: Small-Scale Level,” *IEEE Trans. Mag.*, vol. 43, no. 11, pp. 3991-3998, Nov. 2007.

-
- [145] K. G. N. B. Abeywickrama, T. Daszczyński, Y. V. Serdyuk and S. M. Gubanski, “Determination of Complex Permeability of Silicon Steel for Use in High-Frequency Modeling of Power Transformers,” *IEEE Trans. on Mag.*, vol. 44, no. 4, pp. 438-444, April 2008.
- [146] Magnetic materials-Part 2: Methods of measurement of the magnetic properties of electrical steel strip and sheet by means of an Epstein frame, IEC 604044-2:1998+A1:2008, 2008.
- [147] T. Humiston and P. Pillay, “Parameter measurements to study surge propagation in induction machines,” *IEEE Trans. Ind. Appl.*, vol. 40, no. 5, pp. 1341-1348, Sept.-Oct. 2004.
- [148] A. Hoffmann, B. Knebusch, J. O. Stockbrügger, J. Dittmann and B. Ponick, “High-frequency analysis of electrical machines using probability density functions for an automated conductor placement of random-wound windings,” in *Proc. International Electric Machines & Drives Conference (IEMDC)*, 2021, pp. 1-7.
- [149] A. Boglietti, A. Cavagnino, M. Lazari, “Experimental high-frequency parameter identification of AC electrical motors,” *IEEE Trans Ind. Appl.*, vol. 43, no. 1, pp. 23-29, January/February 2007.
- [150] Y. Li, P. A. A. F. Wouters, P. Wagenaars, P. C. J. M. van der Wielen and E. F. Steennis, “Temperature dependent signal propagation velocity: possible indicator for mv cable dynamic rating,” in *IEEE Trans. Dielectrics Electrical Insul.*, vol. 22, no. 2, pp. 665-672, April 2015.
- [151] W. Zhou, M. S. Diab and X. Yuan, “Impact of parasitics and load current on the switching transient time and motor terminal overvoltage in SiC-based drives,” in *Proc. IEEE Energy Conversion Congress and Exposition (ECCE)*, Detroit, Michigan, USA, 2020, pp. 225-232.
- [152] O. Magdun, A. Binder, C. Purcarea, A. Rocks and B. Funieru, “Modeling of asymmetrical cables for an accurate calculation of common mode ground currents,” in *Proc. IEEE Energy Conversion Congress and Exposition (ECCE)*, San Jose, CA, USA, 2009, pp. 1075-1082.

-
- [153] M. Pastura *et al.*, “Partial discharges in electrical machines for the more electric aircraft—Part I: A comprehensive modeling tool for the characterization of electric drives based on fast switching semiconductors,” *IEEE Access*, vol. 9, pp. 27109-27121, 2021.
- [154] N. S. Nise, *Control System Engineering*, 7th ed. Hoboken, New Jersey, John Wiley & Sons, Inc., 2015.
- [155] B. Wu, M. Narimani, *High-Power Converters and AC Drives*, 2nd ed., Hoboken, New Jersey, John Wiley & Sons, Inc., 2017.
- [156] C. Petrarca, A. Maffucci, V. Tucci, *et al.*, “Analysis of the voltage distribution in a motor stator winding subjected to steep-fronted surge voltages by means of a multiconductor lossy transmission line model,” *IEEE Trans. Energy Convers.*, vol. 19, no. 1, pp. 7-17, March 2004.
- [157] S. M. Lambert, B. C. Mecrow, R. Abebe, G. Vakil and C. M. Johnson, “Integrated Drives for Transport - A Review of the Enabling Electronics Technology,” in *Proc. IEEE Vehicle Power and Propulsion Conference (VPPC)*, Montreal, Canada, 2015, pp. 1-6.
- [158] W. Zhou and X. Yuan, “Experimental Evaluation of SiC Mosfets in Comparison to Si IGBTs in a Soft-Switching Converter,” *IEEE Trans. Ind. Appl.*, vol. 56, no. 5, pp. 5108-5118, Sept.-Oct. 2020.
- [159] O. V. Thorsen and M. Dalva, “Interaction of system parameters on AC motor transients in PWM inverter drives,” in *Proc. IEEE International Electric Machines and Drives Conference (IEMDC)*, Cambridge, MA, USA, 2001, pp. 300-303.
- [160] M. Schweizer, I. Lizama, T. Friedli and J. W. Kolar, “Comparison of the chip area usage of 2-level and 3-level voltage source converter topologies,” in *Proc. IEEE 36th Annual Conference on IEEE Industrial Electronics Society (IECON)*, Glendale, AZ, 2010.
- [161] M. Schweizer and J. W. Kolar, “Design and implementation of a highly efficient three-level T-type converter for low-voltage applications,” *IEEE Trans. Power Electron.*, vol. 28, no. 2, pp. 899-907, Feb. 2013.

-
- [162] S. Lee and K. Nam, "An overvoltage suppression scheme for AC motor drives using a half-DC-link voltage level at each PWM transition," *IEEE Trans. Ind. Electron.*, vol. 49, no. 3, pp. 549-557, June 2002.
- [163] M. S. Diab and X. Yuan, "A quasi-three-level PWM scheme to combat motor overvoltage in SiC-based single-phase drives," *IEEE Trans. Power Electron.*, vol. 35, no. 12, pp. 12639-12645, Dec. 2020.
- [164] H. Akagi and S. Tamura, "A passive EMI filter for eliminating both bearing current and ground leakage current from an inverter-drive motor," *IEEE Trans. Power Electron.*, vol. 21, no. 5, pp. 1459-1469, Sep. 2006.
- [165] K. Hatua, A. K. Jain, D. Banerjee, and V. T. Ranganathan, "Active damping of output LC filter resonance for vector-controlled VSI-fed AC motor drives," *IEEE Trans. Ind. Electron.*, vol. 59, no. 1, pp. 334-342, Jan. 2012.
- [166] D. Zhang, T. Fan, P. Ning and X. Wen, "An automatic EMI filter design methodology for electric vehicle application," in *Proc. IEEE Energy Conversion Congress and Exposition (ECCE), Cincinnati, Ohio, USA*, pp. 4497-4503, 2017.
- [167] L. Zhai, G. Hu, C. Song, M. Lv and X. Zhang, "Comparison of two filter design methods for conducted EMI suppression of PMSM drive system for electric vehicle," *IEEE Trans. Vehicular Tech.*, vol. 70, no. 7, pp. 6472-6484, July 2021.
- [168] Mellor, P.H., "Voltage transients in power electronic controlled AC machines", in *Proc. IEE 3rd Int. Elect. Mach. and Drives Conf.*, 1987, 282, p. 216-220.
- [169] I. Tsyokhla, A. Griffo and J. Wang, "Online Condition Monitoring for Diagnosis and Prognosis of Insulation Degradation of Inverter-Fed Machines," *IEEE Trans. Ind. Electron.*, vol. 66, no. 10, pp. 8126-8135, Oct. 2019.
- [170] W. Hofheinz, *Protective Measures with Insulation Monitoring Application of Unearthed IT Power Systems in Industry, Mining, Railways, Marine/ Oil and Electric/Rail Vehicles*, 3rd ed, VDE Verlag, 2006.
- [171] Datasheets, Schaffner Group, pp 1-4 [Online] Available: <https://www.schaffner.com/product-storage/datasheets/fn-510/> Accessed On: Jan. 2022.
- [172] Motors and Generators, NEMA MG1-2016, 2016.

